Operando Characterization of Supported Alloy Nanoparticles during Catalytic CO Oxidation by Surface Sensitive X-Ray Diffraction

Dissertation with the aim of achieving a doctoral degree

at the Faculty of Mathematics, Informatics and Natural Sciences

Department of Physics

of Universität Hamburg

submitted by

Uta Elisabeth Hejral

2015 in Hamburg

Gutachter der Dissertation:
Prof. Dr. A. Stierle
Prof. Dr. W. Wurth

Gutachter der Disputation:
Prof. Dr. A. Stierle
Prof. Dr. W. Wurth
Prof. Dr. E. Lundgren
Prof. Dr. P. Gaal

Vorsitzende der Prüfungskommission:
Prof. Dr. D. Pfannkuche

Tag der Disputation:
30. November 2015

Eidesstattliche Versicherung

Declaration on oath

Hiermit erkläre ich an Eides statt, dass ich die vorliegende Dissertationsschrift selbst verfasst und keine anderen als die angegebenen Quellen und Hilfsmittel benutzt habe.

I hereby declare, on oath, that I have written the present dissertation by my own and have not used other than the acknowledged resources and aids.

Hamburg, den *city and date* *Unterschrift* *signature*

Abstract

Noble metal nanoparticles (Pt, Rh, Pd, and alloys thereof) supported on oxide carrier materials are widely employed as heterogeneous catalysts with applications ranging from exhaust gas treatment in cars (CO oxidation, NO_x reduction) to the preferential oxidation of CO in low temperature fuel cells.

To improve the catalyst efficiency, selectivity and lifetime an understanding of the atomic level processes that occur during catalytic reactions is essential. Accordingly, the interplay between changes in the catalytic activity, the emergence of oxide phases on the nanoparticle facets and the particle structure needs to be unraveled. Particle sintering - i.e. the agglomeration of smaller particles into larger ones - is viewed as one of the main causes for catalyst deactivation, and a detailed knowledge of its mechanism is required. Special attention has in recent years been paid to the use of alloy metal particles (Pt-Rh, Pt-Pd, Rh-Pd) as promising systems for improving and tailoring catalyst characteristics.

The objective of this thesis was the structural characterization of supported single and alloy metal nanoparticles during catalytic CO oxidation reactions ($2CO+O_2 \rightarrow 2CO_2$) at ambient pressures by means of surface sensitive x-ray diffraction. The sample environment was created inside the flow reactor of a dedicated in-situ catalysis chamber. It allowed the direct correlation of the sample structure, encoded in the x-ray data, to the sample's catalytic activity, monitored by in-situ mass spectrometry.

The samples consisted of supported Pt-Rh and Pt-Pd alloy particles with varying compositions and sizes. They were epitaxially grown by means of physical vapour deposition on oxide single crystal supports ($MgAl_2O_4(001)$ and α-$Al_2O_3(0001)$), where the choice of substrate also determined the particle epitaxy. Moreover, it was concluded that the particle shape can be systematically influenced by the alloy composition, where Pt-rich particles feature small, Rh-rich and Pd-rich particles high height-to-diameter aspect ratios. Accordingly, a variety of samples with different characteristics were prepared, which allowed the systematic investigation of particle growth as well as the structural changes that the particles undergo during catalytic CO oxidation.

For the samples' investigation during catalytic activity, x-rays of two different energy regimes were employed.

Using x-rays of conventional photon energies (E=11.2 keV), high resolution reciprocal space maps and linescans through particle Bragg peaks were measured with a point detector, which allowed for the first time to track and quantitatively analyze the oxygen-induced shape changes of $MgAl_2O_4$(001)-supported $Pt_{0.33}Rh_{0.67}$ alloy particles under reaction conditions. It was concluded that the (001)-type particle facets increase due to the formation of the c(2×8) Rh surface oxide, while the (111)-type facets shrink despite the formation of the p(9×9) Rh surface oxide. Time-resolved measurements on oxide signals while changing the gas composition allowed for the operando monitoring of the formation and dissolution of oxide phases on the nanoparticle facets, and provided the possibility to identify the c(2×8) Rh surface oxide as the catalytically most active phase.

For the first time, high energy surface x-ray diffraction (E=78-85 keV) was employed to investigate combinatorial samples during catalytic activity, where 2D detectors allowed the time-resolved measurement of large reciprocal space areas without the need to scan. The study of the shape- and composition-dependent sintering behaviour of α-Al_2O_3(0001)- and $MgAl_2O_4$(001)-supported alloy particles (Pt-Rh, Pt-Pd) under identical sample conditions revealed that the extent of sintering depends on the initial particle shape: Pt-rich, disk-like particles were concluded to be most prone to sintering and were found to double their heights at the expense of the particle coverage on the sample surface, while keeping their diameter constant. Contrary, the sintering in height was found to be progressively reduced for particles with increasing Rh or Pd content. This implies that Rh-rich and Pd-rich particles adopt stable equilibrium shapes, characterized by a large height to diameter aspect ratio, already during growth, while the Pt-rich and originally flat particles use the energy released in the catalytic reaction to adopt this stable shape.

Zusammenfassung

Edelmetall-Nanopartikel (Pt, Rh, Pd, sowie deren Legierungen) auf Oxidträgermaterialien finden als heterogene Katalysatoren vielfältigen Einsatz in der Automobilabgasreinigung (CO Oxidation, NO_x Reduktion) oder bei der selektiven CO Oxidation in Niedertemperaturbrennstoffzellen.

Um eine höhere Effizienz, Selektivität und Lebensdauer der Katalysatoren zu gewährleisten ist es wichtig, die bei der Katalyse ablaufenden Prozesse auf atomarer Skala zu verstehen. So ist es erstrebenswert den Zusammenhang zwischen Änderungen in der katalytischen Aktivität, der Ausbildung von Oxidphasen auf den Partikelfacetten und der Partikelstruktur zu erfassen. Zur Verringerung der Katalysatordeaktivierung ist ein detailiertes Vertändnis der zugrunde liegenden Mechanismen notwendig, wobei Partikelsintern - das Zusammenwachsen kleinerer Partikel zu größeren - eine der Hauptursachen darstellt. In jüngster Zeit sind insbesondere Legierungsnanopartikel (Pt-Rh, Pt-Pd, Rh-Pd) in den Fokus der Forschung gerückt, da sie vielversprechende Systeme bezüglich der Verbesserung und der gezielten Entwicklung von Katalysatoren darstellen.

Diese Promotionsarbeit hat sich die strukturelle Charakterisierung von geträgerten Edelmetall- und Legierungsnanopartikeln während des Ablaufs katalytischer CO Oxidationsreaktionen ($2CO+O_2 \rightarrow 2CO_2$) in anwendungsnahen Druckbereichen mittels oberflächensensitiver Röntgenbeugung zum Ziel gesetzt. Die Probenumgebung wurde mit einer in-situ Katalysekammer geschaffen, deren kleines Reaktorvolumen die Untersuchung der Probe im Gasdurchfluss ermöglichte. Der experimentelle Aufbau erlaubte somit die direkte Korrelation zwischen der aus den Röntgendaten gewonnenen strukturellen Änderungen der Legierungspartikel und der durch in-situ Massenspektrometrie ermittelten katalytischen Aktivität.

Die untersuchten Proben enthielten Legierungspartikel unterschiedlicher Größe und Legierungskonzentration (Pt-Rh, Pt-Pd, Pd-Rh) und wurden mittels physikalischer Gasphasenabscheidung auf Oxideinkristalloberflächen epitaktisch gewachsen, wobei durch die Wahl des jeweiligen Substrats ($MgAl_2O_4$(001) oder α-Al_2O_3(0001)) die Wachstumsrichtung der Partikel bestimmt werden konnte. Außerdem zeigte sich, dass die Form der Partikel systematisch durch den Legierungsgehalt beeinflusst werden kann, wobei Pt-reiche Partikel durch ein niedriges, Rh- und Pd-reiche Partikel hingegen durch ein großes Höhe-zu-Durchmesser Verhältnis gekennzeichnet sind. Somit konnte eine Vielzahl an Proben unterschiedlicher Charakteristika hergestellt werden, die eine systematische Untersuchung des Wachstums der Partikel sowie deren struktureller Änderungen während CO Oxidation ermöglichten.

Die Untersuchung der Proben während katalytischer Aktivität wurde mit Röntgenstrahlen zwei verschiedener Energiebereiche durchgeführt.

Unter Verwendung konventioneller Photonenenergie (E=11.2 keV) wurden mit einem Punktdetektor hochaufgelöste reziproke Gittermappen und Linienscans durch Partikel-Braggreflexe aufgenommen, die die Beobachtung und quantitative Analyse Sauerstoff-induzierter Formänderungen von $MgAl_2O_4$(001)-geträgerten $Pt_{0.33}Rh_{0.67}$ Legierungspartikeln während Reaktionsbedingungen erstmals ermöglichten. So zeigte sich, dass sich die (001)-Facetten der Partikel unter Bildung des c(2×8) Rhodiumoberflächenoxids vergrößern, während die (111)-Facetten trotz der Bildung des p(9×9) Rhodiumoberflächenoxids an Fläche verlieren. Durch zeitaufgelöste operando Messungen an Oxidsignalen während der Änderung der Gaszusammensetzung konnte die Bildung und Auflösung der Oxidphasen auf den Nanopartikelfacetten während Reaktionsbedingungen verfolgt werden, wobei das c(2×8) Rhodiumoberflächenoxid durch in-situ Massenspektrometrie als katalytisch aktivste Phase identifiziert wurde.

Unter Verwendung von hochenergetischer Röntgenstrahlung (E=78-85 keV) wurden erstmals kombinatorische Proben während katalytischen Bedingungen untersucht, wobei 2D Detektoren die zeitaufgelöste Messung von Mappen größerer reziproker Gitterbereiche, ohne die Notwendigkeit zu Scannen, ermöglichten. Die Erforschung des form- und konzentrationsabhängigen Sinterverhaltens der α-Al_2O_3(0001)- und $MgAl_2O_4$(001)- geträgerten Legierungspartikel (Pt-Rh, Pt-Pd) unter identischen Bedingungen zeigte, dass die Stärke des Sinterns von der anfänglichen Partikelform abhängt: Während Pt-reiche, flache Partikel am stärksten sintern und ihre Höhe auf Kosten der prozentualen Substratbedeckung bei gleichbleibendem Durchmesser verdoppeln, nimmt die

sinterbedingte Höhenzunahme der Partikel mit zunehmender Rh- oder Pd-Konzentration kontinuierlich ab. Dies deutet darauf hin, dass Rh- und Pd-reiche Partikel bereits nach dem Wachstum in einer stabilen Gleichgewichtsform, charakterisiert durch ein größeres Höhe-zu-Durchmesser Verhältnis, vorliegen, während die anfänglich flachen Pt-reichen Partikel die bei der Reaktion frei werdende Energie verwenden um diese stabilere Form zu erreichen.

Contents

Chapter 1

Introduction

> *'Many bodies ...have the property of exerting on other bodies an action...... By means of this action they produce decomposition in bodies, and form new compounds into the composition of which they do not enter. This new power, hitherto unknown.....I shall ....call it **catalytic power**. I shall also call **catalysis** the decomposition of bodies by this force.'* [1]
>
> ——— J. J. Berzelius (1836) ————

One hundred and eighty years ago it was still a feasible task for one man to write an annual report on the progress of the whole field of chemistry [2]. In 1836, this task was accomplished by the Swedish chemist J. J. Berzelius, who, after revising earlier works of other scientists, coined the term *catalysis*. By today, Berzelius' 'catalytic power' has attracted various Nobel prizes[1] and has become an integral part not only of chemical industry, but also of numerous scientific disciplines ranging from materials technology to life sciences.

Hence, more than 90% of all fine chemicals worldwide are today produced by the aid of catalysts. The increasing demand for the application of catalyst materials in fuel cells, gas sensors and exhaust control systems makes them essential for the population's energy supply and the protection of the environment. And it is the catalysis-based production of ammonia used in fertilizers that guarantees the required vegetable food of two thirds of the world's steadily growing population.

---

[1]

Wilhelm Ostwald, 1909
Fritz Haber, 1918, and Carl Bosch, 1931
Irving Langmuir, 1932
Gerhard Ertl, 2007

The wide application makes catalysis also an economic issue. Hence, the global demand on catalysts was valued at 33.5 billion US dollar in 2014 [3]. A further increase of this number can be expected in future years due to the worldwide scarcity of noble metals, which are mostly used as catalyst material, and due to increasing environmental regulations and the call for green chemistry. Accordingly, catalyst deactivation constitutes a severe economic concern, since the costs to industry for catalyst renewal and process shutdown are estimated to amount to tens of billions per year.

The above mentioned clarifies the needs for a sustainable handling of catalyst material and for improvements in catalyst performance, characterized by an increase in catalyst *activity*, in *selectivity* towards desired chemical reactions, and by the prolongation of catalyst *lifetime* by suppressing catalyst deactivation mechanisms.

To achieve these characteristics, a thorough understanding of the processes that occur on an atomic level during catalytic reactions is required. The deduction of this atomistic view by means of experimental and theoretical investigations is, however, hampered by the complexity of both, the catalyst material system and the environment surrounding the catalyst during reaction conditions. Hence, most catalyst systems currently employed are mainly the result of trial and error procedures.

The top part of Fig. 1.1 illustrates the interior of a three-way catalyst employed for exhaust gas treatment (CO oxidation, NO_x reduction, oxidation of unburnt hydrocarbons H_mC_n) in cars, which is typical of the inner life of catalysts in general. Each of its constituents is designed to increase the effective catalyst surface area. Hence, the catalyst materials (Pt, Rh, Pd) are in the form of particles, typically in the size range of 1-10 nm, and dispersed onto oxide carriers, mainly Al_2O_3 but also other oxides such as CeO_x, TiO_2 or SiO_2, featuring irregular, highly branched surfaces.

As can be inferred from the cross section TEM image in Fig. 1.1, the catalyst particles are terminated by particle facets, which correspond to crystal planes. Since the particles usually feature different sizes and orientations, different crystal surfaces, along with edges and corners, are exposed to the gas mixture inside the catalytic converter. Instead of solely using monometallic particles, bimetallic particles (Pt-Rh, Pt-Pd, Rh-Pd) are increasingly employed in addition. They are expected to display enhanced catalytic properties due to synergetic effects between the parent metals, but add a further level of

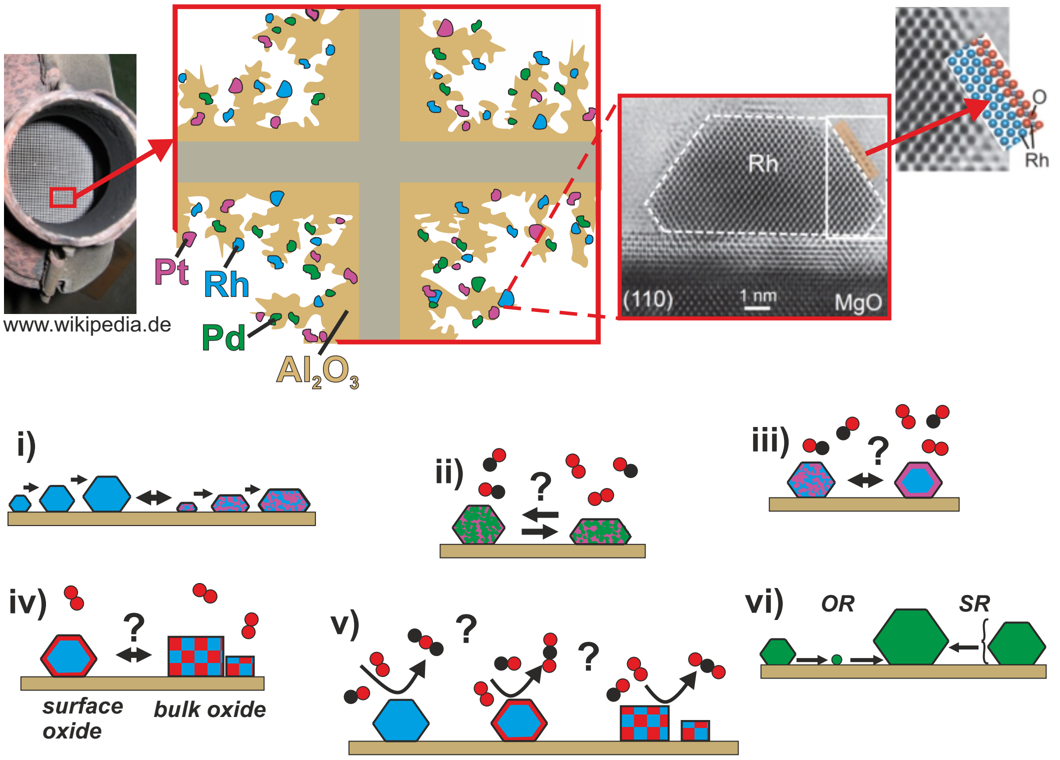

Figure 1.1: **Catalyst interior and atomic-level processes during reaction: top:** sequence of close ups on the precious metal particles dispersed on oxide carriers, the right side displays a cross-section TEM image of a MgO(001)-supported Rh nanoparticle and the O-Rh-O trilayer surface oxide on the particle (111)-type side facet [4]; **bottom:** potential atomic-level processes for alloy particles addressed in this thesis (see text for more information).

complexity to the catalyst material system. During operation the catalytic converter is exposed to gases in the ambient pressure regime, including CO, NO_x, H_mC_n as well as the reaction products CO_2, N_2 and H_2O, typically at elevated temperatures between 800 K up to 1300 K.

Key questions

To tackle the problem, early surface science studies investigated rather simple model catalysts systems, usually single crystal surfaces mimicking the corresponding particle facets, under controlled low pressure conditions. This opened the so-called *pressure- and materials gap* (see Fig. 1.2), since it is not sure whether the obtained results are also valid for high pressures and for the high material complexity of real catalyst systems. With the advent of high-pressure compatible in-situ techniques (HP-STM, HP-AFM, EXAFS, SXRD, HESXRD, SFG, PM-IRAS) and the investigation of more complicated sample systems, such as vicinal surfaces and supported nanoparticles, the gaps are being progressively bridged.

Despite past progresses, there is still a tremendous need for investigations in this field, especially with respect to supported nanoparticles under *realistic catalytic reaction conditions*. Moreover, while monometallic systems have been vastly studied in the past, the study of alloy systems, especially of *alloy nanoparticles*, is still at its infancy. Accordingly, there is a lack of structure-sensitive studies for the investigation of alloy nanoparticles during catalytic reactions as well as for tracing potential catalytically active phases.

The following key questions constitute central aspects that are vital for a deeper understanding of catalytic processes on the atomic level, and have been addressed in the framework of this thesis. They are depicted at the bottom of Fig. 1.1.

i **Tailoring of monometallic and alloy catalyst particles**

Detailed knowledge about the growth mechanisms of catalyst particles are of utmost importance in two respects: (1) it provides the possibility to grow numerous test samples with differing characteristics, (2) once catalyst particles with improved characteristics are identified, they can be reproduced. What is the result of differing treatments to the substrate surfaces (e.g. presence of surface defect sites, adsorbates) and to which extent do they influence the nanoparticle growth? Can the presence of internal particle defects, the growth of tilted particles and of minor epitaxies be suppressed? Which effect does alloying have on the particle shape and growth in general? How does the particle shape evolve during growth and what is the influence of the alloying state? How does seeding, i.e. the sequential deposition of two metals, influence the particle characteristics?

ii **Reaction-induced shape changes of alloy particles at near ambient pressures**

Monometallic particles undergo adsorption-induced shape changes when the gaseous environment changes during catalytic reactions. Comparable operando measurements addressing the structural changes of alloy particles are lacking so far, especially close to ambient pressures. Which shape changes do they undergo and under which conditions do they occur? Are they solely induced by gas adsorption or are there also other driving forces?

iii **Segregation effects under reaction conditions**
Apart from the morphological particle changes addressed in ii), alloy particles may also be prone to chemical restructuring driven by changes in the gas environment during catalytic reactions. Does segregation of a certain element to the particle surface occur? Does phase separation for Pt-Rh particles into their parent metals take place, as can be expected from the miscibility gap in the Pt-Rh bulk alloy phase diagramme, or are these elements miscible due to finite size effects in nanoparticles?

iv **Oxide formation on alloy nanoparticles**
While there are several investigations on the oxidation of monometallic particles to be found in literature, the study of oxide formation on alloy particles is still at its infancy. Do the same type of oxide structures (thin 2D surface oxides, thick 3D bulk oxides), known from monometal oxidation, also form on bimetallic structures? Under which conditions (p_{gas}, T) do they form and can they be lifted again under reducing conditions?

v **Catalytically active phases**
For catalytic oxidation reactions at ambient pressures it has not yet been generally solved whether it is oxygen chemisorbed on the particle facets, thin surface oxide layers or 3D bulk oxides that are catalytically most active. Which is the catalytically most active phase and under which conditions is it stable? Are there phases whose emergence leads to a decrease in the catalytic production rate, i.e. by means of poisoning?

vi **Catalyst deactivation**
One of the main reasons for catalyst deactivation is the loss of effective catalyst surface area due to particle sintering, i.e. the coalescence of smaller particles into larger ones. The two main scenarios discussed in literature are sintering by means of (1) atomic transport from smaller to larger particles ('Ostwald ripening') or (2) the coalescence of two particles ('Smoluchowksi ripening'). Which is the predominant sinter mechanism during CO oxidation or are there other potential scenarios? How can sintering be suppressed? What is the influence of the alloying state, the shape of the particles or the substrate?

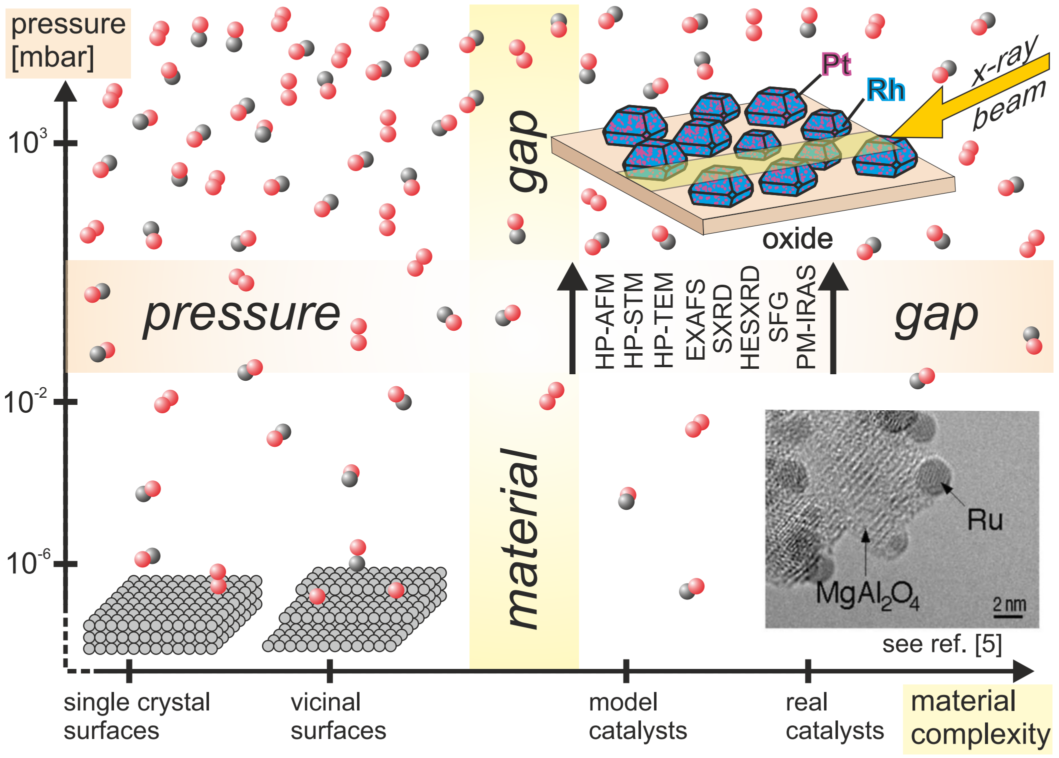

Figure 1.2: **Pressure and materials complexity gap:** in this thesis, the materials gap was bridged by epitaxial monometallic and alloy nanoparticles supported on oxide single crystals; the pressure gap by using x-ray diffraction to study the samples inside an ambient pressure flow reactor; the inset shows a HRTEM micrograph of a Ba-Ru/$MgAl_2O_4$ catalyst [5].

Experimental strategy

To address the aforementioned key questions of this thesis, monometallic and alloy nanoparticles supported on oxide substrates were investigated during catalytic CO oxidation ($2CO+O_2 \rightarrow CO_2$) at ambient pressures (typically p_{tot}=50-200 mbar) by means of surface sensitive x-ray diffraction, thus bridging the pressure and materials complexity gap. The sample environment was created inside a flow reactor of a dedicated in-situ catalysis chamber, which allows for simultaneous x-ray diffraction and in-situ mass spectrometry measurements, hence providing the possibility to correlate potential structural changes of the sample or the emergence of transient phases to variations in the measured catalytic activity.

Using either $MgAl_2O_4(001)$ or α-$Al_2O_3(0001)$ as particle support provided the possibility to trigger the growth of differently shaped particles, featuring either truncated octahedral shapes with (100)-type facets at the interface, or rather disk-like shapes with (111)-type facets at the interface, respectively. Furthermore, growing particles with different sizes and/or alloy compositions (mainly Pt-Rh and Pt-Pd) as well as by making use of the sequential deposition of two materials ("core-shell" particles) provided the possibility to systematically study the growth and the particles' behaviour during catalytic reactions as a function of various particle parameters.

In terms of surface sensitive x-ray diffraction, two different photon energy regimes were used.

In the approach using conventional energies (E≈10 keV), the measurement of high resolution reciprocal space maps and of high resolution linescans through particle Bragg peaks along high symmetry directions with a point detector allowed for retrieving the qualitative and quantitative particle shape and shape changes during reaction conditions. The repeated performance of reference scans for potential oxide phases while changing gas composition allowed for ascribing changes in the sample's catalytic activity to the emergence of certain oxide phases.

In the high energy approach (E≈80 keV) the fast (on the order of seconds) mapping of large area reciprocal space maps with a 2D detector while changing gas compositions was used as an operando probe for potential changes in the particle diffraction pattern and hence in particle structure, such as sintering-induced height changes. Containing a large area of reciprocal space, the 2D maps yield moreover an immediate view on potential signals from other particle domains or internal particle defects and are accordingly appropriate for the study of particle growth. Thanks to the high energy, the diffraction angles are very small (typically on the order of 6°) and a focused beam at the sample position allows for studying individual particle stripes of combinatorial samples at a time, hence providing the possibility to investigate various particle sizes/alloy compositions under identical reaction conditions.

For both energy regimes the beam size is large enough to cover large particle ensembles, hence the obtained data represents in each case the statistical behaviour of the studied sample.

Outline of this thesis

All of the aforementioned key questions were addressed in the course of this thesis and the corresponding findings are discussed in the chapters presenting the experimental results (chapters 6-8).

The results with respect to nanoparticle growth (i) of the different sample systems are summarized in chapter 6. Oxygen-induced shape changes (ii) of

$MgAl_2O_4(001)$-supported $Pt_{0.33}Rh_{0.67}$ particles during reaction conditions as well as sintering-induced and composition-dependent shape changes (ii) of α-$Al_2O_3(0001)$-supported Pt-Rh alloy particles are subject matter of sections 7.1-7.3 and 8.1-8.2, respectively. Segregation effects (iii) for changing sample environments have been addressed for almost all sample systems investigated under catalytic reaction conditions in terms of tracing the respective particle lattice parameters. The results for the various systems can be found in sections 7.3, 8.1.6 and 8.2.2. For $MgAl_2O_4(001)$-supported $Pt_{0.33}Rh_{0.67}$ particles, the formation of various oxide structures (iv) during different conditions for catalytic CO oxidation has been investigated and correlated to the sample's catalytic activity, yielding information on the catalytically most active phase (v), the respective results are subject matter of section 7.2. Operando particle sintering and hence catalyst deactivation (vi) has been extensively studied for different Pt-Rh compositions of α-$Al_2O_3(0001)$-supported particles (see section 8.1), but has been addressed for other sample systems of this thesis as well (see sections 7.3, 7.4 and 8.2.1).

Chapter 2

Growth and Shape of Alloy Nanoparticles

All samples studied in this thesis consist of monometallic or alloy nanoparticles that were grown by means of physical vapour deposition on oxide substrates. The present chapter will yield an insight into the processes that occur on the atomic level during this deposition method (section 2.1). Special attention will be given to potential alloying patterns (section 2.2) and the thermodynamic and kinetic shapes (section 2.3) of the grown particles. The chapter will close with section 2.4, which considers the influence of the supports employed in this thesis, $MgAl_2O_4(001)$ and $\alpha\text{-}Al_2O_3(0001)$, on particle growth.

The general concepts on particle growth and shapes introduced in this chapter are based on review articles and books covering this topic [6, 7, 8, 9, 10, 11, 12, 13].

2.1 Principles of nucleation

In the following, the initial stages of nucleation and particle growth will be discussed; the corresponding atomic level processes are displayed in Fig. 2.1. The first step of particle growth is the adsorption of atoms from the vapour phase onto the sample surface, where it can be assumed that the atoms stick with almost unit probability [8]. Once adsorbed, an atom can either immediately re-evaporate into the vapour phase or diffuse along the substrate surface, typically until it hits a nucleation site. Depending on the nature of this site one distinguishes between homogeneous and heterogeneous nucleation [8].

In case of *homogeneous nucleation*, the atom agglomerates with one or more of

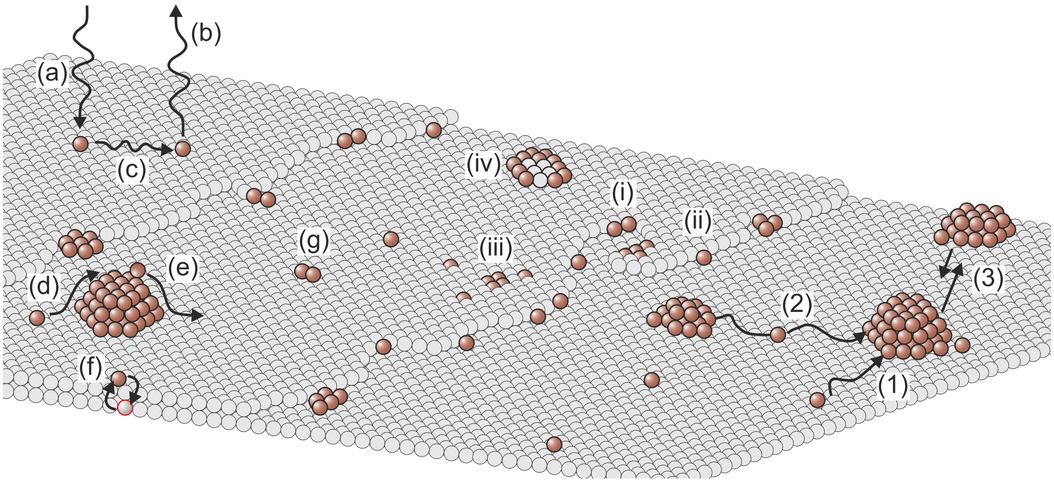

Figure 2.1: **Initial stages of particle growth on the atomic level:** they include atom **(a):** adsorption, **(b):** re-evaporation, **(c):** surface diffusion, **(d):** up-step diffusion, **(e):** down-step diffusion, **(f):** inter-diffusion, **(g):** homogeneous nucleation; centres for heterogeneous nucleation include substrate **(i):** kinks, **(ii):** steps, **(iii):** (oxygen) vacancies, **(iv):** adatoms; once stable nucleii have formed, the particle growth may proceed via **(1):** capturing diffusing adatoms, **(2):** Ostwald ripening, **(3):** particle coalescence.

the other adsorbed atoms to form a nucleus on a regular substrate site. Unless this nucleus reaches a *critical cluster size*, it is thermodynamically unstable and may dissolve again. Once the critical size is reached, the nucleus may incorporate further adatoms and grow, where 3D growth requires *supersaturation* $\xi = \frac{p}{p_0} > 1$, hence, a local vapour pressure p higher than the equilibrium vapour pressure p_0 [10]. A higher supersaturation ξ results in a smaller critical cluster size and in a higher saturation density N of nucleii [10], which represents the maximum number of nucleii forming on a surface. The relation $N \propto (F/D)^{1/3}$ holds, where F denotes the vapour flux of impinging atoms and D the atom diffusion coefficient, which scales with temperature and decreases as a function of adsorption energy [8].

The other borderline case, *heterogeneous nucleation*, is characterized by the trapping of diffusing adatoms at substrate defect sites such as kinks, steps, vacancies, adatoms or colour centres (see Fig. 2.1 (i)-(iv)). While homogeneous nucleation occurs especially in homoepitaxial systems, heterogeneous nucleation dominates heteroepitaxial growth, such as the one of metal particles on oxide substrates [8]. The latter bear a relatively high number of defects, often oxygen vacancies [14], which can be created by Ar ion sputtering [7]. For het-

erogeneous nucleation, the saturation density N is independent of the atomic flux F [8] but decreases with increasing temperature T [7] and can be increased by means of Ar ion sputtering [7].
Once the saturation density N is reached, no further particle nucleii are created and the actual growth process sets in. Whether it proceeds via a layer-by-layer ('Frank-van der Merwe'), layer-plus-particle ('Stranski-Krastanov') or pure particle ('Volmer-Weber') growth depends on the surface and interface energies γ_{oxide}, γ_{metal}, and $\gamma_{\mathrm{interface}}$ of the oxide substrate, the deposited metal and the created interface, respectively. They can also be interpreted as force per unit length ('surface tension') and are depicted in Fig. 2.6 b) for the simplified model of a supported and truncated sphere. The equilibrium force at the triple phase boundary can be expressed by means of the *Young equation*

$$\gamma_{\mathrm{oxide}} = \gamma_{\mathrm{metal}} \cdot \cos(\theta) + \gamma_{\mathrm{interface}} \quad , \tag{2.1}$$

where θ describes the contact angle [10]. It illustrates that Volmer-Weber growth occurs if γ_{oxide} is smaller than the right side of equation 2.1, which is usually the case for the growth of metals on oxide substrates [8]. Particle growth is a non-equilibrium process when considering the whole system including the gas phase. Hence, changes in the Gibbs free energy G, when an atom is transferred from the gas phase to the surface, have to be considered in addition [10] and the term $\Delta G = n\Delta\mu = Ck_{\mathrm{B}}T \cdot ln(\frac{p_0}{p})$ needs to be added to the right side of equation 2.1. Its presence indicates that a higher degree of supersaturation $\xi = \frac{p}{p_0}$ favours layer-by-layer growth.
Another, easier way to control growth is by means of the substrate temperature T. The rate ν of atoms that may take part in surface processes such as surface or up-step diffusion is given by an Arrhenius-type exponential law with

$$\nu \propto e^{-\frac{E_{\mathrm{act}}}{k_{\mathrm{B}}T}} \quad , \tag{2.2}$$

where E_{act} denotes the activation energy of a certain process [9, 10]. Hence, a high enough surface temperature T during deposition is required to ensure that particle growth is not kinetically hindered. As indicated in Fig. 2.1, this may proceed via the incorporation of further adatoms, but also via Ostwald ripening or particle coalescence (for more information on these growth processes, see section 3.3). On the other hand, a too high temperature may result in too large particles with high and bimodal size distributions [15].

2.2 Alloying of nanoparticles

The previous section considered the arrival of only one type of atom onto the sample surface during deposition. In this thesis, however, also binary alloy nanoparticles were grown by the simultaneous deposition of two materials. The following section will discuss how their atoms may arrange inside the growing alloy nanoparticles.

Little is known about the detailed nucleation process of alloy nanoparticles. Experimental studies suggest that the particle composition may vary as a function of deposition time, since an atom's sticking coefficient as well as its probability for incorporation into a growing cluster from the vapour phase may differ for the two elements [7]. For instance, for Pd-Au particles, nucleation occurs mainly by the agglomeration of Pd atoms, while predominantly Au atoms are incorporated from the vapour phase at a later stage of particle growth [16].

If the atomic sizes of the two materials A and B differ to a great extent, *interstitial alloys* may form, in which the smaller B-atoms occupy the interstices of the A-lattice. Contrary, if the atomic sizes of the parent metals A and B are of comparable size, their mixing results in a *substitutional alloy*, in which the B-atoms occupy the lattice sites of material A.

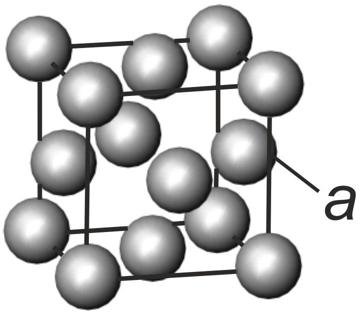

Figure 2.2: **fcc metal unit cell:** the lattice parameter a of the fcc metals Pt, Rh and Pd comprises 3.9242 Å, 3.8013 Å and 3.8907 Å, respectively.

The materials used as parent metals in this thesis (Pt, Rh, Pd) all crystallize in an fcc structure with comparable lattice parameters (Pt: 3.9242 Å, Rh: 3.8013 Å and Pd: 3.8907 Å), the fcc unit cell is shown in Fig. 2.2. Since the atoms of all three elements are of similar size, the mixing of two of these elements results in a substitutional alloy with an fcc unit cell.

The lattice parameter a_{AB} of an alloy can be expressed in terms of *Vegard's law* [17]:

$$a_{\mathrm{AB}} = x_{\mathrm{A}} \cdot a_{\mathrm{A}} + \underbrace{(1 - x_{\mathrm{A}})}_{x_{\mathrm{B}}} \cdot a_{\mathrm{B}} \quad , \tag{2.3}$$

where a_{A} and a_{B} denote the respective lattice parameters, x_{A} and x_{B} the respective molar fractions of the parent metals A and B.

So far, unrestricted mixing of the two alloy elements for all compositions has been assumed. In case of Pt-Rh and Pd-Rh bulk alloys, however, the phase diagramme reveals *miscibility gaps* in the solid phase.

Fig. 2.3 shows the phase diagramme of bulk Pt-Rh [18], which can be divided into four main regions (A-D). The pure liquid phase (A) is characterized by the complete solubility of the two materials Pt and Rh. In the transition region (B) the liquid composition (B') coexists in equilibrium with the corresponding solid composition (B"). At lower temperatures, there is a vast solid phase region of complete miscibility for all Pt-Rh compositions (C). Below the temperature $T^{\mathrm{G}}_{\text{Pt-Rh}}$=1033 K the aforementioned miscibility gap opens up, and solid phase mixing is not possible for all Pt-Rh compositions. Hence, at a temperature of 673 K (which corresponds to the temperature at which the $\mathrm{Pt_{0.33}Rh_{0.67}}$ particles of sample "spinel-1" were investigated, see sections 7.1-7.3) the diagramme predicts the coexistence of two solid fcc phases with compositions of 87% Pt/13% Rh (D') and 12% Pt/88% Rh (D").

The phase diagramme of bulk Pd-Rh looks similar to the one of Fig. 2.3 with a miscibility gap below $T^{\mathrm{G}}_{\text{Pd-Rh}}$=1183 K [19]. Contrary, in the case of Pt-Pd, unrestricted miscibility in the solid phase is predicted for all composition and temperature ranges [20].

The phase diagrammes discussed above correspond to the case of *bulk* alloys. For the alloying of *nanoparticles*, however, further levels of complexity are added due to finite size effects. The latter are for instance triggered by the presence of a high number of edge or corner atoms, which on the other hand may cause changes of surface energies, lattice parameters or melting points [21]. As a consequence, nanoparticles may feature alloy structures that do not exist in the bulk, or form alloys despite a bulk miscibility gap [22, 23]. Also the presence of a support may greatly influence the internal alloy structure. Hence, alloy nanoparticles display an incredibly high level of complexity and a concise picture is lacking so far. Some possible mixing patterns are displayed in Fig. 2.4. As will be discussed in subsection 3.2.2, the internal alloy patterning is not even static, but may vary greatly as a function of sample condition.

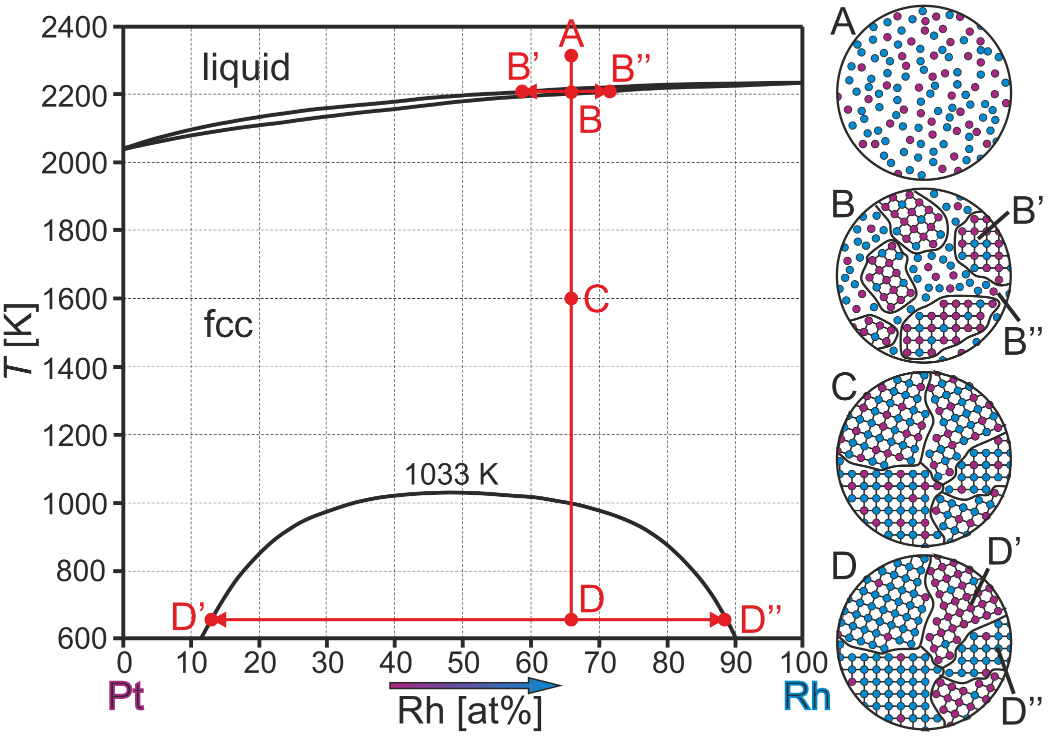

Figure 2.3: **Phase diagramme of bulk Pt-Rh:** four different phases can be distinguished: (A): the liquid phase with complete solubility of Pt and Rh, (B): the coexistence of a solid and a liquid phase, (C): a solid fcc phase with unrestricted miscibility, (D): the miscibility region with the coexistence of two fcc phases. Adapted from [18].

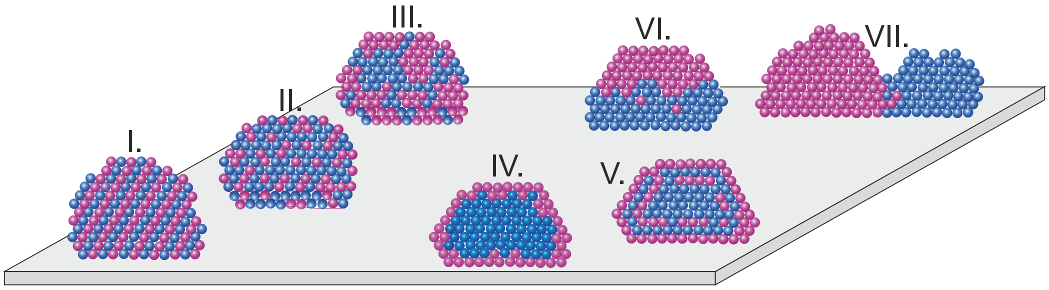

Figure 2.4: **Possible mixing patterns in supported alloy particles:** the different patterns include **I.-III.:** mixed alloys with I. ordered, II. random, and III. subcluster mixing; **IV.-V.:** core-shell alloys with IV. single shell pattern and V. multishell pattern; **VI.-VII.:** subcluster segregated alloys with VI. subclusters sharing mixed interface and VII. subclusters sharing only small numbers of bonds. Partly adapted from [23].

2.3 Shape of nanoparticles

This section deals with thermodynamic equilibrium shapes which particles ideally may adopt during growth (subsection 2.3.1). Furthermore, deviations from this ideal shape (subsection 2.3.2), which are usually present in realistic sample systems, will be discussed.

2.3.1 Thermodynamic equilibrium shape

Contrary to liquids, the surface energy γ_i of crystalline solids is not isotropic but depends on the surface lattice plane i considered, since in each case different atomic bonds have to be broken. Hence, the most stable equilibrium particle shape is the one which is limited by crystal planes that minimize the Gibbs free surface energy $G = \sum_i \gamma_i A_i$, where γ_i and A_i denote the surface energy and surface area of a crystal plane i.

It can be obtained by means of the *Wulff construction*, in which the scalar surface energies $\gamma_i(\hat{n}_i)$ of the crystal planes are plotted in polar coordinates as a function of their surface normals $\hat{n}_i$. The equilibrium particle shape is then given by the inner envelope of the tangents to the Wulff plot and adheres to the *Wulff theorem* [24]:

$$\frac{\gamma_i}{h_i} = const. \quad , \tag{2.4}$$

which states that the ratio of a crystal plane's surface energy γ_i to the distance h_i between the same plane and the particle centre is constant.

Fig. 2.5 shows the Wulff construction performed for pure Pt (a)), pure Rh (c)) and $Pt_{0.5}Rh_{0.5}$ alloy (b)) particles using the surface energies summarized in Table 2.1. For the $Pt_{0.5}Rh_{0.5}$ alloy particles, Vegard's rule was extended to the alloy particle facet surface energies, which were accordingly determined by linear extrapolation from the surface energies of the corresponding parent metals.

The above approach for the shape determination of alloy particles is justified for several reasons: (1) the overall shapes of the monometallic Pt, Pd and Rh particles are very similar, consisting mainly of (111)- and (100)-type facets with comparable $\frac{\gamma_{100}}{\gamma_{111}}$ ratios, while high index facets barely contribute to the inner envelope of the Wulff plot, hence, similar shapes can also be expected for the corresponding alloy nanoparticles; (2) a recently deduced analytical solution to

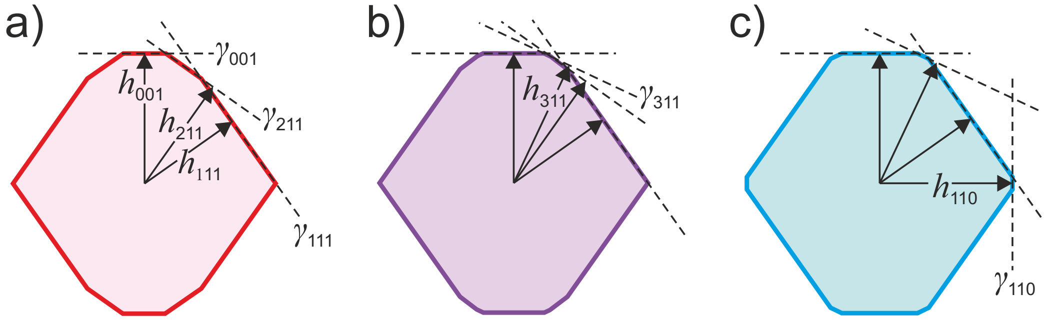

Figure 2.5: **Wulff construction:** the construction was performed based on equation 2.4 using the surface energies of Table 2.1 for **a):** pure Pt particles neglecting surface reconstructions, **b):** $Pt_{0.5}Rh_{0.5}$ alloy particles, and **c):** pure Rh particles.

surface	**Pt**	**Rh**	**Pd**
(111)	0.093	0.124	0.084
(100)	0.113 ((1×5): 0.098)	0.144	0.094
(110)	0.123 ((1×2)-MR: 0.103)	0.147	0.099
(211)	0.103	0.144	0.095
(311)	0.110 (MR: 0.108)	0.148	0.098

Table 2.1: **Surface energies for selected close-packed surfaces of Pt, Rh and Pd:** they refer to clean, unreconstructed surfaces and are given in $\left[\frac{\text{eV}}{\text{Å}^2}\right]$; surface energies of reconstructed surface (if existent, 'MR' implies missing row) are given in brackets. Adapted from [25].

the Wulff construction of alloy nanoparticles under consideration of segregation effects [26] yields results on the particle shape which are within ~10% of the ones obtained with the above mentioned approach; (3) no consistent literature values on the surface energies of alloys are available.

While the Wulff theorem describes the shape of free particles, the equilibrium shape of supported particles follows the *Wulff-Kaishew theorem*

$$\frac{\Delta h}{h_i} = \frac{E_{\text{adh}}}{\gamma_i} \quad , \tag{2.5}$$

where Δh denotes the truncation of the particle at the interface, which scales with the adhesion energy E_{adh}. Fig. 2.6 a) shows a sketch of a truncated particle drawn based on the Wulff-Kaishew construction. It is notable that for isotropic materials the magnitude of the contact angle θ, as shown in Fig. 2.6 b), depends on the degree on truncation, while the contact angle of a faceted particle is only determined by its crystallography.

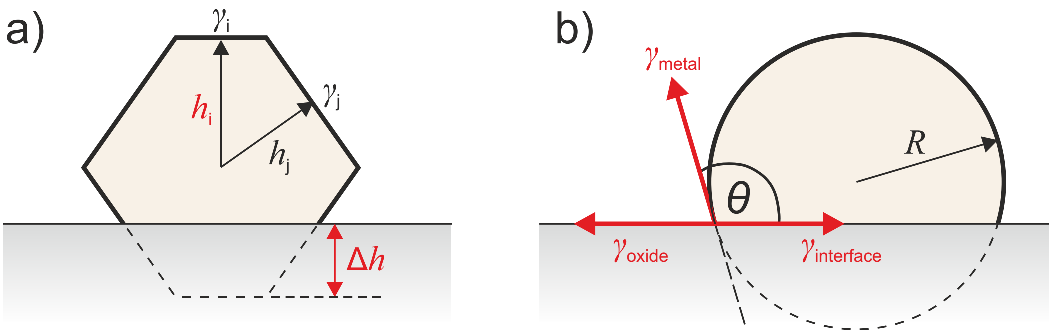

Figure 2.6: **Wulff-Kaishew construction: a):** of a truncated particle; **b):** truncation of an isotropic material with contact angle θ, surface energies γ_{metal} and γ_{oxide} of the metal and the oxide, respectively, and the interface energy $\gamma_{\mathrm{interface}}$.

The extent of truncation depends on the interaction of the particle with the substrate, as is illustrated by the *Dupré equation*

$$E_{\mathrm{adh}} = \gamma_{\mathrm{metal}} + \gamma_{\mathrm{oxide}} - \gamma_{\mathrm{interface}} \quad , \tag{2.6}$$

where the sum $\gamma_{\mathrm{metal}}+\gamma_{\mathrm{oxide}}$ denotes the energy gained by the interface formation, as the corresponding particle and oxide surface areas disappear upon forming the interface, while $\gamma_{\mathrm{interface}}$ represents the energy needed to build up the interface. The latter becomes smaller and the adhesion energy E_{adh} and hence the truncation Δh become larger with increasing interaction between the metal deposit and the substrate. In general, $\gamma_{\mathrm{interface}}$ decreases with the metal's increasing tendency to form oxides [8], but increases with the occurrence of dislocations at the interface [27] (see also discussions in sections 2.3.2 and 2.4).

2.3.2 Kinetic particle shape

The grown particle shapes often differ from the equilibrium shapes defined by the Wulff-Kaishew construction. The arriving adatoms may lack the energy to overcome the various diffusion processes discussed in section 2.1 and are kinetically trapped. Criteria that determine the resulting *kinetic particle shape* will be elucidated in the following.

One important factor is the *anisotropy of the environment* during growth [6]. It might be triggered by spatial differences in supersaturation or in temperature. The resulting anisotropic atom flux provides certain particle facets with more atoms than others. Environmental differences are also created by anisotropies of the sample surface, such as the presence of terraces, which may increase the growth rate along a certain direction.

Deviations from the equilibrium particle shape can also be traced back to differences in *particle facet growth rates.* Hence, close-packed facets grow in general more slowly than stepped or kinked ones [28] as in the latter case each adatom is already part of a facet and does not need to rearrange itself.

Atomic level *defects* inside the particle, some of them are displayed in Fig. 2.7, may propagate during particle growth and influence the macroscopic particle shape [6]. Thus, the presence of a screw dislocation may support growth along one direction resulting in elongated shapes. Similar shapes can be triggered by internal twinning, which denotes a change in the atomic layer stacking sequence along the (111)-surface normal, see top left inset in Fig. 2.7. Furthermore, point defects such as vacancies or interstitial atoms distort the crystal lattice and the electronic structure locally, influencing particle growth.

Odd-shaped particles are often the result of incomplete particle *coalescence.* The complete merging of particles is a process that costs a lot of energy, since for instance grain boundaries have to be rearranged (see top right inset in Fig. 2.7).

The remainder of this subsection will deal with the important consequences of the, in heteroepitaxy usually present, *lattice mismatch* $m = \frac{a_{\mathrm{sub}} - a_{\mathrm{par}}}{a_{\mathrm{par}}}$ between the lattice parameter of the particle, a_{par}, and the one of the substrate, a_{sub}, for the particle shape and the adhesion energy E_{adh}.

For mismatches smaller than a critical mismatch m_{c} particles may overcome this discrepancy by building up strain fields at the interface, as is indicated in Fig. 2.8. To maintain the volume of the unit cell, the layers are usually not only strained in in-plane but also in out-of-plane direction following a Poisson's ratio relationship [29] (see bottom right inset in Fig. 2.7). As a consequence, the particle height-to-diameter aspect ratio may differ from the one of unstrained particles [30]. For particles higher than a critical height h_{c} or for a mismatch larger than m_{c}, the strain inside the layer becomes too high and the incorporation of dislocations becomes energetically more favourable. With the formation of dislocations, the particle height approaches the one of unstrained particles [30].

The incorporation of dislocations at the interface has moreover an influence on the adhesion energy E_{adh}. Accordingly, a HR-TEM study concluded a decrease in E_{adh} with the increase in particle size and hence with the formation of inter-

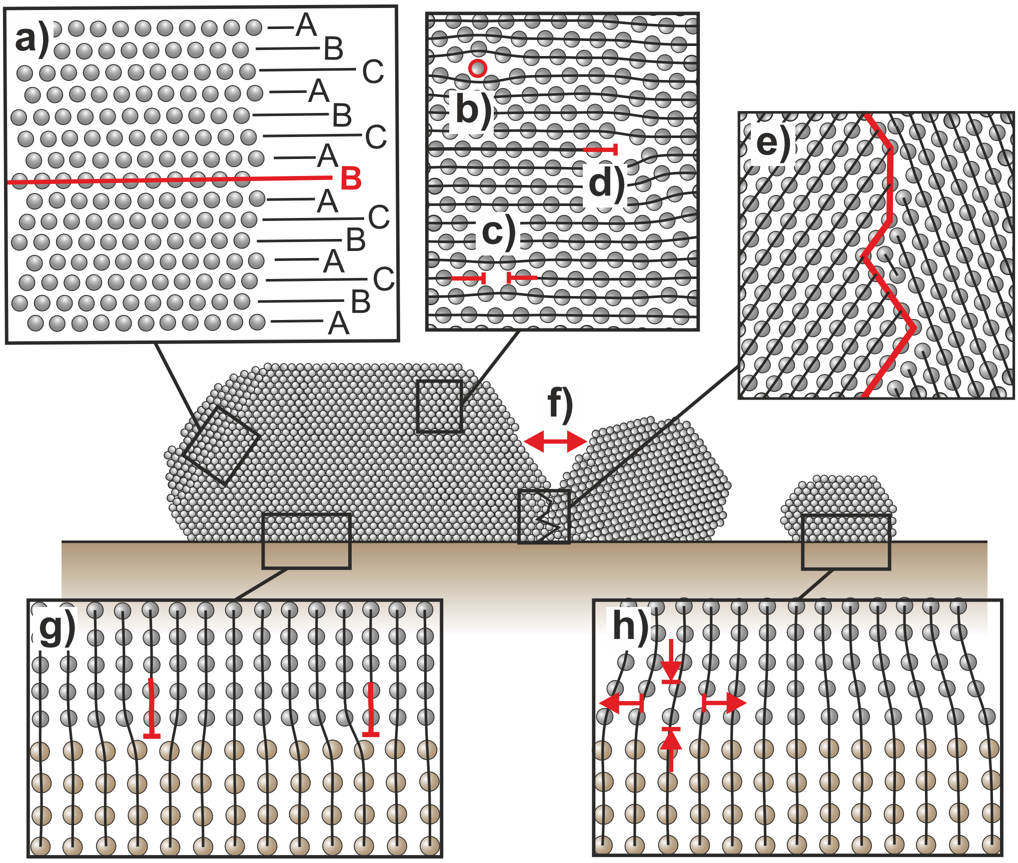

Figure 2.7: **Potential defects within particles:** they include distortions of the internal particle crystallinity such as **a):** internal twinning, **b):** interstitial atoms, **c):** vacancies, **d):** dislocations, and **e):** grain boundaries, which often are the result of **f):** particle coalescence; distortions at the particle/substrate interface may include **g):** interface dislocations, especially in the case of large particles, or **h):** interface stain, especially in the case of small particles.

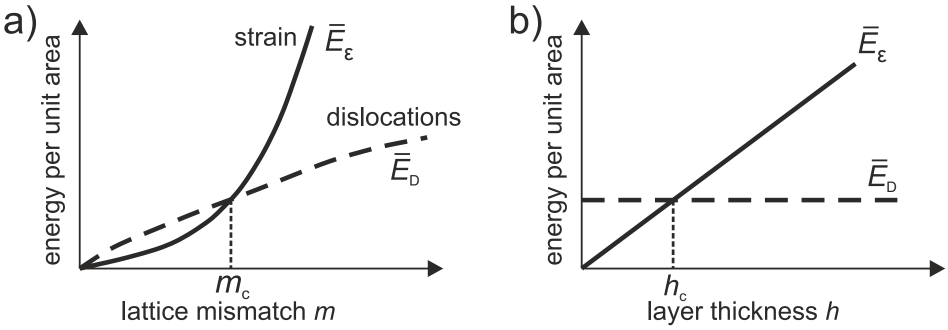

Figure 2.8: **Lattice energy stored at the interface per unit area:** the qualitative plots show the respective lattice energies created solely by strain (solid lines, $\bar{E}_\varepsilon$) and by incorporation of dislocations (dashed lines, $\bar{E}_\mathrm{D}$) as a function **a):** of the lattice mismatch $m = \frac{a_\mathrm{sub} - a_\mathrm{par}}{a_\mathrm{par}}$, **b):** of the layer thickness h; m_c and h_c denote the critical mismatch and the critical layer thickness, respectively [10].

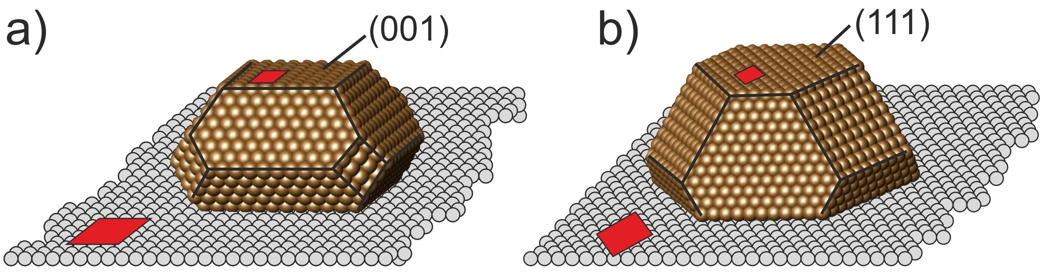

Figure 2.9: **Main particle epitaxies: a):** (001)-oriented particle with squared unit cell at the top and interface facet; **b):** (111)-oriented particle with hexagonal unit cell at the top and interface facet.

face defects [27]. As smaller particles are more prone to incorporate interface strain fields, they may adapt more easily to different substrate configurations. As a consequence, they may display a higher angular distribution compared to larger particles and/or display a higher number of possible epitaxies [31].

2.4 Influence of the support: substrates used in this thesis

This last section yields a closer look at the characteristics of the substrates used in this thesis, $MgAl_2O_4(001)$ and α-$Al_2O_3(0001)$. They were chosen since they facilitate the growth of differently shaped particles: on $MgAl_2O_4(001)$ particles grow predominantly in a (001)-orientation, featuring (001)-type facets at the top and at the interface. The growth of this shape is triggered by the cubic surface unit cell of $MgAl_2O_4(001)$. Contrary, the hexagonal surface cell of α-$Al_2O_3(0001)$ favours the growth of (111)-oriented particles, characterized by (111)-type facets at the top and at the interface. Typical shapes of truncated (001)- and (111)-oriented particles are displayed in Fig. 2.9.

The following will yield an overview of the substrates' specific features that may further influence particle growth, such as surface adsorbates (α-$Al_2O_3(0001)$), special defect sites ($MgAl_2O_4(001)$) and lattice mismatches to the differently alloyed metal particles.

2.4.1 The α-$Al_2O_3(0001)$ substrate

Being one of the most common ceramics, the numerous applications of alumina (Al_2O_3) include its use as thermal and corrosive barrier coating, as potential

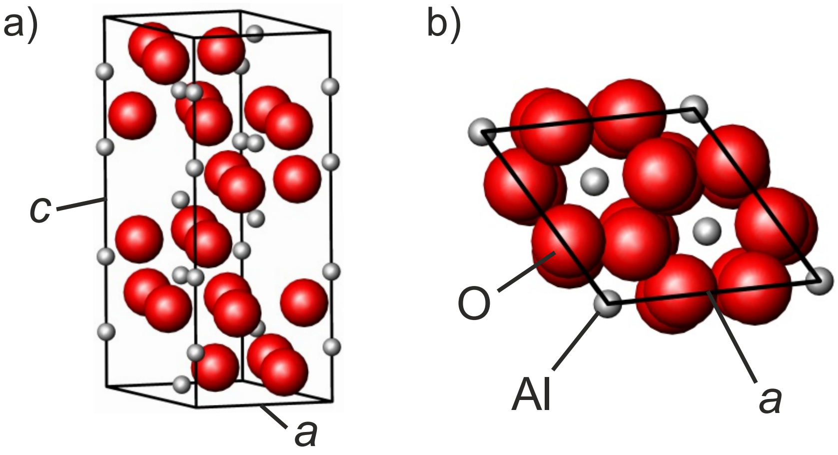

Figure 2.10: **α-Al_2O_3 unit cell: a):** side view, **b):** top view; the lattice parameters of the hexagonal unit cell comprise a=b=4.763 Å, c=13.003 Å; α=β=90°, γ=120°.

substitute to silica in microelectronic devices, or as support for catalyst materials [32, 33].

The corundum structure α-Al_2O_3(0001), is the most stable alumina phase [9]. Its unit cell with the lattice parameters a=b=4.763 Å, c=13.003 Å; α=β=90°, γ=120° is displayed in Fig. 2.10. The lattice mismatch at the interface to the metal particle (111) surface cell is summarized in Table 2.2 for various alloy compositions. It reveals that the best match at room temperature is obtained for either pure Pd particles, or for Pt-Rh alloy particles with a composition of 70% Pt and 30% Rh.

The hexagonal α-Al_2O_3(0001) unit cell contains six formula units of Al_2O_3 [34]. It is made up of six close-packed hexagonal oxygen layers with buckled Al layers in between. Along the out-of-plane c-axis, the repeating layer stacking can be expressed as R-$AlAlO_3$-R, where R denotes the continuing sequence in the bulk [34]. This allows for three different surface terminations, (1) an O layer termination (O_3AlAl-R), (2) a double Al layer termination ($AlAlO_3$-R), and (3) a single Al layer termination (AlO_3Al-R), their respective occurrences can partly be influenced by the α-Al_2O_3(0001) surface treatment [34].

Depending on the termination, the surface displays varying thermodynamic stabilities [34] and greatly differing effects on the adhesion of the deposited material [32]. Hence, the O-terminated surface is energetically very unstable, as it is polar, and contains surface dangling bonds [34]. As a consequence, it exerts a very strong ionic- and covalent-like interaction to metal deposits [9, 32]. The double Al-terminated surface features the second-strongest, metallic covalent-like, interaction [9, 32]. It is prone to reconstructions to lower its surface energy (see [34] and references therein).

The single Al terminated, or 'stoichiometric' surface is unpolar, the thermodynamically most stable unreconstructed surface configuration and represents the normal termination of UHV-clean α-$Al_2O_3(0001)$ [34, 35]. Its stability can be traced back to the inward relaxation of the Al atoms, resulting almost in coplanarity with the second oxygen layer [34]. It displays the weakest chemical metal-surface interaction, mainly characterized by polarization effects [9], which increases from Pt over Pd to Rh [32].

The α-$Al_2O_3(0001)$ surface energy may be lowered by *hydroxylation* [32, 34, 36], especially in the case of O and double Al terminated surfaces [32]. It is the result of water dissociation that occurs if the sample comes into contact with low pressures or air [9, 36]. The OH-groups were found to withstand oxygen-plasma treatment [35] and to not be completely removed by annealing in UHV [33]. Their presence greatly increases the adhesion energy E_{adh}, which was suggested to be a consequence of the oxidation of the metal upon impact onto the hydroxylated interface according to [35, 36]

$$\{Al^{3+}OH^{-}\} \ + \ Me^{0} \ \rightarrow \ \{Al^{3+}O^{2-}\}Me^{+} \ + \ H \quad . \tag{2.7}$$

The metal cations act at the interface as strongly binding atoms that prevent diffusion and promote laminar layer instead of island growth [35, 37]. Apart from the Co/α-$Al_2O_3(0001)$ system [35] such scenarios were also suggested for Cu/α-$Al_2O_3(0001)$ [38, 39], and extended to other metals including Rh [37].

2.4.2 The $MgAl_2O_4(001)$ substrate

The ternary oxide $MgAl_2O_4$ is used in ceramics technology, as catalyst support [40], as material for humidity-sensory [41] or ultrafiltration membranes [42]. In catalysis, $MgAl_2O_4$ is particularly employed due to its stability in the case of harsh reaction conditions like steam reforming [43, 44, 45].

$MgAl_2O_4$ features a cubic unit cell and a lattice parameter of 8.086 Å [46], the relatively large lattice mismatch to the lattices of (001)-oriented particles of various Pt-Rh compositions are summarized in Table 2.3.

Inside the $MgAl_2O_4$ unit cell, the O^{2-} anions are arranged in a slightly deformed lattice of cubic close packing, with Mg^{2+} cations located in $\frac{1}{8}$ of the tetrahedral interstices and Al^{3+} cations in $\frac{1}{2}$ of the octahedral interstices. As

Pt	-0.90%	**Pd**	-0.04%	**Pt**	-0.90%
$\mathbf{Pt_{0.85}Rh_{0.15}}$	-0.43%	$\mathbf{Pd_{0.75}Rh_{0.25}}$	+0.53%	$\mathbf{Pt_{0.85}Pd_{0.15}}$	-0.77%
$\mathbf{Pt_{0.7}Rh_{0.3}}$	+0.04%	$\mathbf{Pd_{0.6}Rh_{0.4}}$	+0.88%	$\mathbf{Pt_{0.7}Pd_{0.3}}$	-0.64%
$\mathbf{Pt_{0.5}Rh_{0.5}}$	+0.68%	$\mathbf{Pd_{0.5}Rh_{0.5}}$	+1.12%	$\mathbf{Pt_{0.5}Pd_{0.5}}$	-0.47%
$\mathbf{Pt_{0.3}Rh_{0.7}}$	+1.32 %	$\mathbf{Pd_{0.4}Rh_{0.6}}$	+1.35%	$\mathbf{Pt_{0.3}Pd_{0.7}}$	-0.30%
$\mathbf{Pt_{0.15}Rh_{0.85}}$	+1.81%	$\mathbf{Pd_{0.25}Rh_{0.75}}$	+1.71%	$\mathbf{Pt_{0.15}Pd_{0.85}}$	-0.17%
Rh	+2.31%	**Rh**	+2.31%	**Pd**	-0.04%

Table 2.2: **Lattice mismatches m for various particle alloy compositions to the α-Al_2O_3(0001) lattice at room temperature:** for (111)-oriented particles the particle atom distances given by $a^*_{\text{par}}=\frac{\sqrt{3}\,a_{\text{par}}}{\sqrt{2}}$ accommodate to the atomic distance a_{sub}=4.763 Å of the α-Al_2O_3(0001) surface, where a_{par} denotes the fcc lattice parameter of the particles according to Vegard's law (see Fig. 2.2 for the values of a_{par} of the pure metals); the above listed lattice mismatches were obtained using $m = \frac{a_{\text{sub}}-a^*_{\text{par}}}{a^*_{\text{par}}}$.

Pt	$\mathbf{Pt_{0.7}Rh_{0.3}}$	$\mathbf{Pt_{0.5}Rh_{0.5}}$	$\mathbf{Pt_{0.33}Rh_{0.67}}$
+3.03%	+4.01%	+4.67%	+5.22%

Table 2.3: **Lattice mismatches m for various particle alloy compositions to the $MgAl_2O_4$(001) lattice at room temperature:** the mismatches were obtained using $m = \frac{a^*_{\text{sub}}-a_{\text{par}}}{a_{\text{par}}}$, where a^*_{sub}=4.043 Å denotes half of the in-plane spinel lattice parameter and a_{par} the respective particle fcc lattice parameter according to Vegard's law (see Fig. 2.2 for the values of a_{par} of the pure metals).

Fig. 2.11 a) reveals, the total unit cell is thus made up of eight MgO_4 primitive tetragonal (green lines) and eight Al_4O_4 conventional cubic unit cells (orange lines) [47]. Fig. 2.11 b) shows the top view of the total $MgAl_2O_4$(001) unit cell and the atomic distances at the surface as unraveled in a recent surface x-ray diffraction study [48]. Its side view, depicted in Fig. 2.12 a), displays the alternating Mg_2 and $O_4Al_4O_4$ layers with their separation distances of 2.02 Å [48].

The $MgAl_2O_4$(001) surface is polar, regardless if Mg_2- or $O_4Al_4O_4$-terminated [49]. The polarity-induced instability of the Al-terminated surface is greatly reduced by swapping the Al^{3+} with the Mg^{2+} of the second layer [49]. Hence, the $O_4Al_4O_4$-terminated surface with Mg^{2+}-Al^{3+} antisites is the thermodynamically stable surface structure, which was concluded to be also favoured under realistic experimental conditions, i.e. upon hydrogen, oxygen or OH-

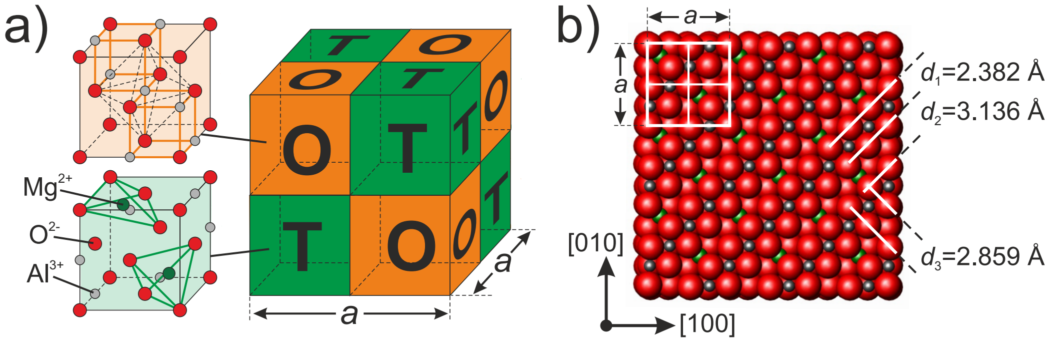

Figure 2.11: **$MgAl_2O_4$ unit cell: a):** total unit cell made up of eight MgO_4 primitive tetragonal (green lines, "T") and eight Al_4O_4 conventional cubic unit cells (orange lines, "O") with lattice parameter a=8.086 Å. **b):** top view of the Al-terminated $MgAl_2O_4$(001) surface; the total unit cell is indicated by the white square, atomic row distances d_x correspond to the ones given in [48].

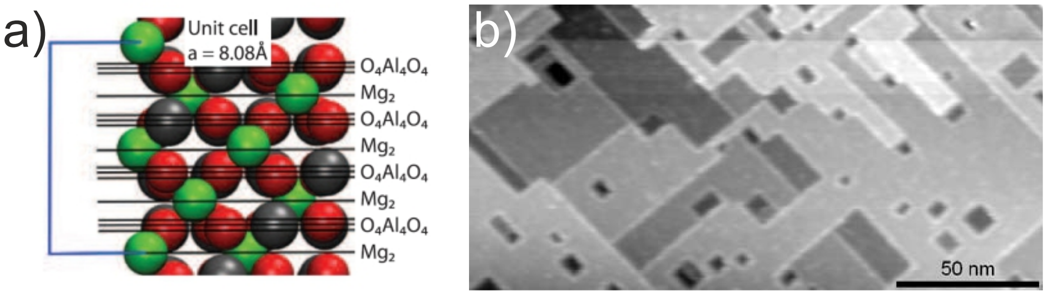

Figure 2.12: **$MgAl_2O_4$(001): potential surface terminations: a):** side view of the $MgAl_2O_4$(001) unit cell illustrating the possible surface terminations Mg_2 and $O_4Al_4O_4$ [48]. **b):** topographic NC-AFM image of the $MgAl_2O_4$(001) surface after sufficient cleaning (see Supporting Information in [48]).

group adsorption [48].

After repeated cycles of Ar^+ sputtering and annealing to 1400 K in 10^{-7} mbar O_2, the $MgAl_2O_4$(001) surface flattens, displays large terraces and is decorated with nanometer-sized square pits [48] (see Fig. 2.12 b)). The latter comprise 20-30% of the surface and feature a depth of 2.02 Å and multiples thereof, which corresponds to the separation distances of the (Mg_2-$O_4Al_4O_4$) layer stacks in [001]-direction. Such pits may act as nucleation sites during particle growth [50] and/or pin nanoparticles during reaction conditions and thus reduce sintering.

Chapter 3

Heterogeneous Catalysis

The present chapter explains the basic concepts of heterogeneous catalysis: section 3.1 presents its underlying principles on the basis of the CO oxidation reaction catalyzed by Pt-group metals (Pt, Rh, Pd), which constitute the reaction and the parent metals of the alloy particles investigated in this thesis. Section 3.2 elucidates the benefits of alloy particles as choice for catalyst material and summarizes their special characteristics under reaction conditions. Finally, section 3.3 deals with the topic of particle sintering, a catalyst deactivation mechanism frequently addressed in this work. The two common theoretical descriptions found in literature will be presented.

3.1 Concepts of heterogeneous catalysis

By definition, a *catalyst* constitutes a substance that changes the rate of a chemical reaction without being consumed. In contrast to *homogeneous* catalysis, the term *heterogeneous* catalysis implies that the phase of the catalyst differs from that of the reactants.

A famous example of a heterogeneous catalytic reaction is CO oxidation on Pt-group metal surfaces ($2CO+O_2 \rightarrow 2CO_2$). It has been the focus of extensive surface science studies dating back to the 1920s [51, 52]. Its popularity for both, experimental and theoretical studies, can on the one hand be traced back to the reaction's relative 'simplicity', which allows to divide the reaction into rudimentary steps of interest. On the other hand it constitutes an essential reaction in everyday pollution control, as it is applied in automotive exhaust catalysts [53].

3.1.1 Potential energy diagramme

A catalyst's principle mode of action is illustrated by the potential energy diagramme in Fig. 3.1. It shows the routes for a non-catalyzed (blue) and a catalyzed (purple) CO oxidation reaction. The non-catalyzed reaction can only occur if the CO and O_2 molecules in the gas phase collide with sufficient energy to overcome the high activation energy E_{act} of about 500 $\frac{\mathrm{kJ}}{\mathrm{mol}}$. The extent of this barrier is mainly due to the strong O-O bond in the oxygen molecule that needs to be broken.

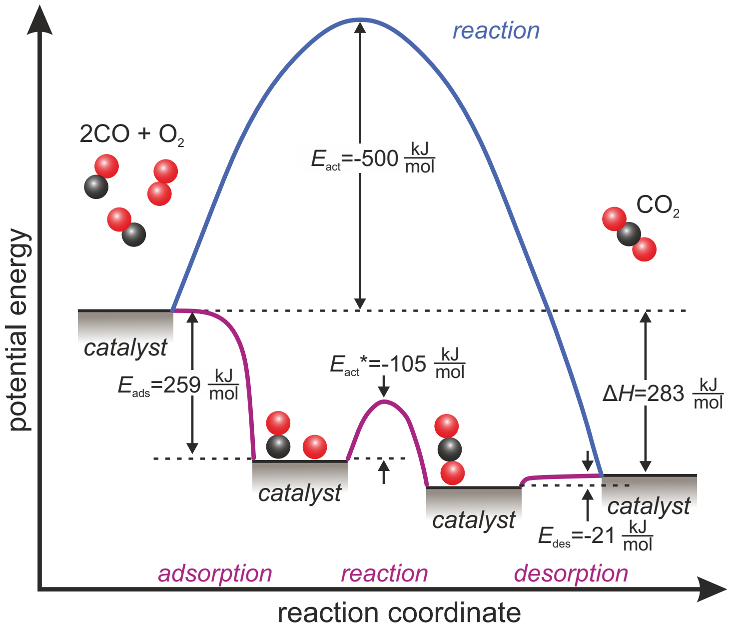

Figure 3.1: **Potential energy diagramme of CO oxidation:** the reaction path is shown for the cases without (blue) and with catalyst (purple). The indicated energy values correspond to a reaction via the Langmuir-Hinshelwood mechanism on Pt(111), assuming low surface coverages. After [54, 55].

Contrary, in the catalyzed reaction, the dissociative chemisorption of oxygen on the catalyst surface (here: Pt(111)) results in a broken O-O bond and even in an energy gain E_{ads} for the system[1]. With the O-O bond broken, the main obstacle of the reaction is removed: the activation energy barrier $E_{\mathrm{act}}{}^{*}$ of the catalyzed reaction is as a consequence greatly reduced and can - along with the small endothermic desorption barrier E_{des} for the CO_2 molecule - easily be overcome. As a result, the rate of the reaction increases.

Fig. 3.1 illustrates that ΔH and hence the overall change in Gibbs free energy $G = H - TS$, is the same for the catalyzed and the non-catalyzed reaction. This implies that the presence of a catalyst does not change the thermodynamics

---

[1] not only the chemisorption of O_2 but also of CO on the catalyst surface is exothermic, but the energy gain amounts in this case only to about 20 $\frac{\mathrm{kJ}}{\mathrm{mol}}$.

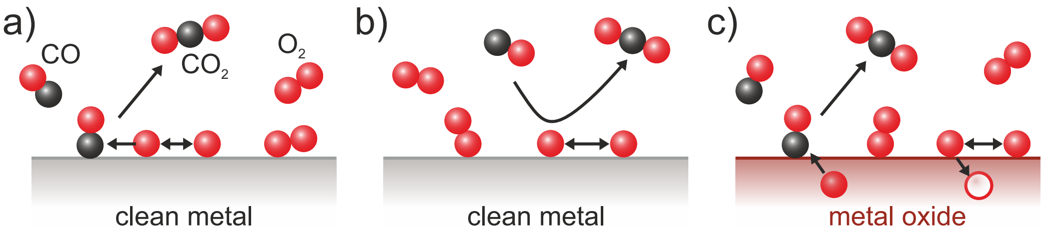

Figure 3.2: **Reaction mechanisms in heterogeneous catalysis:** the example of the CO oxidation reaction ($2CO+O_2 \rightarrow 2CO_2$) is shown to occur via a **a):** Langmuir-Hinshelwood, **b):** Eley-Rideal, **c):** Mars-van-Krevelen mechanism.

of a reaction, but only the kinetics, namely by assisting in the formation and the breaking of molecular bonds [54].

3.1.2 Reaction mechanisms

There are different possible routes along which a catalyzed chemical reaction may occur, they are summarized in Fig. 3.2.

The mechanism already presented in Fig. 3.1 is referred to as *Langmuir-Hinshelwood* mechanism: it combines a strong adsorption of both molecular reactants on the metallic catalyst, their possible dissociation (in case of O_2; CO stays molecular) and diffusion along the catalyst surface. Finally, the adsorbed CO reacts with the chemisorbed oxygen and the reaction product desorbs from the catalyst surface.

In the case of the *Eley-Rideal* mechanism [56] only one of both species strongly adsorbs on the catalyst surface (here: O_2) and reacts with the other reactant (CO) directly from the gas phase or from a weakly adsorbed state (CO). Upon reaction the product escapes instantaneously into the gas phase.

The *Mars-van-Krevelen* mechanism [57] constitutes a third potential pathway: in this case one of the reactants forms a compound with the catalyst material, i.e. oxygen from the gas phase reacts with the catalyst metal to constitute the respective metal oxide. The actual intended reaction then occurs when the second reactant species (CO) adsorbs and reacts with the oxygen atoms from this oxide. The thus created oxygen vacancies inside the metal oxide are constantly being refilled by oxygen molecules from the gas phase, which adsorb and dissociate on the metallic catalyst or its oxide surface.

Which reaction mechanism occurs depends on the one hand on the type of catalyst material, but also on the sample condition (i.e. the pressure and temperature).

Early surface science studies performed by Ertl and coworkers in the **low pressure regime ($p<10^{-6}$ mbar)** revealed that CO oxidation on all Pt-group metals proceeds via the Langmuir-Hinshelwood mechanism, i.e. CO molecules adsorb on the respective metal surface and react with chemisorbed oxygen [58, 59, 60, 61, 62]. Since Pt, Rh, Pd and Ru bulk oxides were concluded to be catalytically inactive at such low pressures, a reaction via the Mars-van-Krevelen mechanism was ruled out [58]. Moreover, experiments verified the adsorption and migration of CO molecules on the catalyst surface prior to reaction [63, 64] resulting in a time delay in CO_2 production [65] which would not be present in the case of an Eley-Rideal mechanism.

With the advent of high pressure compatible measurement techniques including HP-STM, HP-AFM, HP-TEM, SXRD, HESXRD, SFG or PM-IRAS the operando study of model catalyst systems under industrially relevant **near-ambient pressures** has become possible. The landmark discovery that Ru, which displays very poor catalytic activity under UHV conditions via the Langmuir-Hinshelwood mechanism, reveals extremely high CO_2 production rates at atmospheric pressures in form of $RuO_2(110)$ by means of a Mars-van-Krevelen mechanism [66], launched the concept of a **pressure gap**, i.e. of the inability to transfer the reaction mechanism determined for low pressures to the high pressure regime. For Pt, Rh and Pd sample systems the prevailing reaction route and the catalytically most active phase at industrially relevant pressures are partly still under debate [59, 67, 68, 69]. The current research status will be given in the following subsection.

3.1.3 CO oxidation at near atmospheric pressures

At near atmospheric pressures there is an ignition sample temperature T_{i} (typically at about 600 K for stoichiometric partial pressures) above which very high catalytic activities are reached. This 'roll over point' divides the reaction into: i): the low activity regime below T_{i}, and ii): the high activity region above T_{i}. In addition, a third transient regime of highest activity rate, iii), located around the roll over point was proposed and controversially discussed. In the following, these three regimes and the debate concerning the catalytically most active phase will be elucidated more thoroughly based on the Arrhenius plots shown in Fig. 3.3. Therein, two data sets are shown obtained on Pd(100) for various p_{O2}/p_{CO} ratios that reveal the catalyst activity in terms of the turnover frequency ('TOF': number of produced CO_2 molecules per site per second) as a function of the inverse temperature.

Regime i): In this regime the temperature is smaller than the ignition temperature ($T<T_i$). It is characterized by a temperature-dependent linear increase in the turnover frequency (see Fig. 3.3). The reaction proceeds via the Langmuir-Hinshelwood mechanism, as was concluded for various single crystal surfaces of Pd [60, 70, 71], Pt [60, 62] and Rh [61, 72], but also in the case of supported Rh/Al_2O_3 nanoparticles [73]. CO has a higher sticking coefficient at low temperatures compared to oxygen, and thus blocks catalyst sites on which otherwise oxygen could dissociate. Hence, it is CO desorption that constitutes the rate-limiting step of the reaction [62]. With increasing temperature, CO progressively desorbs from the surface and leaves empty sites for oxygen to dissociate. This results in a rise of the reaction rate, as can be deduced from the linear increase of the logarithmic rate in Fig. 3.3 a) and b). The data shown in Fig. 3.3 moreover reveal that a rise in the reaction rate can also be obtained by increasing the p_{O2}/p_{CO} ratio while keeping the temperature constant [60, 61, 62].

Regime ii): The transition above the ignition temperature T_i - or above a certain p_{O2}/p_{CO} ratio at sufficiently high temperatures - is in general characterized by a sudden increase in the reaction rate (*'light off'*). The reaction becomes self-sustained due to its exothermicity. Regime ii) is in Fig. 3.3 a) represented by the plateau-like region(s). The sharp bends in the reaction rate at the respective T_i mark that the transition between i) and ii) comes along with a change of the rate-limiting mechanism: spectroscopy measurements on Pt(111) revealed that the CO sitting on top of Pt and working as an inhibitor at $T<T_i$ becomes indeed hardly detectable for $T>T_i$ [62]. The reaction rate is no longer collision-limited like at lower temperatures, but becomes mass transfer limited, i.e. the diffusion in the gas phase of the surface reactants to the surface becomes the rate limiting factor.

A number of complementary operando studies under high pressure reaction conditions (STM, SXRD, HESXRD, AFM) find that the high activity of regime ii) correlates with the sudden formation of oxide phases on Pd, Rh and Pt,

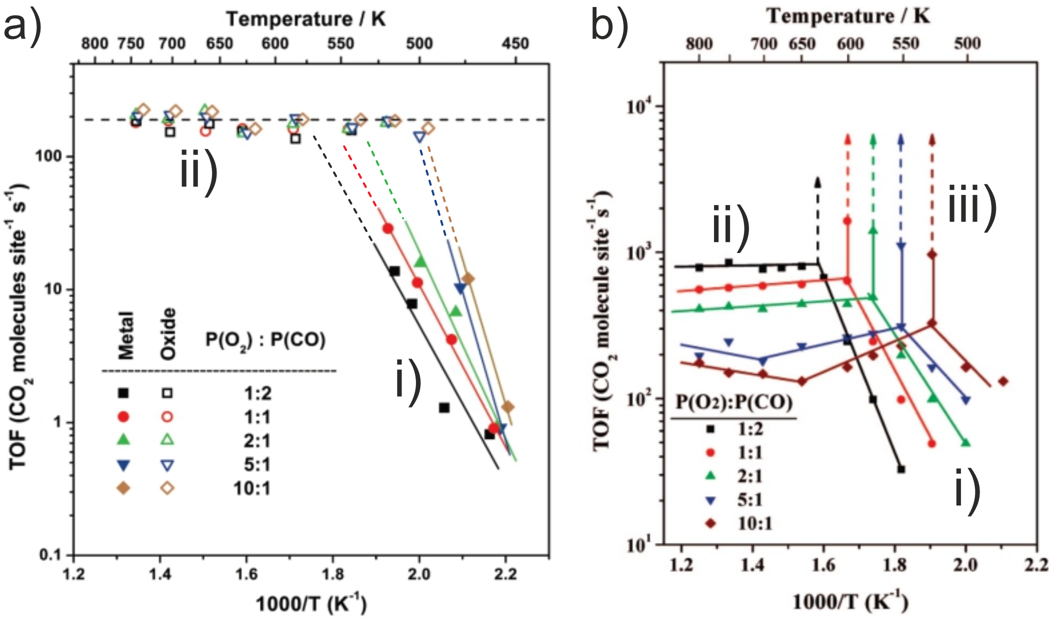

Figure 3.3: **Arrhenius plots for the CO oxidation on Pd(100) at near-ambient pressures:** the turn over frequencies (‘TOF’: produced CO_2 molecules per site per second) are shown as a function of the inverse temperature **a):** as obtained from operando SXRD using a flow reactor p_{CO}=8 Torr for all ratios with He used as carrier gas in each case to keep the total pressure constant at 152 Torr, [71]), **b):** as obtained from PM-IRAS using a batch reactor (p_{CO}=8 Torr for all ratios, [60]). i): low activity regime, ii): high activity regime, iii): proposed ‘hyperactive’ transient states [60].

thus proposing a Mars-van-Krevelen-like reaction mechanism[2]:
The operando SXRD study of **Pd(100)** during high pressure CO oxidation from which the data shown in Fig. 3.3 a) was obtained, concluded the appearance of different Pd oxides when switching to the high activity regime ii) [71]. Although the data did not allow for identifying the catalytically most active oxide phase, all oxides were concluded to be active enough to sustain the ‘TOFs’ in the mass transfer limited regime. Recent HESXRD studies disentangled the oxides’ order of appearance, ascribing the formation of the $(\sqrt{5}\times\sqrt{5})R27°$ surface oxide to the light off, succeeded by PdO bulk oxide islands on top of the surface oxide and finally by polycrystalline PdO at later stages in the mass transfer limited regime with higher p_{O2}/p_{CO} ratios [74, 75, 76]. Contrary, it was proposed that bulk oxide formation on Pd(100) poisons the reaction, as can be inferred from Fig. 3.3 b) and the reduced CO_2 ratios in the mass transfer limited regime for partial pressure ratios $\frac{p_{O2}}{p_{CO}} \geq \frac{5}{1}$ [60, 77].

---

[2] information on oxide formation is given in section 3.1.5

For **Pd(111)** enhanced catalytic activity was observed when the Pd_5O_4 surface oxide was present, while oxide clusters and bulk oxide PdO were concluded to suppress the reaction [78]. There is theoretical evidence that the reaction follows the Eley-Rideal mechanism: CO from the gas phase is claimed to react with the three-fold oxygen atoms of the Pd_5O_4 surface oxide after its approach has been guided by the neighbouring Pd atoms [78, 79, 80].

In the case of **all low index surfaces of Rh** the presence of the O-Rh-O trilayer surface oxide (see Fig. 3.6 a) and b)) was consistently found to coincide with the mass transfer limited regime of high activity [81, 82, 83]. Contrary, on all surfaces the appearance of Rh bulk oxides was concluded to poison the reaction [72, 81, 82, 84]. The O-Rh-O trilayer surface oxide as catalytically active phase was also proposed for alloy $Pt_{0.25}Rh_{0.75}(001)$ model catalyst surfaces [81, 85].

For Pt the results concerning the catalytically most active phase are rather inconsistent: on **Pt(111)** an in-situ SXRD study revealed a higher catalytic activity for the α-PtO_2 trilayer oxide compared to the metallic surface [86]. Contrary, recent IR spectroscopy and SXRD investigations suggest the mixture of an oxidic phase and chemisorbed oxygen to be present in the mass transfer limited regime [87]. Moreover, a combined XPS and XAS study concluded that chemisorbed oxygen reveals higher catalytic activity than the PtO-like surface oxide or the α-PtO_2 trilayer oxide [88].

On **Pt(110)** model catalyst surfaces the transition to the high activity regime was found to correlate with the formation of a (1×2) surface oxide, which was concluded to only be stable under reaction conditions [89, 90, 91]. A combined AP-XPS, HP-STM and DFT study revealed that chemisorbed oxygen on Pt(110) reacts faster with CO than multilayered α-PtO_2 islands [92].

Regime iii): In addition to the mass transfer limited regime ii) of enhanced activity discussed above, Goodman and coworkers proposed the existence of transient 'hyperactive' states with even higher activity rates, during which the reaction proceeds via a Langmuir-Hinshelwood mechanism with a chemisorbed oxygen-dominated surface [59, 93]. These states are supposed to be located in the transition between regimes i) and ii), just as the temperature is high enough for all inhibiting CO to desorb from the metal surface. The corresponding jumps in the reaction rate for the CO oxidation on Pd(100) are highlighted by arrows in Fig. 3.3 b). The concept of the 'hyperactive' phase has been controversially discussed [67, 68, 69], but there are studies supporting the notion of chemisorbed oxygen as the catalytically most active phase reacting via a Langmuir-Hinshelwood mechanism [92, 94, 95, 96].

Apart from ascribing the catalytic activity solely to one particular phase (i.e. chemisorbed oxygen: Langmuir-Hinshelwood ↔ oxide: Mars-van-Krevelen), there are concepts and measurements that suggest a synergy between oxide phases and chemisorbed oxygen, thus blurring the lines between the Langmuir-Hinshelwood and Mars-van-Krevelen mechanisms.
Hence, a combined TPD, TPR and LEED study proposes that the chemisorbed c(2×2) oxygen on Pd(100) reacts with CO, while adjacent $(\sqrt{5}\times\sqrt{5})R27^\circ$ surface oxide islands act as oxygen reservoirs refilling the chemisorbed phase, where the transport of oxygen to the chemisorbed phase appears to be rapid [94]. For Pt(111) the perimeter regions of α-PtO_2 surface oxide islands were concluded to exhibit sites where CO atoms may adsorb easily and which are characterized by reduced energy barriers for reaction with oxygen from the surface oxide [97]. Similarly, a recent DFT study ascribed the nature of Goodman's 'hyperactive phase' to the coexistence of the CO covered Pd(111) and the Pd_5O_4 surface oxide at the phase boundary between the CO-inhibited low temperature regime i) and the mass transfer limited regime ii) [79]. Likewise, for all studied Rh surfaces and the alloy $Pt_{0.25}Rh_{0.75}(100)$ surface adsorption of CO on the metallic surface and reaction at the border of the O-Rh-O trilayer surface oxide patches was proposed [81, 82, 85]. Accordingly, partially oxidized Pt particles displayed the highest activity during CO oxidation reaction [98].

3.1.4 Interaction of molecules with catalyst surfaces

In case of a Langmuir-Hinshelwood mechanism (see regimes i) in Fig. 3.3 a) and b)) the oxygen and CO molecules interact directly with the catalyst surfaces. The present subsection explains the enhanced ability of Pt-group metals to catalyze reactions via this mechanism.
The schematic plots of Fig. 3.1 and Fig. 3.2 imply that a good catalyst must allow both, the adsorption of the reactants, but also the reaction product's desorption. This notion forms the basis of the *Sabatier principle*, which states that highest activity rates are achieved if the interaction between a catalyst and the reactants is neither too strong nor too weak. If the interaction is too strong, the adsorbates and the reaction products would stick to the catalyst

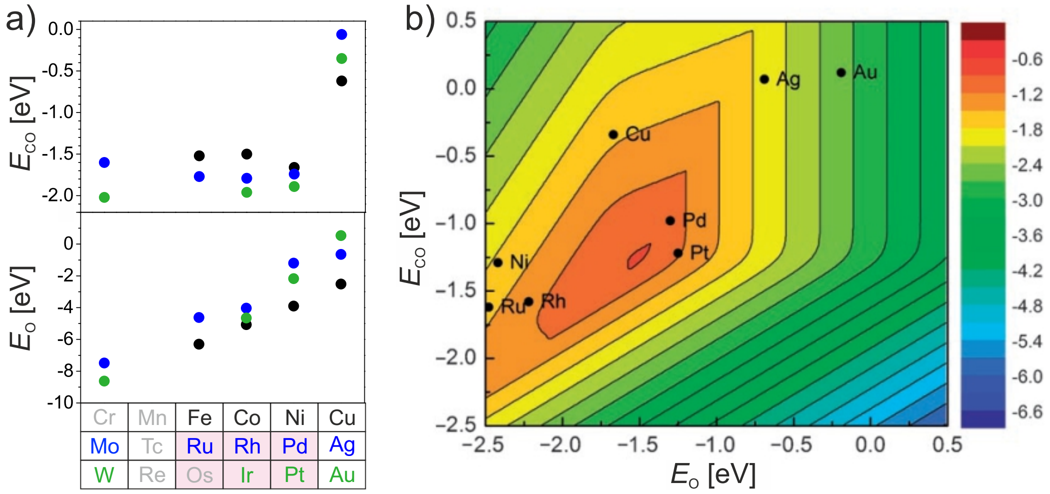

Figure 3.4: **Enthalpies of adsorption and contour plot: a):** calculated energies for molecular (CO) and dissociative (O) chemisorption on a number of transition metal surfaces (fcc (211) surfaces in all cases expect for Fe, Mo and W, for which bcc (210) was considered) with respect to vacuum, adapted from [99]; **b):** contour plot of the calculated Sabatier activity over various (111) surfaces as a function of E_{CO} and E_O at T=600 K, p_{O2}=0.33 bar and p_{CO}=0.67 bar, after [100].

surface and block its active sites. Contrary, if it is too weak, the reactants' stay on the catalyst surface would be too short to result in a reaction.

The enthalpy of adsorption can be seen as a measure for the reactant-catalyst interaction. Fig. 3.4 a) shows its values for the molecular and dissociative adsorption of CO and O_2 on various transition metal surfaces [99]. While the platinum-group metals display the desired moderate interactions, the transition metals further to the left in the periodic system reveal too strong, the ones to the right too weak adsorption enthalpies.

Plotting the reaction rate as a function of a reactant's respective enthalpies of adsorption, results in so-called *volcano-plots* [101]. Fig. 3.4 b) shows a 2-dimensional volcano plot for the calculated CO oxidation activity on various transition metals, which is enhanced for the probed Pt-group metals (Pd, Pt, Rh, Ru) [102].

The reason lies in their *d*-band structures [103]. Fig. 3.5 shows the change of the electronic structure for the scenario of a CO-molecule adsorbing on a Pt-group metal surface. Contrary to the metal's extended *s*- and *p*-orbitals, the *d*-orbitals are highly localized with only little overlap between each other. This results in narrow *d*-bands which strongly interact with the 5σ and the 2π* orbitals of the adsorbing CO molecule. As a consequence, the latter split

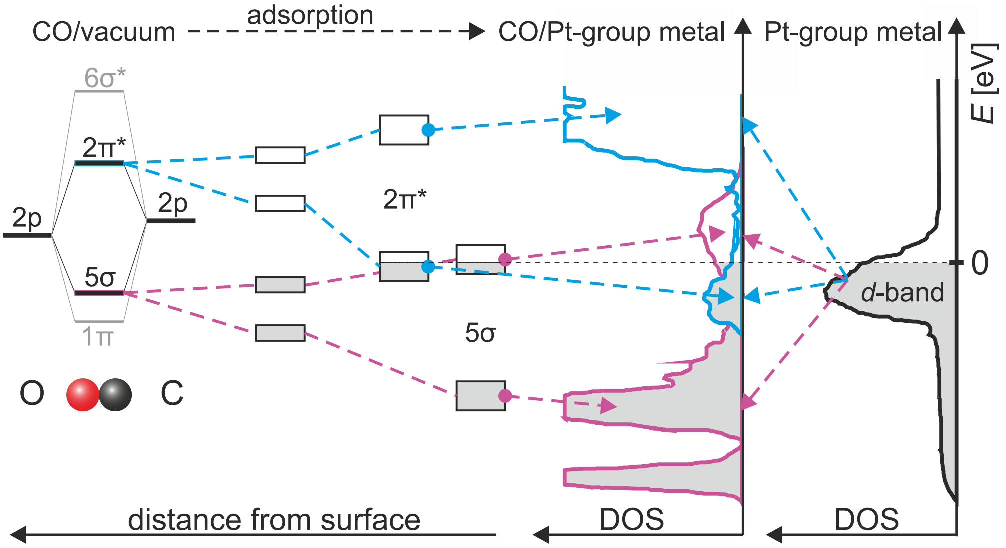

Figure 3.5: **Changes in the electronic structure during adsorption of CO on a Pt-group metal surface: left:** selected molecular orbitals of the CO molecule in vacuum; **centre:** projected density of states 'DOS' of the adsorbed molecule; **right:** electronic structure of the Pt-group metal in vacuum. After [103].

up into a bonding and an anti-bonding orbital. Due to the increasing interaction during approach, they moreover broaden and shift down in energy, as the molecule becomes more stabilized upon adsorption. The resulting projection of the metal density of states is shown in the centre of Fig. 3.5.

For Pt-group metals the situation for the adsorbed molecule is as follows: the partial filling of the anti-bonding 5σ-orbital results in a moderate metal-CO interaction according to the Sabatier principle. In addition, the filling of the bonding 2π-orbital of the adsorbed molecule leads to a weakening of the intra-molecular C-O bond.

The situation is different for transition metals outside the Pt-group: when moving from the left to the right in the periodic system the *d*-bands are progressively filled with electrons and the *d*-band centre shifts accordingly with respect to the Fermi level further down in energy. Correspondingly, for transition metals located to the left of the Pt-group metals, only the bonding 5σ orbital contains electrons, which results in a very strong bond to the adsorbed molecule; the internal C-O bond is not noticeably weakened. For the transition metals to the right of the Pt-group (Cu, Ag, Au), the *d*-bands are completely filled with electrons which exert a repulsive force on the electrons of the adsorbing molecule: the 5σ antibonding orbital is completely filled, making the respective metal-CO bond unstable.

3.1.5 Oxide formation

Metal oxides and a metal's tendency towards oxide formation play an essential role in oxidation catalysis: on the one hand in the Mars-van-Krevelen mechanism (see section 3.1.2), but also in terms of chemical and morphological particle restructuring that may occur under various gas atmospheres (see section 3.2.2).

The onset of oxidation is characterized by *structures of chemisorbed oxygen*, which may induce reconstructions on the respective metal surfaces. At a later oxidation stage, i.e. at higher oxygen chemical potentials $\mu_\mathrm{O}(p_\mathrm{O}, T)$, they transform into *surface oxides*, which are ultrathin oxide layers of defined thickness. They feature similar metal atom densities as macroscopic bulk oxides, although their atomic structures may be different. Finally, the formation of three-dimensional *bulk oxides* sets in. Details on the bulk oxide growth of monometals can be found in [104, 105, 106, 107].

The presence of additional gas phases, like CO, shifts at a given temperature the onset of surface and bulk oxide formation to higher oxygen partial pressures p_O and hence to higher oxygen chemical potentials $\mu_\mathrm{O}(p_\mathrm{O}, T)$ [79, 108, 109]. In addition to the chemisorbed oxygen phases, the stable surface and bulk oxides, the surface phase diagramme then displays stability regions of various CO adsorption structures on the clean metal and on the surface oxide [108, 109].

The oxidation of *alloy* metals is more complex, especially in the case of nanoparticles where finite size effects come into play. It depends on numerous parameters like the concentration and miscibility of the elements, which may also change in the course of the oxidation process. An overview of different bulk alloy oxidation theories is given in [110].

If one element inside an alloy features a higher affinity towards oxygen, *selective oxidation* may occur which can result in segregation effects [111, 112] (see section 3.2.2). The heat of oxide formation can be seen as a measure for an element's affinity towards oxide formation and a summary of calculated and experimental values thereof is given in Table 3.1 for Rh, Pt and Pd.

Accordingly, Rh and Pd should feature comparable tendencies towards oxide formation. However, for nanoparticle systems, the oxidation of Pd was found to be kinetically more hindered than the oxidation of Rh [112]. Accordingly, selective oxidation of Rh occurs in Pd-Rh alloy particles [112]. In the case of Pt-Rh alloys selective oxidation of Rh was concluded for both, single crystal surfaces and nanoparticles [85, 113], which is in line with the values listed in

Table 3.1. Whether selective oxidation occurs on Pt-Pd systems and which element shows a higher affinity towards oxide formation remains a rather controversial issue [111, 114, 115, 116, 117, 118].

The previous paragraph implies that Rh is, compared to Pt and Pd, more prone to form oxides. The different Rh oxide phases will be summarized in the following, an overview is also given in Fig. 3.6.

On **Rh surfaces** various chemisorbed oxygen structures form at low oxygen pressures [119, 120], including the p(3×1)-structure on Rh(100) [121].

The Rh surface oxide consists of a close-packed O-Rh-O trilayer, in which the Rh atoms are hexagonally arranged (see Fig. 3.6 a) and b)). It was found on all close-packed (Rh(111), Rh(100), Rh(110), [122, 123, 124]) and even on vicinal surfaces [81], triggering surface rearrangements into large (111)-type facets in the latter case.

On the (111) surface the O-Rh-O trilayer was experimentally determined to form a coincidence lattice between (8×8) oxide cells and (9×9) substrate cells, although DFT calculations found a (7×7)/(8×8) structure to be more stable [122]. The top and side view of the (7×7)/(8×8) ball model is shown in Fig. 3.6 b). On Rh(100) the surface oxide adapts a c(2×8) superstructure [123] (see Fig. 3.6 a) for top and side view), on Rh(110) a c(4×2) structure [124]. In both cases the hexagonal oxide lattices are slightly distorted compared to the (8×8)/(9×9) structure on Rh(111) [81].

On 8 nm-sized Rh nanoparticles the p(3×1) structure of chemisorbed oxygen on the (100)-type facets, as well as, at an advanced oxidation state, the formation of the c(2×8) surface oxide structure on the (100)-type particle facets and the (8×8)/(9×9) structure on the (111)-type facets was experimentally confirmed using in-situ SXRD [4] (see section 3.2.2).

There are several Rh bulk oxide structures: Rh_2O_3 features a corundum structure (a=b=5.127 Å, c=13.853 Å; α=β=90°, γ=120°) and can transform into an orthorhombic phase if annealed above 1020 K [125]. Its unit cell is depicted in Fig. 3.6 c) and consists of 6 units, each of which contains two slightly separated Rh-layers and one oxygen layer [82]. The RhO_2 bulk oxide displays a rutile structure, its unit cell (a=b=4.489 Å, c=3.090 Å; α=β=γ=90°, [126]) is depicted in Fig. 3.6 d). In a recent in-situ oxidation experiment of Pd-Rh particles, Rh_3O_4 was identified as new bulk oxide phase [112]. It features a hexagonal unit cell (see Fig. 3.6 c), a=b=6.15 Å, c=18.07 Å; α=β=90°, γ=120°) with an internal atomic structure similar to a (111)-oriented spinel

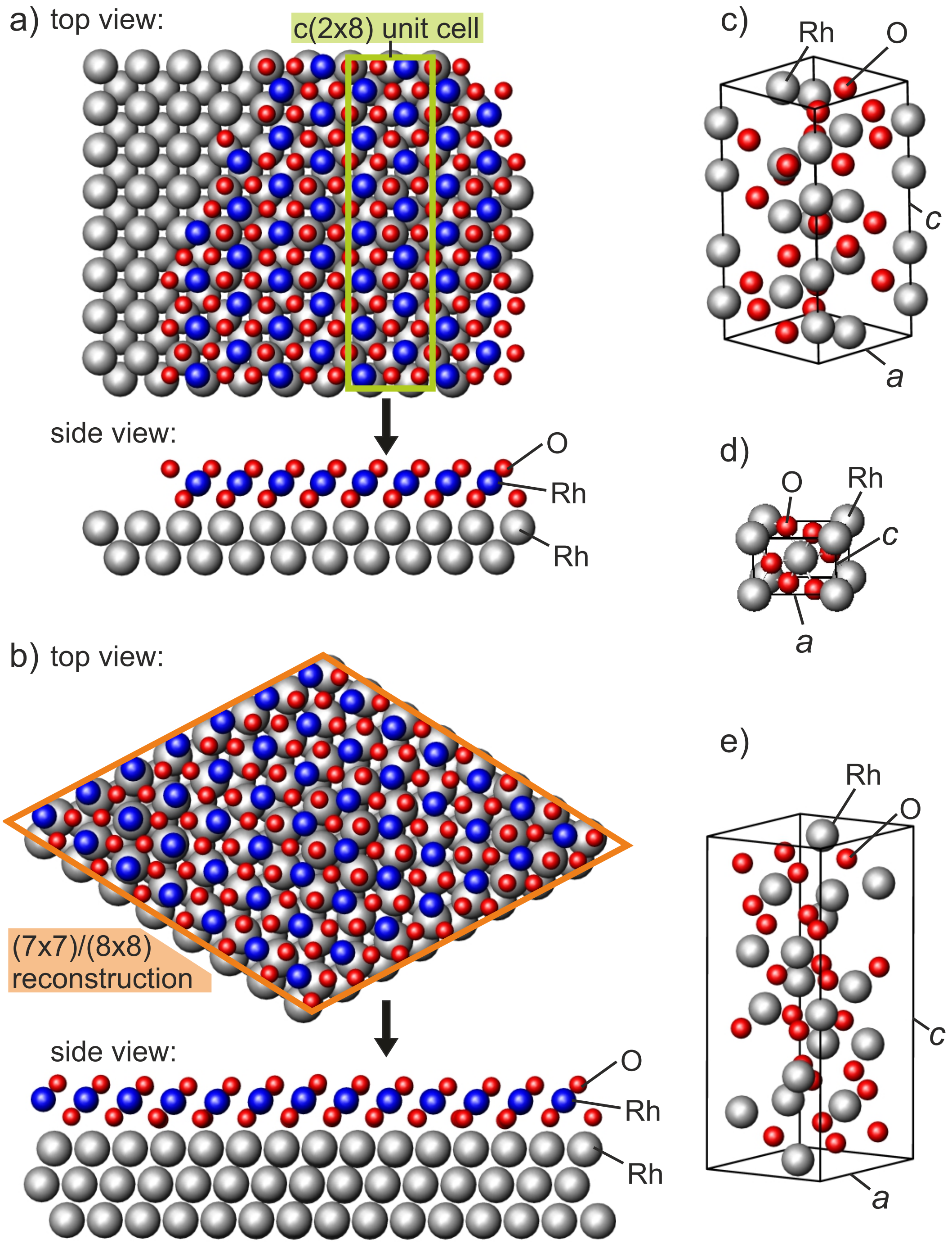

Figure 3.6: **Overview of Rh surface and bulk oxides:** the trilayer O-Rh-O surface oxide forms **a):** on the Rh(100) surface a c(2×8) structure, **b):** on the Rh(111) surface a (8×8)/(9×9) coincidence structure (the plotted structure is the thermodynamically slightly more stable (7×7)/(8×8) structure); stable Rh bulk oxide structures include **c):** Rh_2O_3 (corundum structure: a=b=5.127 Å, c=13.853 Å; α=β=90°, γ=120°, [125]), **d):** RhO_2 (rutile structure: a=b=4.489 Å, c=3.090 Å; α=β=γ=90°, [126]), **e):** Rh_3O_4 (hexagonal unit cell similar to a spinel structure in (111)-orientation: a=b=6.15 Å, c=18.07 Å; α=β=90°, γ=120°, [112]).

structure, with hexagonal close-packed oxygen and partially occupied Rh layers.

3.2 Alloy nanoparticle catalysts

Alloy catalysts came for the first time into the focus of commercial and scientific interest in the 1960s due to the high activity found for Pt-Ir-catalyzed hydrogenation reactions for the production of lead-free gasoline with high octane numbers [127, 128]. Today their widespread commercial use ranges from reforming reactions over pollution control to alcohol oxidation [127, 129].

The high number of recently published review reports and articles in high-impact journals underlines the topicality of this research field [22, 23, 127, 129, 130, 131, 132, 133, 134, 135, 136, 137].

3.2.1 Catalytic properties of alloy nanoparticles

Alloy and bimetallic nanoparticles display a high level of complexity. On the one hand this is due to the fact that they contain different chemical elements: they may arrange in various ways inside the particle, which may completely alter the catalyst performance (some possible mixing patterns are shown in Fig. 2.4 of section 2.2). Accordingly, alloys show different catalytic properties compared to their parent metals: *synergetic effects* between the respective elements may lead to an enhancement of the catalytic *activity* (i.e. the turnover frequency of a reaction), of the catalyst *stability* or of the *selectivity* towards a certain reaction pathway [137, 138, 139, 140].

Hence, Pd-Rh alloy particles were found to display increased *activity* for CO oxidation compared to their respective monometallic catalysts [138]: the synergy was ascribed to the favoured adsorption of CO on Pd, resulting in the formation of CO_2 due to spillover events of oxygen preferentially adsorbed on Rh. The addition of Pd to Pt was concluded to reduce the sintering and thus to increase the catalyst *stability* during NO oxidation, although an explanation is lacking so far [141]. An increase in the *selectivity* in favour of the cyclohexane dehydrogenation reaction at the expense of the ethane hydrogenolysis rate was concluded for Ni catalysts enriched by Cu [142].

The altered catalytic characteristics can, to some extent, be explained by so-called *strain* and *ligand effects* that occur in alloy systems [143, 144]. The strain effect arises from the fact that the bond lengths between the atoms of an alloy differ from the ones of the respective single metals, resulting in changes of the corresponding orbital overlap. The ligand effect is due to the altered electronic environment which builds up around an atom in the presence of a second type of atom.

Both, strain and ligand effect, lead to altered electronic *d*-band structures, which in turn change the catalytic properties (see discussion in section 3.1.4). DFT calculations on slabs of closest-packed surfaces revealed that both effects determine the broadening or narrowing of the *d*-band width [145]. As a consequence, the *d*-band centre lowers or raises in order to retain the respective *d*-band filling.

Apart from alloying, the electronic structure of the catalyst materials and hence their catalytic properties may also be altered due to the particles' finite size effects [21, 131]: these include changes in the band structures due to under-coordinated atoms at particle edges, due to strain effects at the particle-support interface or due to charge transfer phenomena from the support. Moreover, the catalyst performance depends on the particle shape due to the presence and the possible interplay of several particle facets [21, 131].

The desired understanding of the interplay between the catalyst performance and the complicated particle alloy and size effects may lead to 'catalysis by design' [146, 147], the possibility of which has been demonstrated in rare cases [148].

3.2.2 Restructuring under various gas atmospheres

Catalytic reaction conditions, and thus the exposure to various gases, may trigger enormous intra-particle mass transports resulting in a dynamical restructuring of the particles. The restructuring may be characterized by 1.) changes in the elemental distribution inside the alloy particles, leading to the **segregation** of a certain element to the particle surface [111, 149, 150], and 2.) adsorbate-induced **particle shape changes** [4, 25, 151, 152, 153, 154], or, most likely, also the combination of both.

1.) As an example for gas-induced **segregation** effects, Fig. 3.7 summarizes the results of Tao et al. on the distribution of Rh and Pd inside 15 nm sized $Rh_{0.5}Pd_{0.5}$ alloy particles as a function of the probed sample conditions. These include oxidizing (100 mTorr of NO or O_2) and reaction conditions (100 mTorr NO and 100 mTorr CO) [111]. Using Ambient Pressure XPS the composition in the particle shells (outermost 0.7 nm) was tested: the bottom of Fig. 3.7

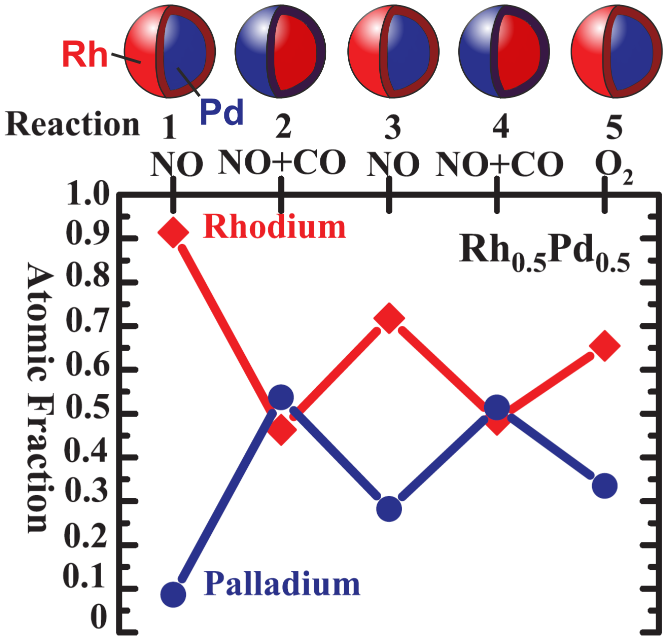

Figure 3.7: **Chemical restructuring of $Rh_{0.5}Pd_{0.5}$ bimetallic particles:** the atomic fractions of Rh (Rh^0 + Rh^{2y+}) and Pd (Pd^0 + Pd^{2y+}) measured by AP-XPS are given as a function of the probed conditions at 573 K (oxidizing: 100 mTorr NO or O_2; catalytic: 100 mTorr NO and 100 mTorr CO). After [111].

shows the thus obtained atomic fractions of Rh and Pd located in the shell, the figure top reveals the corresponding particle segregation profile. Under oxidizing conditions, the particle shell is enriched in Rh, where the majority of the Rh atoms are bound in Rh oxide, suggesting at the same time a Pd-rich core. Under reaction conditions the Rh oxide becomes reduced, Pd segregates to the particle surface and leaves a Rh-rich core.

The driving force for the segregation of Rh under oxidizing conditions lies in the fact that Pd oxidation is greatly kinetically hindered in nanoparticle systems ([112], see also subsection 3.1.5). Contrary, for the reduced particles under reaction conditions the segregation of Pd can be traced back to its lower surface energy compared to Rh (see Table 3.2). The surface energy of the clean metal becomes the critical factor, since the adsorption energies of CO on Pd, Rh and Pt are comparable [58].

Due to the higher affinity of Rh towards oxide formation and due to the lower surface energy of Pt surfaces (see Tables 3.1 and 3.2), Tao et al. find for Pt-Rh alloy nanoparticles Rh segregation under oxidizing and Pt segregation under reaction conditions [150]. In case of Pt-Pd particles a Pd-rich shell and a Pt-rich core were concluded independent of the reaction condition [111].

2.) The driving force for the adsorption-induced **particle shape changes** lies in the fact that the adsorption of molecules most of the time alters the surface energy of a particular particle facet. This leads to an increase or shrinking of the facet size or even to the emergence of new particle facets [25, 151].

oxide	**Rh_2O_3**	**RhO_2**	**PdO**	**α-PtO_2**	**Pt_3O_4**
cal.	-1.27 [155]	-1.27 [156]	-(0.87-1.42) [157]	-1.03 [159]	-0.36 [159]
exp.	-1.19 [155]	–	-1.22 [158]	–	–

Table 3.1: **Heats of oxide formation in [eV/oxygen atom]:** the calculated and (if available) experimental data are given for various bulk oxide structures of Rh, Pt and Pd; the respective references are given in brackets.

element	**Rh**		**Pt**		**Pd**	
surface	**(111)**	**(100)**	**(111)**	**(100)**	**(111)**	**(100)**
cal.: E_{sur} $[\frac{J}{m^2}]$	2.78	2.90	2.35	2.48	1.88	1.90
exp.: E_{sur} $[\frac{J}{m^2}]$	2.70	–	2.48	–	2.05	–

Table 3.2: **Surface free energies E_{sur} under reducing conditions in [J/m^2]:** the calculated and (if available) experimental data are given for the (111)- and (100)-type surfaces of Rh, Pt and Pd; all values are according to [160] and references therein.

For monometallic Rh, Pt, Pd and Cu particles adsorbate-induced shape changes have been experimentally studied [4, 152, 153, 154]. Fig. 3.8 summarizes the findings for supported Rh particles studied under successive oxidation (pure O_2) and reduction (pure CO) cycles [4]. Oxygen adsorption was found to set in on the particle (001)-type facets at 2×10^{-5} mbar O_2 and 500 K, resulting in a (3×1) superstructure with three-fold oxygen adsorption sites. At a slightly higher temperature (550 K) the adsorbed oxygen grows into a O-Rh-O trilayer surface oxide, which occurs at the same time on the (001)- and (111)-type facets as a c(2×8) and a p(9×9) coincidence structure, respectively. The surface oxide greatly reduces the surface energy of the (001)-type facets, which grow in size at the expense of the (111)-type facets, which accordingly shrink. The deduced shape changes were found to be reversible upon CO exposure, thus mimicking the particle shape changes under CO oxidation reactions.

The complexity of the particle shape changes for various elements increases in the following order: Rh>Pd>Pt: for Rh particles exposure to oxygen does not result in the formation of additional particle facets [4]. Contrary, in case of Pd particles (112)-type facets were concluded to emerge in addition upon oxygen exposure [153]. For Pt particles, the formation of various high-index facets was evidenced leading to a round particle shape [152]. While the oxygen-induced

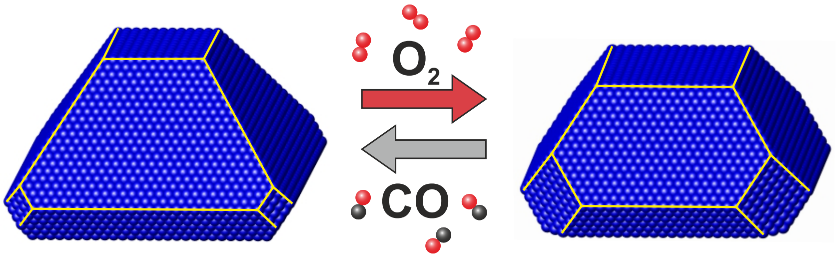

Figure 3.8: **Rh particle shape changes:** induced by surface oxides (O_2), reversed by CO exposure. After [4].

shape changes were found to be reversible for Rh and Pd particles upon CO exposure, they were not in the case of Pt [152].

Experimental evidence on the gas-induced shape changes of *alloy* nanoparticles under realistic reaction conditions is lacking so far. However, in line with the findings for pure Rh particles, studies on $Pt_{0.25}Rh_{0.75}(001)$ model catalyst surfaces reveal the emergence of the (3×1) adsorption structure and of the O-Rh-O trilayer surface oxide [85, 161]. This implies that also Pt-Rh alloy nanoparticles may undergo similar oxygen-induced shape changes.

3.3 Catalyst deactivation by particle sintering

The harsh reaction conditions in ‘real world’ technical catalysis, characterized by elevated temperatures and pressures, lead in general to a gradual degradation of the complex catalyst systems. One major cause of catalyst deactivation often addressed in this thesis is particle sintering, i.e. the coalescence of smaller particles into fewer larger ones, which results in a loss of the effective catalyst surface area.

Particle growth via sintering may not only occur during catalytic reaction conditions, but also during the process of particle growth (see chapter 2).

Although nanoparticle sintering has been widely studied in recent years, there is still much uncertainty about the ongoing mechanisms on the atomic level. This can partly be traced back to a shortcoming of operando studies, since early experiments were often limited to the investigation of sample systems before and after sintering only.

There are two main sintering mechanisms discussed in literature [162, 163]: 1.) sintering via inter-particle mass transport, denoted as *Ostwald ripening*, and 2.) particle migration and coalescence, referred to as *Smoluchowski ripening*.

Ostwald ripening

Ostwald ripening is a spontaneous thermodynamically driven process. Its driving force can be seen in the fact that a particle's vapour pressure p varies inversely with particle size. Assuming spherical particles with radius r this relation is governed by the *Gibbs-Thompson*, or *Kelvin equation*:

$$\ln\left(\frac{p}{p_0}\right) = \frac{2\gamma V_{\mathrm{m}}}{rRT}, \tag{3.1}$$

where p_0 describes the saturated vapour pressure, γ the surface free energy, V_{m} the atomic volume of the cluster, R the universal gas constant and T the temperature. If $p > p_0$ particle adatoms 'evaporate' from the particle's surface, if $p < p_0$ adatoms 'condense' onto the particles' surface. Accordingly, there is a critical particle size $r_0 = \frac{2\gamma V_{\mathrm{m}}}{RT}$ which separates the particle size distribution into larger particles ($r > r_0$) that 'catch' adatoms and smaller particles ($r < r_0$) that 'lose' adatoms.

The resulting process of Ostwald ripening illustrated in Fig. 3.9 a) for the two differently sized particles A ($r < r_0$) and B ($r > r_0$): in the case of A there is an adatom concentration c_{A} adjacent to the particles which is larger than the adatom concentration c_0 on the substrate surface far away from any particle ($c_{\mathrm{A}} > c_0$). Contrary, in the case of particle B the concentration c_{B} in its surrounding is smaller than c_0 ($c_{\mathrm{B}} < c_0$). According to *Fick's law* there is a diffusion net flux of atoms

$$J = -D\frac{\partial c}{\partial x}, \tag{3.2}$$

from the smaller particle A to the support and further to the surface of the larger particle B (D: diffusion coefficient, x: position). Hence, the larger particles ($r > r_0$) grow at the expense of the smaller ones ($r < r_0$).

An example of Ostwald ripening is shown in Fig. 3.10 a), which displays STM images measured on 2D Ag islands on Ag(111) [164].

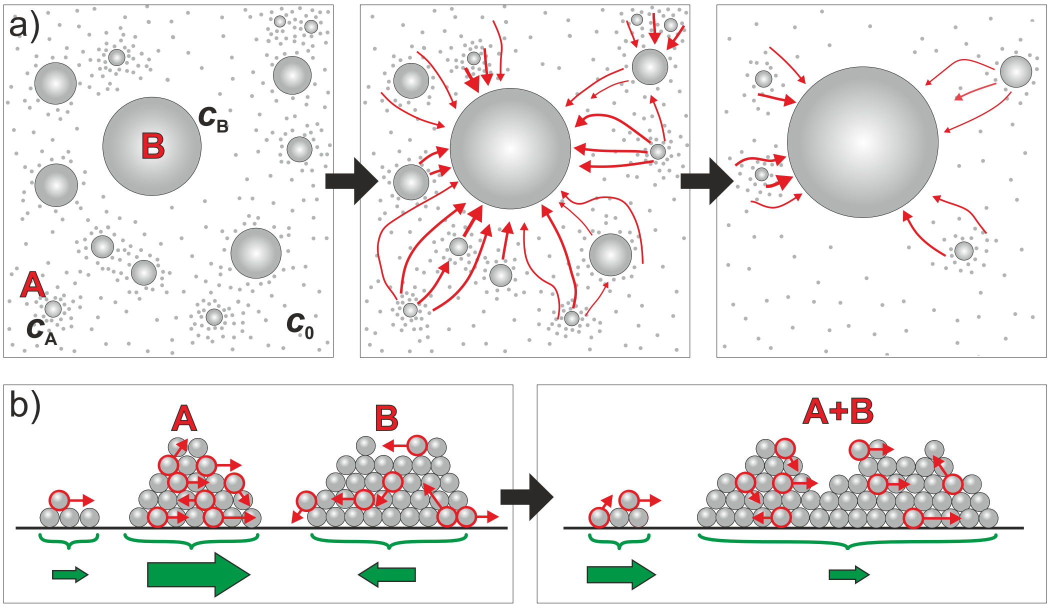

Figure 3.9: **Sinter mechanisms:** particle ripening on the atomic scale is illustrated for the cases of **a):** Ostwald ripening (top view), and **b):** Smoluchowski ripening (side view). In **a):** filled circles: particles; small dots: adatoms with concentrations c_{A}, c_{B} and c_0; red arrows: adatom fluxes. In **b):** red arrows: jump direction of a single atom; green arrows: jump direction of a whole particle. See text for more information.

Smoluchowski ripening

A basic notion of Smoluchowski ripening is the diffusion, or hopping, of the particle adatoms on top of the particle surface due to atomic self-diffusion [162, 163]. The single jumps of the adatoms are in Fig. 3.9 b) illustrated by the red arrows. The sum of their jumps results in a shift of the whole particle's centre of mass, as is indicated by the green arrows. As illustrated in Fig. 3.9 b) for particles A and B, this may result in the migration of whole particles and finally to their coalescence. The diffusion coefficient D_{p} of the whole particle assuming spherical particles is given by [162]

$$D_{\mathrm{p}} = \frac{24}{\pi}\frac{a^4}{d^4}D_{\mathrm{s}}, \tag{3.3}$$

where D_{s} corresponds to the self-diffusion coefficient of the single adatoms, a to the atomic diameter and d to the particle diameter. Accordingly, the particle diffusion is all the more pronounced the smaller the particle diameter. The dependence on the diameter was found to be even stronger ($D_{\mathrm{p}} \propto e^{-d}$) if

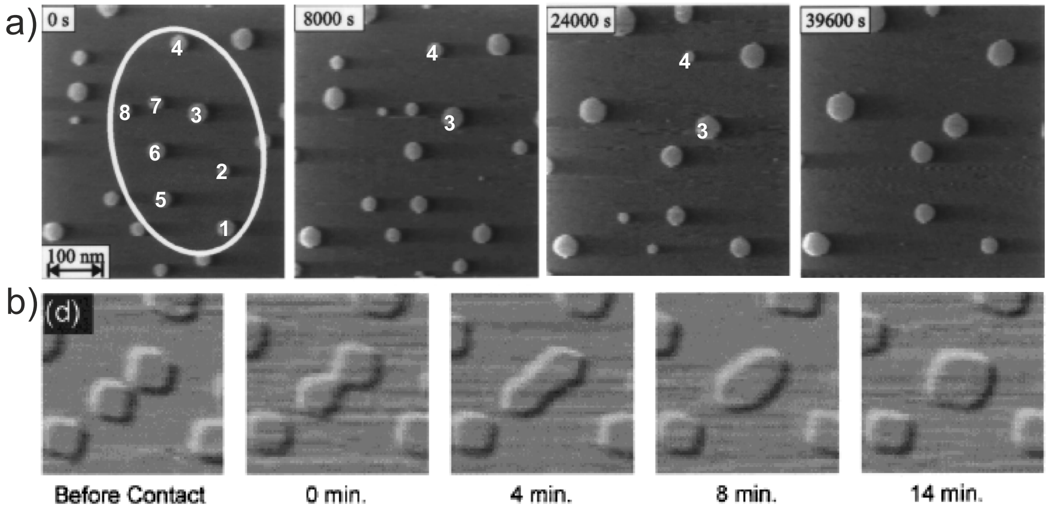

Figure 3.10: **Examples of sintering measured by STM at 300 K: a):** Ostwald ripening of 2D Ag islands on Ag(111), during which particles numbered 2, 8, 7 and 4 successively disappear [164], **b):** Smoluchowski ripening of 2D Ag islands on Ag(100) via a corner-to-corner coalescence (image = 50×50 nm^2, [165]).

faceted particles are considered [162].

An example of Smoluchowski ripening of 2D Ag islands on Ag(100) as measured by STM is shown in Fig. 3.10 b) [165].

Sintering prevention

Redispersion of sintered particles is very difficult, limited to certain systems and often involves the use of undesired chlorine [166]. Hence, there are numerous studies aiming at the realization of sintering prevention (see ref. [167] and references therein). These include the *alloying* of particles, aiming at an enhanced stability by the addition of a second, higher melting point metal (e.g. adding Rh to Pt). Moreover, there are efforts towards the suppression of sintering based on *encapsulation* of particles, where the covering material ranges from silicon shells to carbon nanotubes. Another approach is to suppress the particle movements by *support effects*. Hence, CeO_2 was concluded to display stabilizing effects via an anchoring effect due to a strong Ce-O-M (M: metal) metal-support interaction.

Chapter 4

Surface Sensitive X-Ray Diffraction: Concepts and Measurement Strategies

Surface sensitive x-ray diffraction constitutes the main sample characterization method employed in this thesis. While its general concepts will be outlined in section 4.1, sections 4.2-4.3 demonstrate how surface sensitive x-ray diffraction was in particular employed for the investigation of nanoparticles: while section 4.2 covers surface x-ray diffraction (SXRD) from nanoparticles at conventional photon energies (here: E=11.2 keV), section 4.3 deals with the corresponding high-energy approach of high energy surface x-ray diffraction (HESXRD, E=78-85 keV), which also allows the investigation of combinatorial samples.
The chapter will close with section 4.4, yielding a short survey over additional measurement techniques employed in this thesis, which include x-ray reflectivity (XRR), Auger electron spectroscopy (AES) and atomic force microscopy (AFM).

4.1 General concepts of x-ray diffraction

In the following, a summary of the general concepts of x-ray diffraction will be given based on review articles and books covering this topic [168, 169, 170, 171, 172]. Throughout it will be assumed that x-rays are only weakly scattered from the sample, i.e. that multiple scattering events can be neglected and the *kinematical approximation* is valid.
In the classical description, the electric field of the incoming x-ray exerts a force

on the electron, which as a consequence is being accelerated. The vibrating electron acts as a dipole that radiates a spherical wave of the same wavelength as the incident x-ray beam, since *elastic scattering* is assumed.
Comparison of the amplitudes of the incident and the scattered wave yields the energy-independent scattering amplitude of the free electron, which is given by the *Thomson scattering length*:

$$r_0 = \frac{e^2}{4\pi\epsilon_0 m_\mathrm{e} c^2} = 2.82 \cdot 10^{-5}\ \text{Å}. \tag{4.1}$$

Including a polarization factor $P =$ -$|\hat{\epsilon}\cdot\hat{\epsilon}'|$, where $\hat{\epsilon}$ ($\hat{\epsilon}'$) denotes the polarization of the incident (radiated) field, the *scattering cross section of a free electron* becomes:

$$|\tilde{r}_0|^2 = r_0^2\ |\hat{\epsilon}\cdot\hat{\epsilon}'|^2 = r_0^2 P^2. \tag{4.2}$$

In order to express the *scattering amplitude from an atom* one needs to sum over the contributions of all its electrons while taking the respective phase differences of the scattered waves into account. Hence, assuming that the electrons inside a volume element $d\boldsymbol{r}$ contribute an amount -$r_0\rho(\boldsymbol{r})d\boldsymbol{r}$ to the scattered wave, the total scattering amplitude of an atom is given by the *atomic form factor*:

$$f^0(\boldsymbol{Q}) = \int \rho(\boldsymbol{r}) e^{i\boldsymbol{Q}\boldsymbol{r}} d^3\boldsymbol{r}, \tag{4.3}$$

where $e^{i\boldsymbol{Q}\boldsymbol{r}}$ constitutes the phase factor with the *scattering vector* ***Q*=*k*-*k'***. The latter describes the difference between the incident and the scattered wavevectors, ***k*** and ***k'***, respectively, where due to elastic scattering |***k***|=|***k'***| holds. To obtain the intensity scattered from an atom, equation 4.3 has to be multiplied by its complex conjugate.
Equation 4.3 presumes free electrons, although they are in reality bound inside the atoms. The addition of the x-ray energy-dependent *dispersion correction factors* $f'(\hbar,\omega)$ and $f''(\hbar,\omega)$ compensates for this and a more correct version of the atomic form factor reads:

$$f(\boldsymbol{Q},\hbar\omega) = f^0(\boldsymbol{Q}) + f'(\hbar\omega) + if''(\hbar\omega). \tag{4.4}$$

While $f'(\hbar\omega)$ denotes the amount by which the scattering length $f^0(\boldsymbol{Q})$ is reduced as electrons cannot freely follow the external driving field, $f''(\hbar\omega)$ corresponds to the dissipation of the phase-lagged system in analogy to a forced harmonic oscillator. Both, $f'(\hbar\omega)$ and $f''(\hbar\omega)$, show resonant behaviour if the energy coincides with the one of an atomic absorption edge. For x-ray energies exceeding the ones of atomic absorption edges, $f'(\hbar\omega)$ approaches zero.

4.1.1 Diffraction from different sample systems

Diffraction from an infinite 3D crystal

In order to derive the scattering amplitude from a 3-dimensional crystal the atomic form factors $f_j(\boldsymbol{Q},\ \hbar\omega)$ of the various atoms making up the crystal as well as their respective positions $\boldsymbol{r}_j$ inside the crystal lattice unit cell have to be known. If $\boldsymbol{R}_n = n_x\boldsymbol{a}_x + n_y\boldsymbol{a}_y + n_z\boldsymbol{a}_z$ denotes all possible lattice vectors made up of the unit cell basis vectors $(\boldsymbol{a}_x,\ \boldsymbol{a}_y,\ \boldsymbol{a}_z)$ and a set of integers $(n_x,\ n_y,\ n_z)$, the position of any possible atom inside the crystal is given by $\boldsymbol{R}_n + \boldsymbol{r}_j$. Hence, the *structure factor* $\mathscr{F}^{crystal}$ *of an infinite crystal* becomes:

$$\mathscr{F}^{crystal}(\boldsymbol{Q},\hbar\omega) = -r_0 P \underbrace{\sum_j f_j(\boldsymbol{Q},\hbar\omega) e^{i\boldsymbol{Q}\boldsymbol{r}_j}}_{\text{unit cell struct. factor } F_{UC}^{crystal}} \underbrace{\sum_{n_x}\sum_{n_y}\sum_{n_z} e^{i\boldsymbol{Q}(n_x\boldsymbol{a}_x + n_y\boldsymbol{a}_y + n_z\boldsymbol{a}_z)}}_{\text{lattice sum } S_{x,y,z}^{crystal}}, \tag{4.5}$$

where in the last term the sums over n_x, n_y and n_z run from $-\infty$ to ∞. While the unit cell structure factor $F_{UC}^{crystal}$ determines the *amplitude* of the scattered signal, the lattice sum $S_{x,y,z}^{crystal}$ holds in addition information about the *positions* of constructive interference. To obtain the *scattered intensity*, equation 4.5 has to be multiplied by its complex-conjugate:

$$\mathcal{I}^{crystal}(\boldsymbol{Q},\hbar\omega) = |\mathscr{F}^{crystal}(\boldsymbol{Q},\hbar\omega)|^2 = |r_0 P\ F_{UC}^{crystal}(\boldsymbol{Q},\hbar\omega)\ S_{x,y,z}^{crystal}(\boldsymbol{Q})|^2. \tag{4.6}$$

To clarify the role of the lattice sum $S_{x,y,z}^{crystal}(\boldsymbol{Q})$ in equations 4.5 and 4.6, it will in the following be performed only along one dimension (here: along the

x-axis) up to a finite maximum number of atoms N_x, which results in

$$S_x(x = \boldsymbol{Q}_x \boldsymbol{a}_x) = \sum_{n_x=1}^{N_x} e^{i \cdot n_x \boldsymbol{Q}_x \boldsymbol{a}_x} = \frac{1 - e^{i N_x \boldsymbol{Q}_x \boldsymbol{a}_x}}{1 - e^{i \boldsymbol{Q}_x \boldsymbol{a}_x}}. \tag{4.7}$$

It yields for the scattered intensity the *Laue function*, or N_x-slit interference function:

$$|S_x(\boldsymbol{Q}_x \boldsymbol{a}_x)|^2 = \frac{\sin^2\left(\frac{N_x \boldsymbol{Q}_x \boldsymbol{a}_x}{2}\right)}{\sin^2\left(\frac{\boldsymbol{Q}_x \boldsymbol{a}_x}{2}\right)}, \tag{4.8}$$

which is plotted in Fig. 4.1 for various numbers of atoms N_x. It illustrates that constructive interference occurs if $x = \boldsymbol{Q}_x \boldsymbol{a}_x$ corresponds to multiples of 2π. This notion can be expanded to the other dimensions as well and is generalized in the *Laue condition*:

$$\boldsymbol{Q} = \boldsymbol{G}, \tag{4.9}$$

which states that diffraction only occurs, if the scattering vector $\boldsymbol{Q}$ equals a reciprocal lattice vector $\boldsymbol{G} = h\boldsymbol{b}_x + k\boldsymbol{b}_y + l\boldsymbol{b}_z$, where $\boldsymbol{a}_i \cdot \boldsymbol{b}_j = 2\pi\delta_{ij}$.
Fig. 4.1 moreover clarifies that the resulting Bragg peaks are characterized by a full width at half maximum of FWHM=$\frac{2\pi}{N_x}$ and a peak intensity of N_x^2.
Based on the above mentioned and on equations 4.5 and 4.6, the scattered maximum intensity of a 3-dimensional crystal for which the Laue equation is satisfied in all three dimensions can be rewritten as

$$\begin{aligned}\mathcal{I}^{crystal}(\boldsymbol{Q}, \hbar\omega) &= r_0^2 P^2 |F_{UC}^{crystal}(\boldsymbol{Q}, \hbar\omega)|^2 \; \frac{\sin^2\left(\frac{N_x \boldsymbol{Q}_x \boldsymbol{a}_x}{2}\right) \sin^2\left(\frac{N_y \boldsymbol{Q}_y \boldsymbol{a}_y}{2}\right) \sin^2\left(\frac{N_z \boldsymbol{Q}_z \boldsymbol{a}_z}{2}\right)}{\sin^2\left(\frac{\boldsymbol{Q}_x \boldsymbol{a}_x}{2}\right) \sin^2\left(\frac{\boldsymbol{Q}_y \boldsymbol{a}_y}{2}\right) \sin^2\left(\frac{\boldsymbol{Q}_z \boldsymbol{a}_z}{2}\right)} \\ &\overset{\boldsymbol{Q}=\boldsymbol{G}}{=} r_0^2 P^2 \; |F_{UC}^{crystal}(\boldsymbol{Q}, \hbar\omega)|^2 \cdot N_x^2 N_y^2 N_z^2 \; .\end{aligned} \tag{4.10}$$

Diffraction from a semi-infinite crystal: Crystal Truncation Rods

Above, it was elucidated how diffraction from a 3D infinite crystal results in well-defined Bragg peaks as the ones illustrated in Fig. 4.2 a). If such a 3D crystal is cleaved, scattering is no longer isotropic and streaks of non-zero inten-

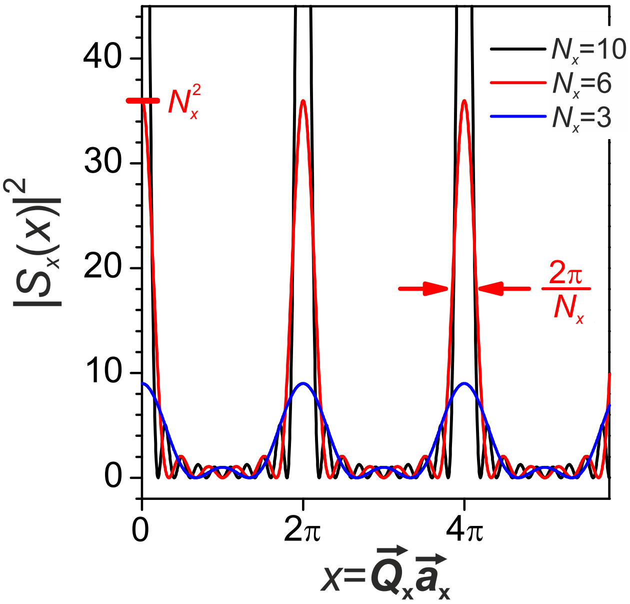

Figure 4.1: **Laue function:** N_x-slit interference function according to equation 4.8 for N_x=3 (red), N_x=6 (blue) and N_x=10 (black) as a function of $x=\boldsymbol{Q}_x \cdot \boldsymbol{a}_x$. The main maxima occur at multiples of 2π with an intensity of N_x^2 and a peak width of $\frac{2\pi}{N_x}$. There are N_x-2 subsidiary maxima which are separated by $\frac{2\pi}{N_x}$.

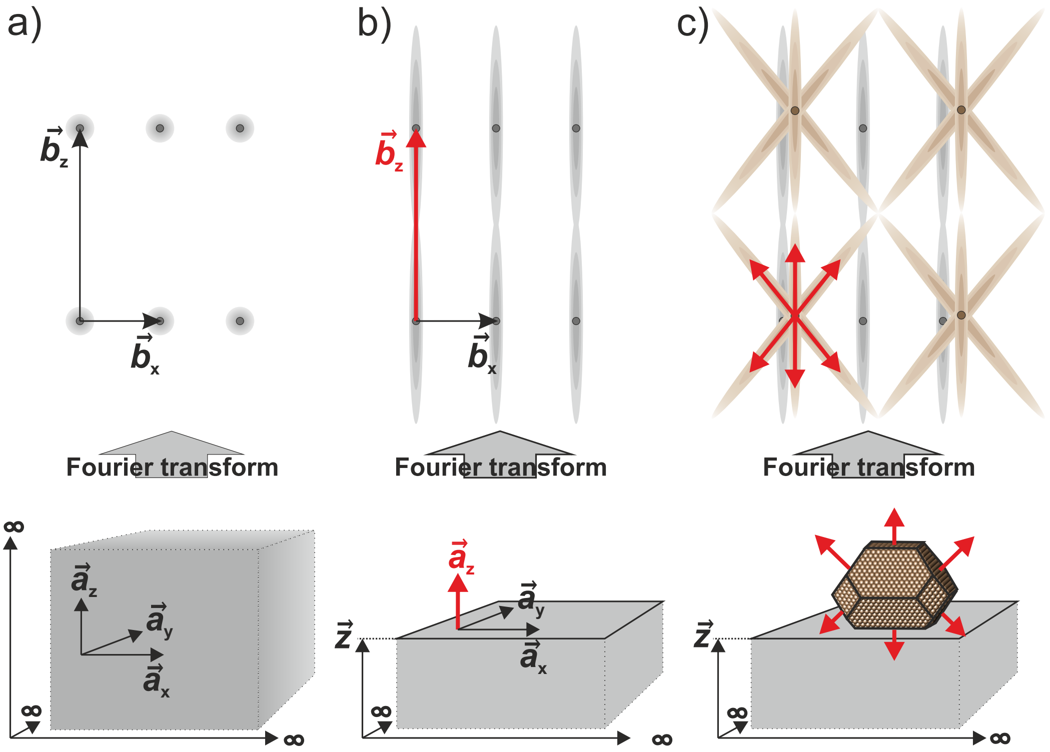

Figure 4.2: **Examples of x-ray diffraction patterns from different sample systems: a):** well-defined Bragg peak pattern induced by scattering from a 3D infinite crystal; **b):** CTR signals intersecting the crystal Bragg peaks and oriented perpendicular to the surface of a semi-infinite crystal; **c):** substrate CTRs coexisting with particle facet signals from epitaxial particles.

sity - called *Crystal Truncation Rods (CTRs)* - emerge. They run through the crystal Bragg peaks and are oriented perpendicular to the cleaved surface, as can be deduced from Fig. 4.2 b). Accordingly, in the case of faceted nanoparticles as the ones that are illustrated in Fig. 4.2 c), the facets also act as surfaces triggering CTR-like signals. These run through the particle Bragg peaks, are oriented perpendicular to the corresponding facet surfaces and coexist with potential CTRs from the substrate. In case of *epitaxial* nanoparticles, the CTR-like signals from equivalently directed facets sum up along the respective directions in reciprocal space. More information on surface x-ray diffraction from nanoparticles can be found in section 4.2.

In order to derive the intensity distribution along a CTR, a semi-infinite crystal cleaved in the (x,y)-plane as the one shown in Fig. 4.2 b), will be considered in the following. The contribution of the atomic layers to the lattice sum in out-of-plane (z-) direction can be written as

$$S_z(\boldsymbol{Q}_z \boldsymbol{a}_z) = \sum_{z=-\infty}^{0} e^{-(i\boldsymbol{Q}_z \boldsymbol{a}_z + \epsilon)z} = \frac{1}{1 - e^{-(i\boldsymbol{Q}_z \boldsymbol{a}_z + \epsilon)}} \ , \tag{4.11}$$

where ϵ constitutes the absorption from one layer to the next. Far away from the Bragg peaks the contribution to the CTR intensity is given by scattering from the topmost layers and $\epsilon \to 0$. As a consequence, equation 4.11 approaches

$$|S_z(\boldsymbol{Q}_z \boldsymbol{a}_z)|^2 = \frac{1}{2\sin^2\left(\frac{\boldsymbol{Q}_z \boldsymbol{a}_z}{2}\right)} \ , \tag{4.12}$$

and the scattered intensity along a CTR in between Bragg peaks becomes:

$$\mathcal{I}^{CTR}(\boldsymbol{Q}, \hbar\omega) \ = \ r_0^2 P^2 |F_{UC}^{crystal}(\boldsymbol{Q}, \hbar\omega)|^2 \cdot N_x^2 N_y^2 \cdot \frac{1}{2\sin^2\left(\frac{\boldsymbol{Q}_z \boldsymbol{a}_z}{2}\right)} \ = \ |\mathscr{F}^{CTR}(\boldsymbol{Q}, \hbar\omega)|^2. \tag{4.13}$$

Since the presence of the surface relaxes the scattering condition only along the $\boldsymbol{Q}_z$-direction, delta-function-like peak patterns are preserved in the horizontal scattering planes, as can be expected for a semi-infinite crystal with $N_x \to \infty$ and $N_y \to \infty$.

Typical CTR signals from a perfectly truncated, unrelaxed Rh(100) surface are represented by the black lines in Fig. 4.3 d). The intensity distribution in the valley between the Bragg peaks stems from the topmost atomic layers only. As a consequence, CTR signals are very sensitive to the registry of atoms inside surface layers, and would be readily altered by e.g. atom relaxations perpendicular to the surface or occupancy variations.

Diffraction from a 2D adlayer

In the following, diffraction patterns from quasi-2D atomic layers will be discussed. Examples for such layers are for instance (1) reconstructed surfaces that display a distinct in-plane lattice periodicity compared to the bulk lattice and that may occur on truncated crystals as the one shown in Fig. 4.2 b), or (2) thin surface oxides that form on crystal surfaces or particle facets.

Fig. 4.3 a) shows the example of an oxidized Rh(100) surface, where the real space rectangular unit cell of the thin c(2×8) surface oxide (light-green) differs from the squared one of the Rh(100) surface (grey) underneath. It also reveals, that the surface oxide, apart from its rectangular unit cell (light-green), displays some internal hexagonal patterning (dark green unit cell). Sketches of the corresponding in- and out-of-plane reciprocal space maps are displayed in Fig. 4.3 b) and c), respectively.

The out-of-plane diffraction pattern from the truncated Rh(100) surface displays according to equation 4.13 CTR signals that run through Rh bulk Bragg peaks, they are indicated in purple in Fig. 4.3 c). In the case of a 2-dimensional surface oxide layer expanded along x- and y-direction, the number of atoms N_z in z-direction has to be set to N_z=1, and the scattered intensity becomes

$$\mathcal{I}^{2D}(\boldsymbol{Q},\hbar\omega) \;=\; |\mathscr{F}^{2D}(\boldsymbol{Q},\hbar\omega)|^2 \;=\; r_0^2 P^2\, |F_{UC}^{2D}(\boldsymbol{Q},\hbar\omega)|^2 \cdot N_x^2 N_y^2, \qquad (4.14)$$

where $\mathscr{F}^{2D}(\boldsymbol{Q},\hbar\omega)$ and $F_{UC}^{2D}(\boldsymbol{Q},\hbar\omega)$ denote the total and the unit cell structure factor of a 2-dimensional layer, respectively. Their superstructure rods are represented in dark green in Fig. 4.3 c). Intensity modulations along them are only determined by the out-of-plane arrangements of the atoms inside the quasi-2D unit cell, while Bragg peaks are absent due to the lack of any 3D oxide bulk structure.

In the special case of the c(2×8) surface oxide, considerable intensity along the

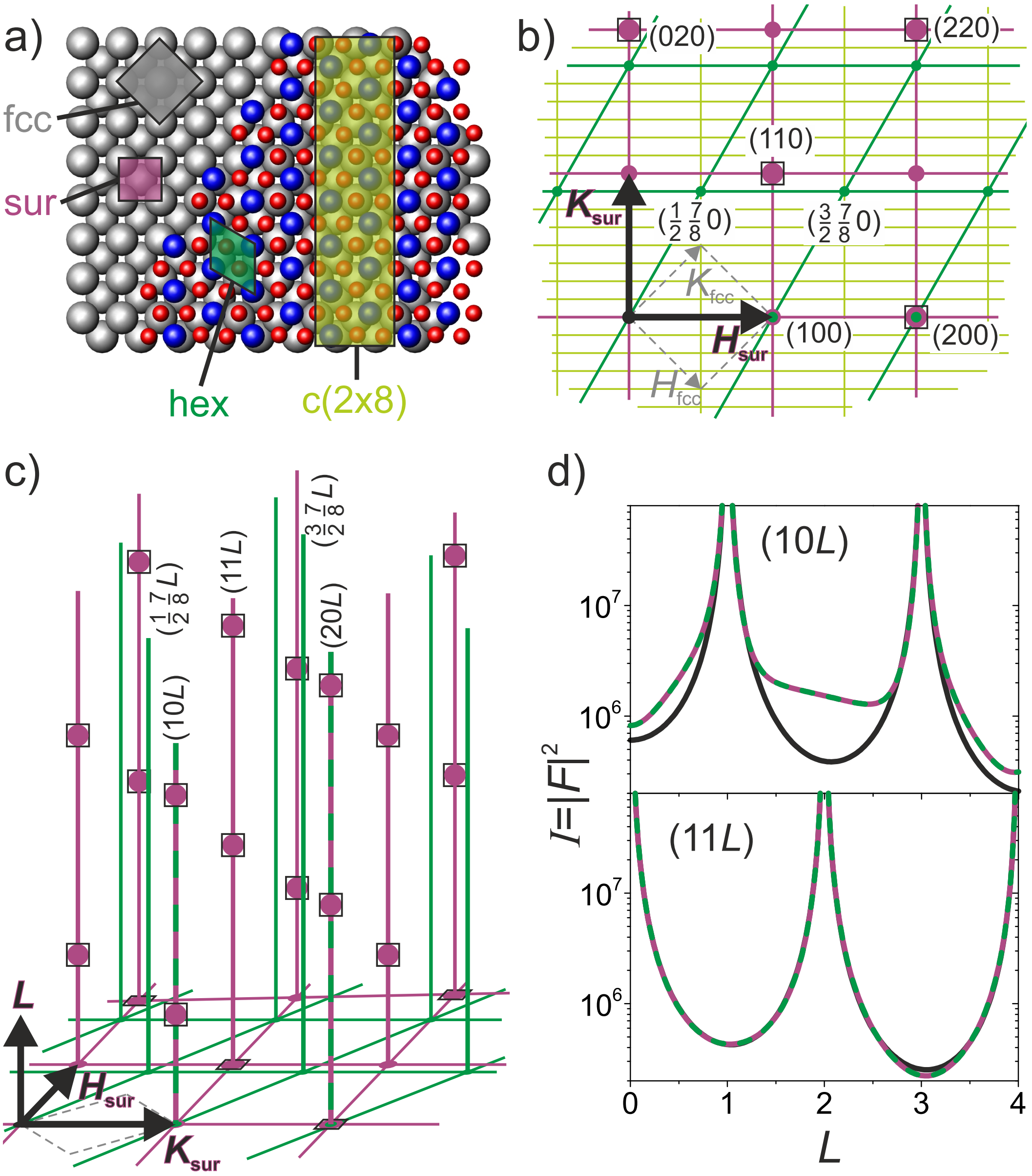

Figure 4.3: **Diffraction from oxidized Rh(100): a):** ball model of the c(2×8) surface oxide (Rh: blue, O: red) on Rh(100) (grey atoms); the unit cells of the Rh fcc lattice ("fcc", grey), the Rh surface lattice ("sur", purple), the rectangular c(2×8) surface oxide (light-green) and its hexagonal subcell ("hex", dark green) are indicated; **b):** in-plane reciprocal space map of the unit cells shown in a), the colour coding is maintained; in-plane reciprocal space vectors of the Rh fcc cell (indexed "fcc") and the Rh surface cell (indexed "sur") are given; black squares: in-plane Bragg peak positions expressed in terms of Rh surface coordinates; filled circles: rod positions; **c):** out-of-plane reciprocal space map including CTRs of the Rh surface (purple) along with c(2×8) superstructure rods (dark green); **d):** intensity distribution along $(10L)$ and $(11L)$; black: scattered intensity solely from the Rh(100) surface, purple-green dashed lines: sum of contributions from Rh(100) and the surface oxide.

superstructure rods is only present for rods whose positions coincide with the ones from the hexagonal subcell, indicated in dark green. For this reason, the potential positions of the superstructure rods from the rectangular unit cell (indicated in light-green in Fig. 4.3 a) and b)) are omitted in Fig. 4.3 c).
Fig. 4.3 b) and c) reveal, that in some cases the CTRs from the Rh(100) substrate and the superstructure rods from the surface oxide layer coincide, as is for instance the case for the Rh $(10L)$ or $(20L)$ CTRs. The scattering amplitude along such a rod is given by the sum of the structure factors for the truncated Rh crystal, $\mathscr{F}^{CTR}$, and the 2-dimensional adlayer, $\mathscr{F}^{2D}$ (compare with equations 4.13 and 4.14):

$$\mathscr{F}^{tot}(\boldsymbol{Q},\hbar\omega) \;=\; \mathscr{F}^{CTR}(\boldsymbol{Q},\hbar\omega)+\mathscr{F}^{2D}(\boldsymbol{Q},\hbar\omega), \qquad (4.15)$$

where the respective scattering intensity is given by multiplying equation 4.15 with its complex-conjugate:

$$\mathcal{I}^{tot}(\boldsymbol{Q},\hbar\omega) \;=\; |\mathscr{F}^{tot}(\boldsymbol{Q},\hbar\omega)|^2\ . \qquad (4.16)$$

Fig. 4.3 d) shows the intensity distribution along selected CTRs of the Rh(100) substrate with and without the intensity contribution from a thin c(2×8) surface oxide layer. The CTRs were simulated using the programme package ROD [173], including four surface oxide domains rotated with respect to each other by 90° around the surface normal. It can be inferred from Fig. 4.3 b) and c) that the intensity along the $(10L)$ CTR is greatly altered by the addition of the surface oxide. Contrary, the intensity distribution along the substrate Rh $(11L)$ CTR is only negligibly varied.

4.1.2 Grazing incidence diffraction geometry

Surface sensitive signals, such as crystal truncation rods and particle facet signals, are in general rather faint. An enhancement of the signal-to-noise ratio and the surface sensitivity can be achieved by using grazing incidence geometry, as will be discussed in the following.
In this geometry the incident angle $\alpha_{\mathrm{i},0}$ displayed in Fig. 4.4 is smaller than or equal to the critical angle $\alpha_{\mathrm{c},1}$ of the sample. Hence, the angle of the

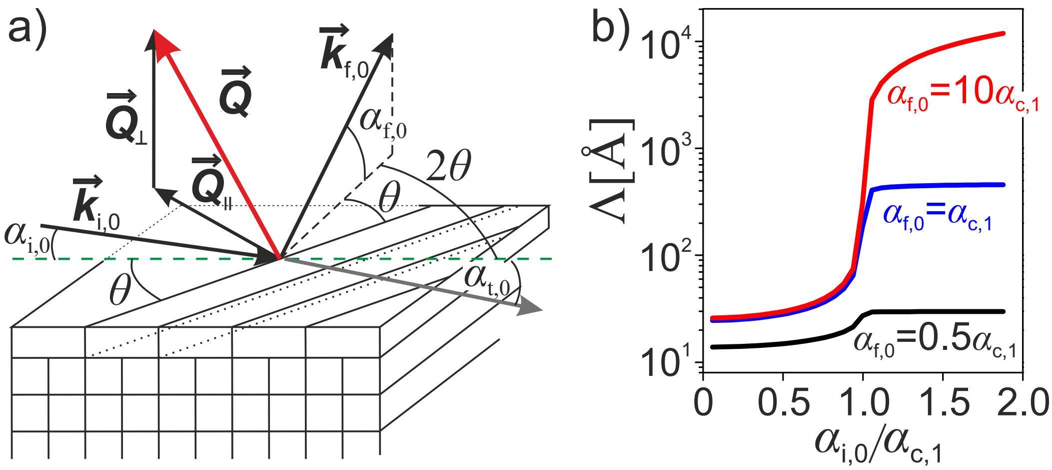

Figure 4.4: **Grazing incidence diffraction geometry and 1/e penetration depth Λ: a):** grazing incidence geometry for scattering at in-plane lattice planes; the incident and exit wavevectors, $\boldsymbol{k}_{i,0}$ and $\boldsymbol{k}_{f,0}$, respectively, define the scattering vector $\boldsymbol{Q}=\boldsymbol{Q}_{\|}+\boldsymbol{Q}_{\perp}=\boldsymbol{k}_i-\boldsymbol{k}_f$; incident, exit and Bragg angles are denoted as $\alpha_{i,0}$, $\alpha_{f,0}$ and θ, respectively; **b):** x-ray penetration depth Λ as a function of the normalized incident angle $\frac{\alpha_{i,0}}{\alpha_{c,1}}$ for various exit angles $\alpha_{f,0}$. They were calculated according to equation 4.17 for a $MgAl_2O_4$ sample and a wavelength of λ=1.107 Å (E=11.2 keV).

transmitted wave $\alpha_{t,0} \approx \sqrt{\alpha_{i,0}^2 - \alpha_{c,1}^2}$ becomes complex, as does the out-of-plane component of the transmitted wavevector $\boldsymbol{k}_{t,0}$. As a consequence, the transmitted wave becomes exponentially damped with increasing distance from the surface and travels as *evanescent wave* for $\beta_1 = 0$ parallel (for $\beta_1 \neq 0$ almost parallel) to the surface. The $\frac{1}{e}$ penetration depth Λ of the evanescent wave follows [171]

$$\Lambda^{-1} = \frac{\sqrt{8}\pi}{\lambda}\left(\sqrt{(\alpha_{i,0}^2 - \alpha_{c,1}^2)^2 + 4\beta_1^2} + \alpha_{c,1}^2 - \alpha_{i,0}^2\right)^{1/2} \quad , \qquad (4.17)$$

and thus depends on the respective incident and exit angles $\alpha_{i,0}$ and $\alpha_{f,0}$. This is illustrated in Fig. 4.4 b), which shows the penetration depth Λ for a $MgAl_2O_4(001)$ substrate as a function of $\alpha_{i,0}/\alpha_{c,1}$ for various values of $\alpha_{f,0}$ at a wavelength of λ=1.107 Å. For incident angles $\alpha_{i,0}$ smaller than the critical angle $\alpha_{c,1}$ the probed depth amounts to only ~25 Å and can even be minimized to ~15 Å for exit angles $\alpha_{f,0}<\alpha_{c,1}$.

Apart from increasing the surface sensitivity, the grazing incidence geometry also allows for enhancing the signal-to-noise ratio. The measured intensity of a reflection depends on both, the transmission amplitudes of the incident, $t_{0,1}$, and exit, $t_{1,0}$, beams and is given by [174]:

$$\mathcal{I} \propto |t_{0,1}|^2 \, I_{\mathrm{Bragg}}(\boldsymbol{Q}_{\|}) \, |t_{1,0}|^2 \quad , \tag{4.18}$$

where $I_{\mathrm{Bragg}}(\boldsymbol{Q}_{\|})$ denotes the intensity of a Bragg signal close to the surface with in-plane scattering vector $\boldsymbol{Q}_{\|}$, see also Fig. 4.4 a). It can be inferred from Fig. 4.11 b) that increased transmission amplitudes and hence increased intensity is achieved for incident, $\alpha_{\mathrm{i},0}$, and exit, $\alpha_{\mathrm{f},0}$, angles close to the critical angle $\alpha_{\mathrm{c},1}$. In this case the incident and exit waves are in phase and the evanescent wave becomes a standing wave with greatly enhanced signal. While in experiments often $\alpha_{\mathrm{f},0} > \alpha_{\mathrm{c},1}$ holds, keeping the incident angle $\alpha_{\mathrm{i},0}$ just below the critical angle may still allow for enhancing the intensity of the measured features by a factor of $\sim$4.

In the case of the grazing incidence geometry, multiple scattering may occur and the kinematical approximation may no longer be valid. Hence, equation 4.18 is based on the *distorted wave approximation* including first order perturbations [175]. Therein, a scattering field, produced by the interaction of an incident plane wave with a simplified model of the sample, is considered to interact with all elements of the sample. This results in another scattering field which, for the deduction of equation 4.18, scatters from the sample's atomic structures that give rise to $I_{\mathrm{Bragg}}(\boldsymbol{Q}_{\|})$ in a kinematical fashion, which is a good approximation for samples containing nanoparticles or mosaic crystals.

4.2 Surface x-ray diffraction from nanoparticles

This section deals with surface x-ray diffraction from epitaxial nanoparticles at *conventional photon energies* ($E\approx$10-20 keV). The first subsection 4.2.1 shows how high resolution reciprocal space mapping allows for obtaining information on the particle shape and for tracking in-situ reaction-induced particle shape changes. In subsection 4.2.2 it will be elucidated how scans performed along high symmetry directions through particle Bragg peaks allow a detailed *quantitative* particle shape analysis. The importance of the particle size distribution in this respect will be clarified in subsection 4.2.3.

The measurement and analysis strategies presented in this section were in this thesis employed for $\mathrm{MgAl_2O_4}$(001)-supported $\mathrm{Pt_{0.33}Rh_{0.67}}$ particles studied at a photon energy of 11.2 keV, the results of which are shown in sections 7.1-7.3.

4.2.1 High resolution reciprocal space mapping

Section 4.1 revealed that nanoparticle facets can be viewed as little surfaces, which in x-ray diffraction give rise to CTR-like signals. Since they are oriented perpendicular to the respective particle facets, mapping them in reciprocal space allows for retrieving *qualitative information* about the particle shape.

Fig. 4.5 shows a high resolution reciprocal space map measured with a point detector in the (H+K=2, L)-plane on $MgAl_2O_4$(001)-supported $Pt_{0.33}Rh_{0.67}$ particles, which contains particle facet signals. They are indicated by black dashed lines[1]. Their orientation suggests that they stem from (100)- and (111)-type particle facets. This and the absence of any further facets signals is in accordance with a truncated octahedral particle shape, as the one shown in Fig. 4.5.

In addition, there is *quantitative information* on the sizes of the particle facets encoded in the intensity of the respective particle rods: equation 4.13 reveals that the measured intensity along a CTR signal is proportional to $N_x^2 N_y^2$, and hence to the squares of the number of atoms that span the truncated surface, or in the present case, the particle facet. Accordingly, the particle rod intensity increases (decreases) if the facet size becomes larger (smaller).

However, especially in the case of Rh-containing particles, care has to be taken with the evaluation of particle facet intensity changes: as was shown in section 4.1.1, the presence of the c(2×8) surface oxide on Rh(100)-type surfaces alters the intensity along Rh(100)-type rods dramatically. Hence, an intensity increase of the (001)-type facet signal probed in a reciprocal space map as the one shown in Fig. 4.5 might not only be ascribed to the enlargement of the corresponding facet size, but also to the formation of a thin O-Rh-O trilayer surface oxide. Contrary, in the case of the trilayer p(9×9) surface oxide forming on Rh(111) surfaces, none of the Rh CTRs and the oxide superstructure rods coincide and intensity contributions along the (111)-type particle facets due to surface oxide formation can be excluded.

Independent of the presence of surface oxides, the intensity of the particle facet signals can also be altered by relaxations of the topmost particle facet layers. Hence, complementary data on the particle shapes and shape changes need to be considered. The particle shapes obtained from the high resolution Bragg peaks scan analysis, which will be discussed in the following subsection, is in-

---

[1] the current section focuses on particle facets only, additional signals visible in the reciprocal space map of Fig. 4.5 and their origins will be subject matter of section 7.3

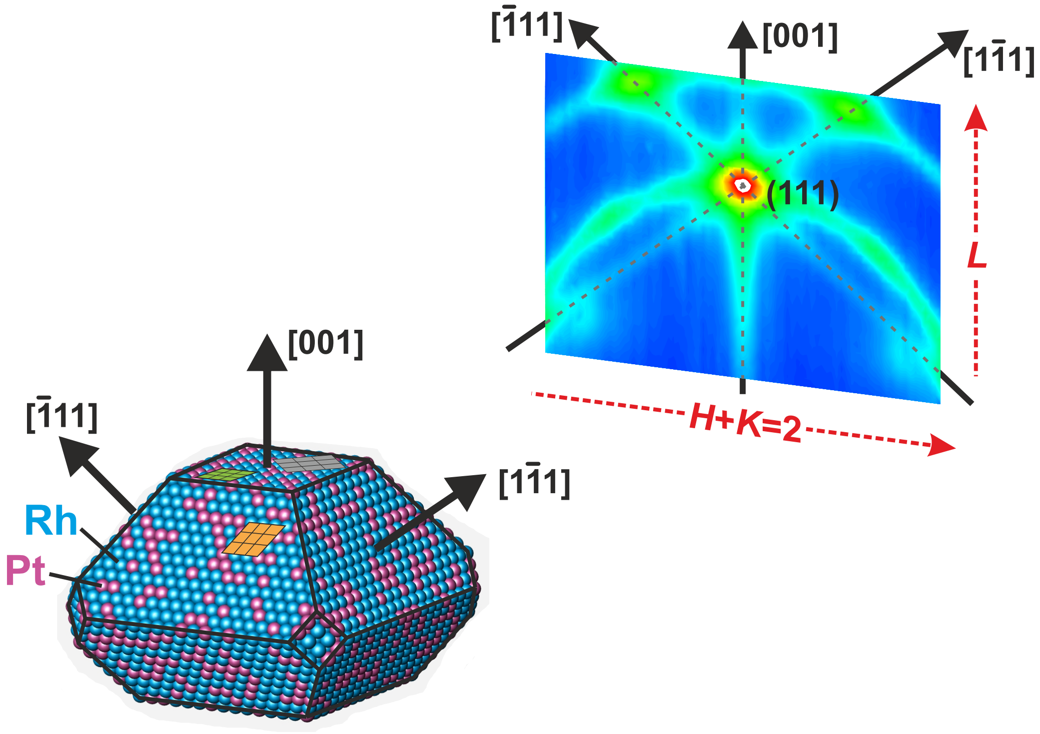

Figure 4.5: **Particle facet signals:** reciprocal space map measured on $Pt_{0.33}Rh_{0.67}$ particles epitaxially grown on $MgAl_2O_4(001)$; the map was measured in the (H+K=2, L)-plane and is centered around the particle (111) Bragg peak and contains particle rod signals from (111)- and (100)-type facets (see section 7.3 for more information).

dependent of the presence of surface oxides or surface layer relaxations and hence constitutes such a complementary analysis technique.

4.2.2 Bragg peak scans for particle shape analysis

Fig. 4.1 illustrates that the particle size $D_x = N_x \cdot a_x = \frac{2\pi}{\Delta Q_x}$ along a certain direction x can be determined from the corresponding Bragg peak width ΔQ_x. Making use of this particle-size induced peak broadening, it was shown that not only the size, but also the *quantitative particle shape* can be determined from Bragg peak widths of scans performed along defined high symmetry directions [176]. This data analysis approach will be elucidated in the following. It can be inferred from Fig. 4.5 that the generic shape of a (001)-oriented particle corresponds to a truncated octahedron defined by (100)- and (111)-type facets. Fig. 4.6 a) and b) disclose that such a shape can be expressed in terms of four particle parameters: N_P, N_E, N_T and N_B:

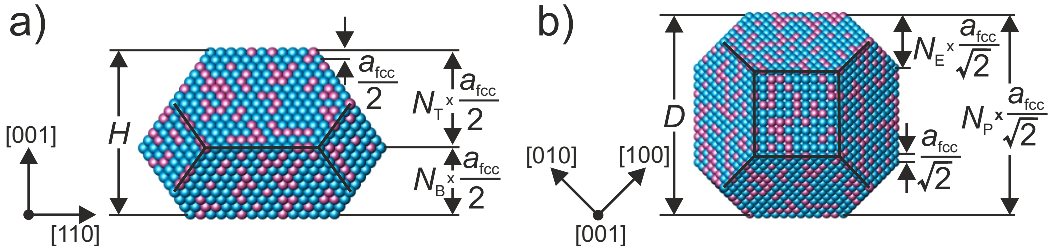

Figure 4.6: **Particle parameters of (001)-oriented particles: a):** side, and **b):** top view of the particle; its height H and diameter D can be expressed by means of the particle parameters $\{N_\mathrm{P},\, N_\mathrm{E},\, N_\mathrm{T},\, N_\mathrm{B}\}$ and the fcc bulk lattice parameter a_fcc via $H{=}\frac{(N_\mathrm{T}+N_\mathrm{B})a_\mathrm{fcc}}{2}$ and $D{=}\frac{N_\mathrm{P}a_\mathrm{fcc}}{\sqrt{2}}$, respectively.

Parameter N_P describes the side length of the in-plane atomic layer with the largest periphery. Accordingly, the particle diameter is given by $D = \frac{N_\mathrm{P}\cdot a_\mathrm{fcc}}{\sqrt{2}}$, where a_fcc corresponds to the particle lattice parameter in fcc bulk coordinates. The particle height $H = \frac{(N_\mathrm{T}+N_\mathrm{B})a_\mathrm{fcc}}{2}$ is determined by the parameters N_T and N_B, which describe the heights of the particle top and bottom part, respectively. The degree of truncation of the particle's side corners is expressed by means of parameter N_E.

The particle parameters $N_i = \{N_\mathrm{P}, N_\mathrm{E}, N_\mathrm{T}, N_\mathrm{B}\}$ allow to express the **particle structure factor** $S(N_i,\, \boldsymbol{Q})$ as a function of the particle shape:

$$\begin{aligned} S(N_i,\, \boldsymbol{Q}) = f(\boldsymbol{Q}) \Bigg[& \sum_{z=-N_\mathrm{B}}^{N_\mathrm{T}} \; \sum_{y=-(\frac{N_\mathrm{P}-1}{2}-|z|)}^{\frac{N_\mathrm{P}-1}{2}} \; \sum_{x=-(\frac{N_\mathrm{P}-1}{2}-|z|)}^{\frac{N_\mathrm{P}-1}{2}} e^{i\boldsymbol{Q}[(x-\frac{|z|}{2})\boldsymbol{a}_x-(y+\frac{|z|}{2})\boldsymbol{a}_y+z\boldsymbol{a}_z]} - \\ & - \Bigg\{ \sum_{z=-(N_\mathrm{E}-1)}^{N_\mathrm{E}-1} \; \sum_{y=0}^{N_\mathrm{E}-1-|z|} \; \sum_{x=0}^{N_\mathrm{E}-1-|z|-y} \Bigg(e^{i\boldsymbol{Q}[(N_\mathrm{P}-x-\frac{|z|}{2})\boldsymbol{a}_x+(N_\mathrm{P}-y-\frac{|z|}{2})\boldsymbol{a}_y+z\boldsymbol{a}_z]} + \\ & + \sum_{k=-1}^{1} e^{i\boldsymbol{Q}[(-1)^k(\frac{N_\mathrm{P}-1}{2}-x-\frac{|z|}{2})\boldsymbol{a}_x+(-1)^{k+1}(\frac{N_\mathrm{P}-1}{2}-y-\frac{|z|}{2})\boldsymbol{a}_y+z\boldsymbol{a}_z]} \Bigg) \Bigg\} \Bigg] \quad . \end{aligned}$$

It is obtained by summing over all possible atom positions within the particle, neglecting strain effects and assuming a constant atomic form factor $f(\boldsymbol{Q})$ in the Bragg peak vicinity [176]. The atom coordinates are expressed in terms of the surface lattice coordinates with the origin of the coordinate system placed in the centre of the atomic layer of largest periphery (see Fig. 4.7).

Accordingly, the scattered intensity $I(\boldsymbol{Q})$ reads:

$$I(\boldsymbol{Q}) = \sum_{N_\mathrm{P},N_\mathrm{E},N_\mathrm{T},N_\mathrm{B}} D(N_\mathrm{P},N_\mathrm{E},N_\mathrm{T},N_\mathrm{B}) \cdot |S(N_\mathrm{P},N_\mathrm{E},N_\mathrm{T},N_\mathrm{B},\boldsymbol{Q})|^2 \quad , \tag{4.19}$$

where $D(N_\mathrm{P},N_\mathrm{T},N_\mathrm{B},N_\mathrm{E})$ denotes a factor accounting for a Gaussian-shaped particle size distribution, assuming a fixed $\{N_\mathrm{P},N_\mathrm{E},N_\mathrm{T},N_\mathrm{B}\}$-ratio for the various particle sizes. Hence, equation 4.19 is the sum of intensities from differently sized particles, whose contributions are weighted according to the size distribution function. Such an incoherent sum is appropriate since the particles grow incommensurably on the $\mathrm{MgAl_2O_4}(001)$ substrate, and the scattering from different particles is accordingly not in phase. A qualitative plot of the size distribution function $D(N_i)$ is shown in Fig. 4.8 a), its influence on the simulated Bragg peak shape discussed in subsection 4.2.3.

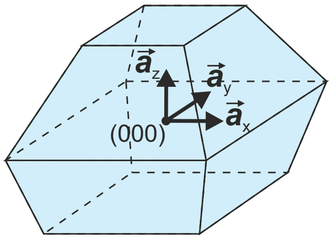

Figure 4.7: **Coordinate system:** for the calculation of the particle structure factor $S(N_i,\boldsymbol{Q})$.

In the **quantitative particle shape analysis**, particle Bragg peaks are simulated based equation 4.19 along high symmetry directions as a function of different combinations of the particle parameters and hence as a function of different particle shapes, where a large parameter space of $\{N_\mathrm{P},N_\mathrm{E},N_\mathrm{T},N_\mathrm{B}\}$ is covered. The FWHMs of the simulated Bragg peaks, $FWHM(j)_\mathrm{sim}$, are compared to the experimentally obtained ones, $FWHM(j)_\mathrm{exp}$, following

$$\chi^2 = \sum_j \left(\frac{FWHM(j)_\mathrm{sim}}{FWHM(j)_\mathrm{exp}} - 1\right)^2 \quad , \tag{4.20}$$

where $j = \{[001],[111],[100],[110]\}$ denote the different high symmetry directions expressed in fcc bulk coordinates. The particle shape that matches the experimental data best is made up of the particle parameters that yield the smallest figures of merit χ^2.

In contrast to the high resolution reciprocal space mapping, which also contains information about misoriented particles (i.e. due to the presence of Debye-Scherrer-like mosaicity rings), the Bragg peak scan analysis is only sensitive to particles of one crystal structure and orientation. Moreover, it yields no information on whether the particles display well-defined facets or about the amount of internal twinning. Information about the latter is, however, enclosed in reciprocal space maps as discussed in section 4.2.2. Hence, the combination of both analysis techniques yields an integral view on the particle characteristics.

It was shown in [176] how the widths of Bragg peak scans along selected high symmetry directions vary as a function of the particle parameters. Parameters which greatly vary the total particle size along a certain direction also have a large influence on the width of the scan performed along that direction. Hence, the parameter N_P greatly influences the Bragg peak width of the scan performed along the in-plane (100), and (110)-directions, while the parameters N_T and N_B have a great impact on the width of the scan performed along the (001)-direction. The Bragg peak scan analysis is least sensitive to the parameter N_E.

4.2.3 Influence of the particle size distribution

In the following, the influence of the particle size distribution function $D(N_i)$ of equation 4.19 on the Bragg peak line shape and hence on the particle size deduced from equation 4.20 will be discussed.

To this end, the one-dimensional Laue function $S_x(\boldsymbol{Q}_x \boldsymbol{a}_x)$ of equation 4.8 is in the following weighted by a one-dimensional normalized size distribution function $D(N_x)$ by forming the integral

$$\int\limits_{-\infty}^{\infty} \frac{2}{\sqrt{\pi}} \frac{\sqrt{\ln(2)}}{r \cdot N_0}\, e^{-\frac{(N_x - N_0)^2}{(r \cdot N_0)^2}\ 4\ln(2)} \quad N_x^2\, e^{\frac{(\boldsymbol{Q}_x - \boldsymbol{Q}_0)^2}{(2\pi)^2} N_x^2 \boldsymbol{a}_x^2\ 4\ln(2)}\ dN_x\ , \qquad (4.21)$$

where the Laue function $S_x(\boldsymbol{Q}_x \boldsymbol{a}_x)$ is approximated by

$$S_x(\boldsymbol{Q}_x \boldsymbol{a}_x) \approx N_x^2\, e^{\frac{(\boldsymbol{Q}_x - \boldsymbol{Q}_0)^2}{(2\pi)^2} N_x^2 \boldsymbol{a}_x^2\ 4\ln(2)} \quad . \qquad (4.22)$$

In equation 4.21 $\boldsymbol{Q}_0$ denotes the position of the Bragg peak maximum determined by $\boldsymbol{Q}_0 = \frac{2\pi}{\boldsymbol{a}_x}$, N_0 corresponds to the average size and $\Delta N_{\frac{1}{2}} = r \cdot N_0$ to

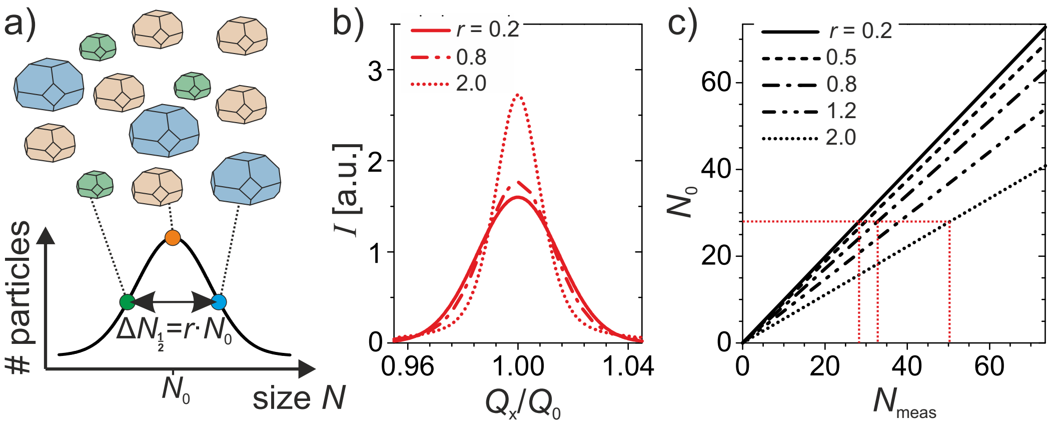

Figure 4.8: **Influence of the particle size distribution: a):** Gaussian size distribution with fixed $\{N_\text{P}{:}N_\text{E}{:}N_\text{T}{:}N_\text{B}\}$ ratio as taken into account in the Bragg peak scan analysis; **b):** simulated Bragg peak shapes based on equation 4.23 for a fixed atom number N_0 (here: N_0=28) but different size distributions r, where r and the FWHM $\Delta N_{\frac{1}{2}}$ are connected via $\Delta N_{\frac{1}{2}}=r\cdot N_0$; **c):** biased particle size N_meas as deduced from Bragg peak FWHMs for $r\neq 0$ vs. the average size N_0 for r=0; red lines: guide to the eyes for the examples shown in b) with N_0=28, r=0.2, 0.8 and 1.2.

the width of the size distribution function $D(N_x)$, where r denotes the width of the size distribution in percent of the average value N_0.
Solving the integral of equation 4.21 yields the Bragg peak function $I_\text{meas}(r\cdot N_0)$, which would be measured in an experiment and which depends on the particle size distribution r:

$$I_\text{meas}(r\cdot N_0)=\sqrt{B}\;e^{-\frac{ABN_0^2}{(A+B)}}\cdot\left(\frac{1}{2}\frac{1}{(A+B)^{3/2}}+\frac{B^2N_0^2}{(A+B)^{5/2}}\right)\quad, \tag{4.23}$$

where

$$A=\frac{(\boldsymbol{Q}_x-\boldsymbol{Q}_0)^2\;\boldsymbol{a}_x^2\;4\ln(2)}{(2\pi)^2}\quad,\quad B=\frac{4\ln(2)}{(r\cdot N_0)^2}\quad. \tag{4.24}$$

Fig. 4.8 b) shows equation 4.23 plotted as a function of various size distributions r. It reveals that the width ΔQ_x of the measured Bragg peaks decreases with increasing size distribution r. As a consequence, the particle size $N_\text{meas}=\frac{2\pi}{\Delta Q_x\cdot a_x}$ as obtained from the FWHM ΔQ_x of the measured peak is increasingly overestimated with increasing particle size distribution r. Fig. 4.8 c) shows the discrepancy between the average particle size N_0 and the measured size N_meas for different size distributions r.

4.3 High energy surface x-ray diffraction

While the previous section considered surface x-ray diffraction at conventional photon energies (E≈10 keV), this section is dedicated to the *high energy approach* (E=70-80 keV) which allows a *fast* mapping of *large areas in reciprocal space* when using a 2D detector. It thus allows for monitoring plenty of information within a short time frame (order of seconds), which is of utmost importance for catalytic in-situ studies [74]. In the framework of this thesis, the 2D mapping was employed for the investigation of nanoparticle growth (chapter 6) and as an in-situ probe for tracking potential particle shape or size changes (chapters 7.4 and 8) in the course of catalytic CO oxidation.

The scattering geometry and its advantages compared to conventional surface x-ray diffraction will be elucidated in subsection 4.3.1. In this thesis, particle rods subtracted from high energy 2D maps were for the first time used to quantitatively determine the particle shape changes during catalytic CO oxidation (subsection 8.1.2 and appendix B). Subsection 4.3.2 will elucidate why an extraction of these data from the measured 2D maps is possible.

4.3.1 High energy reciprocal space mapping

In order to illustrate the differences between surface sensitive x-ray diffraction performed at conventional and at high energies, Fig. 4.9 shows the respective scattering geometries including the corresponding Ewald spheres. The sample Bragg peaks and out-of-plane rod signals are represented by circles and lines, respectively. The incoming wavevector $\boldsymbol{k}_0$ scales with photon energy and defines the Ewald sphere which is accordingly small for conventional photon energies, but large for high energies. Furthermore, the diffraction angles are larger for conventional photon energies than in the high energy approach.

In order to map a sample signal of interest, e.g. a sample Bragg peak or part of a crystal truncation rod, two conditions need to be fulfilled: (1) the sample has to be aligned such that the signal of interest intersects the Ewald sphere and (2) the detector needs to be adjusted in a way to detect the scattered signal [74].

As is illustrated for the case of low photon energies, only a relatively small area of reciprocal space can be probed at a time, even when using a large area detector. This is due to the large curvature of the sphere at a given point and the accordingly large diffraction angles, as is illustrated in Fig. 4.9 a). In

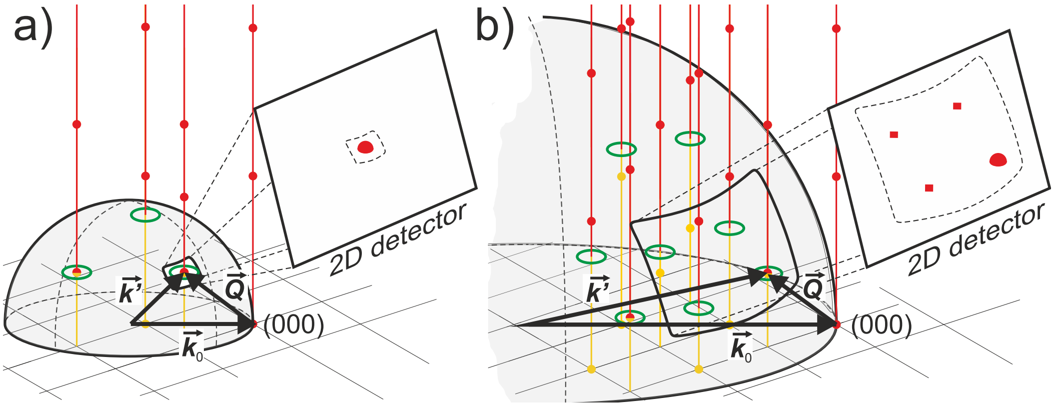

Figure 4.9: **Scattering geometry at a): conventional, and b): high photon energies:** crystal truncation rods and Bragg peaks are represented by lines and closed circles, respectively (red: above the Ewald sphere surface, yellow: below the Ewald sphere, green circles indicate intersection points with the sphere surface).

order to measure different sample signals, the movement of both, sample and detector is required, which is often very time-consuming [74].

Contrary, when using high photon energies, the small diffraction angles in combination with a large area detector allow for mapping the projection of a full reciprocal space plane at a time. In Fig 4.9 b) the simultaneously mapped sample signals intersecting the flat Ewald sphere are shown.

Accordingly, the high energy approach enables a fast data acquisition of a large reciprocal space area. With respect to the *investigation of particle growth* (chapter 6) the mapping of large areas holds the advantage of obtaining instantaneously information on different particle epitaxies, potential defects (signals from internal twinning) or other features such as tilted particles, which would be difficult to detect by means of conventional x-ray diffraction. Moreover, high energy x-ray diffraction constitutes a perfect probe for the *operando investigation of model catalyst systems* under realistic reaction conditions as it allows the fast detection of changes in the diffraction pattern which may be caused by particle shape changes or the emergence of oxide phases. Furthermore, thanks to the small diffraction angles and to the highly collimated beam, it allows for the investigation of *combinatorial samples*, i.e. samples that display a gradient in particle size and/or material composition, and hence of different sample systems under *identical* reaction conditions.

Recently, high energy surface x-ray diffraction has proven to allow for the in-situ tracking of the dynamic restructuring of a Pd(100) surface during CO oxidation with sub-second time resolution [74, 75] and to monitor the in-situ oxidation of supported Pd and Pd-Rh nanoparticles [112, 177].

4.3.2 Nanoparticle rods for quantitative shape analysis

In conventional surface x-ray diffraction, the data points along a CTR are measured with a point or 2D detector by varying the rocking angle $\theta(L)$ of the sample according to each L-value along the rod. In this thesis' approach, the particle rods were extracted from 2D reciprocal space maps measured with a stationary detector (for more detailed information on the particle rod analysis, see subsection 8.1.2 and appendix B).

Fig. 4.10 shows an extract of such a 2D map measured on α-Al_2O_3(0001)-supported Pt nanoparticles. It reveals clear Laue oscillations in out-of-plane direction, where information on the underlying particle shape is encoded in their intensity modulation. As will be discussed in the following it is due to the imperfectness of the sample, namely to the presence of particle mosaicity, that these particle out-of-plane rods are clearly visible.

If all particles on the sample were perfectly arranged - i.e. aligned along one in-plane direction determined by the substrate - the measured reciprocal space map would contain only *sharp* diffraction signals at positions determined by intersection points of the crystal truncation rods with the Ewald sphere.

On real sample systems with epitaxially grown nanoparticles, however, the particles display a certain angular distribution of usually 1-2° around the surface normal (particle mosaicity). This is illustrated at the bottom of Fig. 4.10. The orange particles are perfectly aligned with the support, whereas the blue and green particles feature a slight rotation of $\pm\Delta\theta$ around the surface normal (blue: $+\Delta\theta$, green: $-\Delta\theta$). The particles' angular distribution around their preferential orientation is well described by a Gaussian function, as is shown in the inset at the figure top. During x-ray diffraction, the orange particles just fulfill the diffraction condition for the particle $(3\bar{1}1)$ Bragg peak, whereas the particles which are horizontally rotated give at the same time rise to diffraction above (blue) and below (green) this peak. Since the diffracted intensities are proportional to the number of scattering particles the particle rod intensity is also modulated by a Gaussian function, for which the linescans extracted from the maps need to be corrected. Hence, it is the particle mosaicity that compensates for the aforementioned θ-scan, which needs to be performed in conventional crystal truncation rod analysis approach.

There are further factors that lead to an increase of detectable scattering sig-

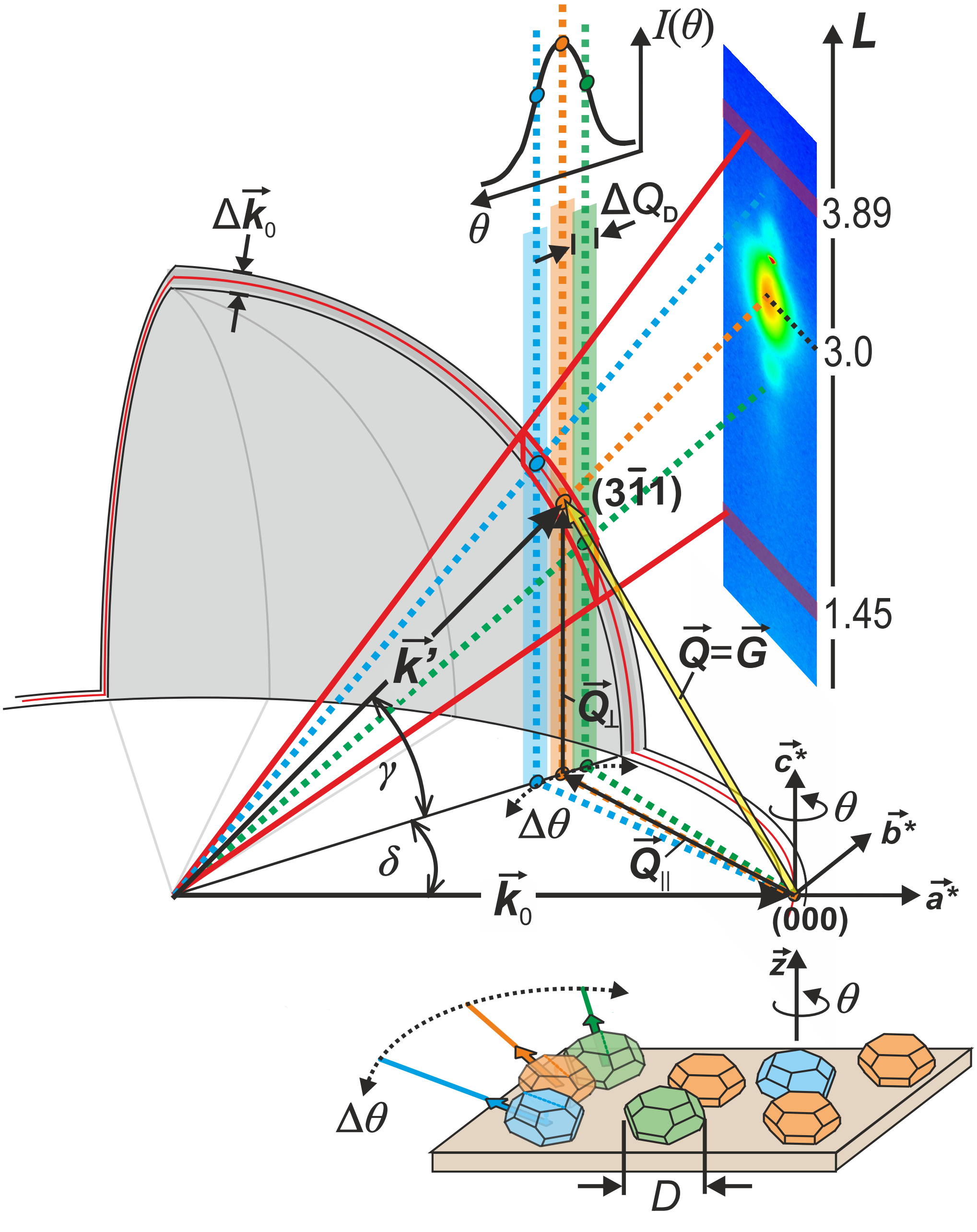

Figure 4.10: **High energy scattering geometry and particle mosaicity:** the angular distribution $\Delta\theta$ of the particles, the particles' average diameter D and the non-zero energy resolution $\Delta \boldsymbol{k}_0 = \frac{\Delta E_0}{E_0} \cdot \boldsymbol{k}_0$ lead to the detectability of a wide range of particle diffraction signals along the particle rod, which can be probed with a single 2D detector snapshot at a fixed rocking angle θ.

nals. Hence, while an infinite particle diameter would result in sharp intersection points of the rods with the Ewald sphere (vertical dashed lines in Fig. 4.10), the finite particle width D makes them expand to $\Delta Q_{\mathrm{D}} = \frac{2\pi}{D}$. This is in Fig. 4.10 indicated by the red, blue and green vertical bars. The non-zero energy distribution of the beam, ΔE_0, leads to a broadening $\Delta \boldsymbol{k}_0 = \frac{\Delta E_0}{E_0} \cdot \boldsymbol{k}_0$ of the Ewald sphere which further enlarges the measurable range along the particle rod.

The partial reciprocal space map shown in Fig. 4.10 was measured on the pure Pt particles of sample “alumina-1” (see section 6.2). It shows the particle $(3\bar{1}1)$ Bragg peak and its Laue oscillations. The red horizontal bars indicate the borders of the, due to the above listed reasons, vast detectable signal range along the particle L-rod which amounts in this case to L=3.89-1.45=2.44 r.l.u..

4.4 Further characterization techniques

4.4.1 X-ray reflectivity

In this thesis, x-ray reflectivity was mainly used to obtain complementary information on the particle height and coverage on the sample substrate. In addition, information on the vertical particle morphology and vertical size distribution were retrieved from the deduced electron density profiles.

Fresnel equations

The sample geometry for x-ray reflectivity is displayed in Fig. 4.12: the directions of $\boldsymbol{k}_{\mathrm{i},0}$ and $\boldsymbol{k}_{\mathrm{r},0}$, the incident and reflected wavevectors, respectively, are varied such that the angles $\alpha_{\mathrm{i},0}$ and $\alpha_{\mathrm{r},0}$, defined by the wavevectors and the sample surface plane, are being gradually increased while $\alpha_{\mathrm{i},0} = \alpha_{\mathrm{r},0}$ holds. In this *specular geometry* the scattering vector $\boldsymbol{Q}_z$ probes the sample's electron density perpendicular to the sample surface.

Upon hitting the sample surface, the x-ray beam is not only reflected but also refracted. As x-ray frequencies are generally higher than electronic transition frequencies in atoms, the refractive index n_j of a probed material j

$$n_j = 1 - \delta_j + i\beta_j \quad , \tag{4.25}$$

is less than unity. It is connected to the scattering properties of the sam-

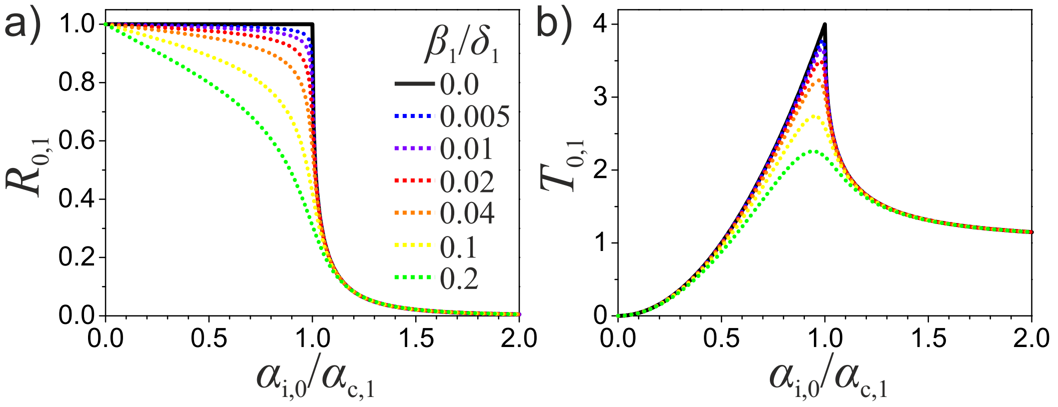

Figure 4.11: **Reflection and transmission of x-rays: a):** intensity reflectivity $R_{0,1}$, and **b):** intensity transmittivity $T_{0,1}$ as a function of the normalized glancing angle $\frac{\alpha_{\mathrm{i},0}}{\alpha_{\mathrm{c},1}}$ for selected values of $\frac{\beta_1}{\delta_1}$ based on equations 4.26 and 4.27.

ple material and can be expressed as a function of the dispersion corrections f' and f'' of equation 4.4 via $\delta_j = \frac{\lambda^2 \rho_{\mathrm{at},j} r_0}{2\pi}\left(f_j^0(\boldsymbol{Q}) + f_j'(\hbar\omega, \boldsymbol{Q})\right)$ and $\beta_j = \frac{\lambda^2 \rho_{\mathrm{at},j} r_0}{2\pi} f_j''(\hbar\omega, \boldsymbol{Q})$, where $\rho_{\mathrm{at},j}$ and r_0 denote the atomic number density and the Thomson scattering length, respectively. *Total external reflection* from the sample surface layer occurs for incident angles $\alpha_{\mathrm{i},0}$ smaller than the critical angle $\alpha_{\mathrm{c},1} = \sqrt{2\delta_{j=1}}$.

Fig. 4.12 illustrates the reflections and refractions from a multilayer sample. To start with, the following will only consider the interaction of the x-ray beam with the surface, i.e. the respective incident, reflected and transmitted wavevectors $\boldsymbol{k}_{\mathrm{i},0}$, $\boldsymbol{k}_{\mathrm{r},0}$ and $\boldsymbol{k}_{\mathrm{t},1}$. Consideration of boundary conditions of the wave and its derivative at the surface yields the respective amplitudes of the reflected and transmitted waves $r_{0,1}$ and $t_{0,1}$. Their intensities are expressed in the *Fresnel equations*:

$$R_{0,1} = |r_{0,1}|^2 = \frac{I_{\mathrm{r},0}}{I_{\mathrm{i},0}} = \frac{(\alpha_{\mathrm{i},0} - A^2)^2 + B^2}{(\alpha_{\mathrm{i},0} + A^2)^2 + B^2} \quad , \tag{4.26}$$

$$T_{0,1} = |t_{0,1}|^2 = \frac{I_{\mathrm{t},1}}{I_{\mathrm{i},0}} = \frac{4\alpha_{\mathrm{i},0}^2}{(\alpha_{\mathrm{i},0} + A^2)^2 + B^2} \quad , \tag{4.27}$$

where

$$A = \frac{1}{\sqrt{2}}\{[(\alpha_{\mathrm{i},0}^2 - \alpha_{\mathrm{c},0}^2)^2 + 4\beta_1^2]^{\frac{1}{2}} + (\alpha_{\mathrm{i},0}^2 - \alpha_{\mathrm{c},0}^2)\}^{\frac{1}{2}} \quad , \tag{4.28}$$

$$B = \frac{1}{\sqrt{2}}\{[(\alpha_{\mathrm{i},0}^2 - \alpha_{\mathrm{c},0}^2)^2 + 4\beta_1^2]^{\frac{1}{2}} - (\alpha_{\mathrm{i},0}^2 - \alpha_{\mathrm{c},0}^2)\}^{\frac{1}{2}} \quad . \tag{4.29}$$

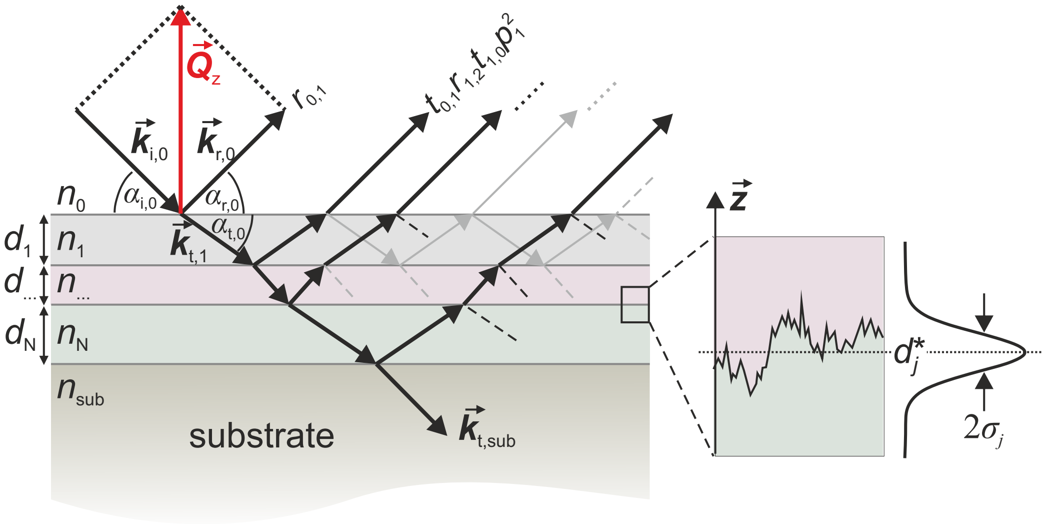

Figure 4.12: **Reflectivity from a multilayer sample:** the scattering vector $\boldsymbol{Q}_z$, determined by wavevectors $\boldsymbol{k}_{i,0}$ and $\boldsymbol{k}_{r,0}$, probes the sample perpendicular to the surface. The x-rays are reflected and refracted at every sample interface with layer thicknesses d_j and refractive indices n_j, multiple reflection/refraction is only indicated for layer $j = 1$. The inset reveals the interface, whose height fluctuations can be described using the standard deviation σ_j around an average layer thickness d_j^*.

The intensity reflectivity $R_{0,1}$ and transmittivity $T_{0,1}$ are plotted in Fig. 4.11 for various values of $\frac{\beta_1}{\delta_1}$, hence illustrating the influence of absorption. For incident angles below the critical angle $R_{0,1}$ is close to 1, above it falls off according to $R_{0,1} \propto \frac{1}{Q_z^4}$. Contrary, the transmitted wave adopts its largest value (≈4) for incident angles close to the critical angle.

Reflectivity from multilayers - Parratt formalism

While equation 4.26 yields the reflection amplitude from a single interface, the *Parratt formalism* [178] constitutes an *exact* method to calculate the intensity reflectivity from a multilayer system and will be explained in the following.
Fig. 4.12 illustrates multiple reflections inside the topmost layer ($j = 1$), any contributions from deeper layers will be ignored for the moment. The total amplitude reflection $r_{0,1}^{\text{tot}}$ from such a single layer of finite thickness $d_{j=1}$ is obtained by summing over all contributions via $r_{0,1}^{\text{tot}} = r_{0,1} + t_{0,1}r_{1,2}t_{1,0}p_1^2 + ...$, where $p = e^{i\boldsymbol{Q}_z d_1}$ denotes the obligatory phase factor. The resulting geometric series can be worked into an equation that expresses the amplitude reflectivity from a single layer and is in the case of the Parratt method used to express the amplitude reflectivity from the deepest layer ($j = N$) of the multilayer system:

$$r_{N-1,N}^{tot} = \frac{r_{N-1,N} + r_{N,\mathrm{sub}}^{\mathrm{tot}}\ p_N^2}{1 + r_{N-1,N} r_{N,\mathrm{sub}}^{\mathrm{tot}}\ p_N^2} \quad . \tag{4.30}$$

Since there are no multiple reflections at the interface between the lowest layer $j = N$ and the substrate, the amplitude reflectivity $r_{N,\mathrm{sub}}^{\mathrm{tot}}$ and thus equation 4.30 can directly be calculated. Using the obtained result for $r_{N,N-1}^{\mathrm{tot}}$, the amplitude reflectivity of the second-lowest layer $j = N - 1$ can be obtained via

$$r_{N-2,N-1}^{\mathrm{tot}} = \frac{r_{N-2,N-1} + r_{N-1,N}^{\mathrm{tot}}\ p_{N-1}^2}{1 + r_{N-2,N-1} r_{N-1,N}^{\mathrm{tot}}\ p_{N-1}^2} \quad . \tag{4.31}$$

These calculations need to be performed recursively, until the total amplitude reflectivity of the surface, $r_{0,1}^{\mathrm{tot}}$ is derived.

Roughness

Up to now, all surfaces and interfaces were considered to be ideally flat. In reality, however, they are characterized by a certain *roughness* σ_j (see inset of Fig. 4.12) which leads to an *off-specular, diffuse* component. The amplitude of the *specular* reflectivity is as a consequence exponentially damped at every interface, while the transmitted amplitude is exponentially amplified. Since the specular reflectivity probes the scattering vector $\boldsymbol{Q}_z$ perpendicular to the surface, this intensity damping becomes a function of the vertical component of the interface roughness, while lateral height-to-height correlations are encoded in the off specular intensity component.
There are various mathematical models that treat the problem of diffuse scattering [179, 180, 181, 182]. In the ansatz by Névot and Croce [183] the vertical roughness of layer j is viewed as Gaussian-distributed height fluctuations $g(z)$ around the average layer thickness d_j^*, as is indicated in the inset of Fig. 4.12, given by

$$g(z) = \frac{1}{\sqrt{2\pi\sigma_j}}\, e^{\frac{(z-d_j^*)^2}{2\sigma_j^2}} \quad , \tag{4.32}$$

where the roughness σ_j denotes the standard deviation from the ideal layer height d_j^*.

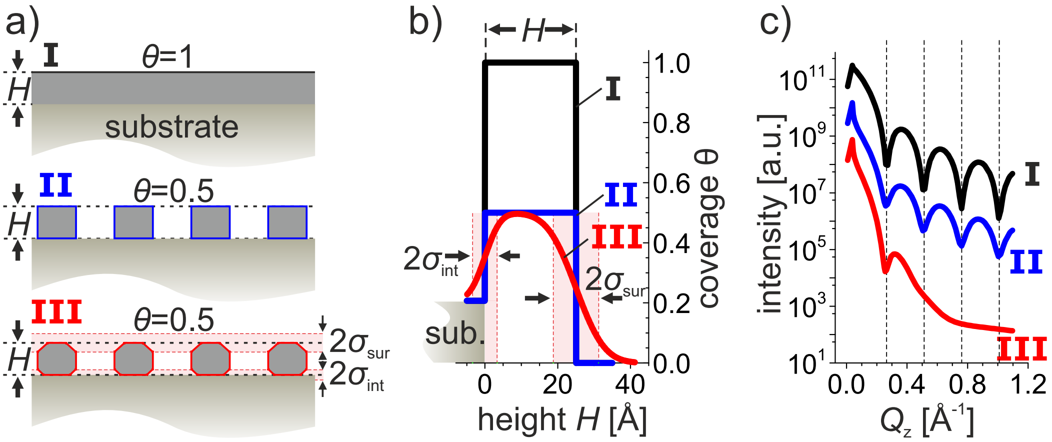

Figure 4.13: **Impact of sample characteristics on x-ray reflectivity curves: a):** examples of single layer sample systems: I: closed layer, height H=25 Å, no surface or interface roughness; II: cubic particles, H=25 Å, surface coverage θ=0.5, no surface or interface roughness; III: 'realistic' particles, H=25 Å, θ=0.5, σ_{sur}=6.21 Å and σ_{int}=3.38 Å; **b):** electron density profiles based on data in a); **c):** x-ray reflectivity curves simulated for the systems in a) using FEWLAY [184], assuming Pt layers/particles on $MgAl_2O_4$(001) at E=85 keV; the data are offset for clarity.

Reflectivity from nanoparticles - the fit programme FEWLAY

In this thesis, the fit programme FEWLAY [184], originally written for the analysis of multilayer sample systems, was used to analyze Fresnel reflectivity curves from nanoparticle samples. FEWLAY is based on the Parratt formalism and incorporates interface roughness effects according to the ansatz by Névot and Croce. In addition, effects of the measurement geometry on the reflected intensity are taken into account.

The programme ascribes to each layer j of the fit model four fit parameters: the layer thickness d_j, the roughness σ_j, and the parameters δ_j and β_j. In addition, a fit parameter for the substrate roughness σ_{sub} is included. In the case of nanoparticle samples, the comparison between the fitted parameter $\delta_{j,\mathrm{fit}}$ and the literature value $\delta_{j,\mathrm{lit}}$ of a closed layer via $\theta = \frac{\delta_{j,\mathrm{fit}}}{\delta_{j,\mathrm{lit}}}$ yields the percental coverage θ of the particles on the substrate. Moreover, the surface and interface roughnesses σ_j account in the case of nanoparticles for their faceted shape and a potential vertical particle size distribution. Good fit results for reflectivity curves from nanoparticle samples were in this thesis obtained considering one- or two layered fit models.

In order to illustrate the impact of the sample characteristics on the shape of Fresnel reflectivity curves, Fig. 4.13 displays such curves simulated with

FEWLAY for three different sample systems. The latter are displayed in Fig. 4.13 a) and comprise I) a completely closed layer neglecting any interface roughness, II) idealized cubic particles with a coverage of $\theta = 0.5$ and also without any interface roughness, and III) more 'realistic' faceted particles with $\theta = 0.5$, whose shape is accounted for by including a surface and interface roughness. Fig. 4.13 b) shows the corresponding electron density profiles perpendicular to the sample surface, which are block-shaped in the case of models I and II, but display a roughness-induced smearing at the surface and interface in the case of model III.

The simulated reflectivity curves are shown in Fig. 4.13 c) and display in all cases highest intensity in the regime of total external reflection. The slight increase in intensity up to the critical angle is due to the finite size of the sample, which is not completely hit by the incident x-rays at very shallow incident angles. At higher angles, all curves display maxima in intensity due to constructive interference of waves reflected at the sample surface and interface. In case of model II, the maximum intensity is diminished due to the reduced surface and interface areas, for model III the smearing out along the electron density profile leads in addition to a strong damping of the interference oscillations.

4.4.2 Auger electron spectroscopy

Auger electron spectroscopy (AES) is an electron spectroscopy technique that is used to study the chemical composition of surfaces. In this thesis, AES was employed to test the cleanliness of the oxide substrates prior to particle deposition and for some samples also to confirm the deposited material after the physical vapour deposition of the catalyst materials.

During AES a primary electron beam is accelerated onto the sample surface. An incident primary electron may produce a hole in the core level of a sample atom (usually in the K or L shell), which as a consequence becomes ionized as the primary and the core level electron leave. The remaining core level hole is filled by an electron from a higher shell, where its energy can either be used (1) to emit an x-ray photon of characteristic energy (*x-ray fluorescence*), or (2) to transfer the energy to an electron of the same or a higher shell, which as a consequence leaves the atom (*Auger process*). During measurement the kinetic energy of this leaving *Auger electron* is analyzed as it depends on the energy levels of the sample atom and can accordingly be used for the chemical analysis of the sample. The very short mean free path of electrons makes AES a very surface sensitive technique with probing depths of typically 10-30 Å. The combined LEED/AES setup used in this thesis is equipped with a lock-in amplifier which yields the derivative $\mathrm{d}N/\mathrm{d}E$ of the measured number of electrons $N(E)$. This allows for suppressing the background of the primary and secondary electrons.

4.4.3 Atomic force microscopy

Atomic force microscopy (AFM) was used in this thesis to obtain complementary real space information on the particle morphology and surface coverage in addition to the data retrieved from the x-ray-based techniques.

During measurement, an AFM-tip, sized in the nm-range and attached to a cantilever, scans the sample surface. In the *tapping mode*, which was employed in this thesis, the cantilever oscillates close to its resonance frequency with a certain amplitude. Changes in the surface topography, such as bumps or holes, exert forces on the tip according to Hooke's law. They include van der Waals forces, electrostatic forces or dipole-dipole interactions and change the oscillation frequency and/or amplitude. These changes are detected in terms of spatial deflections of a LASER beam, which is reflected from the backside of the cantilever tip towards a split photodiode, and information on the surface topography can be derived.

The choice for the tapping mode over the AFM contact mode (tip in mechanical contact with the sample surface) for measuring the nanoparticle samples can be explained as follows: in the contact mode the tip might grab a particle and move it along the surface, while in the tapping mode the vertically moving tip does not apply any shear forces that might push surface material sideways [185]. The tapping mode is accordingly in general appropriate for samples which display a large surface roughness or which are easily damaged, as it allows scanning without scratching [186]. Moreover, sufficiently high oscillation amplitudes enable the tip to overcome tip-sample adhesion energies and hence prevent the tip from sticking to the surface.

Chapter 5

Experimental Setups for Sample Preparation and Characterization

This chapter deals with the experimental setups used within this thesis. Section 5.1 introduces the stationary UHV growth chamber that was used for sample preparation and yields an overview over all samples investigated in this thesis. The mobile in-situ catalysis chamber was employed to study the samples during catalytic reaction conditions by means of surface sensitive x-ray diffraction at various synchrotron endstations. Its mode of operation is elucidated in section 5.2, a survey over the experimental synchrotron endstations is given in section 5.3.

5.1 Ultra high vacuum growth chamber

All samples investigated in this thesis were prepared in the UHV growth chamber displayed in Fig. 5.1. Its pumping system, consisting of turbo pump, ion getter pump and Ti sublimation pump, allows to reach base pressures in the low 10^{-11} mbar range. A load lock chamber, connected to the growth chamber via a valve, and a transfer system enable to load and remove samples from the main growth chamber without destroying the ultra-high vacuum within.
The chamber is equipped with various devices needed for sample preparation. There is a filament heating station to which electron beam heating can be added in order to reach sample temperatures above 1700 K. A permanently installed gas line system provides the required gases such as oxygen or argon.

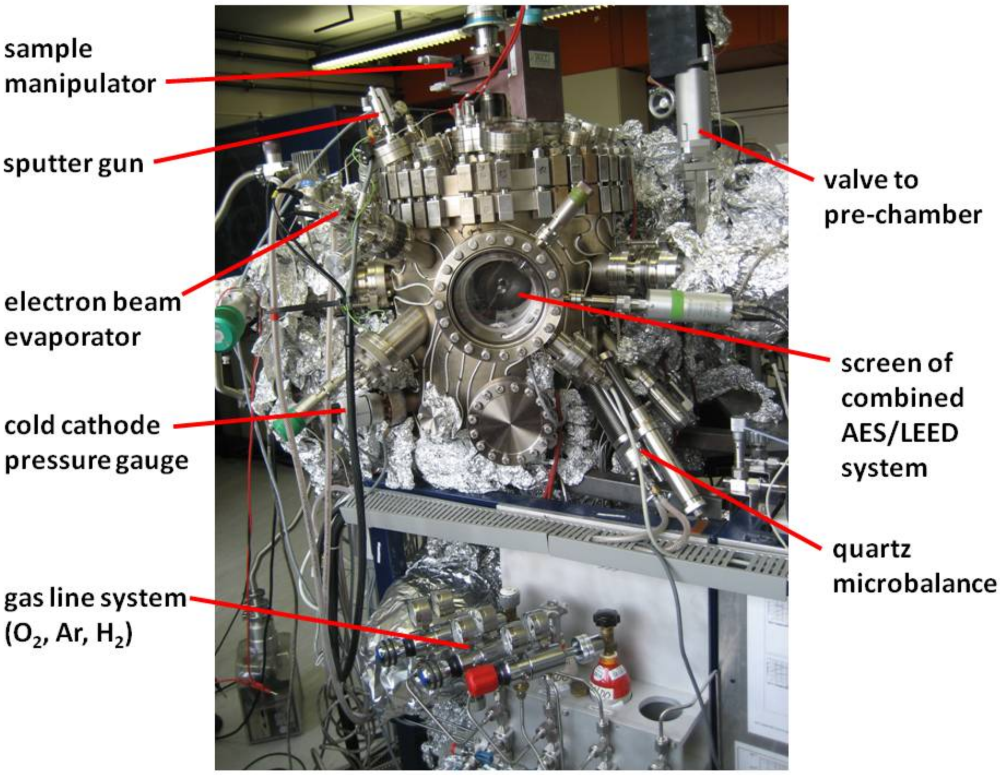

Figure 5.1: **Growth chamber:** stationary UHV growth chamber that was used for sample preparation.

A thermal cracker cell is mounted which splits molecular oxygen into reactive atomic oxygen that removes impurities from the sample surface. An argon ion sputter gun provides a further possibility to clean sample surfaces. The chemical composition and crystallinity of the samples can be studied by a combined AES/LEED system. The overall pressure inside the chamber is measured by a cold cathode gauge, residual gases can be monitored by a quadrupole mass spectrometer.

There are various e-beam evaporators mounted, which are used for thin film or particle growth by means of physical vapour deposition. For the growth of the alloy nanoparticle samples of this thesis, a *triple evaporator* was used as it facilitates the simultaneous deposition of two materials, a sketch of it is displayed in Fig. 5.2 a). It contains three evaporation cells, each of which was equipped with one rod of the materials to be evaporated: Pt, Rh and Pd. For the growth of alloy nanoparticles, the fluxes of the two materials were set according to the required composition, where the settings were based on calibration samples grown before for the individual materials. This allowed for obtaining the desired compositions with an error of ±10%.

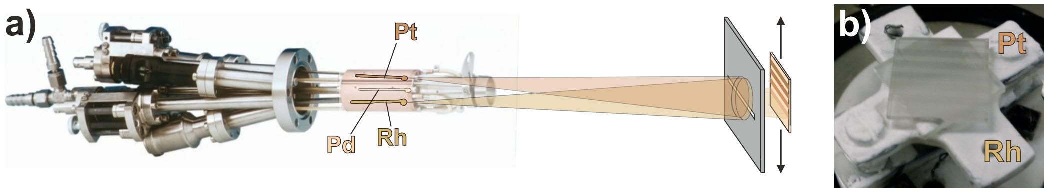

Figure 5.2: **Preparation of samples with composition and/or size gradient: (a):** sketch of triple evaporator loaded with different material rods (Pt, Rh, Pd) and slit mask in front of sample substrate; **(b):** sample "alumina-1" (see Table 5.1) with seven stripes of particles with varying Pt-Rh composition and/or height. The sample is mounted on the sample holder (ceramic heater) of the catalysis chamber.

sample labelling	**deposited material(s)**	**studied at beamline...**	**microscopy studies**	**results see ch.**
"spinel-1"	$Pt_{0.33}Rh_{0.67}$	P09 (11.2 keV)	AFM, SEM	6.1; 7.1-7.3
"spinel-2"	Pt, Pt-Rh, Rh	P07 (78 keV)	AFM, SEM	6.1; 7.4
"spinel-3"	Pt, Pt-Rh, Rh	P07 (85 keV)	–	6.1
"alumina-1"	Pt, Pt-Rh, Rh	ID15 (78.7 keV)	AFM, SEM	6.2; 8.1; A; B
"alumina-2"	Pt, Pt-Rh, Rh	ID15 (78.7 keV)	–	6.2; C
"alumina-3"	Pt, Pt-Rh, Rh	P07 (78 keV)	SEM	6.2; 8.1.5
"alumina-4"	Pd, Pd-Rh, Rh	P07 (85 keV)	–	6.2
"alumina-5"	Pt, Pt-Pd	P07 (78 keV)	SEM	6.2; 8.2

Table 5.1: **Survey of samples investigated in this thesis:** the label "spinel-x" ("alumina-x") indicates that $MgAl_2O_4(001)$ (α-$Al_2O_3(0001)$) was used as sample substrate; the growth characteristics of the particles are discussed in chapter 6, the behaviour of $MgAl_2O_4(001)$-supported (α-$Al_2O_3(0001)$-supported) particles during reaction conditions in chapter 7 (8).

For the preparation of *combinatorial samples* to be studied with high photon energies, a slit mask was installed in front of the sample, see Fig. 5.2 a). This allowed for growing particle stripes with various alloy compositions and/or particle sizes on one sample. Fig. 5.2 b) shows such a gradient sample mounted on the sample holder of the in-situ catalysis chamber (see section 5.2).

An overview of all samples investigated in this thesis is given in Table 5.1 including the beamlines and photon energies at which they were studied. More detailed information on the individual sample preparation is contained in the corresponding sections of chapter 6.

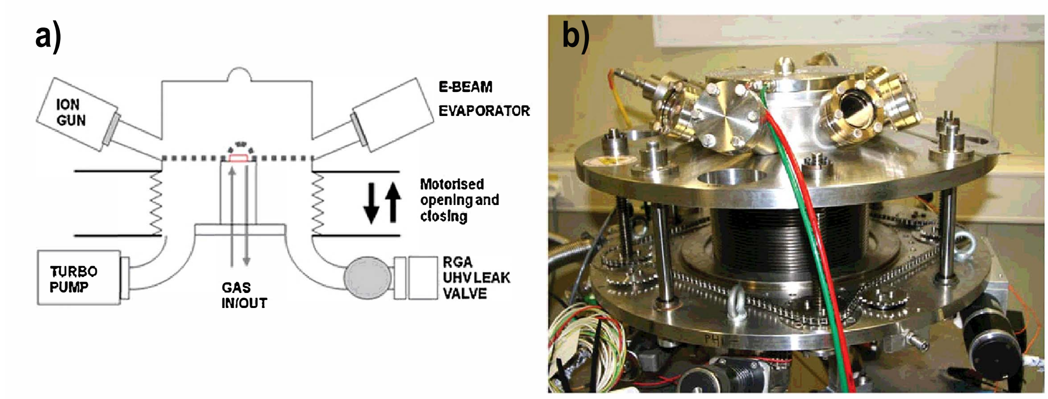

Figure 5.3: **In-situ catalysis chamber** [187]**: (a):** side view sketch illustrating the two possible chamber positions for I): sample preparation (chamber plates apart), II): in-situ catalysis (chamber plates closed); **(b):** picture of chamber with plates apart.

5.2 In-situ catalysis chamber

All catalytic reaction studies of this thesis were performed with an in-situ catalysis chamber, which can be operated as a flow reactor for catalysis. A sketch and picture of the chamber are shown in Fig. 5.3. The chamber was constructed for the sample investigation at beamlines and hence allows to correlate a sample's catalytic activity to its structure and morphology investigated by synchrotron x-rays. In addition, it provides the possibility for in-situ sample preparation.

The chamber's design was originally developed in a collaboration between the Interface Physics Group at Leiden University and beamline ID03 at the ESRF [187, 188]. This prototype chamber was in this thesis used for the samples studied at beamline ID15, ESRF (see Table 5.1). For all other samples, the catalysis chamber of the DESY NanoLab[1] was used, purchased from Leiden Probe Microscopy [189], from where such chambers are by now commercially available.

---

[1] The design of the NanoLab version displays only slight modifications compared to the prototype chamber: its flanges on the top part are shortened and put to lower angles, which allowed to lower the surface of the top plate by 10 mm, while the sample surface inside the chamber remained fixed. As a consequence, flight tubes can be installed closer to the sample to suppress background, see Fig. 5.6. Further differences are found in the design of the gas flow system, see subsection 5.2.2.

5.2.1 Chamber design

Fig. 5.3 shows that the chamber consists of a top and a bottom part interconnected by a flexible bellow. The bottom contains UHV devices such as a turbo pump, a residual gas analyzer, a cold cathode gauge and a leak valve for gas dosing. The upper part contains side flanges onto which sample preparation tools such as an argon ion sputter gun or e-beam evaporators can be installed. Moreover, a Be window, which constitutes the flow reactor volume, is centered in the top part. The sample is mounted inside the chamber on a sample holder foot attached to the chamber bottom. Its interior contains capillary tubes for the in- and outlet of the required reactant gases to the flow reactor.

The chamber is equipped with a drive chain mechanism that allows for moving the top part up and down while the position of the sample remains fixed. This provides two different chamber operation modes:

I) top part moved up → sample preparation

If the top part is moved up, the turbo pump evacuates the whole chamber vessel, where base pressures down to 4×10^{-9} mbar can be reached. In this position, the flanges equipped with the sample preparation tools point towards the sample position and allow the treatment of its surface. The required gases may be introduced via a UHV leak valve. The sample is mounted on a graphite heater embedded into a boron nitride holder which allows sample temperatures up to 1500 K under UHV conditions. There are manual valves with which the connection of the capillary tubes to the chamber can be closed during sample preparation.

II) top part moved down → flow reactor for catalysis

When the top part is moved down the small reactor volume (11.5 ml), defined by the Be dome, is sealed off from the remainder of the system, which keeps being pumped. The Be dome now acts as a flow reactor for catalysis: the manual valves of the capillary tubes to and from the reactor can be opened and a computer-controlled gas mixture of defined composition flows through, where the total flow and pressure inside the reactor can be set (see next subsection for more information on the gas flow system). Thanks to the small reactor volume, the time of gas refreshment when switching between different gas settings is relatively short and on the order of 20 seconds [187].

Information on the gas composition including the reaction products inside the reactor is obtained by leaking into the UHV part of the system where it is monitored by the residual gas analyzer. With the top flange lowered, the sample surface can be reached by x-rays and x-ray based surface studies can be performed simultaneously.

The down position of the chamber top part provides moreover the possibility to use the reactor as a load lock and thus allows a fast sample exchange without the need for a further chamber bake-out.

5.2.2 Gas flow system

The previous subsection mentioned that a well-defined mixture of reactant gases can be led into the flow reactor via its capillary tubes. The following will elucidate the gas flow scheme that provides such distinct gas settings.

Fig. 5.4 shows a sketch of the gas flow system the major part of which is installed inside an individual gas cabinet, its borders are indicated by blue-dashed lines. The system allows the simultaneous use of up to five gases (at the moment installed: Ar, O_2, CO, H_2, NO). The flow of each gas is individually set by calibrated mass flow controllers ('MFC's), their flow range comprises 0.8-100 $\frac{\mathrm{ml_n}}{\mathrm{min}}$ (prototype chamber at the ESRF: 1-50 $\frac{\mathrm{ml_n}}{\mathrm{min}}$)[2].

The gases are mixed and led to the reactor via the 'MIX'- and the 'MRS'-valve, respectively. The total gas pressure inside the reactor is set via the back pressure control 'BPC' on the outlet side, which throttles the total gas flow accordingly. The total pressure can be controlled in the range of 20 to 1200 mbar (prototype chamber: 100-1200 mbar). The ratio of the partial pressures of the various gases is determined by the ratio of the individually set mass flows. Hence, setting for instance the mass flow of gas 1 to f_1=10 $\frac{\mathrm{ml_n}}{\mathrm{min}}$ and of gas 2 to f_2=40 $\frac{\mathrm{ml_n}}{\mathrm{min}}$ at a total gas pressure of 100 mbar, results for a binary gas mixture in partial gas pressures of p_1=20 mbar and p_2=80 mbar, respectively.

The composition of the gas mixture is monitored by leaking a small amount of gas from the reactor to the residual gas analyzer mounted to the UHV part of the system. The gas mixture leaves the reactor through the outlet tube which is connected to the gas cabinet pump and gas exhaust.

In addition, the gas flow system provides via the 'INJ'-valve the possibility to introduce defined gas pulses to the reactor. In this thesis, however, only constant gas flows were used. The 'MRS'-valve not only opens a potential connection to the reactor, but can also open via the shunt 'MFC' to the gas cabinet pump. The shunt was used to pump and purge the gas lines to the

---

[2] 1 $\frac{\mathrm{ml_n}}{\mathrm{min}}$ corresponds to 1 $\frac{\mathrm{ml}}{\mathrm{min}}$ at 0 °C and 1013 bar

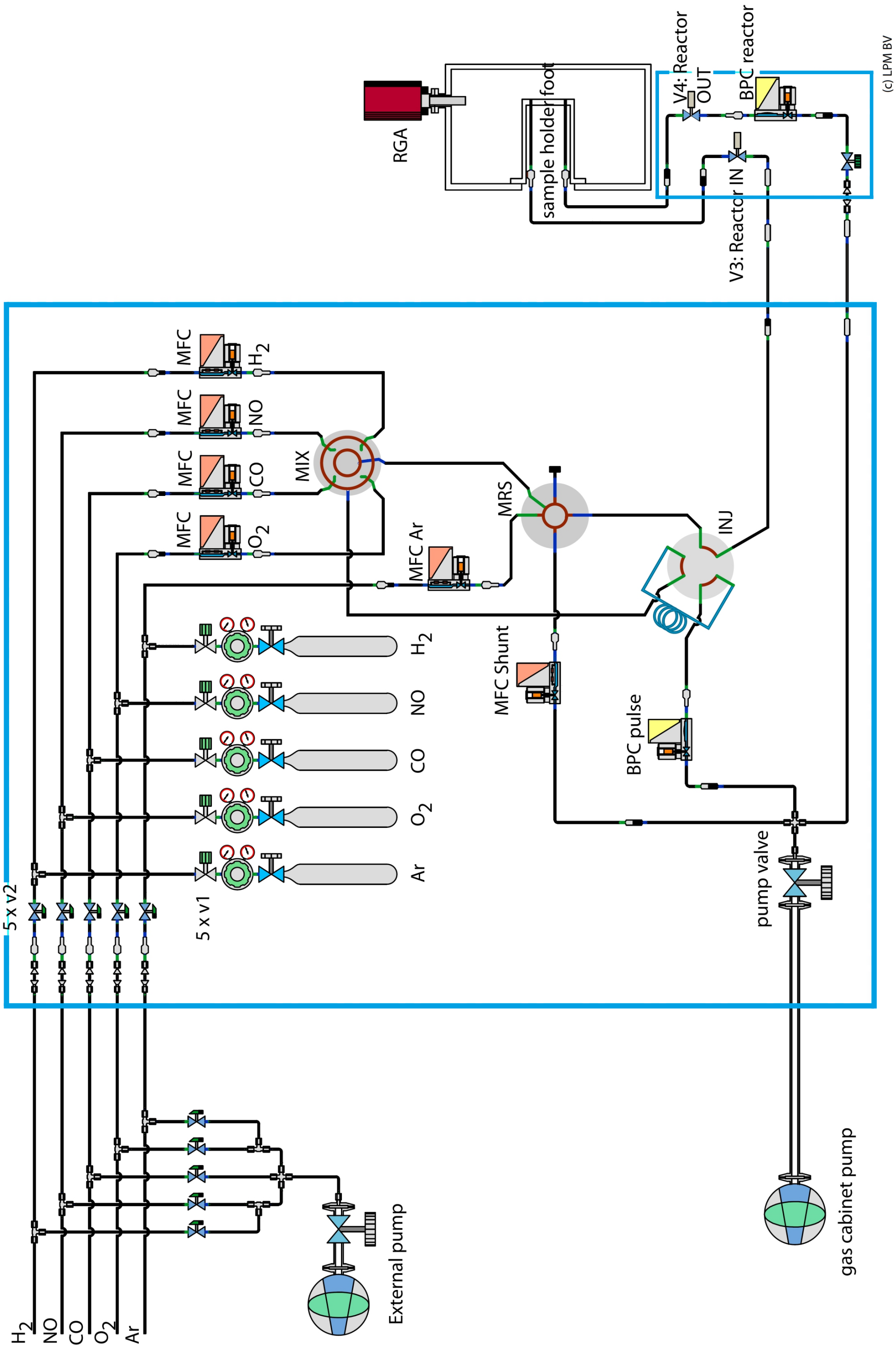

Figure 5.4: **Gas flow scheme [189]:** flow scheme inside the in-situ catalysis chamber gas cabinet and chamber reactor. Explanation of abbreviations: **'MFC'**: **m**ass **f**low **c**ontroller; **'MIX'**: **mix**ing valve; **'MRS'**: valve enabling connection between **m**ixing valve - **r**eactor - **s**hunt; **'INJ'**: valve for gas pulse **inj**ection; **'BPC'**: **b**ack **p**ressure **c**ontroller; **'RGA'**: **r**esidual **g**as **a**nalyzer. Blue lines: fixed internal valve connections; green lines: optional valve connections. See text for more information.

reactor prior to the experiment. In addition, a carbonyl trap, installed to the CO gas line, ensured the removal of potential carbonyls which may form in the gas lines or the gas bottle and lead to a deactivation of the catalyst sample.

5.3 Synchrotron endstations for x-ray diffraction

As was elucidated in chapter 3, catalysis is a dynamic process that involves continuous sample restructuring such particle shape changes or the formation of transient oxide phases. Such features often produce elusive and rather faint signals in x-ray diffraction (see chapter 4) and require high x-ray photon fluxes to be detected in a reasonable time frame, which is needed to enable a correlation to changes in the sample's catalytic activity. Hence, all operando x-ray diffraction studies performed in this thesis were carried out with the aforementioned in-situ catalysis chamber at beamlines of the 3$^{\mathrm{rd}}$ generation synchrotron facilities of the ESRF ('European Synchrotron Radiation Facility') or of Petra III at DESY ('Deutsches Elektronen-SYnchcrotron'), which deliver photon fluxes of high brilliance.

At the ESRF the brilliance comprises about $10^{21}\ \frac{\mathrm{photons}}{\mathrm{s{\cdot}mrad^2{\cdot}mm^2{\cdot}0.1\%BW}}$, the one at Petra III even exceeds this number, which makes both world-leading synchrotron radiation facilities. In both storage rings the particle energy comprises 6 GeV, the electron beam current amounts to 100 mA in the case of Petra III and to 200 mA in the case of the ESRF.

In the following, a short overview of the beamlines at which the data presented in this thesis were measured, will be given. They include beamline P09, Petra III, which allows surface x-ray diffraction studies at conventional photon energies, and the high photon energy beamlines ID15A, ESRF, and P07, Petra III. In each case, the individual experimental setups and equipments will be discussed.

5.3.1 Resonant scattering and diffraction beamline P09 at Petra III

The 'Resonant Scattering and Diffraction Beamline P09' [190], Petra III, is an undulator beamline that provides photon energies in the range from 2.7 to 24 keV. In this thesis it was used for surface sensitive x-ray diffraction studies

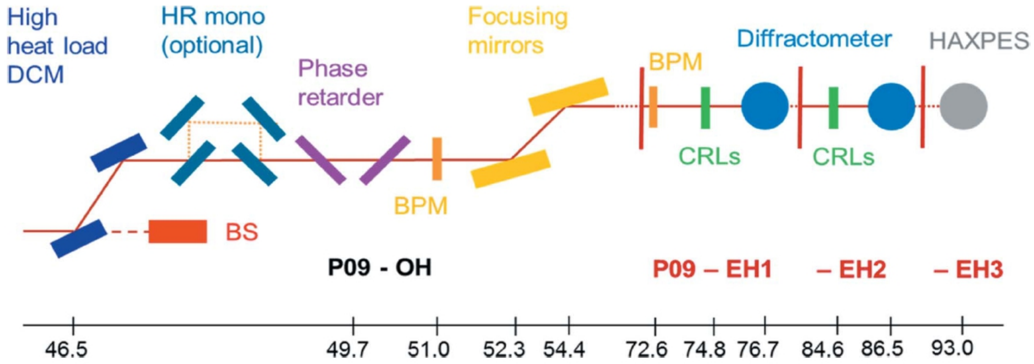

Figure 5.5: **Beam path through the optics of beamline P09 [190]:** distances from the source are given in m; the optics hutch ('OH') hosts a high-heat-load double-crystal monochromator ('DCM'), a beam stop for the white beam ('BS'), a high-resolution monochromator ('HR mono'), a phase retarder, a beam positioning monitor ('BPM') and focusing mirrors; experimental hutches ('EH') 1 and 2 may host further optical elements such as compound refractive lenses ('CRL'); positions of the diffractometers ('EH1' and 'EH2') and the spectrometer ('EH3') are indicated.

at conventional photon energies in the medium energy x-ray regime (E=11.2 keV). They included the point-detector-based high resolution reciprocal space mapping of particle facet signals to obtain information on particle shapes and shape changes as well as time-resolved in-situ gas switching experiments for tracking the formation and dissolution of transient oxide phases on nanoparticle facets. The results of these investigations are summarized in sections 7.1-7.3.

As can be deduced from the beam path displayed in Fig. 5.5 beamline P09 hosts three experimental hutches ('EH'). The last hutch, 'EH3', is dedicated to hard x-ray photoelectron spectroscopy (HAXPES), the first two experimental hutches, 'EH1' and 'EH2', are designed for resonant x-ray diffraction (RXD) experiments for the investigation of electronic or magnetic ordering phenomena. The experiments of this thesis were carried out in 'EH2'.

The first component in the beam path inside the optics hutch is a high-heat-load double crystal monochromator, which is cryogenically cooled by liquid N_2 and for which either Si(111) or Si(311) crystal pairs can be used. Using Si(311) instead of Si(111) allows a factor of five higher energy resolution (energy bandwidth at E=8 keV: $(\Delta E/E)_{(311)}$=0.28×10^{-4} instead of $(\Delta E/E)_{(111)}$=3×10^{-4}), however, at the expense of the photon flux by a factor of five. The beam direction and position can be aligned by adjusting the second crystal's position and pitch. This beam alignment is controlled by means of the beam positioning

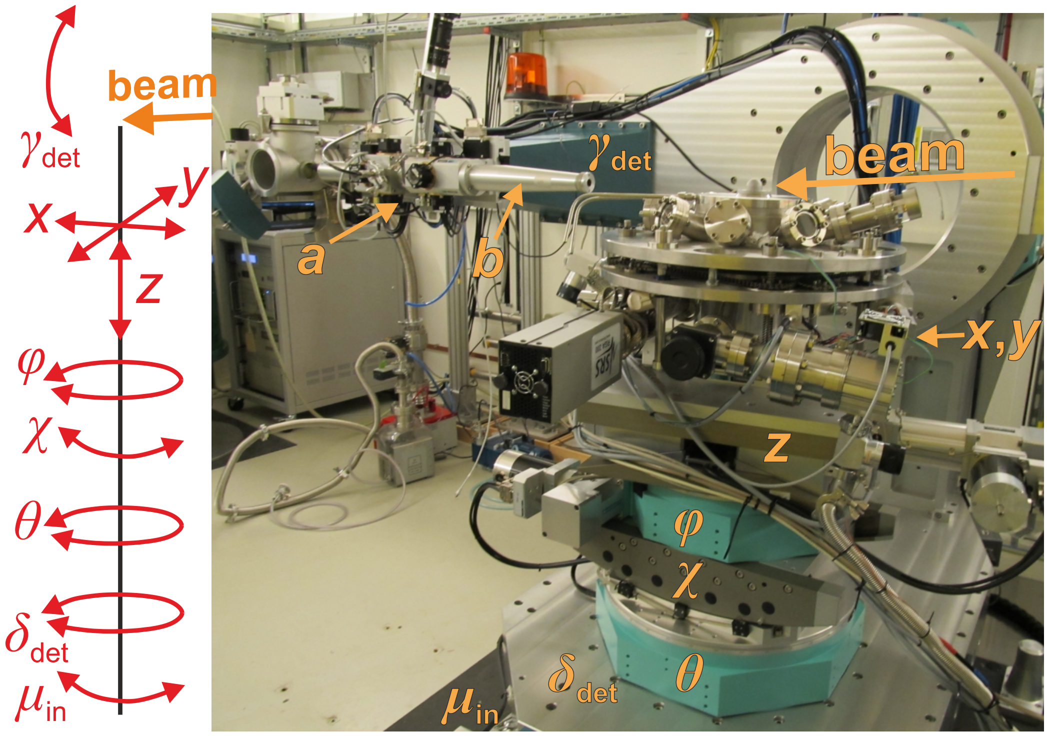

Figure 5.6: **Experimental setup at beamline P09, Petra III:** in-situ catalysis chamber mounted on the heavy load diffractometer with vertical scattering angle γ_{det}, sample xy- and z-stage, rocking angle ϕ, cradle χ, rocking angle θ, horizontal scattering angle δ_{det}, and incident angle μ_{in}; the detector arm is equipped with a NaI point detector with a slit system (a) and a flight tube (b).

monitors in the optics and the first experimental hutch 'EH1'.

Further down-stream, two 1 m long and 130 mm wide focusing mirrors are located. They are of fused silica (SiO_2) but are also partly coated with Pd. Combining different settings of the two mirrors allows for suppressing higher harmonics for almost the whole photon energy range (6-24 keV) and to focus the beam down to 150×30 μm (at the sample position in 'EH1'). Further focusing down to 4 μm vertical and 50 μm horizontal (FWHM) focal sizes are achieved with compound reflective lenses, which were also set up in the experiments of this thesis.

Fig. 5.6 shows the catalysis chamber mounted on the heavy load six-circle diffractometer in z-axis geometry in 'EH2' of beamline P09. The diffractometer's degrees of freedom are indicated. A scintillation NaI point detector was used. It was equipped with a two slit system and a pumped flight tube in front, allowing for beam collimation and the suppression of background, respectively.

5.3.2 Beamlines for high energy x-ray diffraction: ID15A (ESRF) and P07 (Petra III)

In this thesis, the mapping of large area high energy reciprocal space maps with a 2D detector was employed as in-situ probe while switching gas flows and hence the conditions during catalytic reaction conditions. These type of experiments were carried out at the 'High Energy Scattering Beamline ID15A' [191, 192], ESRF, and the 'High Energy Materials Science Beamline P07' [74, 193, 194], Petra III. The experimental results of these measurements are summarized in chapters 6, 7.4 and 8.

The principle beamline setup and the setups inside the experimental hutches are very much comparable for both beamlines. The detailed beamline layout and the respective optical elements along the beam path are for beamlines ID15A and P07 summarized in Fig. 5.7 and Fig. 5.8, respectively.

In the case of the wiggler beamline ID15A, x-ray energies below 40 keV are in the primary beam filtered by an Al absorber. Further downstream, the white beam is monochromatized by a Si(111) double crystal monochromator in Laue geometry (the first crystal is cooled), which is tunable in an energy range between 40 and 300 keV (energy bandwidth ($\Delta E/E$)=2×10^{-3}), and led into the experimental hutch of ID15A.

At the undulator beamline P07, low energy harmonics are cut out of the primary beam using a filter box inside the ring tunnel. A single bounce monochromator defines the beam for the test facility 'EH1'. The main beam of the experimental hutches ('EH2', 'EH3', 'EH4') is monochromatized by a bent Si(111) double Laue monochromator (the first crystal is water-cooled), which is tunable in a photon energy range between 33 and 200 keV ($\Delta E/E$)=2×10^{-3}). The experiments of this thesis were carried out in 'EH2'.

At both beamlines, focusing of the beam to the sample position is performed by means of a variable number of Al compound refractive lenses. In the case of P07, these are located inside the optics hutch 'OH1', at ID15A they are inside the main experimental hutch. Hence, beam spot sizes (vertical×horizontal) down to 2×30 μm^2 (P07) and down to 5×15 μm^2 (ID15A) can be reached.

The work with high energy x-rays requires an utmost high precision of the experimental setup parts involved, since the scattering geometry is characterized by extremely small incident angles (typically 0.03°) and small scattering angles (difference between Pt(220) and Rh(220) in-plane Bragg angles: only $\sim$0.2°) in general. At both beamlines this is realized by using a specifically designed

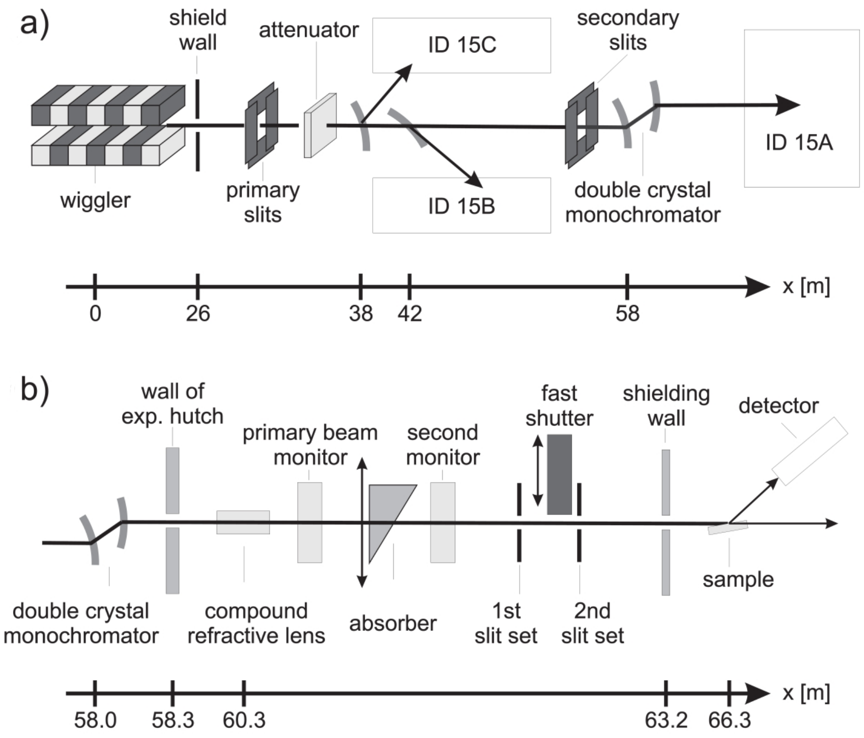

Figure 5.7: **Beam path at beamline ID15A, ESRF [192]: a):** general beamline layout; **b):** optical elements and beam path in experimental hutch ID15A. See text for more information.

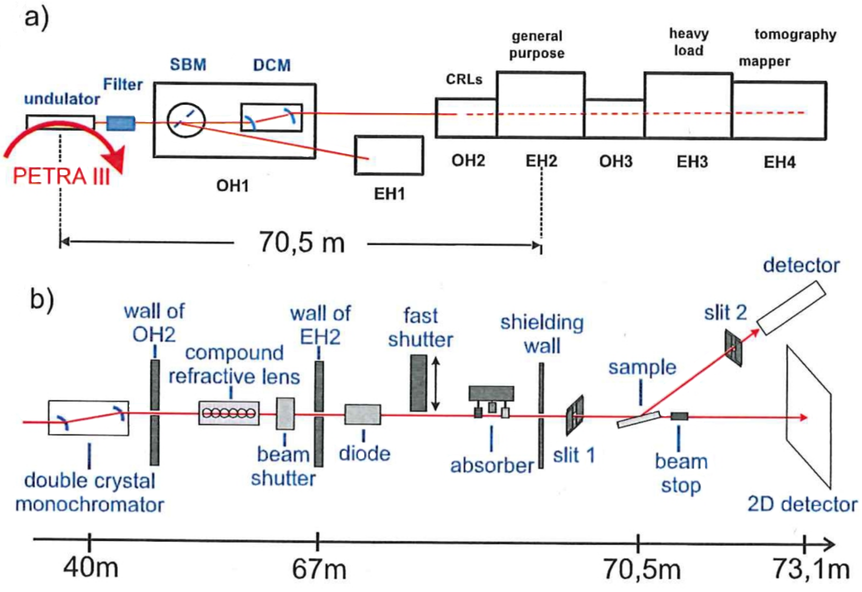

Figure 5.8: **Beam path at beamline P07, Petra III [193]: a):** general beamline layout; **b):** optical elements and beam path in optics hutch 2 ('OH2') and experimental hutch 2 ('EH2'). See text for more information.

manipulation tower with z-axis geometry for the mounting of the sample environment, and a large detector table which is totally separated from the sample tower. Together, the sample tower and detector table feature all degrees of freedom of a six-circle diffractometer.

Fig. 5.9 shows the sample tower for the case of beamline P07, carrying the in-situ catalysis chamber. The degrees of freedom are indicated, which allow for the alignment of the sample surface and the rocking around the surface normal. The high precision of the motors guarantees for the incident angle μ_{in} a resolution $<0.0001°$, for the z-stage a resolution <0.1 μm.

In Fig. 5.10 a) the detector stage is shown for the case of beamline ID15A. Its separation from the sample tower and the fact that the motions of the detectors are realized by a combination of linear motions increase the accuracy and stability during measurement. For all experiments the combination of a 2D detector, for the mapping of large areas in reciprocal space, and a point detector, for sample alignment and the measurement of x-ray reflectivity curves, was used. A fast switching (on the order of seconds) between the two detectors is possible. At both beamlines, a NaI scintillation point detector was used. For the 2D mapping at ID15A, a 14 bit FReLoN CCD camera (107.7×107.7 mm^2, pixel size 52.58×52.58 μm^2) was employed, at P07 a Perkin Elmer 2D area detector (409.6×409.6 mm^2, pixel size 200×200 μm^2).

To block the direct beam and scattering signal from the chamber's Be dome, a combination of beamstop and mask, both made of Ta, were used. In the setup at beamline ID15A, shown in Fig. 5.10 b), beamstop and mask were individually adjustable. In the setup at P07, shown in the inset of Fig. 5.9, the beamstop was mounted inside the surrounding mask.

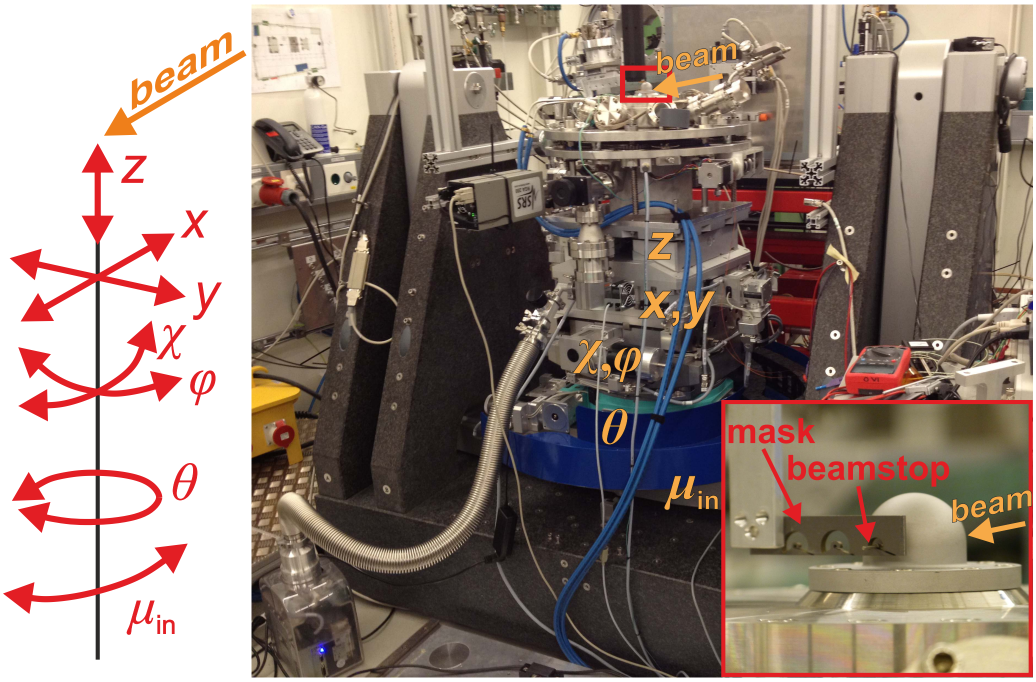

Figure 5.9: **Experimental setup at beamline P07, Petra III:** the catalysis chamber is mounted onto the sample tower, its degrees of freedom are indicated on the left side, they include the z-, x-, and y-stages, χ- and ϕ-tilt stages, the rocking angle θ and the incident angle μ_{in}; the inset shows a close-up of the chamber's reactor dome, the beamstop and the mask.

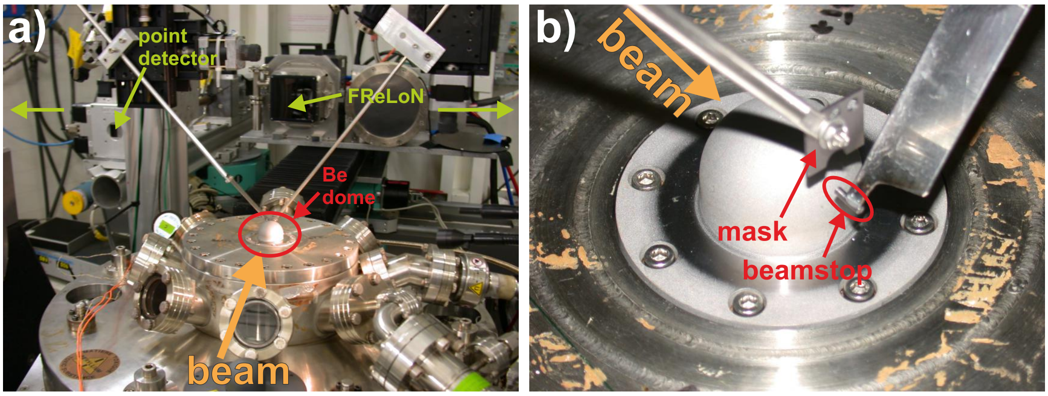

Figure 5.10: **Experimental setup at beamline ID15A, ESRF: a)**: catalysis chamber mounted on the diffractometer, the used detectors (FreLoN 2D camera and point detector) can be seen in the background; **b)**: Be dome with beamstop and mask.

Chapter 6

Size- and Composition-Dependent Growth of Alloy Nanoparticles on Oxide Substrates

To allow a systematic study of nanoparticles under reaction conditions, a series of samples was prepared in the framework of this thesis. They consisted of alloy particles of varying compositions and sizes which were grown on two different support materials, either $MgAl_2O_4(001)$ or α-$Al_2O_3(0001)$.

This chapter yields an overview of the growth characteristics of the as-prepared particles *before* CO oxidation: the different particle epitaxies and the particle morphologies will be discussed for the two substrates as a function of the particle composition, the particle size, the deposition mode (alloy vs. "core-shell") and the support pretreatment.

It will be shown that in the case of $MgAl_2O_4(001)$-supported nanoparticles the (001)-type epitaxy, and in the case of α-$Al_2O_3(0001)$-supported particles the (111)-type epitaxy, are predominant, independent of the respective particle composition or size investigated. The behaviour of particles belonging to these main epitaxies under activity conditions will be subject matter of chapters 7 and 8.

6.1 Growth on the $MgAl_2O_4(001)$ substrate

This section summarizes information on particle growth on $MgAl_2O_4(001)$ as obtained from the three samples schematically depicted in Fig. 6.1. One of them ("spinel-1") was fully covered with particles of only one composition ($Pt_{0.33}Rh_{0.67}$) and was investigated using conventional surface x-ray diffraction at a photon energy of 11.2 keV at beamline P09, Petra III. The combinatorial samples "spinel-2" and "spinel-3" contained stripes with particles of different Pt-Rh compositions and/or particle sizes. They were studied by means of grazing incidence high energy x-ray diffraction at beamline P07, Petra III, using photon energies of 78 and 85 keV. More information on the experimental setup and the measurement strategies can be found in sections 7.1 and 7.4.

Details on the sample preparation

The bare substrates had undergone similar pretreatments which mainly differed in the number of sputtering and annealing cycles; the respective chronological procedures are described in the following and are also depicted in Fig. 6.2. The main differences in the preparation of the individual substrates are juxtaposed in Table 6.1.

For all samples the preparation included chemical cleaning in acetone and ethanol using an ultrasonic bath. After annealing under UHV to get off water from the sample surface (T=573-613 K for 60-140 min) the C contamination was removed by thermal cracking under atomic oxygen ($p_{O2}=1\times10^{-7}$ mbar, T=573 K, 60-120 min). The substrates of samples "spinel-1" and "spinel-3" underwent one long lasting cycle of Ar^+ sputtering ($p_{Ar}=1\times10^{-6}$ mbar, U_{acc}=1 keV, I_{em}=10 mA; "spinel-1": 44 min, "spinel-3": 20 min) and subsequent annealing under 2×10^{-7} mbar O_2 ("spinel-1": 100 min, "spinel-3": 43 min). Contrary, the substrate of "spinel-2" underwent five fast cycles of Ar^+ sputtering and annealing under 1×10^{-7} mbar O_2 at an elevated temperature of 1173 K, where each sputtering and annealing lasted only 10 and 30 minutes, respectively.

As discussed in subsection 2.4.2, repeated sputtering and annealing cycles result in large terraces on the $MgAl_2O_4(001)$ surface along with nanometer sized pits of 2-8 Å depth [48]. Such holes, which may act as nucleation sites during particle growth and may serve as an anchor for stabilizing the particles during reaction conditions, are accordingly expected to be present on "spinel-2", but

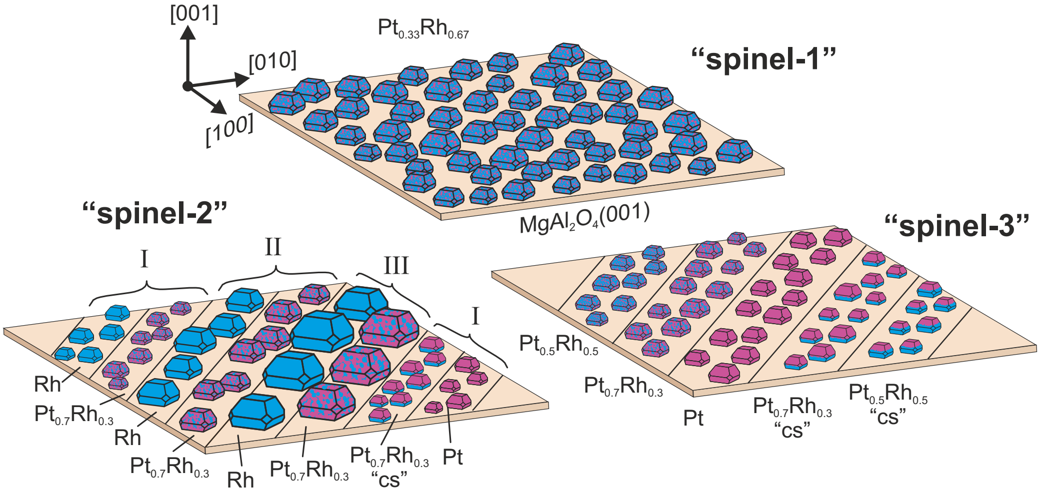

Figure 6.1: **Overview of MgAl$_2$O$_4$(001)-based samples: "spinel-1":** substrate equally covered with Pt$_{0.33}$Rh$_{0.67}$ alloy particles (H=60 Å, D=90 Å). **"spinel-2":** combinatorial sample containing particle stripes of varying Pt-Rh compositions and/or sizes (three size regimes: I: H=32-34 Å, D=44-52 Å; II: H=52-58 Å, D=89-102 Å; III: H=95-122 Å, D=157-192 Å). **"spinel-3":** combinatorial sample containing particles of the same size (H=35-40 Å, D=55-60 Å) but varying Pt-Rh compositions. The abbreviation "cs" refers to "core-shell" nanoparticles characterized by the sequential deposition of Rh and Pt.

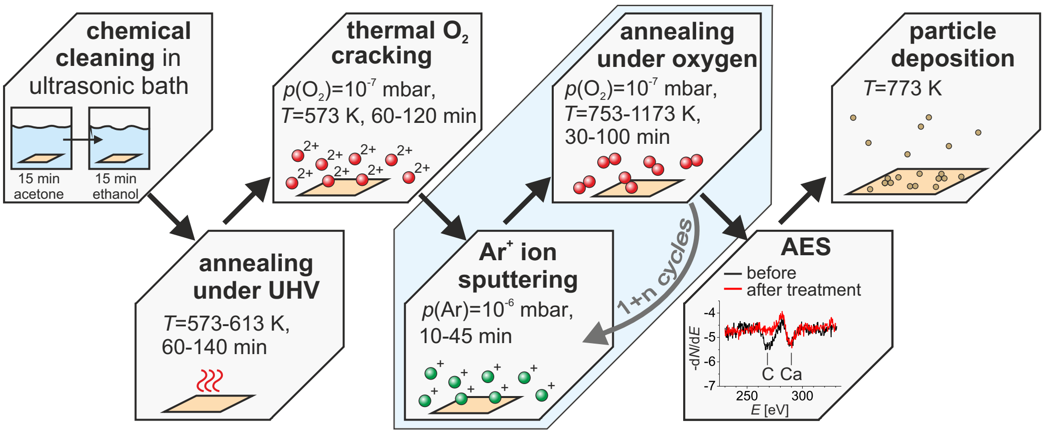

Figure 6.2: **Substrate pretreatment of MgAl$_2$O$_4$(001):** General steps, see text for more information.

sample	**“spinel-1”**	**“spinel-2”**	**“spinel-3”**
compositions	$Pt_{0.33}Rh_{0.67}$	Pt $Pt_{0.7}Rh_{0.3}$ $Pt_{0.7}Rh_{0.3}$ “cs” Rh	Pt $Pt_{0.7}Rh_{0.3}$ $Pt_{0.7}Rh_{0.3}$ “cs” $Pt_{0.5}Rh_{0.5}$ $Pt_{0.5}Rh_{0.5}$ “cs”
remarks	one composition	combinatorial (size, composition)	combinatorial (composition)
	1 long cycle of Ar^+-sputtering (45 min) and annealing under O_2 (100 min, T=843 K)	5 quick cycles of Ar^+-sputtering (10-20 min) and annealing under O_2 at higher temperatures (30 min, T=1173 K)	1 cycle of Ar^+-sputtering (20 min) and annealing under O_2 at lower temperatures (43 min, T=753 K)
	deposition in 1 step	deposition in 4 steps	deposition in 1 step
	flashing sample after deposition to 843 K for 15 min	no flashing after deposition	no flashing after deposition

Table 6.1: **Differences in substrate preparation of $MgAl_2O_4(001)$-based samples:** the acronym “cs” refers to “core-shell” particles for which first Rh was deposited at 803 K and later Pt at a lower temperature of 523 K. A sketch of the samples is depicted in Fig 6.1.

absent on samples “spinel-1” and “spinel-3”.

Before deposition the cleanliness of the substrate was confirmed by Auger electron spectroscopy. All **alloy and monometallic** nanoparticles were grown at a substrate temperature of 773 K by means of a *simultaneous* physical vapour deposition of Pt and Rh, where the corresponding fluxes were adjusted according to the desired alloy composition (see section 5.1).

In the following, and throughout this thesis, the term **“core-shell” (“cs”)** denotes particles that were grown by a *sequential* deposition of Rh and Pt. In all cases, also on α-$Al_2O_3(0001)$ (see section 6.2), Rh was first deposited at 773 K, thereafter, Pt was deposited “on top” at a lower substrate temperature of 548 K to suppress mixing of the two elements [195, 196]. The idea behind the “core-shell” nanoparticles was to test whether Rh at the interface might act as an anchor suppressing nanoparticle movement and thus sintering via Smoluchowski ripening (see section 3.3).

Only in the case of “spinel-2” the particle deposition was carried out in four steps, which entailed a cooling down of the sample to room temperature in between, and repeated and long total annealing cycles of the previously deposited particles. The latter implicates that the particles might have undergone heat-induced sintering already during sample preparation. Only sample “spinel-1” was after deposition flashed to 843 K for 15 minutes.

After particle deposition the samples were transported through air and mounted inside the in-situ catalysis chamber. Therein, they underwent annealing under hydrogen to remove possible oxides (“spinel-1”: p_{H2}=2.0×10^{-5} mbar at T=623 K for 90 minutes; “spinel-2”: p_{H2}=2.0×10^{-5} mbar at T=653 K for 60 minutes; “spinel-3”: p_{H2}=1.1×10^{-5} mbar, T=603 K for 60 minutes). Sample “spinel-1” was in addition flashed to 873 K for 7 minutes and later to 973 K for 15 more minutes. The data presented in this section were obtained under Ar flow (“spinel-1”: p_{Ar}=50 mbar, T=673 K; “spinel-2”: p_{Ar}=50 mbar, T=648 K; “spinel-3”: p_{Ar}=220 mbar, T=553 K).

Growth of MgAl$_2$O$_4$(001)-supported Pt$_{0.33}$Rh$_{0.67}$ particles studied with conventional surface x-ray diffraction (sample “spinel-1”)

“Spinel-1” is the only sample of this thesis that was studied by means of conventional surface x-ray diffraction at the ‘Resonant Scattering and Diffraction Beamline P09’ at Petra III, the growth characteristics of its Pt$_{0.33}$Rh$_{0.67}$ particles will be discussed in the following.

They were concluded to grow predominantly in a **(001)-orientation** (see Fig. 6.3 a) for a typical shape) and epitaxial with respect to the substrate unit cell (*‘cube-on-cube epitaxy’*). High resolution reciprocal space maps (see sections 7.1 and 7.3) revealing signals from (001)- and (111)-type particle facets confirmed the shape of a truncated octahedron. From the full width at half maximum of linescans through the particle Bragg peaks the particle height and diameter were found to comprise H=60 Å and D=90 Å, respectively. The absence of Bragg peak splitting confirmed the presence of alloy particles with one distinct Pt-Rh composition.

Apart from the (001)-type epitaxy, the presence of particles growing as (111)- and (110)-orientations was concluded, typical respective shapes are depicted in Fig. 6.3 b) and c). Their coexistence was deduced from the rocking scans shown in Fig. 6.4 a) and b), in which they give rise to in-plane Bragg peaks of minor intensity. Contrary, the (220), ($2\bar{2}0$), (020) and (200) Bragg peaks of

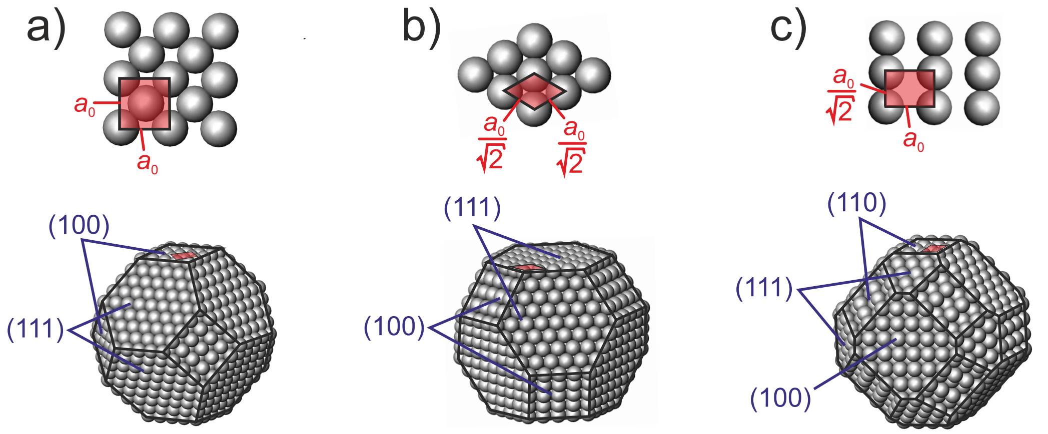

Figure 6.3: **Different particle orientations.** Particle surface unit cells (top) and corresponding particle shapes (bottom) of **a):** (001)-oriented particles (a=b=c=a_0; α=β=γ=90°), **b):** (111)-oriented particles (a=b=$\frac{a_0}{\sqrt{2}}$, c=$\sqrt{3}a_0$; α=β=90°, γ=120°), **c):** (110)-oriented particles (a=a_0, b=c=$\frac{a_0}{\sqrt{2}}$; α=β=γ=90°), where a_0 denotes the fcc lattice parameter of the respective Pt-Rh composition. For a) and b) potential (110)-type facets are neglected.

highest intensity occurring every 90° stem from (001)-oriented particles.

The presence of **(111)-oriented particles** was deduced from the rocking scan shown in Fig. 6.4 a). The peaks occurring every 30° (labeled II and III) can be ascribed to two (111)-orientation domains whose in-plane unit cells are rotated with respect to each other by 90°. This type of (111)-orientation is referred to in literature as the $[1\bar{1}0](111)_{\text{film}}\|[110](001)_{\text{sub}}$-epitaxy [31, 152]. A top view sketch of (111)-oriented particles along with their unit cells drawn in purple (II) and orange (III) is shown in Fig. 6.4 e). They are depicted with respect to the unit cells of $MgAl_2O_4(001)$ and the (001)-oriented particles. The corresponding reciprocal space unit cells of the same colour are displayed in Fig. 6.4 c) along with Bragg peak positions of the substrate, of (001)-oriented particles and the position of the rocking scan of Fig. 6.4 a). Contrary to particle growth on MgO(001), no traces of the $[1\bar{1}0](111)_{\text{film}}\|[100](001)_{\text{sub}}$-orientation were observed, whose peaks would occur every 15° in the scan of Fig. 6.4 a) [31, 152].

The rocking scan of Fig. 6.4 b) gives experimental evidence to the presence of eight domains of **(110)-oriented particles**. A top view of the particles belonging to four of these domains is shown in Fig. 6.4 f). The figure includes the particles' unit cell orientations with respect to the unit cell of $MgAl_2O_4(001)$. They are rotated by 0° (yellow, IV), 45° (green, V), 63°=90°-27° (dark blue,

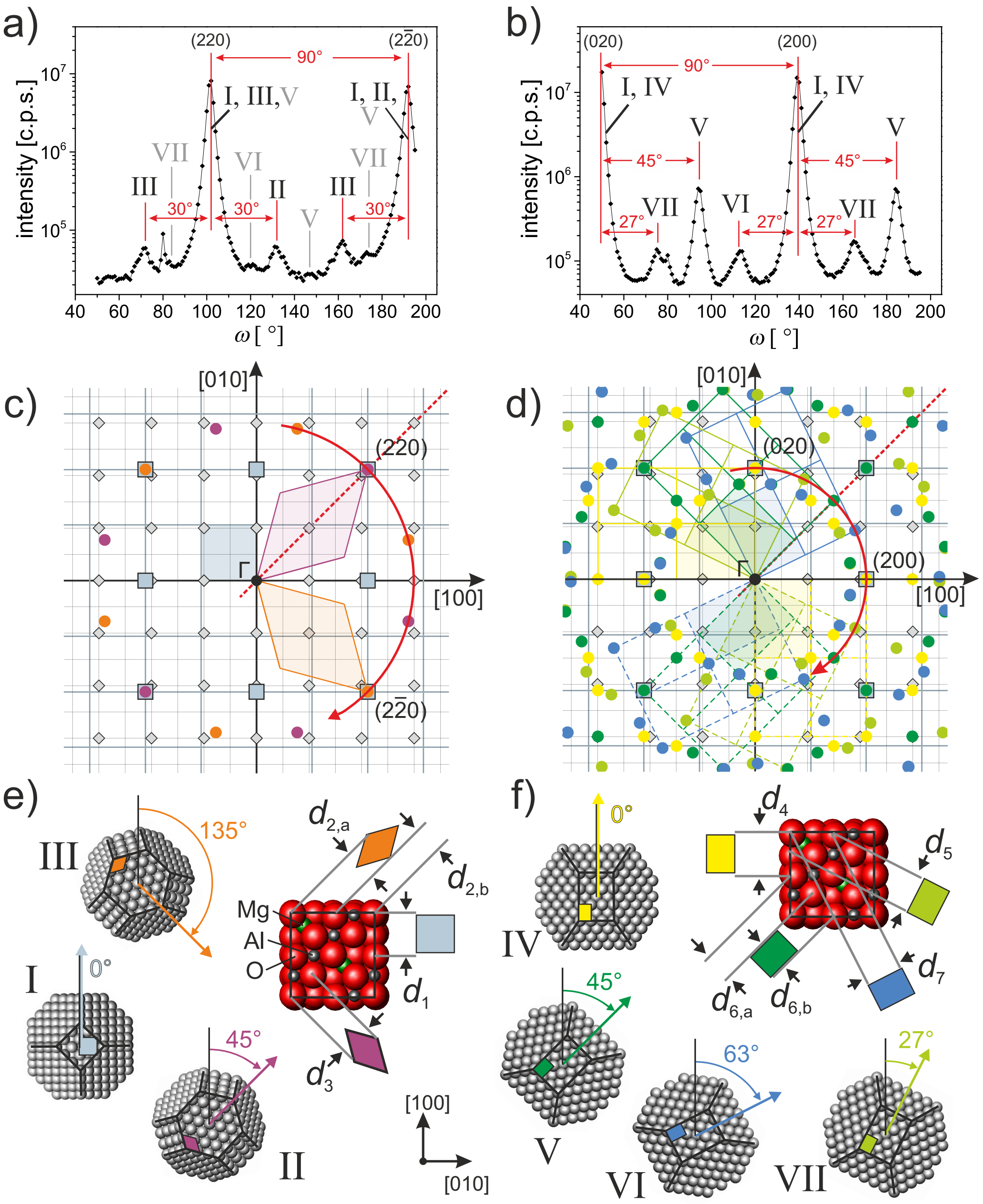

Figure 6.4: **Particle epitaxies found for the growth on sample "spinel-1": a), b):** rocking scans through (220)- and (200)-type Bragg peaks of (001)-oriented $Pt_{0.33}Rh_{0.67}$ particles; **c), d):** in-plane reciprocal space maps, where the scans of a) and b) are represented by red arrows. The anticipated Bragg peak positions from the substrate and the (001)-oriented particles are denoted by grey diamonds and blue squares, respectively; **c):** Bragg peak positions from two domains of the (111)-epitaxy (orange and purple circles) and **d)** from four domains of (110)-oriented particles (yellow, light-green, green and blue circles) are drawn in addition. The same colour coding is used for the respective reciprocal unit cells; **e), f):** ball models of particles belonging to (001)- and (111)-type epitaxies (d)) and (110)-type epitaxies (f)); the respective real space unit cells are drawn with respect to the $MgAl_2O_4(001)$ unit cell; using the same colour coding as in c), d).

VI), and 27° (light-green, VII) with respect to the substrate [100]-axis around the surface normal. Fig. 6.4 d) displays the resulting reciprocal space map containing the Bragg peaks in the respective colour coding. In addition, the anticipated Bragg peaks of the other four domains - which are rotated by 90° with respect to the ones shown in f) - are displayed. The circular segment of reciprocal space, which is probed by the rocking scan, is indicated by the red arrow.

Bragg peak signals from (110)-oriented particles are also present in Fig. 6.4 a), their anticipated peak positions are indicated by their respective roman numbers in grey colour.

Information on the relative percentages of the different particle epitaxies was obtained from the integrated peak intensities of the rocking scans in 6.4 a) and b). Accordingly, the peaks belonging to the two domains of (111)-oriented particles make up 6.4% of the intensities in the scan of Fig. 6.4 a). In Fig. 6.4 b), the peaks of the four domains of (110)-oriented particles that are represented by the yellow and the dark green unit cells (domains IV and V) comprise even 20.8%, while the peaks of the four domains growing with the $(\sqrt{5}\times\sqrt{5})R27°$ superstructure (domains VI and VII) amount to 11.9% of the intensity.

For **(001)-oriented particles** the particle atomic row distances of 3.8423 Å match the substrate atomic rows $d_1=\frac{1}{2}\cdot 8.086$ Å along both, the [100]- and the [010]-direction, with a lattice mismatch of 5.22%.

The atomic distances of the **(111)-oriented particles** amount to $\frac{3.8423}{\sqrt{2}}$ Å and match the substrate atomic rows along the [110]-direction, determined by $d_3=\frac{\sqrt{2}}{4}\cdot 8.086$ Å, also with a mismatch of 5.22%. The same average mismatch is present along the substrate $[1\bar{1}0]$-direction, as the alternating spacings between the oxygen atomic rows yield the average spacing of $d_{2,\mathrm{a}}+d_{2,\mathrm{b}}=2\cdot d_3$.

A mismatch of 5.22% was also concluded for **(110)-oriented particles** that grow as is indicated in Fig. 6.4 d) and f) by the yellow unit cells (particle atomic spacing 3.8423 Å matches substrate spacing $d_4=\frac{1}{2}\cdot 8.086$ Å) and by the dark green unit cell (particle atomic spacing $\frac{3.8423}{\sqrt{2}}$ Å matches the average substrate row distances $\frac{d_{6,\mathrm{a}}+d_{6,\mathrm{b}}}{2}=\frac{\sqrt{2}d_4}{2}$). (110)-oriented particles, which grow as is indicated by the light-green and the dark-blue unit cells, stabilize themselves on the substrate by rotating 26.57° around the surface normal with respect to the [100]- or the [010]-direction. This corresponds to an aligning of the particle atomic rows along the $[1\bar{2}0]$- and $[2\bar{1}0]$-directions of the substrate unit cell in a $(\sqrt{5}\times\sqrt{5})R27°$ superstructure. The mismatch amounts to -5.89% between

the particle atomic row distance 3.8423 Å and the distance between the corresponding substrate atomic rows d_5=d_7=cos(26.57°)$\cdot\frac{1}{2}\cdot$8.086 Å.
In summary, above results on the particle growth of Pt$_{0.33}$Rh$_{0.67}$ particles obtained by conventional surface x-ray diffraction using a point detector revealed that the particles grow predominantly in a (001)-orientation, but that there is also a relatively large portion of (110)-oriented particles (especially of particles growing with the yellow and dark green orientation, see Fig. 6.4) which are clearly favoured compared to the (111)-epitaxies. The results of the following subsection will show that a large portion of (110)-oriented particles is typical of the growth for Rh and Rh-rich particles, which is probably due to the relatively small surface energies of the particle (110)-type facets (see Table 2.1 in subsection 2.3.1).

Size- and composition-dependent particle growth on MgAl$_2$O$_4$(001) studied with grazing incidence high energy x-ray diffraction (samples "spinel-2", "spinel-3")

This subsection presents the characteristics of particle growth on the combinatorial samples "spinel-2" and "spinel-3" (see Fig. 6.1) obtained by means of grazing incidence high energy x-ray diffraction (sample "spinel-2": E=78 keV; "spinel-3": E=85 keV). Large areas in reciprocal space were mapped in the substrate (110, L)-plane, where the substrate [110]-direction is in Fig. 6.4 c) and d) indicated by the red dashed line. The high energy approach allowed for measuring Bragg peaks of different particle epitaxies, including the (111) Bragg peak of the (001)-oriented particles and potential peaks of the (110)-epitaxy domain, which is indicated by dark green colour in Fig. 6.4 d) and f). Hence, it facilitated the direct comparison of the growth characteristics as a function of particle size, Pt-Rh composition and substrate preparation.
Fig. 6.7 yields an overview of the reciprocal space maps of all particle sizes and Pt-Rh compositions on samples "spinel-2" and "-3". Before comparing the differences of the growth characteristics for the various systems, potential diffraction signals will be discussed based on the map measured on the Pt particles of "spinel-3", as it contains all features found in other maps.
Fig. 6.5 a) displays this 2D map measured on the pure **Pt particles of sample "spinel-3"**. It discloses the coexistence of particles growing in (001)-, (111)- and (110)-orientations. Comparison of the respective Bragg peak intensities confirms that the (001)-type epitaxy dominates. No distinct particle

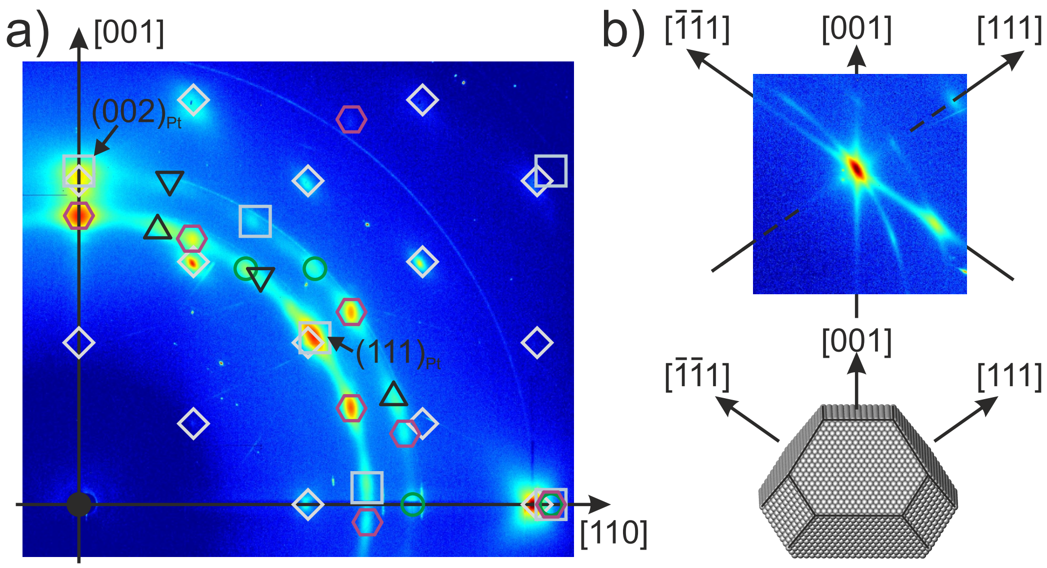

Figure 6.5: **High energy reciprocal space map of the pure Pt particles on sample "spinel-3": a):** (110, L)-map centered around the Pt(111) Bragg peak. The in-plane [110]-direction is in Fig. 6.4 c) and d) represented by red-dashed lines. It contains Bragg peaks from the substrate (grey diamonds), (001)-oriented particles (light-blue squares), two domains of (110)-oriented particles (green circles), two domains of (111)-oriented particles (purple hexagons) and signals from internal twinning of (001)-oriented (triangles pointing up) and (111)-oriented particles (triangles pointing down); **b):** (111) Bragg peak of the largest Rh particles of sample "spinel-2" featuring strong facet signals.

facet signals around its Pt(111) Bragg peak are visible, which can be ascribed to not well established facets due to the small particle size (H=40 Å; D=56 Å). Contrary, the map shown in Fig. 6.5 b), measured on the largest Rh particles (H=122 Å; D=192 Å) of sample "spinel-2", shows pronounced signals from the (001)- and (111)-type particle facets, thus affirming a truncated octahedral shape for (001)-oriented particles of a certain size. In contrast to the linescans of Fig. 6.4, the 2D map yields instantaneous information on the presence of internal twinning inside the (001)- and (111)-oriented particles.

The 2D map in Fig. 6.5 a) moreover reveals a novel phenomenon found for the sample systems studied in this thesis, namely that (111)- and (001)-oriented particles may accommodate on the sample surface by tilting themselves, by 23° and 32°, respectively, along the substrate in-plane [1$\bar{1}$0]-direction. The diffraction signals from both, the tilted and non-tilted particles, are in Fig. 6.5 a) denoted by grey squares and purple hexagons. The same 2D map, denoting the signals from the tilted particles only and indicating their respective tilt, is

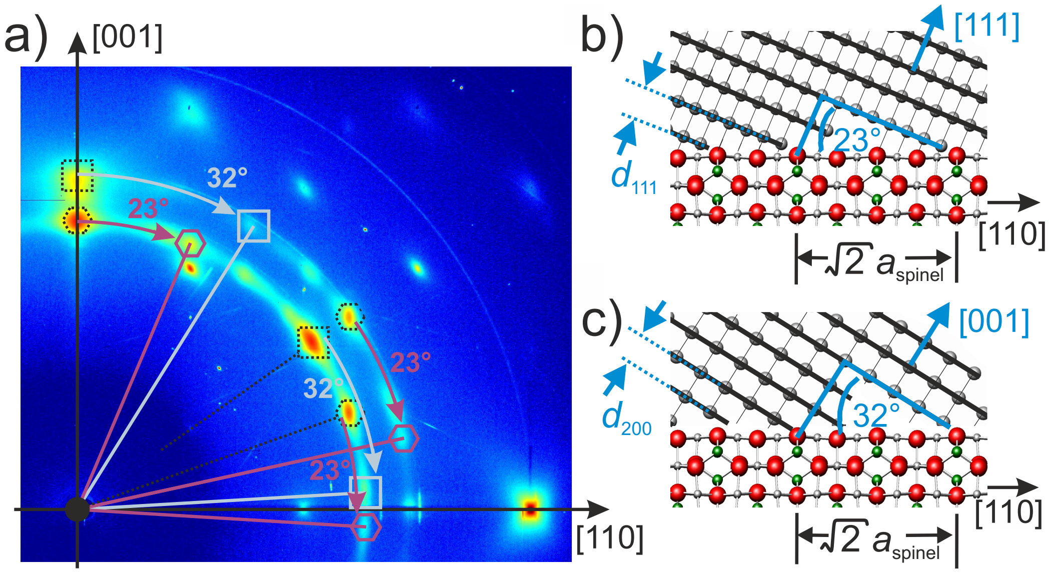

Figure 6.6: **Growth of tilted Pt particles on "spinel-3": a):** Bragg peaks from (111)-oriented particles rotated by 23° (purple hexagons), and from (001)-oriented particles rotated by 32° (grey squares) around the substrate [110]-direction; **b):** interface along the substrate [110]-direction for (111)-oriented particles rotated by 23°, and **c):** for (001)-oriented particles rotated by 32°.

shown for clarity once again in Fig. 6.6 a).

Fig. 6.6 b) shows the scenario for the tilted (111)-oriented particles: the tilt by 23° results in a match of the projection of their atomic row distances given by $\frac{d_{111}}{\sin(23°)}=\frac{3.9242}{\sqrt{3}\cdot\sin(23°)}$ Å onto the distances between substrate atomic rows $\frac{a_{\text{spinel}}}{\sqrt{2}}=\frac{8.086}{\sqrt{2}}$ Å along the substrate [110]-direction with a mismatch of -1.39%. In the same manner the tilt of the (001)-type particles results in a 3:2 match to the substrate: as is indicated in Fig. 6.6 c), the projection of every third particle layer along the particle [001]-direction, given by $\frac{d_{002}}{\sin(32°)}=\frac{3.9242}{2\cdot\sin(32°)}$ Å, corresponds to two diagonals of the substrate unit cell, given by $\frac{2}{3}\frac{a_{\text{spinel}}}{\sqrt{2}}=\frac{2}{3}\frac{8.086}{\sqrt{2}}$ Å, with a mismatch of 2.95%.

In the following, the growth characteristics found for particles with **different Pt-Rh compositions and/or particle sizes** will be discussed. Fig. 6.7 shows 2D maps measured on the different particle stripes of samples "spinel-2" and "spinel-3"[1] containing the same area of reciprocal space as discussed above for the pure Pt particles. The maps are sorted by particle size and composi-

---

[1] The map shown for the pure Pt particles of sample "spinel-2" and the correspondingly deduced particle values of Table 6.2 were not obtained as the others under Ar flow but during low activity conditions for CO oxidation at 1 $\frac{\text{ml}}{\text{min}}$ O$_2$ and 4 $\frac{\text{ml}}{\text{min}}$ CO, see section 7.4. Since the epitaxial relationship was found not to change during catalytic activity it is justified to present the map and the particle values deduced thereof.

tion, where the ones of sample “spinel-3”, placed along the second column, are marked by a red vertical line. The green horizontal lines indicate the maps measured on “core-shell” particles of a certain composition.

Despite the differing substrate pretreatments, particles of all sizes and compositions were found to grow on both samples predominantly in a (001)-type epitaxy as can be deduced from the intensity of the (111) Bragg peaks, which is the strongest in all cases. Independent of the particle composition, well-pronounced (111)- and (001)-type particle facet signals occur only for larger particles with a height and diameter of at least 50 Å and 90 Å, respectively. They testify the presence of (111)- and (001)-type facets and thus an octahedral particle shape. The smaller particles are likely to feature a rounder shape decorated by higher indexed facets and, as a consequence, the main facets are too small to yield distinct signals.
Already at a first glimpse it becomes obvious that the particles on sample “spinel-2” grew more well-ordered, since their reciprocal space maps display less pronounced powder rings compared to the maps measured on sample “spinel-3”. Moreover, peaks from the tilted particles discussed above, are only present in the maps of sample “spinel-3”, where their intensities were found to scale with Pt content. This implies that a substrate pretreatment as performed for sample “spinel-2”, characterized by repeated sputtering and annealing cycles at elevated temperature, promotes a more regular particle growth of the main (001)-type epitaxy and suppresses the growth of tilted particles.

Tables 6.2 and 6.3 summarize quantitative information on the different particle systems. The particle heights H and diameters D of the (001)-oriented particles were obtained from the full widths at half maximum (FWHMs) from fits to scans through the respective Bragg peaks. The particle aspect ratios $\frac{H}{D}$ vary between 0.51 and 0.71, with a tendency towards lower values for increasing Pt content and particle size. The data on the relative amount of particles growing with (111)- and (110)-type epitaxies and of internal twinning were obtained by integrating the peak intensities in out-of-plane scans running through the respective signals, and normalizing them to the integrated intensity of the corresponding (111) Bragg peak of the (001)-oriented particles of the same map. The numbers disclose that the particle epitaxies show dependencies on the particle composition and size, the substrate preparation and the particle deposition (“core-shell” vs. alloy particles).

The composition-dependence is characterized by Pt-rich particles having a

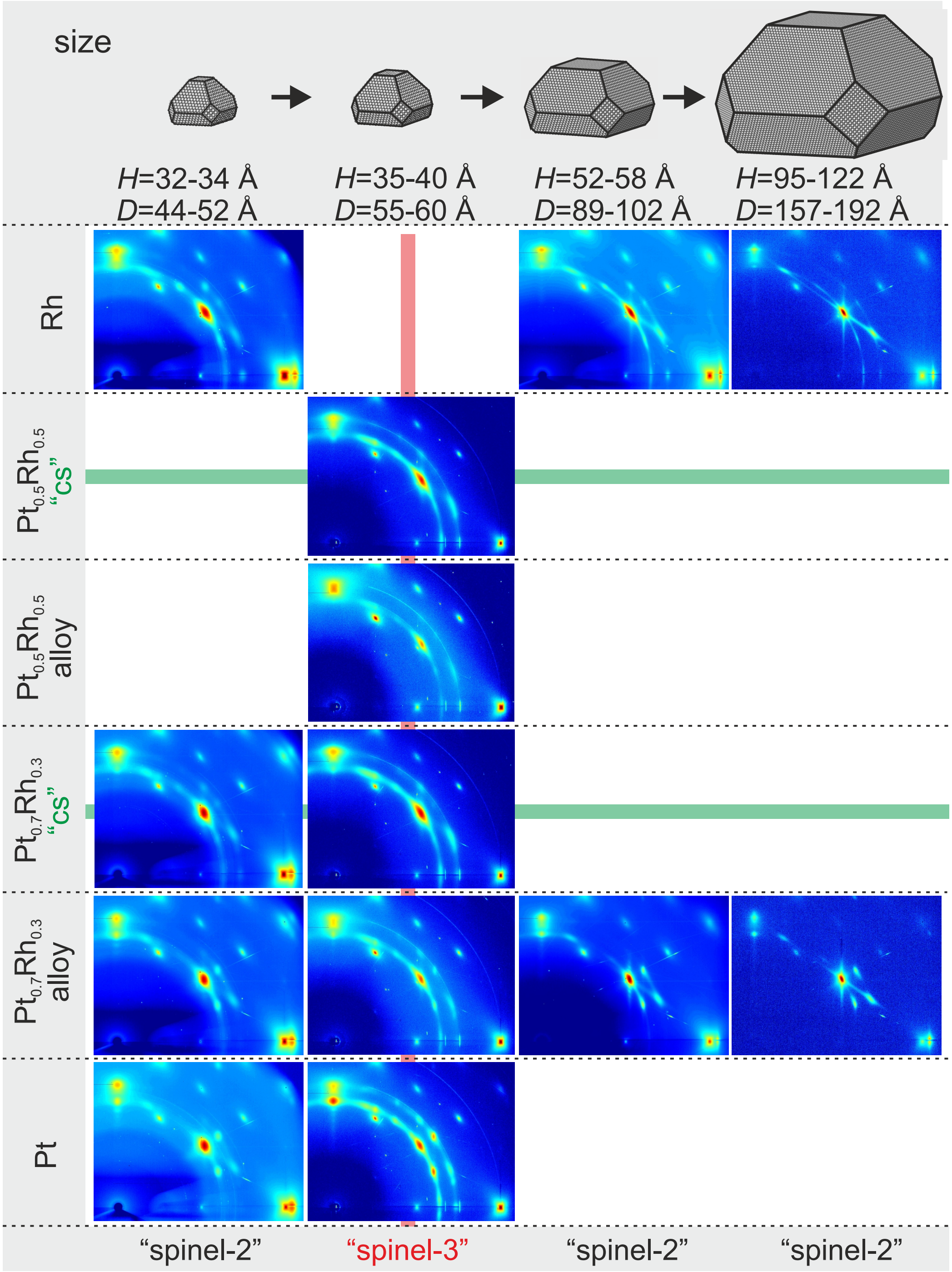

Figure 6.7: **Size- and composition-dependent growth of particles on the MgAl$_2$O$_4$(001)-based samples "spinel-2" and "spinel-3":** overview of high energy reciprocal space maps centered around the particle (111) Bragg peak of the predominant (001)-type epitaxy measured on the as-prepared particles of various Pt-Rh compositions and particles sizes. The maps of the second column belong to particles grown on sample "spinel-3", the maps of columns 1, 3 and 4 to particles of sample "spinel-2".

composition	***H*** [Å]	***D*** [Å]	***H/D***	**(111)**[%]	**(110)**[%]	**twin.**[%]
^{2}Pt	38	57	0.66	1.7	–	0.6
$^2Pt_{0.7}Rh_{0.3}$	34	52	0.65	2.1	1.5	1.5
$^2Pt_{0.7}Rh_{0.3}$	52	102	0.51	2.4	0.4	0.4
$^2Pt_{0.7}Rh_{0.3}$	95	157	0.61	0.4	0.0	0.1
^{2}Rh	32	44	0.73	1.3	3.1	3.1
^{2}Rh	58	89	0.65	0.7	1.4	1.3
^{2}Rh	122	192	0.64	0.0	0.2	0.2
^{3}Pt	40	56	0.71	44.1	6.1	11.1
$^3Pt_{0.7}Rh_{0.3}$	38	61	0.62	5.7	2.5	4.2
$^3Pt_{0.5}Rh_{0.5}$	37	60	0.62	4.7	1.0	5.2

Table 6.2: **Overview of parameters for monometallic and alloy particles:** the results for samples “spinel-2” (top) and “spinel-3” (bottom, see composition superscripts) are sorted by particle composition and/or size. The particle height H and diameter D were obtained by fitting linescans running through the respective Bragg peaks. The columns labeled “(111) [%]”, “(110) [%]” and “twin. [%]” refer to the percentage of integrated intensities obtained from linescans running through peaks from (111)-, (110)- oriented particles and from internal twinning signals compared to the corresponding integrated Bragg peak intensity from (001)-oriented particles of the same map. The error is on the order of 10%.

composition	***H*** [Å]	***D*** [Å]	***H/D***	**(111)**[%]	**(110)**[%]	**twin.**[%]
$^2Pt_{0.7}Rh_{0.3}$ “cs”	33	50	0.66	0.5	2.0	2.0
$^3Pt_{0.7}Rh_{0.3}$ “cs”	35	54	0.62	0.8	1.6	6.5
$^3Pt_{0.5}Rh_{0.5}$ “cs”	38	61	0.62	0.5	2.1	6.2

Table 6.3: **Overview of parameters for “core-shell” (“cs”) nanoparticles:** summarized results for “core-shell” particles of samples “spinel-2” and “spinel-3” (see composition superscripts). For more information see caption of Table 6.2.

high proportion of (111)-oriented particles, while Rh-rich particles favour the (110)-type epitaxy over the (111)-type epitaxy. A potential explanation for this composition-dependent growth behaviour are the relative surface energies of the particle facets (see Table 2.1 in section 2.3.1). Since in the case of Pt, the surface energy of the (111)-type facets is much lower than the ones of the (100)- and (110)-type facets, the epitaxy whose particle shape is dominated by (111)-type facets - namely the (111)-type epitaxy - is favoured. In the case of Rh-rich particles the (110)-type facets have a comparable low surface energy and accordingly the growth of (110)-oriented particles is favoured.

Table 6.2 moreover reveals that an increased amount of deposited material results in a reduction of internal twinning and of particles growing in a (111)- or (110)-type epitaxy.

The comparison of the upper and lower part of Table 6.2 - containing the respective results for samples “spinel-2” and “-3” - reveals in the case of “spinel-3’ an extremely high number of particles growing with non-cube-on-cube epitaxies and internal twinning. This can be due to the aforementioned lack of repeated sputtering and annealing cycles during substrate preparation.

The data moreover discloses that the choice of the deposition mode has a striking impact on the particle growth. This becomes obvious in the comparison of Tables 6.2 and 6.3, which contain the growth characteristics of alloy and “core-shell” nanoparticles of both samples. For Pt-rich “core-shell” nanoparticles the data reveal a comparatively low number of (111)-oriented and a high number of (110)- oriented particles and thus growth characteristics rather typical of pure Rh particles. This implies that seeding with Rh allows for tailoring the particle growth characteristics of particles towards the ones of Rh.

6.2 Growth on the α-Al_2O_3(0001) substrate

This section deals with the composition-dependent growth and morphology of α-Al_2O_3(0001)-supported Pt-Rh, Pt-Pd and Pd-Rh alloy nanoparticles. Schematic drawings of the studied combinatorial samples are shown in Fig. 6.8 which reveals that in the case of two samples (“alumina-1” and “alumina-3”) some particle compositions featured a size gradient in addition.

All samples discussed in this section were studied using grazing incidence high energy x-ray diffraction: samples “alumina-1” and “alumina-2” were investigated at the ‘High Energy Scattering Beamline ID15A’ at the ESRF at a photon energy of 78.7 keV; the other samples were studied at the 'High Energy Materials Science Beamline P07' at Petra III, employing a photon energy of either 78 keV ("alumina-3", "alumina-5") or 85 keV ("alumina-4"). More detailed information on the experimental setups and the experimental strategy can be found in subsections 5.3.2 and 8.1.1.

Details on the sample preparation

The treatment of the bare alumina substrates followed the same steps as discussed earlier for $MgAl_2O_4(001)$, yet any sputtering and annealing cycles were omitted. The general steps are summarized in Fig. 6.9.

For some samples the treatment slightly deviated from this common scheme: after thermal cracking and prior to particle deposition the substrates of samples "alumina-2" and "alumina-5" were exposed to pressures in the 10^{-8} mbar range. This may have resulted in the hydroxylation of the α-$Al_2O_3(0001)$-substrates which may greatly alter the particle growth (see section 2.4.1). The substrate preparation also slightly differed for samples "alumina-1" and "alumina-4": they were not flashed to higher temperatures prior to thermal cracking. The individual differences in the substrate preparation procedure are summarized in Table 6.4 and are indicated in Fig. 6.9.

For all samples the particles were deposited by means of physical vapour deposition of Pt and Rh at a substrate temperature of 803 K, where the respective fluxes were set according to the desired alloy composition. The particle stripes were either grown along the substrate's $[1\bar{2}10]$-direction (samples "alumina-1" and "alumina-5") or along its $[10\bar{1}0]$-direction (samples "alumina-2", "alumina-3" and "alumina-4"). As will be pointed out in the next subsection this allowed for either probing the particle $(3\bar{1}1)$ or $(11\bar{1})$ Bragg peak, respectively.

After preparation, samples "alumina-1", "-2", "-3" and "-5" were transported through air and mounted inside the in-situ catalysis chamber. The samples underwent a one hour lasting annealing (employed temperatures: "alumina-1": 543 K; "alumina-2": 493 K; "alumina-3" and "alumina-5": 653 K) in 2×10^{-5} mbar hydrogen in order to remove potential oxides from the particles.

The measurements presented in this section were performed before CO oxidation and thus yield information on the composition-, size- and substrate treatment-dependent particle growth. In the case of samples "alumina-1" and "alumina-2" the data presented in this section were obtained under CO flow (p_{tot}=200 mbar; $f_{\mathrm{tot}}=100\ \frac{\mathrm{ml}}{\mathrm{min}}$; $f_{\mathrm{CO}}=2\ \frac{\mathrm{ml}}{\mathrm{min}}$; $f_{\mathrm{Ar}}=98\ \frac{\mathrm{ml}}{\mathrm{min}}$; T=573 K), in the case

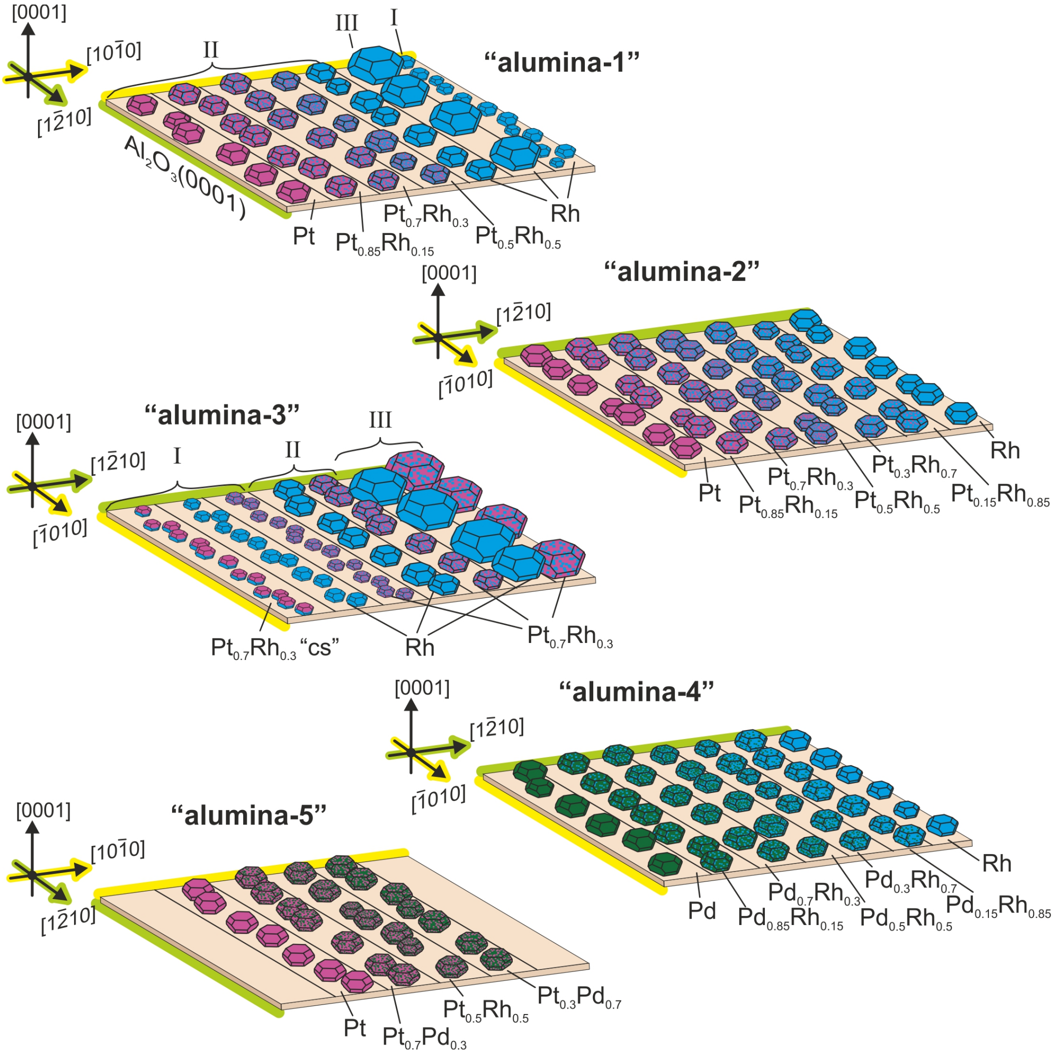

Figure 6.8: **Overview of α-Al$_2$O$_3$(0001)-based samples: "alumina-1":** combinatorial sample containing equally-sized (II) particles with a composition-gradient in Pt-Rh and particles with a size gradient in Rh (sizes I, II and III); **"alumina-2":** equally-sized particles with a gradient in Pt-Rh composition; **"alumina-3":** particles of pure Rh and Pt$_{0.7}$Rh$_{0.3}$ composition (alloy and "core-shell") of three different size regimes (I, II and III); **"alumina-4":** equally-sized particles with a gradient in Pd-Rh composition; **"alumina-5":** equally-sized particles with a gradient in Pt-Pd composition. The particle stripes where either grown along the [1$\bar{2}$10]-direction ("alumina-1", "alumina-5") or the [10$\bar{1}$0]-direction ("alumina-2", "alumina-3", "alumina-4") of the α-Al$_2$O$_3$(0001)-substrate as is indicated by the respective substrate coordinate systems.

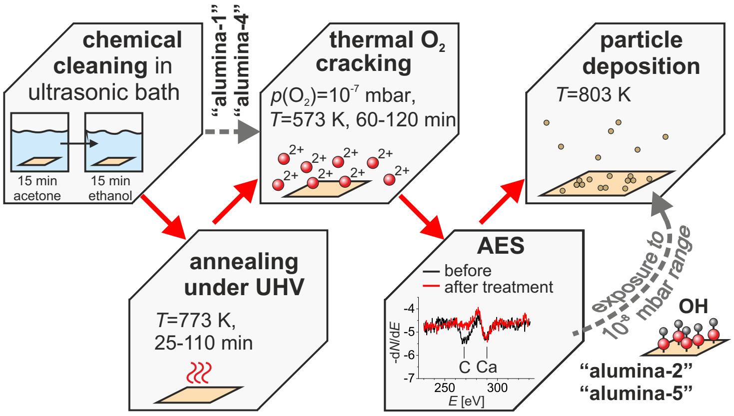

Figure 6.9: **Substrate pretreatment of α-Al$_2$O$_3$(0001)-based samples:** the general steps are indicated by red arrows; deviations are indicated by dashed grey arrows (see also Table 6.4).

sample “alumina-	**flashed prior to cracking**	**exposed to 10^{-8} mbar**	**further remarks on the particle deposition**
-1”	no	no	→ Pt-rich particles were deposited first (total deposition time: t_{tot}=415 min)
-2”	yes	yes	→ Rh-rich particles were deposited first (t_{tot}=400 min) → flashing prior to cracking under 10^{-5} mbar O_2
-3”	yes	no	→ deposition (t_{tot}=737 min) started with larger particles → deposition in two steps because of “core-shell” nanoparticles (see text)
-4”	no	no	→ deposition (t_{tot}=389 min) started with Rh-rich particles at slightly lower temperature T=793 K
-5”	yes	yes	→ deposition (t_{tot}=550 min) in two steps (1st step: $Pt_{0.3}Pd_{0.7}$, $Pt_{0.7}Pd_{0.3}$; 2nd step: $Pt_{0.5}Pd_{0.5}$, Pt)

Table 6.4: **Differences in the substrate preparation of α-Al$_2$O$_3$(0001)-based samples:** the table summarizes deviations from the general sample preparation procedure depicted in Fig. 6.9. The samples are sketched in Fig. 6.8.

of samples "alumina-3" and "alumina-5" under Ar flow (p_{tot}=50 mbar; f_{tot}=50 $\frac{\mathrm{ml}}{\mathrm{min}}$; f_{CO}=4 $\frac{\mathrm{ml}}{\mathrm{min}}$; f_{Ar}=46 $\frac{\mathrm{ml}}{\mathrm{min}}$; T=648 K). Contrary, sample "alumina-4" was not mounted inside the catalysis chamber but was simply measured in air and at room temperature.

Composition-dependent growth of α-Al$_2$O$_3$(0001)-supported Pt-Rh particles (samples "alumina-1" and "alumina-2")

In this section the results of the growth of Pt-Rh particles on samples "alumina-1" and "alumina-2" will be discussed.

Their adjacent particle stripes were characterized by a progressive gradient in Pt-Rh composition (see schematic drawing in Fig. 6.8), where for each stripe the same amount of material was deposited. This was confirmed by x-ray reflectivity measurements which revealed in each case an initial particle height of 21±3 Å and a percentaged coverage of 50-60%. Sample "alumina-1" contained in addition two stripes of pure Rh particles with slightly larger (H_{XRR}=24 Å) and smaller (H_{XRR}=15 Å) particles, which will in the following be denoted by "L" and "S", respectively. The reflectivity data and the fit results are represented in black colour and can be found in Fig. 8.3 in subsection 8.1.1 and Fig. 6.23 in the appendix to this chapter.

In the case of sample "alumina-1" the stripes were grown along the $[1\bar{2}10]$-direction of the substrate, in the case of sample "alumina-2" along the perpendicular $[10\bar{1}0]$-direction. In order to fulfill the scattering condition, the particle stripes were rotated with respect to the incoming x-ray beam by the in-plane scattering angle θ, which was due to the use of high energies very small (on the order of 3°) and allowed the collimated x-ray beam for still illuminating the whole length of the stripe. Since the $\boldsymbol{Q}$-vector thus probed the direction perpendicular to the respective stripe direction, this resulted in mapping the substrate $(10\bar{1}0, L)$-plane in the case of sample "alumina-1", and the $(1\bar{2}10, L)$-plane in the case of "alumina-2".

Fig. 6.10 b) and c) show the thus monitored 2D maps measured on the as-prepared Pt particles on samples "alumina-1" and "alumina-2". Apart from peaks that can be traced back to the α-Al$_2$O$_3$(0001) substrate, reflections are present whose pattern can be explained by the coexistence of four domains of (111)-oriented particles. The orientation of their corresponding unit cells with respect to the unit cell of the substrate is depicted in Fig. 6.10 a) along with the resulting in-plane reciprocal space map. The particles of domains I and II

Pt	**$Pt_{0.85}Rh_{0.15}$**	**$Pt_{0.7}Rh_{0.3}$**	**$Pt_{0.5}Rh_{0.5}$**	**Rh**
1.29%	1.03%	0.55%	0.20%	0.77%

Table 6.5: **Composition-dependent Bragg peak intensities from particles of domain IV:** the numbers represent the relative intensities of domain IV compared to the ones of the particle $(3\bar{1}1)$ peak (domains I and II) as found for particles on sample **"alumina-1"**. In each case the respective background was subtracted.

grow both in a $(\sqrt{3}\times\sqrt{3})R30°$ relation to the substrate. The particles of domain II are rotated with respect to the particles of domain I by 60° around the substrate normal, which corresponds to an inversion of the internal ABCABC stacking to CBACBA for domain II particles. Particles of domains III and IV correspond to particles of domains I and II, respectively, but rotated by 90° around the surface normal.

Fig. 6.10 b) and c) disclose that the intensities of the Pt peaks belonging to domains I and II are much higher than the ones of domains III and IV. Fig. 6.20 in the appendix to this chapter reveals that this tendency also holds true for the other probed Pt-Rh compositions.

An explanation for the particles' **preference to grow in domains I and II** over III and IV can be found in their good match of both, the orientation and distance of the particle atomic rows, with respect to the ones of the substrate. Fig. 6.10 a) illustrates this by the straight blue and green lines and the values d_1 and d_2, which denote the respective atomic row distances of the particles. In the case of domain I the distance $d_1 = \frac{a_{\mathrm{par}}}{\sqrt{2}} \cdot \frac{\sqrt{3}}{2}$ matches the substrate row distance corresponding to half of the substrate unit cell $\frac{a_{\mathrm{Al2O3}}}{2}$ along the $[10\bar{1}0]$-direction. For domain II the distance $d_2 = \frac{a_{\mathrm{par}}}{2}$ corresponds to twice the distance of Al- or O-ions given by $\frac{a_{\mathrm{Al2O3}}}{\sqrt{3}}$ along the $[1\bar{2}10]$-direction. According to the lattice constant literature values (a_{Pt}=3.9242 Å, a_{Rh}=3.8013 Å, and a_{Al2O3}=4.763 Å) and under consideration of Vegard's rule, the lattice mismatches for domains I and II of the various Pt-Rh compositions were estimated to comprise 0.91% (Pt), 0.43 % ($Pt_{0.85}Rh_{0.15}$), -0.04% ($Pt_{0.7}Rh_{0.3}$), -0.67% ($Pt_{0.5}Rh_{0.5}$), -1.31% ($Pt_{0.3}Rh_{0.7}$), -1.78% ($Pt_{0.15}Rh_{0.85}$) and -2.25% (Rh). Contrary, for the particles of **domains III and IV** there is no good match between the distances of the particle and the substrate atomic rows. Their presence can only be explained by the orientation of the particle atomic rows, which run along the ones of the substrate as is indicated by the purple and orange lines in Fig. 6.10 a). Table 6.5 summarizes the relative Bragg peak

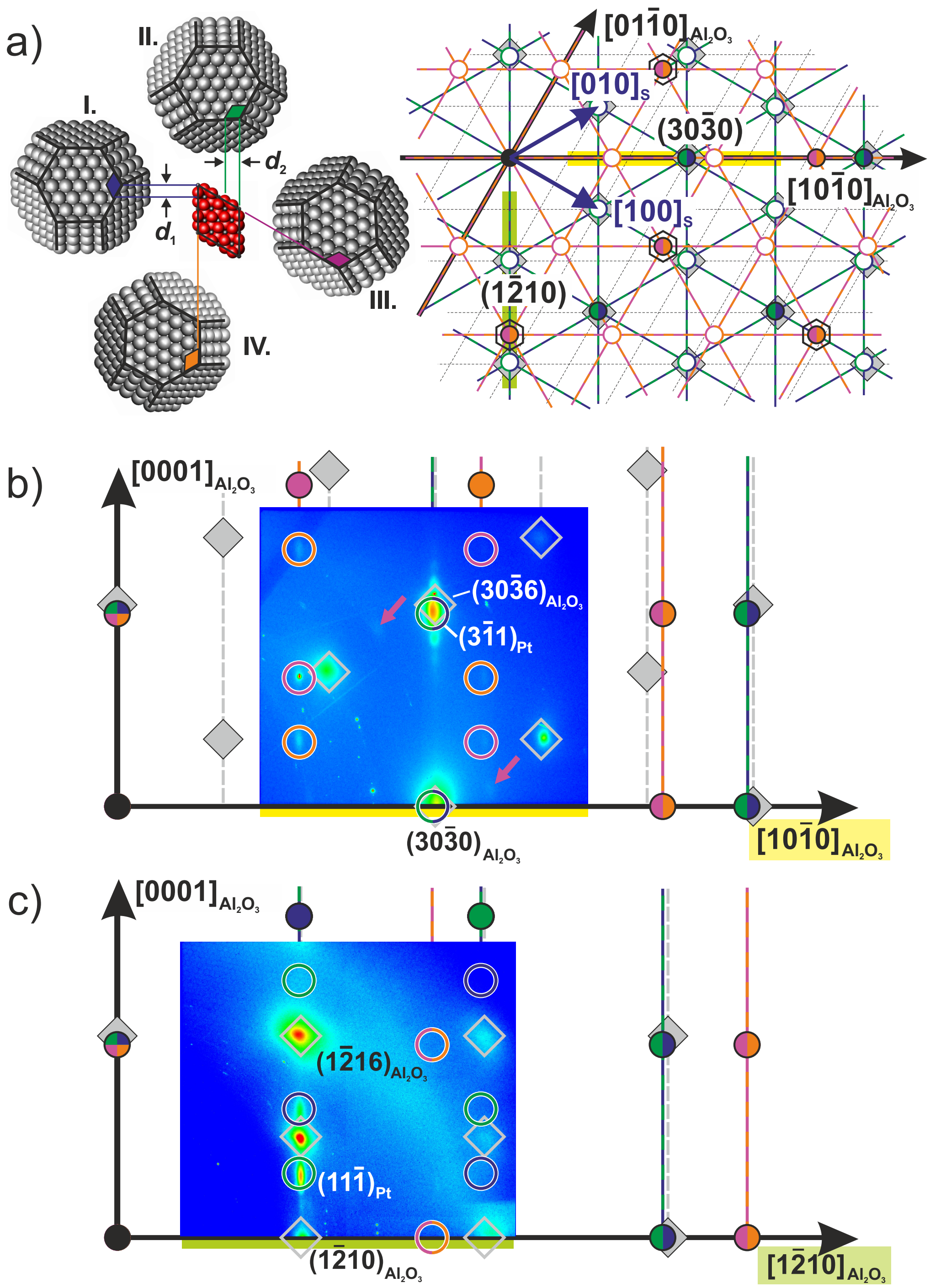

Figure 6.10: **Reciprocal space maps for domains of (111)-oriented particles on α-$\mathbf{Al_2O_3}$(0001): a):** sketch of the four possible domains and orientation of their unit cells to the one of α-Al$_2$O$_3$(0001). They give rise to the in-plane Bragg peak pattern shown on the right; filled and opened circles: respective positions of particle Bragg peaks and rods of the correspondingly coloured domains; grey diamonds: substrate Bragg peak positions; **b):** substrate $(10\bar{1}L)$-plane and 2D map of the Pt particles on "alumina-1", purple arrows indicate peaks from particles tilted by 35°; **c):** substrate $(1\bar{2}1L)$-plane and 2D map of the Pt particles on "alumina-2"; some indicated peaks are not discernible, probably due to misalignment in θ.

sample	**x=1**	**x=0.85**	**x=0.7**	**x=0.5**	**x=0.3**	**x=0.15**	**x=0**
“-1”	0.27%	0.24%	0.24%	0.24%	–	–	1.23%
“-2”	2.77%	1.17%	1.54%	3.60%	5.70%	10.07%	11.91%

Table 6.6: **Composition-dependent Bragg peak intensities from tilted (111)-oriented $\mathbf{Pt_xRh_{x\text{-}1}}$ particles on samples “alumina-1” and “-2”:** the numbers represent the relative intensities of the Bragg peaks from tilted particles to the ones of the particle $(3\bar{1}1)$ peak (in case of sample “-1”) or the particle $(11\bar{1})$ Bragg peak (in case of sample “-2”). In each case the respective background was subtracted.

intensities from particles belonging to domain IV to the ones of the respective $(3\bar{1}1)$ Bragg peak of domains I and II. Their numbers appear to be especially low for Pt-Rh compositions that are characterized by a small mismatch to the substrate lattice. This implies that for these compositions particle growth as domains I and II was favoured in particular.

The data suggest that the composition-dependent lattice mismatch controls the number of (111)-oriented **particles that grow tilted** with respect to the substrate normal. Bragg peaks that can be traced back to the existence of these particles are in the maps of Fig. 6.10 b), c) and Fig. 6.12 indicated by purple arrows. As is shown in the appendix to this chapter, this tilt comprises about 35° around the substrate $[1\bar{2}10]$-direction (probed in the $(10\bar{1}, L)$-plane of sample “alumina-1”) and approximately 30° around the substrate $[10\bar{1}0]$-direction (probed in the $(1\bar{2}1L)$-plane of sample “alumina-2”), where the driving force in both cases can be found in the fact that the projection of the rotated atomic rows onto the surface plane matches the substrate atomic rows (rotation around the $[1\bar{2}10]$-direction: $\frac{d_{111}}{\sin(35^\circ)} \approx \frac{\sqrt{3}}{2} a_{\mathrm{Al2O3}}$; rotation around the $[10\bar{1}0]$-direction: $\frac{d_{111}}{\sin(30^\circ)} \approx a_{\mathrm{Al2O3}}$). Hence, the same epitaxy mechanism that was found for the growth of Pt-Rh particles on $MgAl_2O_4(001)$ (see section 6.1) also holds for the growth on α-$Al_2O_3(0001)$. Table 6.6 yields for both samples the relative intensities of Bragg peaks from tilted particles with respect to the ones of the main Bragg peaks of domains I and II, which are the $(3\bar{1}1)$ peaks in the case of the 2D maps measured on sample “alumina-1” and the $(11\bar{1})$ peaks in the case of the maps of sample “alumina-2”. These relative peak intensities disclose that the number of tilted particles strongly increases with rising Rh content as can also be inferred from Fig. 6.12. The smallest number of tilted particles can be found for Pt-Rh compositions with a small particle-substrate lattice mismatch.

The following paragraphs will deal with the **composition-dependent detailed shape and structure characteristics** of the non-tilted and (111)-oriented particles that grew as domains I and II which, as was discussed above, comprised the vast majority of the particles on sample "alumina-1" and "alumina-2".

Qualitative information can be obtained by looking at the shapes of the respective particle Bragg peaks. The corresponding close-ups on the $(3\bar{1}1)$ peaks in the case of "alumina-1" and on the $(11\bar{1})$ peaks in the case of "alumina-2" are shown for the probed Pt-Rh compositions in Fig. 6.11 and 6.12, respectively. It is striking that the peaks of the Pt-rich particles reveal in the case of both samples very pronounced Laue oscillations. Their presence indicates an almost layer-like particle growth characterized by particles with an internal crystalline perfectness and a rather small out-of-plane size distribution and/or surface roughness. This is underpinned by the x-ray reflectivity data which disclose strong Kiessig oscillations for Pt-rich particles (see Fig. 8.3 in section 8.1.1). With increasing Rh content, they become progressively damped, which is mirrored in the fit results by a particle surface roughness that scales as a function of Rh content. Since the distances of the Laue oscillations to the respective Bragg peaks are approximately the same for all Pt-Rh compositions, comparable particle heights can be assumed for the as-prepared particles. This was confirmed by the fit results of the reflectivity measurements which suggest an initial particle height of 21±3 Å for all Pt-Rh compositions on both samples (see Fig. 8.3 and Fig. 6.23).

It can be inferred from Figs. 6.11 and 6.12 that the higher the Rh content inside the particles (1) the weaker are the Laue oscillation signals, (2) the more tilted are the shapes of the $(11\bar{1})$ Bragg peaks along the direction of the respective Debye Scherrer rings (the orange-dotted lines in Fig. 6.12 act as guides to the eye) and (3) the higher is the peak intensity from particles tilted by 30° (indicated by purple arrows in Fig. 6.12), implying that their number scales with Rh content. These findings are in line with the aforementioned more pronounced tendency of Rh-rich particles to undergo rotation in order to compensate for the larger lattice mismatch to the substrate unit cell.

In contrast to calculations for Pt-Rh bulk alloys predicting a miscibility gap below 1033 K, the present data suggest well-mixed alloy particles over the whole Pt-Rh composition range. This can be inferred from the respective

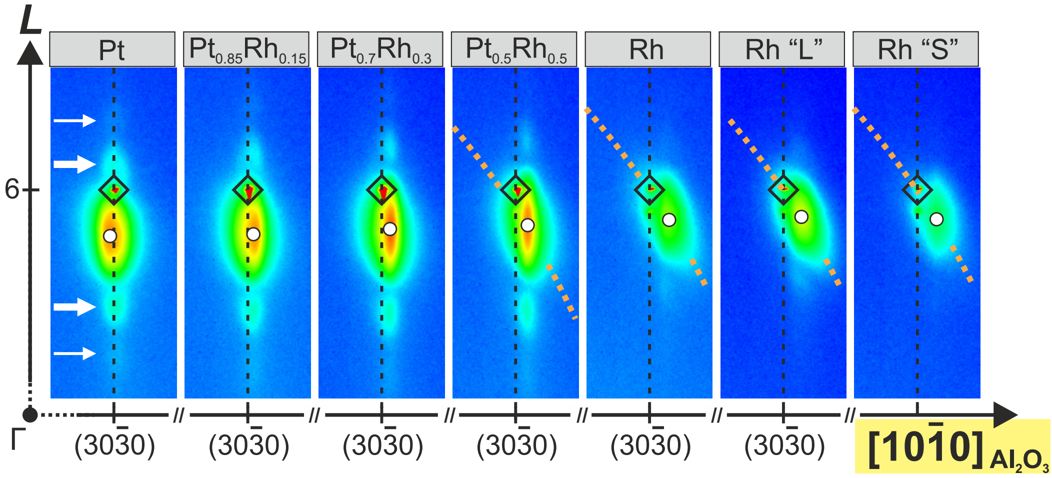

Figure 6.11: **Pt-Rh $(3\bar{1}1)$ Bragg peaks monitored on sample "alumina-1":** white circles represent the respective positions of the main maxima of the particle Bragg peaks for the various Pt-Rh compositions; black diamonds and black vertical dotted lines indicate the positions of the substrate $(30\bar{3}6)$ Bragg peak and the $(30\bar{3}L)$ substrate rods, respectively. White arrows denote particle Laue oscillations; orange circle segments the potential position of Debye Scherrer rings.

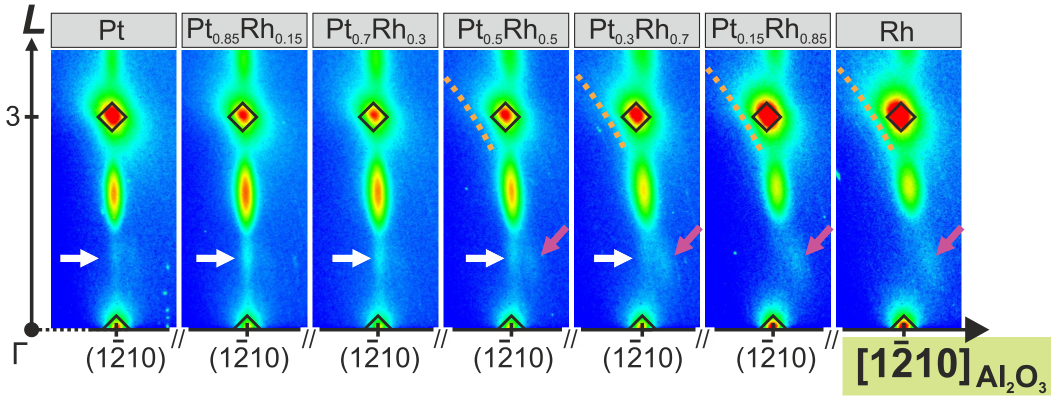

Figure 6.12: **Pt-Rh $(11\bar{1})$ Bragg peaks monitored on sample "alumina-2":** white arrows indicate the pronounced particle Laue oscillations present for Pt-rich particles; purple arrows and orange dotted circle segments denote the presence of signals from tilted particles and particle out-of-plane mosaicity, respectively, which become both progressively dominant with increasing Rh-content. Black diamonds represent substrate Bragg peak positions.

positions of the Bragg peak's main maxima indicated by white circles in the reciprocal space maps shown in Fig. 6.11: with increasing Rh-content they progressively move towards higher Q-values and thus smaller lattice parameters. No Bragg peak splitting, which would suggest phase separation, can be distinguished. These findings justify the aforementioned discussion concerning the composition-dependent lattice misfits based on Vegard's law.

The following paragraphs will deal with the composition-dependent **quantitative particle height-to-diameter aspect ratios** that were deduced by combining data obtained from the analysis of the particle Bragg peaks shown in Figs. 6.11 and 6.12, θ-scans, x-ray reflectivity and AFM measurements, the results of which are summarized in Fig. 6.13.

Fig. 6.13 a) reveals that the as-prepared particles on both samples comprised the same heights independent of the Pt-Rh composition, where the results deduced from the full widths at half maximum (FWHMs) of the respective particle Bragg peaks (filled circles) are in good agreement with the reflectivity data (crosses). The systematic deviation towards smaller values found in the reflectivity results is due the underlying box model used in the fitting procedure, which is not sensitive to the particle shape. As expected, the pure Rh particles of sample "alumina-1" denoted by "L" and "S" were found to be higher ("L") and lower ("S") since in the case of these stripes more and less material was deposited, respectively.

Contrary to the particle heights, a highly pronounced composition-dependence was found for the respective diameters (see Fig. 6.13 b)). In the case of pure Rh particles, they comprised on both samples only about 55 Å and were found to steadily increase as a function of Pt-content, peaking at a value of about 90 Å in the case of the pure Pt particles on sample "alumina-2" and of even 125 Å in the case of the Pt particles on "alumina-1".

The discrepancies in the diameter values of the Pt-rich particles on the two samples can be explained by deviations during sample preparation: material deposition started on sample "alumina-1" with the pure Pt stripe and progressively moved towards the stripes with higher Rh-composition; contrary, on "alumina-2" the Pt particles were the last ones to be deposited (see also Table 6.4). Thus, the total annealing time was shorter in the case of the Pt-rich particles on "alumina-2" (1 vs. 15 hours) and they may accordingly have undergone less sintering during growth.

Furthermore, while the diameter values of sample "alumina-1" were obtained

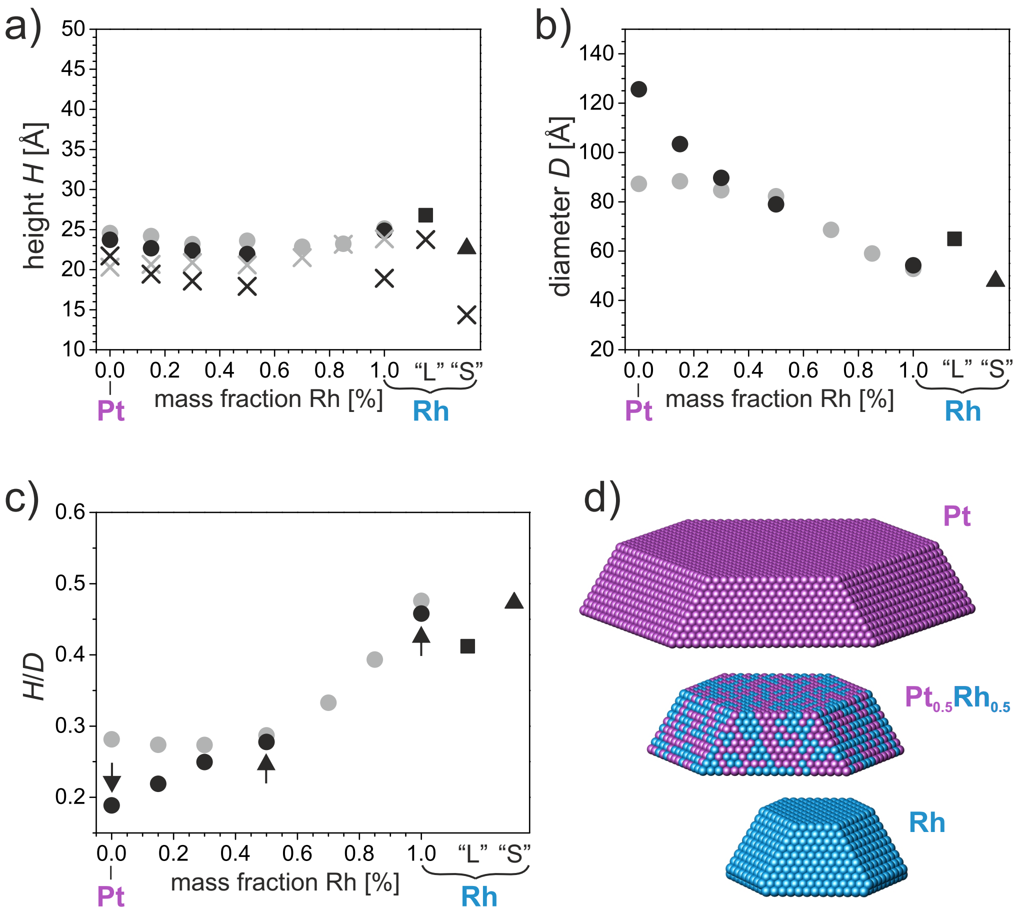

Figure 6.13: **Composition-dependent sizes of (111)-oriented Pt-Rh particles of the main domains (I and II) on "alumina-1" and "alumina-2":** black symbols represent data from sample "alumina-1", grey symbols from sample "alumina-2"; the data points denoted by "L" ("S") refer to pure Rh particles on sample "alumina-1" in the case of which slightly more (less) material was deposited compared to all other particle stripes; **a):** particle heights as deduced from particle Bragg peaks (circles, squares and triangles) and from x-ray reflectivity data (crosses); **b):** particle diameters; for sample "alumina-1" the data represented by circles was obtained from AFM measurements performed after the CO oxidation experiment; for all particle stripes of sample "alumina-2" and the larger and smaller pure Rh particles (represented by squares and triangles) of sample "alumina-1" the data was obtained from the particle Bragg peak analysis; **c):** particle aspect ratios $\frac{H}{D}$ as obtained from the data shown as closed symbols in a) and b); **d):** Wulff-construction of Pt, $Pt_{0.5}Rh_{0.5}$ and Rh particles of sample "alumina-1", indicated by arrows in c), based on the heights and diameters of a) and b) neglecting higher indexed particle facets and assuming a surface energy ratio of $g=\frac{\gamma_{100}}{\gamma_{111}}=1.1$ for the (100) and (111)-type particle facets (see section 8.1.2 for more information on the quantitative particle shape analysis).

by combining results from rocking scan and AFM measurements (see Appendices A.2 and A.3, respectively, at the end of this thesis) the values of sample "alumina-2" were deduced from the full widths at half maximum (FWHMs) of the respective Bragg peaks along the in-plane direction. In the case of sample "alumina-2", the FWHM analysis is justified as the Q-value of the particle $(11\bar{1})$ peak is lower compared to the one of the $(3\bar{1}1)$ peak probed on sample "alumina-1". Thus, strain broadening effects due to particles grown commensurately on the alumina-substrate are negligible (see also Appendix A.1). However, the thus obtained diameter values still constitute a lower limit for the average particle diameters, where the deviation from the real value was estimated to be on the order of 5 Å.

Fig. 6.13 c) shows the composition-dependent particle height-to-diameter aspect ratios $\frac{H}{D}$ of samples "alumina-1" and "alumina-2" based on the respective particle heights and diameters of a) and b), which range from 0.2 in the case of pure Pt to almost 0.5 in the case of pure Rh particles. Fig. 6.13 d) reveals the corresponding particle shapes based on the Wulff-construction shown for some selected Pt-Rh compositions of sample "alumina-1". They illustrate how the particle shape scales with Rh content, ranging from flat, disk-like Pt particles with very large diameters to more 3-dimensional and compact Rh particles. These quantitative findings are in line with the previously discussed particle Bragg peak shapes shown in the maps of Figs. 6.11 and 6.12, which only display strong Laue oscillations in the case of Pt-rich particles, suggesting flat and layer-like particle structures.

An explanation for the composition-dependent particle shapes can be found in the respective mismatch of the particle lattice to the one of the substrate, which is as discussed above, smaller for Pt-rich particles, and has its minimum for particles with a composition of 70% Pt and 30% Rh. The lattice mismatch creates a strain field at the interface which costs energy and which scales with the misfit [10]. For large misfits it may become energetically unfavourable to sustain large interface regions, resulting in smaller particle diameters.

Another reason for the differing particle shapes can be found in the respective surface energies of the catalyst materials. They are smaller in the case of Pt [25], which in general increases the tendency for layer-by-layer growth [10] and accordingly for larger, disk-like particles.

Apart from the composition-dependence discussed so far, the data also revealed a size-dependence for the particle shapes: the results of pure Rh particles of differing sizes grown on sample "alumina-1" suggest that the aspect ratio $\frac{H}{D}$ becomes smaller the more material is deposited, indicating that larger Rh particles are more disk-like, although their $\frac{H}{D}$-values are far from the ones of monometallic Pt particles. The next subsection on the particles on sample "alumina-3" will give more insight into how particles shapes scale with size.

Size-dependent growth of α-Al_2O_3(0001)-supported $Pt_{0.7}Rh_{0.3}$ and Rh particles (sample "alumina-3")

While the previous subsection focused on the growth of equally-sized particles that differed in Pt-Rh composition (samples "alumina-1" and "-2"), this subsection will deal with the size-dependent growth of particles with two distinct compositions, $Pt_{0.7}Rh_{0.3}$ and pure Rh (sample **"alumina-3"**, see also the systematic sketch in Fig. 6.8).

They were chosen to allow for a negligible ($Pt_{0.7}Rh_{0.3}$) and for the largest possible (Rh) lattice mismatch in the Pt-Rh system to the α-Al2O3(0001) substrate (see Table 2.2 in subsection 2.4.1). For both compositions, particles of three different size regimes (I-III) were studied, for each of which the same amount of material was deposited. In the case of size regime I, $Pt_{0.7}Rh_{0.3}$ "core-shell" particles, i.e. particles grown by the sequential deposition of Rh and Pt (see first subsection in section 6.1), were present in addition to the $Pt_{0.7}Rh_{0.3}$ alloy and pure Rh particles. The particle sizes within regime I were comparable to the ones of the previously discussed samples "alumina-1" and "-2".

The particle stripes were deposited along the substrate $[10\bar{1}0]$-direction (see Fig. 6.8), thus enabling to monitor the $(1\bar{2}10$, L)-plane including the particle $(11\bar{1})$ and (111) Bragg peaks of domains I and II. The respective 2D maps aligned on the $(11\bar{1})$ peak and sorted by composition and size are depicted in Fig. 6.14.

The maps disclose that in all cases the particle Bragg peaks belonging to the (111)-oriented particles growing in **domains I and II** are of highest intensity, thus, these particles were also predominant on sample "alumina-3". In the following their composition- and size-dependent particle aspect ratios will be discussed. They are summarized in Fig. 6.15 and are based on the analysis of the FWHMs of the respective $(11\bar{1})$ Bragg peaks. This approach is feasible since strain broadening can be neglected due to the peak's rather small Q-value (see discussion in Appendix A.1). The thus obtained values represent the heights and diameters of the coherently scattering domain sizes which, as

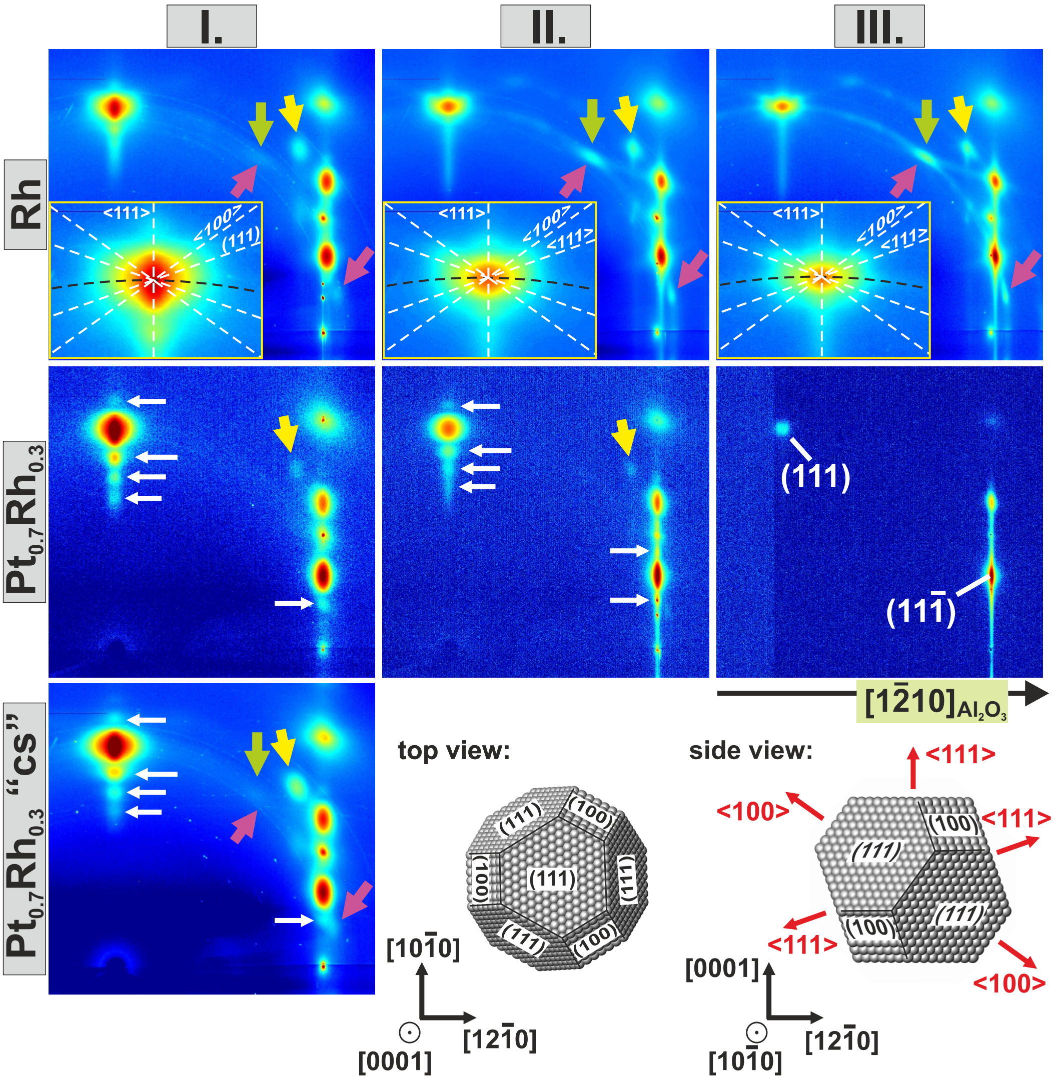

Figure 6.14: **Maps of Rh, Pt$_{0.7}$Rh$_{0.3}$ alloy, and Pt$_{0.7}$Rh$_{0.3}$ core-shell ("cs") particles of varying size (sample "alumina-3"):** they show the substrate (1$\bar{2}$1L)-plane including the particle (11$\bar{1}$) and (111) Bragg peaks; roman numbers indicate the three different particle size regimes (I: H=25-35 Å, D=50-60 Å; II: H=35-50 Å, D=100-160 Å; III: H=50-65 Å, D=160-270 Å; see also Fig. 6.15); additional signals to the ones discussed in Fig. 6.10 can be traced back to particle Laue oscillations (white arrows), (110)-oriented particles (yellow arrows), (111)-oriented particles tilted by 30° (purple arrows); the peaks indicated by purple *and* green arrows may not only be traced back to tilted particles but also to internal twinning. **Insets:** close-ups of the Rh particle (111) Bragg peaks indicating potential signals of (100)- and (111)-type particle facets (white dashed lines) and mosaicity peak broadening (black dashed lines). **Bottom:** orientation of particles belonging to the main domains of (111)-oriented particles (I+II; shown here: domain II) with respect to the substrate coordinate system.

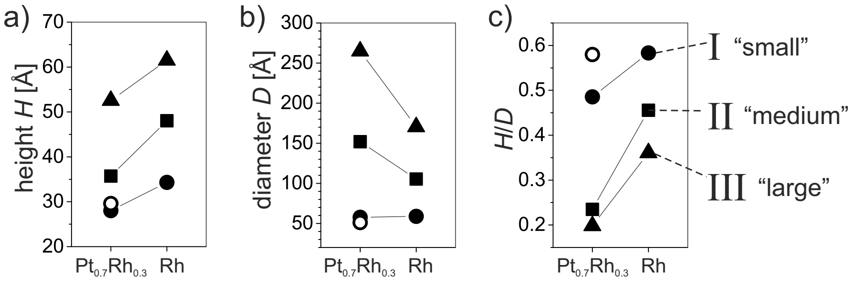

Figure 6.15: **Size- and composition-dependent particle aspect ratios of the particles grown on sample "alumina-3":** data from the Rh and $Pt_{0.7}Rh_{0.3}$ particles of the three size regimes I ("small"), II ("medium") and III ("large") are represented by circles, squares and triangles; data from the "core-shell" particles of size regime I are denoted by open circles. All data were obtained from analyzing the respective particle $(11\bar{1})$ Bragg peaks and thus denote the sizes of the coherently scattering domain sizes; **a):** particle heights; **b):** particle diameters; **c):** aspect ratios $\frac{H}{D}$ as obtained from the data shown in a) and b).

can be deduced from the SEM images shown in Fig. 8.17 in section 8.1.6, agree in the case of size regimes I and II well with the actual values of the respective particle dimensions.

In agreement with the findings for samples "alumina-1" and "-2", Fig. 6.15 a) and b) disclose that the heights of the $Pt_{0.7}Rh_{0.3}$ particles were lower, while the respective diameters were larger compared to the ones of the pure Rh particles. The aspect ratios $\frac{H}{D}$ shown in Fig. 6.15 c) were accordingly smaller for $Pt_{0.7}Rh_{0.3}$ than for pure Rh particles. These tendencies were found to scale with the amount of deposited material and thus with particle size.

The above results are in line with the corresponding particle Bragg peak shapes, as can best be inferred from the respective (111) peaks. In the case of the $Pt_{0.7}Rh_{0.3}$ alloy particles, the shape is characterized by distinct Laue oscillations, indicating rather disk-like particles with negligible side facets, characterized by internal crystallinity and a rather small misfit to the substrate. Contrary, in the case of Rh, the Bragg peak signals from (100)- and (111)-type particle facets are discernible, indicating a rather roundish particle shape in the case of which not only the top but also the side facets are well constructed. Also here, the composition-dependent growth behaviour can most likely be traced back to the smaller misfit and the lower surface energies in the case of Pt-containing particles, and it is found to scale even more with particle size.

Contrary to the samples discussed in the previous subsection, **hydroxylation** of the α-$Al_2O_3(0001)$-substrate prior to particle deposition **can be excluded**

peak	**$Pt_{0.7}Rh_{0.3}$ "cs" I**	**Rh I**	**Rh II**	**Rh III**
(110) [%]	7.74%	2.42%	1.00%	0.50%
tilt. [%]	2.82%	1.42%	0.61%	0.46%
twin. [%]	0.71%	0.38%	0.68%	0.63%

Table 6.7: **Comparison of peak intensities from (110)-oriented ("(110) [%]") and tilted ("tilt. [%]") particles on sample "alumina-3":** the numbers represent the relative intensities of the corresponding Bragg peaks in Fig. 6.14 ("(110) [%]": yellow arrows; "tilt. [%]": purple arrows; "twin. [%]": purple arrows *and* green arrows) to the ones of the respective particle $(11\bar{1})$ peak. In each case the respective background was subtracted.

in the case of sample "alumina-3" since it was during substrate preparation both, flashed prior to thermal cracking and not exposed to pressures in the 10^{-8} mbar range before deposition (see Table 6.4). Its absence may have had a strong impact on the interface energy and may have altered the particle growth behaviour towards more 3-dimensional shapes (see discussion in subsection 2.4.1).

The height-to-diameter aspect ratios of the particles belonging to regime I were indeed found to be much higher than on samples "alumina-1" and "-2", despite the comparable amount of deposited material (comparison: "alumina-1" and "-2": $Pt_{0.7}Rh_{0.3}$: 0.25, Rh: 0.48 ↔ "alumina-3": $Pt_{0.7}Rh_{0.3}$: 0.5, Rh: 0.6).

The absence of hydroxyls may also have promoted the growth of additional particle domains: contrary to samples "alumina-1" and "-2", distinct peaks from **(110)-oriented particles** (indicated by yellow arrows in Fig. 6.14) can be distinguished for both compositions and sizes. The comparison of intensities from Bragg peaks of (110)-oriented particles to the particle $(11\bar{1})$ peak of the (111)-oriented particles growing in domain II reveal that their relative percentage decreases for both compositions with increasing particle size. Table 6.7 shows the respective results for the pure Rh particles. Bragg peaks from (111)-oriented particles of **domains III and IV** are not discernible, pointing towards these particles' absence.

In line with the results found for samples "alumina-1" and "-2", additional peaks from **particles tilted by 30°** with respect to the surface normal were found to be more pronounced for Rh particles than for Pt-containing particles. They give rise to the peaks indicated by purple arrows in Fig. 6.14 and their peak intensities reveal that their percentage decreases with increasing particle size (see Table 6.7). Peaks denoted in addition by green arrows may not only stem from tilted particles, but also from internal twinning, which may explain the differing particle size dependence of their intensities in Table 6.7.

The last paragraph of this subsection will deal with the growth behaviour of the **$Pt_{0.7}Rh_{0.3}$ "core-shell"** particles, i.e. particles that were grown by the subsequent deposition of Rh and Pt. As Fig. 6.15 c) shows, these particles featured an aspect ratio much closer to the one of pure Rh than of the $Pt_{0.7}Rh_{0.3}$ alloy particles. This is in line with the SEM images shown in Fig. 8.17, which reveal a similar morphology of smaller, more disperse particles for both, "core-shell" and Rh particles compared to $Pt_{0.7}Rh_{0.3}$ alloy particles. Furthermore, the strong intensities of peaks belonging to (110)-oriented particles and particles tilted by 30° in the map measured on the "core-shell" particles indicate a similar growth behaviour as found for monometallic Rh. This indicates that, as it was found for particle growth on the $MgAl_2O_4$(001)-substrate (see section 6.1), seeding with Rh triggers the growth of Pt-Rh particles resembling the ones of pure Rh. Only the rather strong Laue oscillations, especially visible for the (111)-type Bragg peak, are rather typical of Pt-containing particles, indicating a perfect internal atomic structure.

Growth of α-Al_2O_3(0001)-supported Pd-Rh particles (sample "alumina-4")

The previous subsections dealt with the growth of Pt-Rh particles. Here, the results on the composition-dependent growth of Pd-Rh alloy particles on sample **"alumina-4"** (see Fig. 6.8) will be presented, which is the only sample in this thesis which was not studied during CO oxidation reactions. The results on the growth of Pd-Rh particles facilitate a better understanding of the growth behaviour of the Pt-Rh and Pt-Pd particle systems. Since Pd was found to resemble Pt in lattice parameter, surface energies [25] and its interaction with the α-Al_2O_3(0001)-substrate [32], it may be expected to trigger a similar growth behaviour for Pd-Rh alloy particles as found in the case of Pt-Rh.

"Alumina-4" contained stripes with particles of different Pd-Rh compositions, where for each stripe the same amount of material was deposited (nominal layer thickness: 15 Å). This was confirmed by x-ray reflectivity measurements, whose fit results revealed particle heights between 28 Å and 33 Å and particle coverages ranging from 40% to 60% (see Fig 6.17 a) and Fig. 6.24). The stripes were grown along the substrate $[10\bar{1}0]$-direction allowing for monitoring the

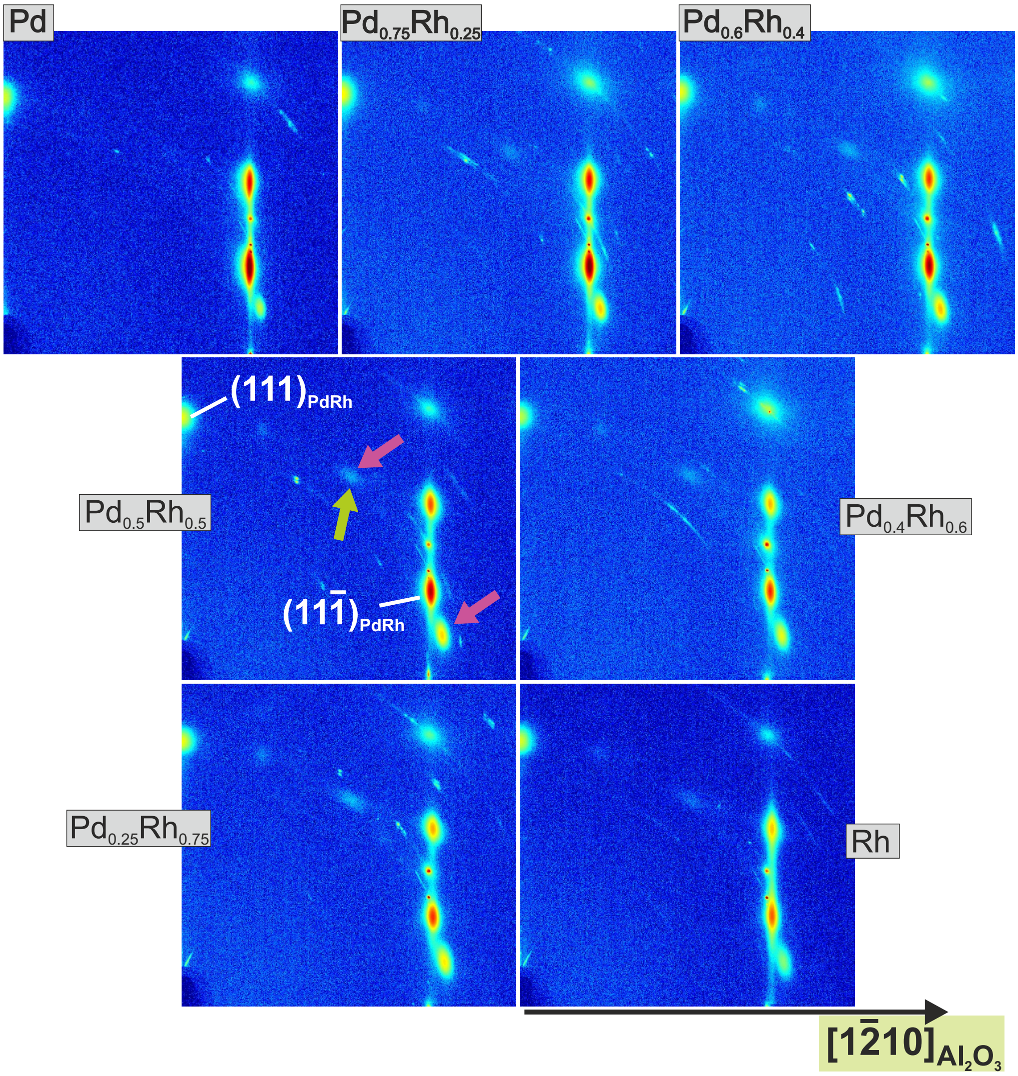

Figure 6.16: **Maps measured on particles of varying Pd-Rh compositions grown on sample "alumina-4":** the maps were measured in the substrate (1$\bar{2}$1L)-plane and include the particle (11$\bar{1}$) and (111) Bragg peaks; purple arrows: signals from (111)-oriented particles that are tilted by 30°; purple *and* green arrows: signals from particles tilted by 30° coinciding with potential signals from internal twinning.

peak	**x=1**	**x=0.75**	**x=0.6**	**x=0.5**	**x=0.4**	**x=0.25**	**x=0**
tilt. [%]	2.65	8.18	12.23	12.49	17.87	27.04	14.07
twin. [%]	–	0.17	0.45	–	0.99	1.73	1.46

Table 6.8: **Composition-dependent peak intensities from tilted (111)-oriented $Pd_xRh_{x\text{-}1}$ particles and from internal twinning on sample "alumina-4":** the numbers represent the relative intensities of the Bragg peaks from tilted particles ("tilt. [%]") and internal twinning ("twin. [%]") to the ones of the particle $(11\bar{1})$ peak. In each case the respective background was subtracted.

$(1\bar{2}10, L)$-plane including the particle $(11\bar{1})$ and (111) Bragg peaks.

The respective 2D maps are shown in Fig. 6.16. They look very similar for all Pd-Rh compositions and are dominated by Bragg peaks that stem from non-tilted (111)-oriented particles growing in domains I and II and from the ones tilted by 30°. No traces from peaks belonging to domains III and IV or from (110)-oriented particles are discernible, pointing towards these particles' absence. It is possible that the lack of (110)-oriented particles can be traced back to a potential hydroxylation of the sample substrate prior to deposition, as these particle domains were also found to be absent on samples "alumina-1" and "-2", but not on sample "alumina-3" (see previous discussion and Table 6.4 for differing substrate pretreatments).

On the present sample, as was also found for the Pt-Rh particles on samples "alumina-1" and "-2", the relative intensity of the peaks belonging to the particles tilted by 30° scales with the lattice mismatch of the particles to the substrate which is smallest in the case of pure Pd (lattice parameter a_{Pd}=3.8907 Å, lattice mismatch m_{Pd}=0.04%) and largest in the case pure Rh (lattice parameter a_{Rh}=3.8013 Å, lattice mismatch m_{Rh}=-2.25%). The relative Bragg peak intensities and lattice mismatches are summarized in Table 6.8. This implies that also for Pd-Rh alloy particles the number of tilted particles scales with the Rh content inside the particles. However, the overall amount of tilted particles was, compared to the Pt-Rh particle system, found to be extremely high for all Pd-Rh compositions.

Fig. 6.17 shows an overview of the composition-dependent particle heights, diameters and aspect ratios $\frac{H}{D}$ of the non-tilted particles as obtained from the FWHMs of the respective particle $(11\bar{1})$ Bragg peaks. Both, the Bragg peak data and the fit results from the x-ray reflectivity measurements, agreed well on a comparable particle height of about 30-40 Å for all Pd-Rh compositions.

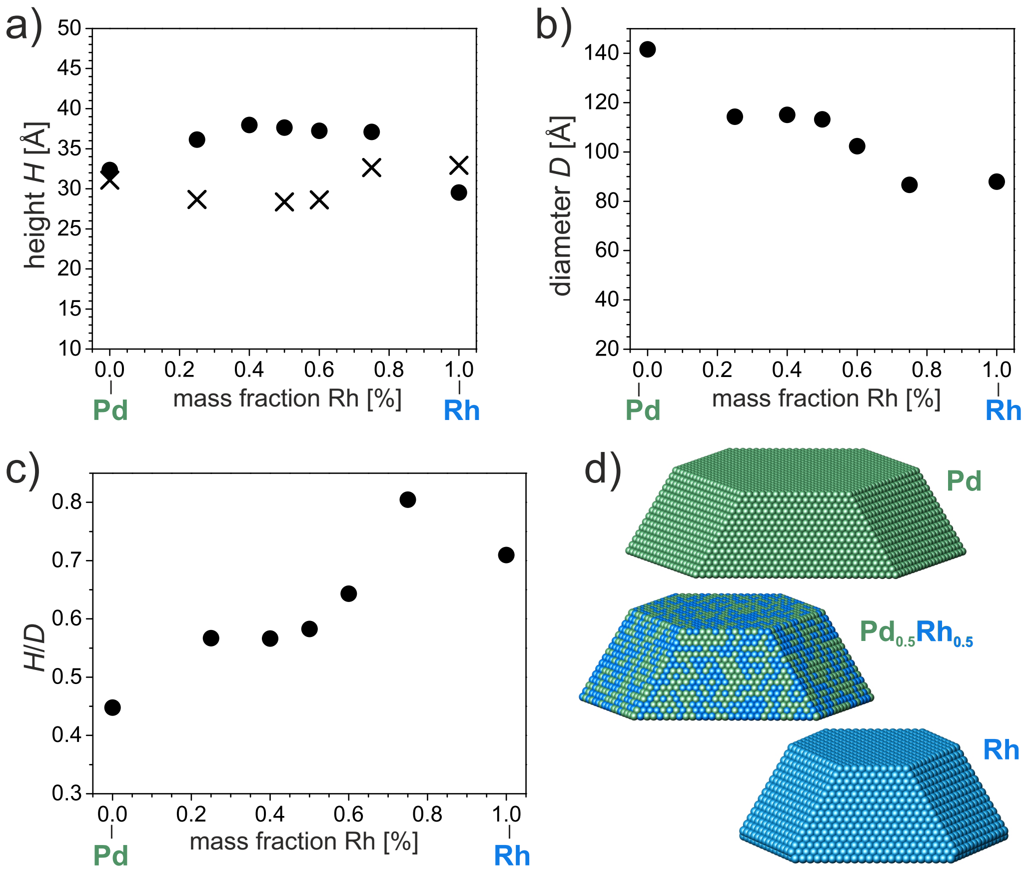

Figure 6.17: **Composition-dependent sizes of (111)-oriented Pd-Rh particles of the main domains (I and II) on sample "alumina-4": a):** particle heights as deduced from the respective particle (11$\bar{1}$) Bragg peaks (circles) and from the x-ray reflectivity data (crosses); **b):** particle diameters as obtained from the particle (11$\bar{1}$) Bragg peaks; **c):** particle aspect ratios $\frac{H}{D}$ as deduced from the arithmetic mean of circles and crosses in a), and from data in b); **d):** Wulff-construction of Pd, Pd$_{0.5}$Rh$_{0.5}$ and Rh particles based on the mean heights of a) and diameters of b) neglecting higher indexed particle facets and assuming a surface energy ratio of g=$\frac{\gamma_{100}}{\gamma_{111}}$=1.1 for the (100)- and (111)-type particle facets.

Contrary, as it was also found for the Pt-Rh particles, the particle diameter was characterized by a strong composition-dependence, where the diameters decreased with increasing Rh content (see Fig. 6.17 b)). This results in the particle aspect ratios shown in Fig. 6.17 c), which range from about 0.25 in the case of Pd to about 0.4 in the case of Rh. The particle shapes, based on the Wulff construction assuming a ratio of $g=\frac{\gamma_{100}}{\gamma_{111}}=1.1$ for the surface energies of the particle (100)- and (111)-type facets, are shown in Fig. 6.17 d) for some selected Pd-Rh compositions.

Thus, while the pure Pd particles are of rather disk-like shape, the progressive addition of Rh leads increasingly to more compact particles, although the overall differences in shape appears to be not as pronounced as between Pt and Rh on samples “alumina-1” and “-2”. An explanation for the growth behaviour of Pd-rich particles towards more 2D-like shapes can - as in the case of Pt-rich particles - be found in the smaller lattice mismatch to the substrate and the smaller surface energy compared to Rh. It is, however, striking that - while the Bragg peaks of all Pt-rich particles display distinct Laue oscillations - no Laue oscillations are present in the case of the Pd-containing particles, pointing towards a less perfect internal particle structure and/or a higher degree of particle height fluctuations.

Growth of α-Al_2O_3(0001)-supported Pt-Pd particles (sample “alumina-5”)

The previous subsections revealed that the addition of both, Pt and Pd, allows for tailoring the growth towards more disk-like Pt-Rh and Pd-Rh nanoparticles. It was for Pt and Pd ascribed to both, their lower surface energies and their smaller lattice mismatch to the substrate, as compared to Rh. In this section, the growth study of Pt-Pd particles will yield the direct comparison between the growth of Pt-rich and Pd-rich particles. Pd, with a slightly smaller lattice mismatch to the α-Al_2O_3(0001)-substrate (see Table 2.2 in subsection 2.4.1), minor lower surface energies (see Table 2.1 in subsection 2.3.1) and a slightly stronger interaction with the substrate [32] compared to Pt, should be expected to form flatter particle shapes as compared to Pt.

The particle stripes of sample“alumina-5” displayed a gradient in Pt-Pd composition (see sketch in Fig. 6.8), where for each stripe the same amount of material was deposited (nominal layer thickness: 10 Å). This was confirmed

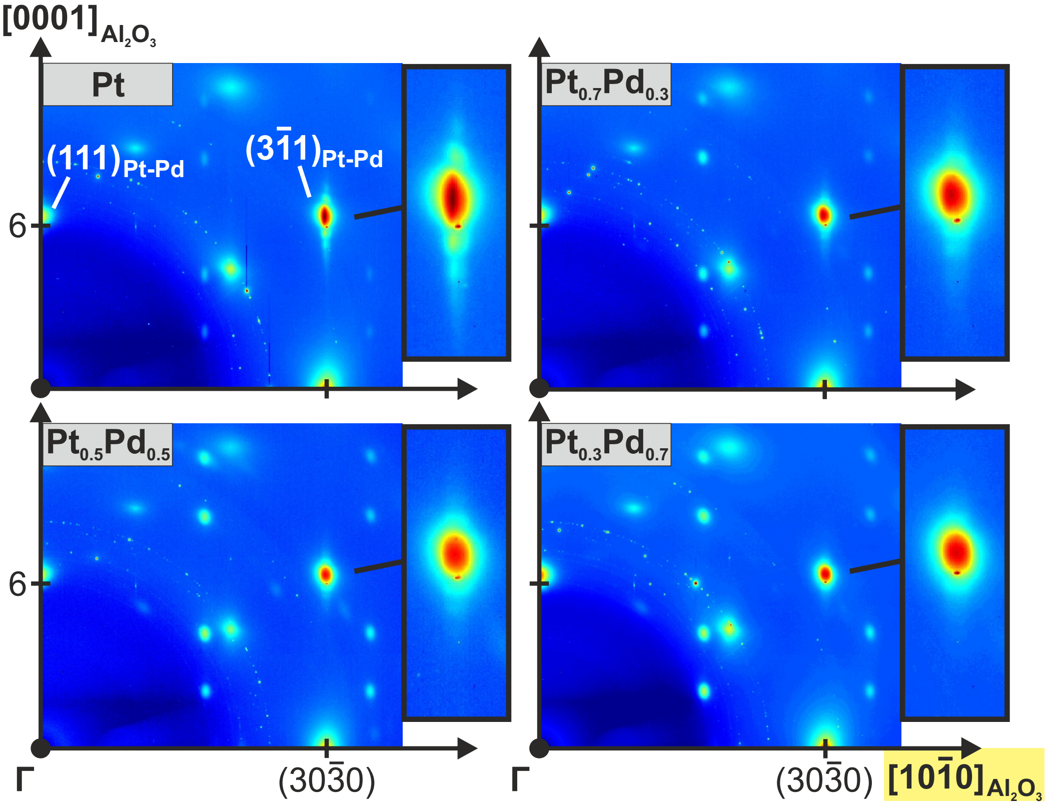

Figure 6.18: **Maps measured on particles of varying Pt-Pd compositions grown on sample "alumina-5":** the maps are measured in the substrate (10$\bar{1}$L)-plane and include the particle (3$\bar{1}$1) and (111) Bragg peaks; the insets display close-ups on the vicinities of the respective particle (3$\bar{1}$1) Bragg peaks.

by the x-ray reflectivity results yielding particle heights between 35 Å and 45 Å (see Fig. 6.19 a)) and particle coverages ranging from 25% to 30%.

The stripes were grown along the substrate [1$\bar{2}$10]-direction allowing for monitoring the particle (3$\bar{1}$1) Bragg peak of domains I and II of the (111)-oriented particles. The respective 2D maps are summarized in Fig. 6.18 along with close-ups on the particle (3$\bar{1}$1) Bragg peaks.

The close-ups reveal once again strong Laue oscillations in the case of the pure Pt particles, which are already strongly diminished in the case of the $Pt_{0.7}Pd_{0.3}$ particles, and not even present for the Pd-rich $Pt_{0.3}Pd_{0.7}$ particles, which implies that the addition of Pd may distort the rather layer-like growth and the low vertical height distribution typical of Pt-containing particles.

Fig. 6.19 reveals the composition-dependent particle sizes, as obtained for the predominant particle domains I and II. While the particle height amounted independent of composition to about 40 Å, the diameter strongly scaled with Pt-content from ≈70 Å in the case of $Pt_{0.3}Pd_{0.7}$ up to ≈120 Å in the case of

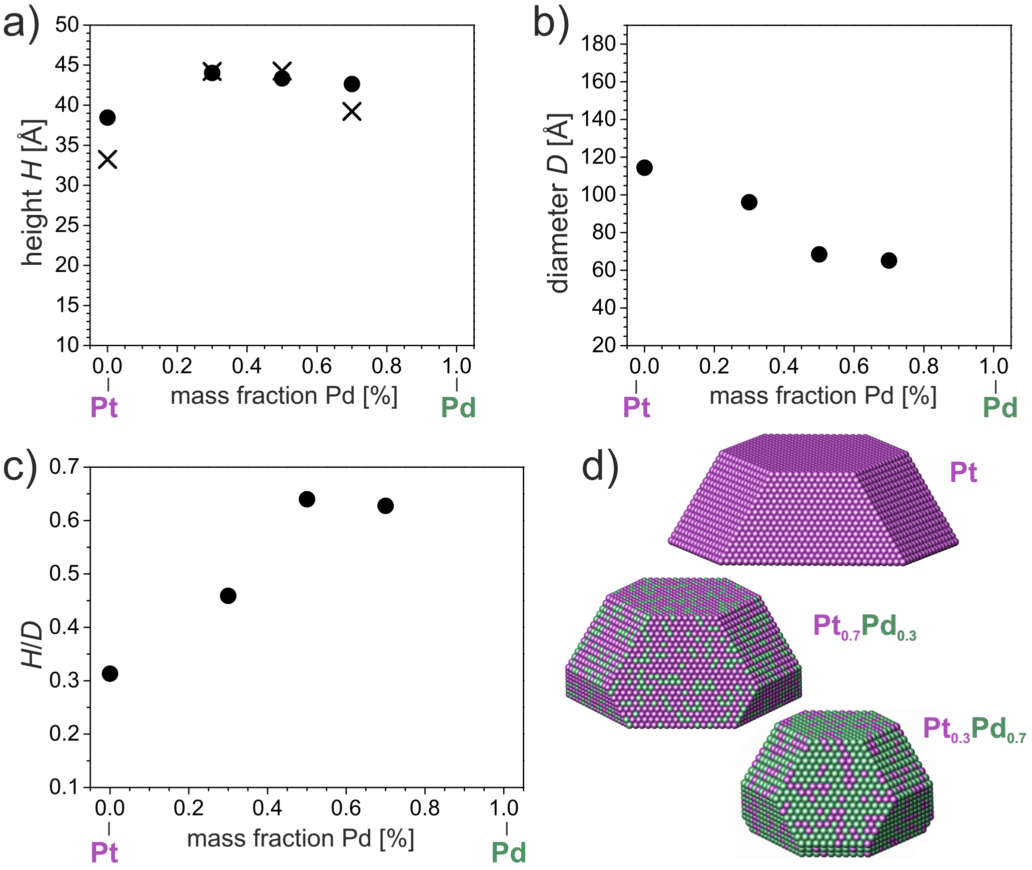

Figure 6.19: **Composition-dependent sizes of (111)-oriented Pt-Pd particles of the main domains on sample “alumina-5”: a):** particle heights as deduced from the respective particle $(3\bar{1}1)$ Bragg peaks (circles) and x-ray reflectivity data (crosses); **b):** particle diameters as deduced by combining θ-scan analysis, Bragg peak scan fitting and SEM microscopy data (see section 8.2 and Fig. 8.19 a) for more information); **c):** particle aspect ratios $\frac{H}{D}$; **d):** Wulff construction of Pt, $Pt_{0.7}Pd_{0.3}$ and $Pt_{0.3}Pd_{0.7}$ based on the heights and diameters of a) and b) neglecting higher indexed particle facets and assuming a surface energy ratio of $g=\frac{\gamma_{100}}{\gamma_{111}}=1.1$ for the (100) and (111)-type particle facets.

stripe	**x=1**	**x=0.7**	**x=0.5**	**x=0.3**
mism. [%]	0.91	0.65	0.48	0.30
III/IV [%]	0.19	1.09	3.75	5.30
tilt. [%]	–	0.03	0.20	0.39

Table 6.9: **Composition-dependent peak intensities from rotated (111)-oriented $\mathbf{Pt_xPd_{x\text{-}1}}$ particles and from internal twinning on "alumina-5":** the numbers represent the relative intensities of the Bragg peaks from tilted particles ("tilt. [%]") and internal twinning ("twin. [%]") to the ones of the particle $(3\bar{1}1)$ peak. In each case the respective background was subtracted.

monometallic Pt. The diameter dependence on the Pt-Pd composition can also be deduced from the SEM images performed after the CO oxidation experiment shown in Fig. 8.22 in subsection 8.2.2. The finding of a larger diameter for Pt-rich particles compared to Pd-rich particles may appear surprising on the basis of the introductory remarks to this subsection. However, earlier results in this chapter implied that the shape of Pt particles is very prone to the substrate preparation and the potential hydroxylation of the substrate surface, which can for sample "alumina-5" not be excluded. Accordingly, a tentative explanation is that hydroxyls have a stronger impact on Pt than on Pd particles, resulting in more disk-like shapes for Pt- compared to Pd-rich particles.

Apart from the Bragg peaks of particle domains I and II, Fig. 6.18 reveals a comparatively high portion of signals from particles growing as domains III and IV, and of particles that grow with a surface normal tilted by 35° around the substrate $[1\bar{2}10]$-direction. The portion of domain III and IV particles scales with increasing Pd-content, as does the number of tilted particles (see Table 6.9). It is indicated in Fig. 6.21 that the tilt by 35° results in a projection of the particle out-of-plane lattice parameter given by $\frac{d_{111}}{\sin(35°)}$ onto the substrate atomic row distance $\frac{\sqrt{3}\cdot a_{\mathrm{Al2O3}}}{2}$, leading to a mismatch of 5.05% in the case of $\mathrm{Pt_{0.3}Pd_{0.7}}$ and a lower mismatch of 4.43% for pure Pt. A possible explanation for the tendency of Pd-rich particles to grow tilted can be seen in the surface energies of Pd, which are almost isotropic for the different facets (see Table 2.1 in subsection 2.3.1). Accordingly, this may allow the Pd particles to grow in more varieties, including turning and tilting, while the Pt particles are rather pinned to the interface - also due to the potential hydroxylation - and display large areas of (111)-type facets, characterized by low surface energies, which in their case is only possible in a layer-like (111)-type epitaxy.

6.3 Summary and conclusion

This chapter contains results on the size- and composition-dependent growth of alloy nanoparticles on $MgAl_2O_4(001)$ and α-$Al_2O_3(0001)$, with Pt, Rh and Pd used as parent metals.

The data clarify the advantages of high energy reciprocal space mapping of combinatorial samples with respect to particle growth studies. Hence, it was shown that one large area reciprocal space map, typically measured within several seconds, contains not only information on the main epitaxies, but also on tilted particles, particles growing in other epitaxies or defects such as internal twinning. When using conventional photon energies, it is often too time-consuming to search for and to map all these features individually and as a consequence, this information is lost. Their capture becomes all the more important on the basis of growing experimental evidence suggesting defect sites or particle peripheries to be the catalytically most active centres [197].

This thesis' growth study revealed that particles grow on $MgAl_2O_4(001)$ predominantly in a (001)-orientation, on α-$Al_3O_3(0001)$ in a (111)-orientation, independent of growth parameters such as substrate pretreatment, particle alloy composition or size.

A key result is that the particle growth features on both type of substrates a composition- and size-dependence, which allows for **tailoring** the **particle shape** of the aforementioned main epitaxies. Hence, the particle $\frac{H}{D}$ aspect ratio was found to decrease with increasing Pt content, i.e. Pt-rich particles are in general found to be flatter than Rh-rich particles. The aspect ratio was moreover found to decrease with increasing particle size.

In the case of $\mathbf{MgAl_2O_4(001)}$, the investigated Pt-Rh alloy particles of the main (001)-epitaxy featured relatively high $\frac{H}{D}$ aspect ratios between 0.5 and 0.7, depending on the Pt content and the particle size. For particles with heights and diameters larger than H=50 Å and D=70 Å, respectively, distinct particle facet signals, confirming a truncated octahedral shape, were discernible.

Several repeated sputtering and annealing cycles of the substrate prior to deposition resulted in a tremendous reduction of signals from internal twinning, from tilted particles and from particles growing with minor epitaxies, such as (110)-and (111)-orientations. Minor epitaxies and internal twinning could also be progressively reduced by increasing the amount of deposited material. In general, pure Rh samples displayed a relatively high amount of (110)-oriented particles, Pt-rich samples a large number of (111)-oriented particles.

The shapes of particles grown on **α-Al_2O_3(0001)** were found to depend even more strongly on the alloy composition, which makes their tailoring more feasible than on $MgAl_2O_4$(001). The shapes were in general concluded to be flatter and more disk-like with aspect ratios $\frac{H}{D}$ ranging from 0.18 to 0.6 and scaling with composition according to Pt<Pd<Rh. As it was found for the growth on $MgAl_2O_4$(001), the aspect ratio was deduced to decrease with increasing particle size. Especially the growth of pure Pt and Pt-rich particles was found to depend on the substrate treatment and the data suggest that a potential hydroxylation of the surface results in a decrease in particle height-to-diameter aspect ratio. In the case of the Pt-rich particles a decrease in aspect ratio was also obtained by longer annealing times during deposition.

On both substrates a **novel growth mechanism** was concluded: therein, particles stabilize themselves by tilting such that the projection of their lattice planes matches the atomic row distances of the substrate.

Independent of aspect ratio or size, only the Pt-containing particles' diffraction patterns featured strong Laue oscillations, which implies an internal structural perfectness and well-developed top facets, while Rh-rich particles were found to be characterized by 3-dimensional and compact shapes. Due to the larger mismatch to the substrate lattice parameter, Rh and Rh-rich samples feature a higher amount of (110)-oriented and tilted (111)-oriented particles as compared to Pt- or Pd-rich particles. Their portion was concluded to decrease with increasing amount of deposited material.

Independent of the substrate used, the sequential deposition of Rh and Pt (**"core-shell" particles**) resulted in particles which featured the growth characteristics of pure Rh particles. Hence, seeding with Rh was found to constitute another possibility to tailor the particle growth characteristics.

For all samples the deduced lattice parameters were found to adhere within error bars to **Vegard's law**, hence, despite potential miscibility gaps reported for some systems, complete alloying can be assumed.

It is worth mentioning that the particle shapes discussed in this chapter correspond to the **kinetic particle shapes**, as will become obvious in the chapters dealing with reaction-induced particle sintering (see chapters 7 and 8).

Appendix A*: Overview of reciprocal space maps measured on the as-prepared Pt-Rh particles of samples “alumina-1”, and “-2”

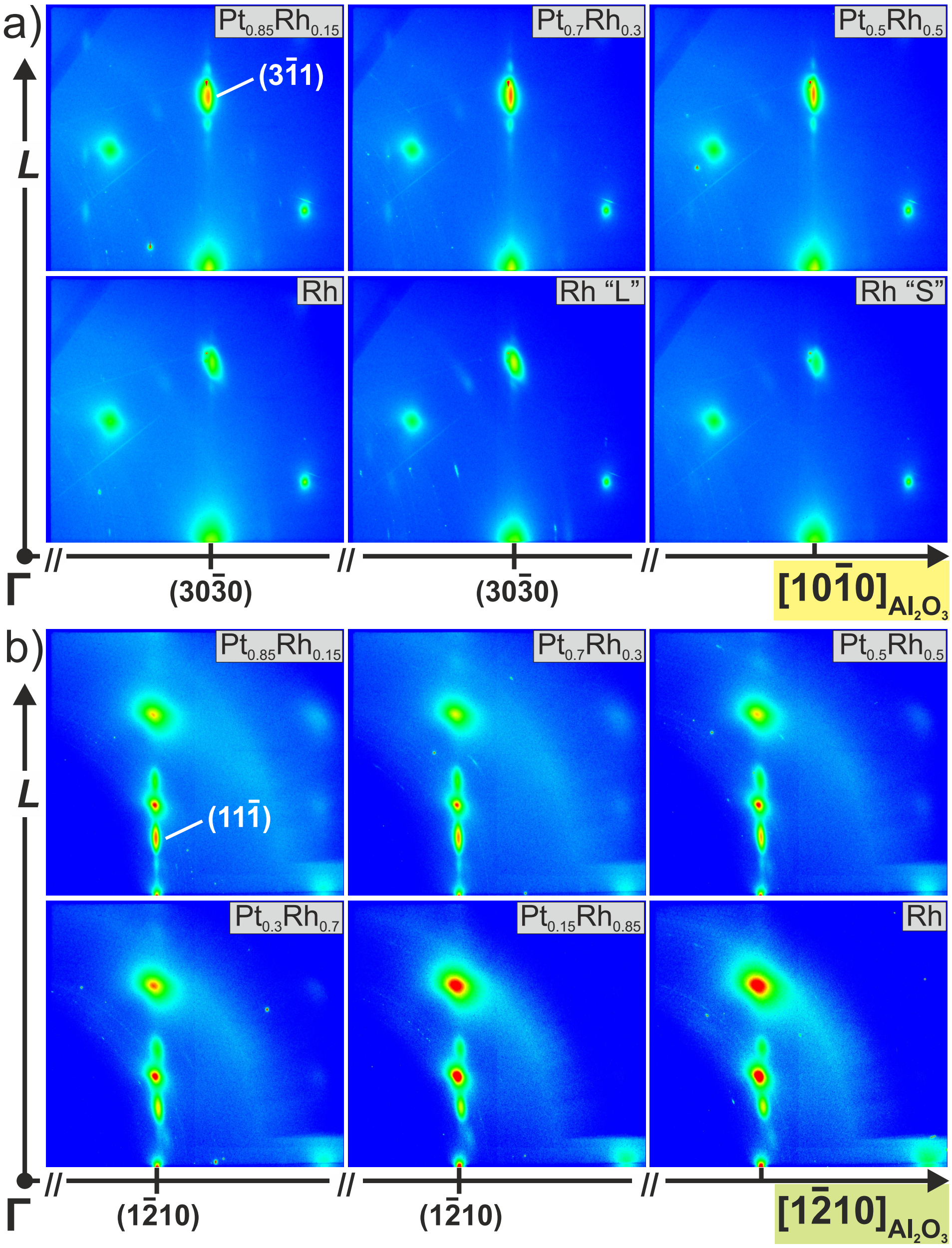

Figure 6.20: **2D maps measured on the as-prepared Pt-Rh particles: a):** of sample “alumina-1” mapping the substrate $(10\bar{1}L)$-plane containing the particle $(3\bar{1}1)$ peak; **b):** of sample “alumina-2” mapping the substrate $(1\bar{2}1L)$-plane containing the particle $(11\bar{1})$ peak.

Appendix B*: Growth of tilted particles

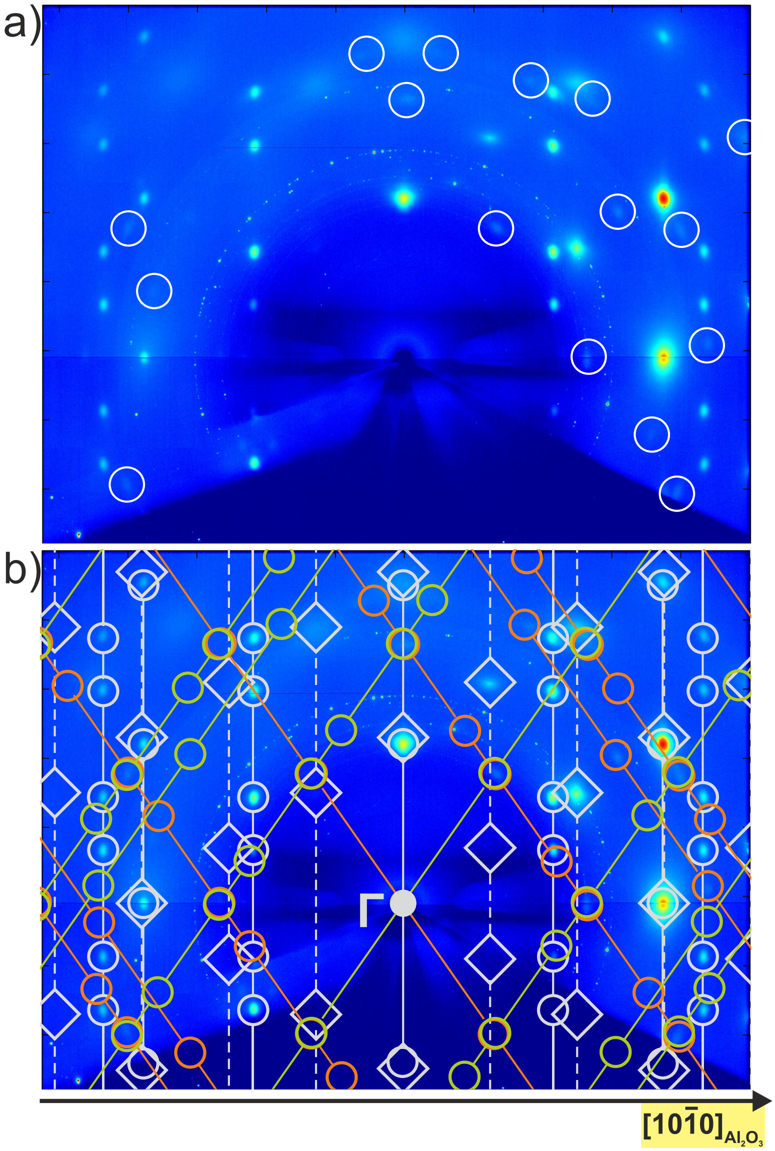

Figure 6.21: **2D maps measured on the $Pt_{0.5}Pd_{0.5}$-particles on sample "alumina-5" showing reflections from tilted particles: a):** white circles indicate additional reflections that cannot be explained by the reflection scheme of non-rotated (111)-oriented particles as shown in Fig. 6.10 b); **b):** reflection scheme of non-rotated (111)-oriented particles (grey circles: particle reflections; grey diamonds: substrate reflections) and particles tilted by 35° clockwise (light-green) and counter-clockwise (orange).

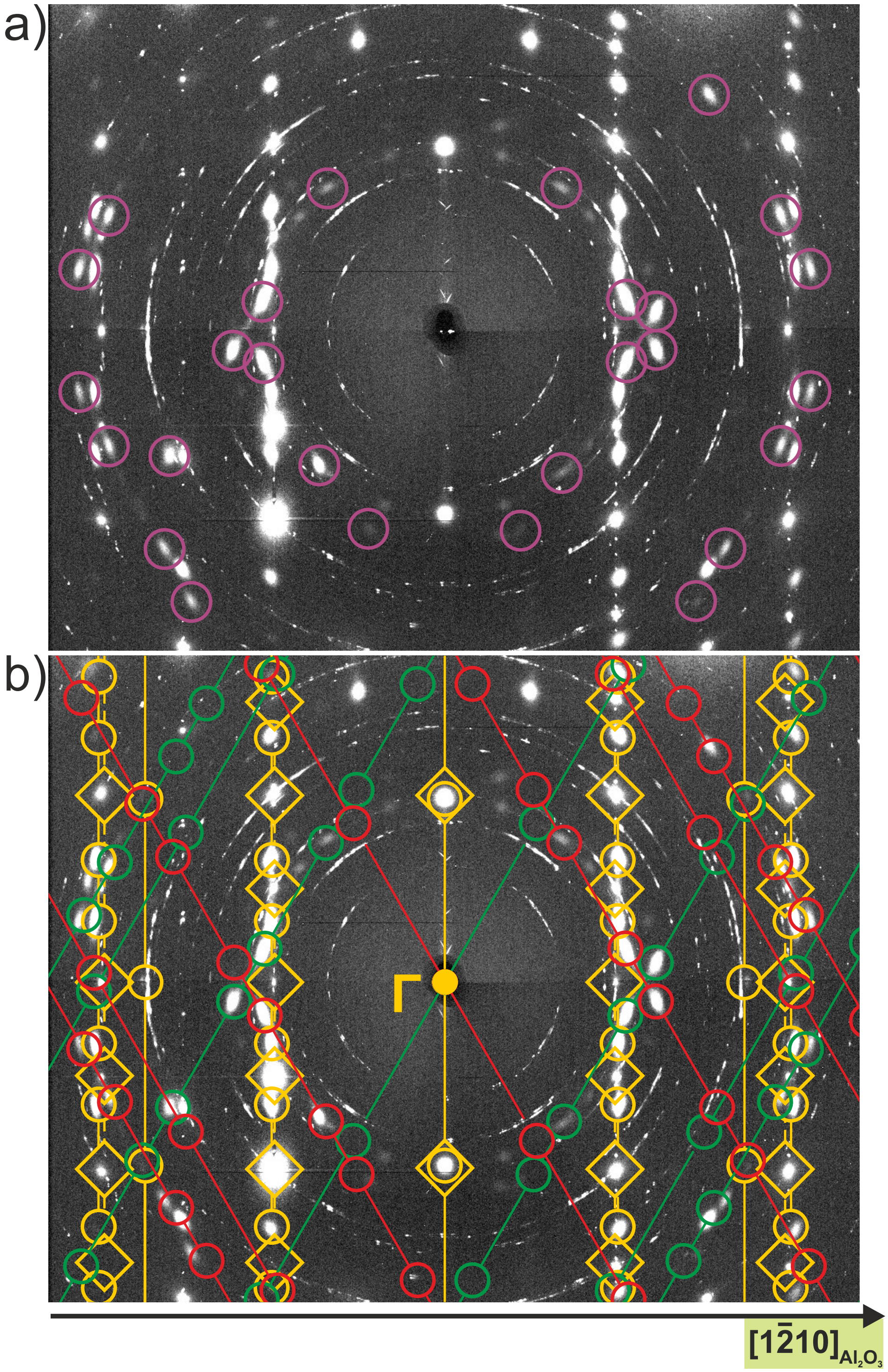

Figure 6.22: **Single image consisting of images collected during a rocking scan on $Pd_{0.6}Rh_{0.4}$-particles on sample "alumina-4" including reflections from tilted particles: a):** purple circles indicate additional reflections from tilted particles that cannot be explained by the reflection scheme of non-rotated (111)-oriented particles in Fig. 6.10 c); **b):** reflection scheme of non-tilted (111)-oriented particles (yellow circles: particle reflections; yellow diamonds: substrate reflections) and particles tilted by 30° clockwise (green) and counter-clockwise (red).

Appendix C*: X-ray reflectivity measurements

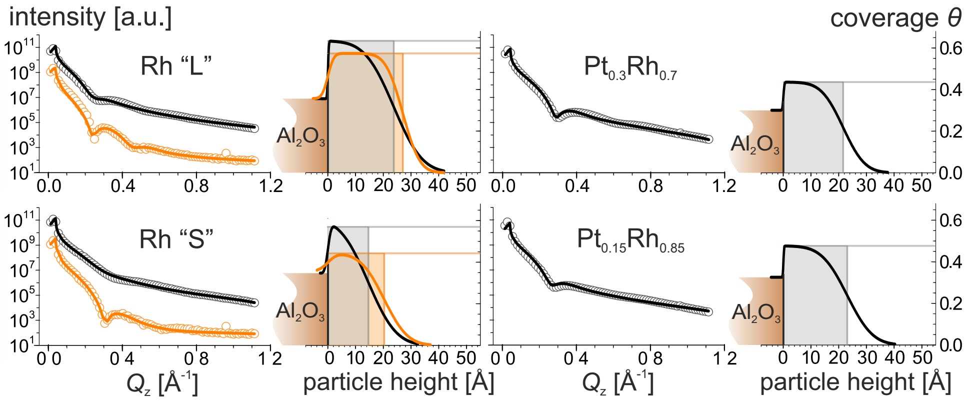

Figure 6.23: **X-ray reflectivity performed on Pt-Rh particles of samples "alumina-1" and "-2":** the left column shows results of the two additional Rh stripes denoted "L" and "S" of sample "alumina-1", the right column results for particles of sample "alumina-2". The measured (open circles) and fitted (solid lines) data are shown on the left, electron density profiles deduced from the fits on the right (black: as-prepared; orange: during CO oxidation at $f_{\mathrm{CO}}=10\ \frac{\mathrm{ml}}{\mathrm{min}}$, $f_{\mathrm{O2}}=7\ \frac{\mathrm{ml}}{\mathrm{min}}$).

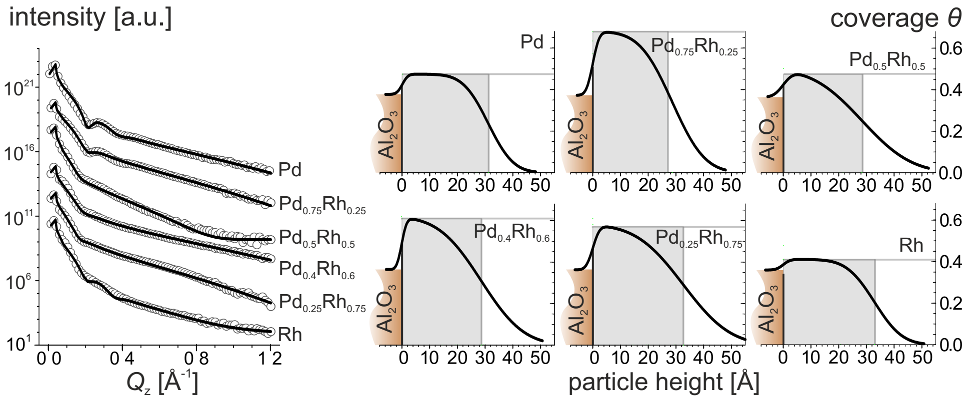

Figure 6.24: **X-ray reflectivity performed on the as-prepared Pd-Rh particles of sample "alumina-4":** the measured (open circles) and fitted (solid lines) data are shown on the left, the electron density profiles obtained from the fits are shown on the right. Note the missing Kiessig oscillations in the reflectivity curves and the correlated rather high surface roughness in the electron density profiles, which imply strong particle height fluctuations. These may explain the absence of Laue oscillations in the Bragg peak pattern of the Pd-Rh alloy particles.

Chapter 7

Operando CO Oxidation Study of $MgAl_2O_4(001)$-Supported Pt-Rh Nanoparticles: Catalytically Active Phases and Particle Shape Changes

This chapter deals with the thorough study of Pt-Rh alloy nanoparticles in the transition to and during high catalytic activity for CO oxidation. The investigation was based on and motivated by experiments preceding the work of this thesis, in which the oxygen-triggered shape changes of pure Rh and Pt nanoparticles were studied [4, 152]. In both cases the particle oxidation was succeeded by exposure to CO, thus mimicking CO oxidation reaction conditions of a real catalyst.

The present study differs in two main aspects from those previous works: first, the particles were investigated in a flow reactor allowing for steady state conditions of CO oxidation, thus achieving more realistic catalyst environments and allowing for relating the observed sample features to catalytic activity. Second, not single metal but alloy nanoparticles were studied, raising the question whether the alloy particles would show a characteristic behaviour of either pure Rh or pure Pt particles with respect to shape changes and oxide formation. The choice of alloy over pure metal was moreover triggered by recent high pressure XPS results on Pd-Rh alloy nanoparticles, which verified the chemical restructuring of the particles in the transition from a reducing to an oxidizing environment [111] (see subsection 3.2.2).

The first part of this chapter, section 7.1, deals with the experimental setup and strategy. Sections 7.2 and 7.3 contain the thus obtained results for the MgAl$_2$O$_4$(001)-supported Pt$_{0.33}$Rh$_{0.67}$ alloy nanoparticles (sample "spinel-1", see Fig. 6.1 in section 6.1) studied under reaction conditions: combining in-situ surface x-ray diffraction at 11.2 keV with in-situ mass spectrometry provided unprecedented atomic scale information on alloy nanoparticles under reaction conditions at near atmospheric pressures. It allowed for monitoring various oxide phases that formed on the Pt$_{0.33}$Rh$_{0.67}$ particle facets in the stepwise transition to and during high activity for CO oxidation and for identifying the catalytically active oxide phase. Further insight into the dynamics of oxide formation was gained by time-resolved in-situ gas switching, as is being discussed in section 7.2. High resolution reciprocal space mapping along with particle Bragg peak scans along high symmetry directions revealed the qualitative and quantitative shape changes that the particles underwent during cycles of reduction and catalytic activity, as is described in section 7.3. This section also deals with the sintering of the Pt$_{0.33}$Rh$_{0.67}$ particles in the course of these cycles.

In order to complete the picture, the last part of the chapter (section 7.4) discusses activity-induced aspect ratio changes of MgAl$_2$O$_4$(001)-supported particles that featured different sizes and/or Pt-Rh compositions (sample "spinel-2", see Fig. 6.1 in chapter 6). The combinatorial sample was studied using grazing incidence high energy x-ray diffraction at 78 keV.

In the case of both samples the x-ray data were completed by AFM and SEM measurements performed after the CO oxidation studies.

7.1 Experimental details

MgAl$_2$O$_4$(001)-supported Pt$_{0.33}$Rh$_{0.67}$ particles (sample "spinel-1"), beamline P09

The total pressure inside the catalysis chamber's flow reactor was put to 50 mbar throughout the experiment. The used gases comprised Ar (carrier gas), O$_2$ and diluted CO (10% CO in 90% Ar). The temperature was set via the sample heater current according to a calibration curve and was held constant at 673 K. It was thus high enough to avoid CO poisoning of the sample even

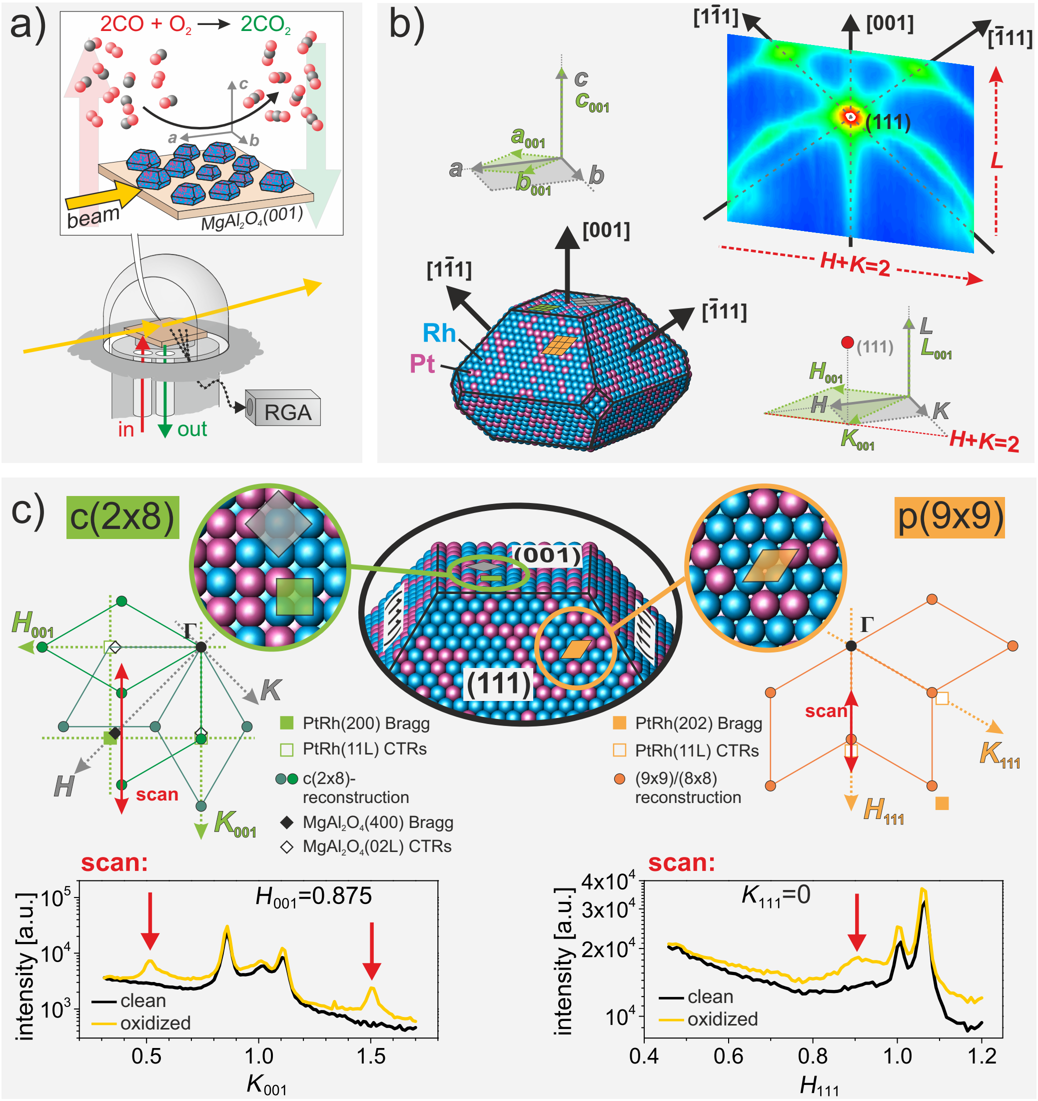

Figure 7.1: **Experimental strategy: a):** inside the chamber's Be dome the structure of the sample was studied while monitoring its catalytic activity; **b):** high resolution reciprocal space maps measured around the particle (111) Bragg peak allow for obtaining information on the particle shapes by monitoring particle facet signals under different sample conditions. The grey and green coordinate systems represent the respective unit cell of the particle fcc structure and the surface unit cell of the (001)-type top facet; **c):** surface unit cells of the particle (001) top facet (green) and the (111)-facet (orange) and their position with respect to expected positions of signals of the c(2x8) (filled green circles) and the p(9x9) oxide (orange filled circles) as well as with respect to the position of the performed oxide reference scans (red arrows). The bottom insets show these reference scans performed under reducing (black, f_{CO}=4 $\frac{\mathrm{ml}}{\mathrm{min}}$) atmosphere on the clean particles and during high catalytic activity (yellow, f_{CO}=4 $\frac{\mathrm{ml}}{\mathrm{min}}$ and f_{O2}=3 $\frac{\mathrm{ml}}{\mathrm{min}}$) when both surface oxides were present.

under reducing conditions, allowing for conditions of high catalytic activity (*'light-off'*) at sufficiently high p_{O2}/p_{CO} ratios (see subsection 3.1.3).

The photon energy comprised 11.2 keV. In order to optimize the beam stability a set of compound refractive lenses was inserted 2.5 m in front of the sample position. The incident angle amounted to α_{in}=0.4° and was thus higher than the critical angle of both, substrate (0.197°) and $Pt_{0.33}Rh_{0.67}$ particles (0.377°). It was chosen in order to obtain a penetration depth Λ (at α_{in}=0.4°: Λ_{Pt}=67 Å, Λ_{Rh}=184 Å) on the order of at least the particle height, thus being able to probe whole particles and to achieve in turn a higher sensitivity for subtle particle facet signals.

From the x-ray data the as-prepared particles were found to have a height and diameter of about 60 Å and 90 Å, respectively. The determined lattice parameter of 3.8365 Å was found to lie between the ones of pure Pt (3.9242 Å) and Rh (3.8013 Å) suggesting an alloying state of the particles with 28% Pt and 72% Rh and thus close to the desired composition of 33% Pt and 67% Rh. The relative positions of particle and substrate Bragg peaks deduced from in-plane scans confirmed that the particles mainly grow in a cube-on-cube epitaxy (see section 6.1).

In Fig. 7.1 the **experimental strategy** for the investigation of the particles at conventional energies is shown. Its results will be presented in the following sections 7.2 and 7.3. It combines in-situ mass spectrometry to probe the sample's catalytic activity (Fig. 7.1 a)), high resolution reciprocal space mapping to obtain information on the particle shape (Fig. 7.1 b)), and oxide reference scans (Fig. 7.1 c)) which act as a fingerprint for the presence of potential oxide signals from the c(2×8) Rh surface oxide on the (001)-type top facets and from the p(9×9) Rh surface oxide on the particle (111)-side facets. The insets in Fig. 7.1 c) reveal the scan positions in reciprocal space and examples of the measured reference scans without (black) and with (yellow) the oxides present.

Fig. 7.1 also shows the different **coordinate systems** that will be used throughout the chapter. The in-plane unit cell of the fcc lattice (see Fig. 2.2, lattice parameters a=b=c=a_0, α=β=γ=90°) is represented by the grey square, its reciprocal lattice vectors are in the following denoted by H, K and L without subscripts.

The coordinates of the (001)-top facet surface lattice, represented by the green square in Fig. 7.1 c), are given by the lattice parameters a=b=$\frac{a_0}{\sqrt{2}}$, c=a_0,

$\alpha=\beta=\gamma=90°$. Their real space lattice vectors with respect to the fcc lattice are described by $\boldsymbol{a}_{100}=\frac{a_0}{2}(1,\bar{1},0)$, $\boldsymbol{b}_{100}=\frac{a_0}{2}(1,1,0)$, $\boldsymbol{c}_{100}=a_0(0,0,1)$. The reciprocal lattice vectors will in the following chapter be denoted by H_{100}, K_{100}, L_{100}, using “100” as subscript.

The coordinates of the (111)-facet surface lattice, represented in Fig. 7.1 c) by the orange rhombus, have the lattice parameters $a=b=\frac{a_0}{\sqrt{2}}$, $c=a_0\sqrt{3}$, the real space lattice vectors with respect to the fcc lattice are described by $\boldsymbol{a}_{111}=\frac{a_0}{2}(1,0,\bar{1})$, $\boldsymbol{b}_{111}=\frac{a_0}{2}(\bar{1},1,0)$, $\boldsymbol{c}_{111}=a_0(1,1,1)$. The corresponding reciprocal lattice vectors will in the following be denoted by H_{111}, K_{111}, L_{111} using “111” as subscript.

7.2 In-situ monitoring of oxide formation

Tracking the catalytically active oxide phase

In the following, the formation and catalytic activity of potential surface oxides on the (001)- and (111)-type particle facets of the $MgAl_2O_4$(001)-supported $Pt_{0.33}Rh_{0.67}$ particles when switching (keeping the CO flow constant and increasing the O_2 flow) towards conditions of high catalytic activity will be discussed.

The top part of Fig. 7.2 shows the relative partial pressures of CO, O_2 and of the reaction product CO_2 as monitored by the mass spectrometer. The CO flow was all the time kept constant at $f_{\mathrm{CO}}=4\ \frac{\mathrm{ml}}{\mathrm{min}}$, while the oxygen flow was stepwise increased up to oxygen overstoichiometry at $f_{\mathrm{O2}}=3\ \frac{\mathrm{ml}}{\mathrm{min}}$. In each step the reference scans of the c(2x8) and p(9x9) Rh surface oxides, whose positions in reciprocal space are indicated by red arrows in Fig. 7.1 c), were performed. The measured data are displayed at the bottom of Fig. 7.2.

Increasing the O_2 flow from 0 to 1 $\frac{\mathrm{ml}}{\mathrm{min}}$ resulted in an increase in CO_2 production accompanied by a decrease in the CO signal as CO was immediately consumed in the reaction. Under these conditions no oxide signals were observed, implying that the particles still featured the pure metallic phase and that conversion to CO_2 followed a Langmuir-Hinshelwood mechanism. Working at 673 K ensured that the latter could not be inhibited by CO poisoning of the particle facet surfaces.

A big jump to the highest CO_2 production was reached when increasing the O_2 flow to $f_{\mathrm{O2}}=2\ \frac{\mathrm{ml}}{\mathrm{min}}$ (stoichiometric conditions). This ‘*light off*’ came along with a sudden decrease in the monitored partial pressure of CO which was more pronounced compared to the transition from 0 to 1 $\frac{\mathrm{ml}}{\mathrm{min}}$ O_2 flow. When further increasing the O_2 flow to 3 $\frac{\mathrm{ml}}{\mathrm{min}}$, the CO_2 production decreased slightly while the CO signal increased again, as less CO was consumed in the reaction and the sample was less catalytically active. While already at f_{O2}=2 $\frac{\mathrm{ml}}{\mathrm{min}}$ O_2 flow clear c(2x8) Rh surface oxide signals were visible, signals from the p(9x9) Rh surface oxide structure were only discernible at f_{O2}=3 $\frac{\mathrm{ml}}{\mathrm{min}}$.

These observations show that in the transition to oxygen overstoichiometry, the $Pt_{0.33}Rh_{0.67}$ particles underwent a chemical restructuring with Rh segregating to the surface and forming its oxides, as was reported for other Rh-based nanoparticle systems under oxidizing conditions [112, 150]. The data suggest that the c(2x8) Rh surface oxide is catalytically more active compared to the p(9x9) Rh surface oxide, since it emerged in the transition to the sample's highest catalytic activity at 2 $\frac{\mathrm{ml}}{\mathrm{min}}$ O_2 flow. The appearance of the p(9x9) Rh surface oxide at 3 $\frac{\mathrm{ml}}{\mathrm{min}}$ O_2 flow, on the other hand, did not add up to the CO_2 productivity. Results obtained on a Rh(111) single crystal surface that was studied inside a batch reactor combining in-situ surface x-ray diffraction and mass spectrometry concluded that the emergence of the p(9×9) surface oxide dramatically increased the catalyst activity [81]. This deviation to the results presented in this chapter underlines the necessity of steady state in-situ studies during reaction conditions and the importance of more realistic model catalyst systems based on nanoparticles.

An explanation for the activity decline at 3 $\frac{\mathrm{ml}}{\mathrm{min}}$ of O_2 flow can be found in a possible poisoning of the catalyst surface by bulk oxides, as has been found on Rh(100) and Rh(111) single crystal surfaces [72, 198]. In the present study, bulk oxide signals were found to be present at 3 $\frac{\mathrm{ml}}{\mathrm{min}}$ O_2 flow (see subsection 'Bulk oxide formation' in section 7.2). The formation of a more bulk-like oxide at 3 $\frac{\mathrm{ml}}{\mathrm{min}}$ O_2 was also underlined by the in-situ gas switching results discussed in the next subsection.

Contrary to oxidation studies of pure Rh particles that were performed at 530 K and 2×10^{-5} mbar O_2 [4] the p(3×1) reconstruction on the (100)-type facets could not be observed in the present case although this reconstruction was also found to form on alloy $Pt_{25}Rh_{75}$(001) single crystals [161].

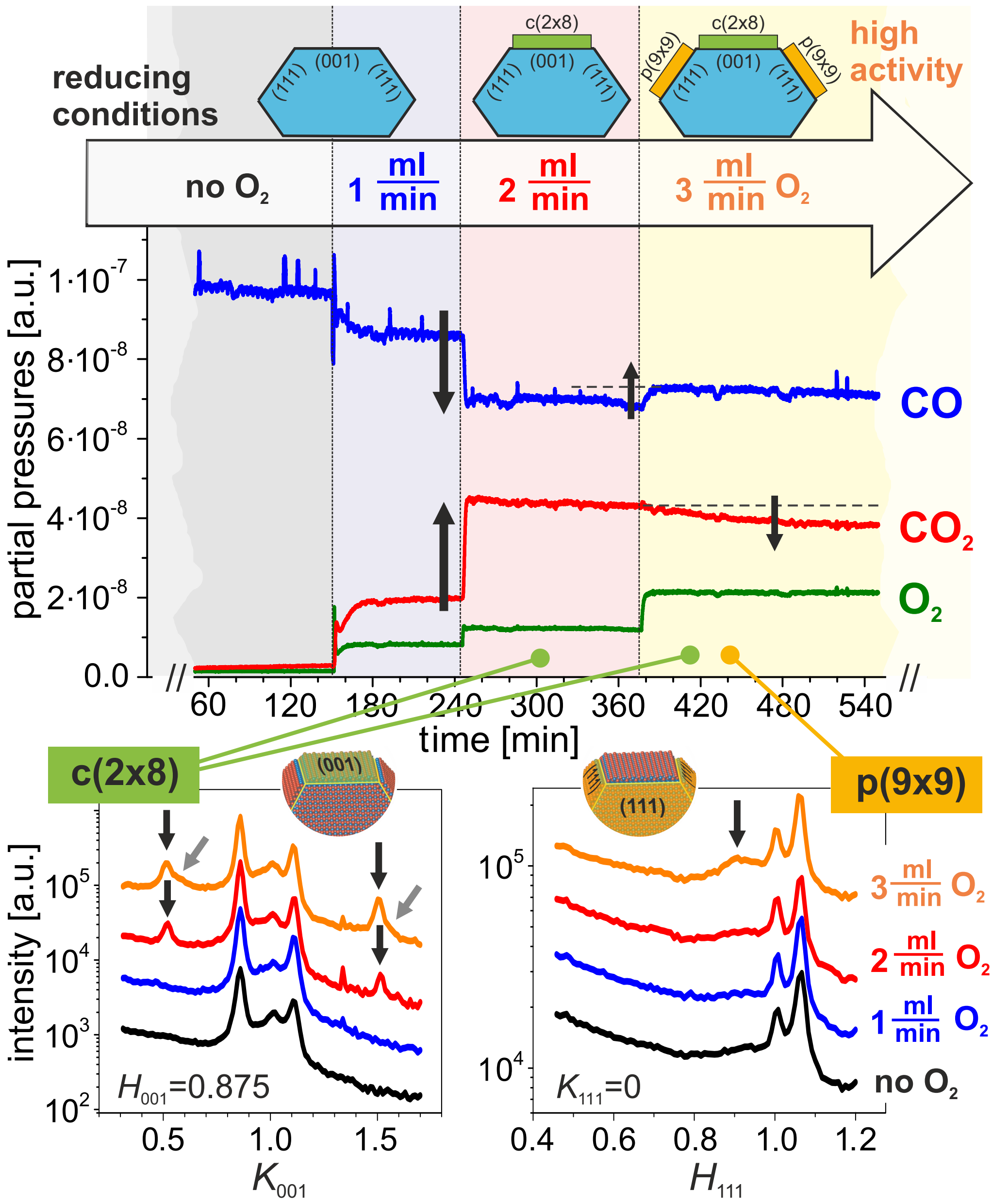

Figure 7.2: **Identification of oxide phases: top part:** Mass spectrum showing the measured partial pressures of CO, CO_2 and O_2 while keeping the inlet flow of CO constant at 4 $\frac{\text{ml}}{\text{min}}$ and stepwise increasing the O_2 flow. In the transition from 1 to 2 $\frac{\text{ml}}{\text{min}}$ of O_2 flow a strong increase of the CO_2 production along with a pronounced decrease of the CO signal was monitored '*light-off*'). **Bottom part:** reference scans for the c(2x8) and the p(9x9) Rh surface oxide structures as measured for the different O_2 flows; black arrows: surface oxide signals, grey arrows: indicate peak shoulders, probably from the RhO_2 bulk oxide. See section 7.1 for explanation of the coordinate systems.

Time-resolved in-situ gas switching

In order to obtain insights into the dynamics of surface oxide formation, the oxide signal intensities of the two surface oxides were monitored while changing the gas composition inside the reactor. The results for the c(2x8) and the p(9x9) Rh surface oxides are shown in Fig. 7.3, where in both cases the CO flow was held constant at f_{CO}=4 $\frac{\mathrm{ml}}{\mathrm{min}}$ while the O_2 gas flow was stepwise varied between f_{O2}=0 $\frac{\mathrm{ml}}{\mathrm{min}}$ and f_{O2}=3 $\frac{\mathrm{ml}}{\mathrm{min}}$.

In the case of the c(2x8) surface oxide on the (001)-type particle facets the oxide signal at $(0.875/0.5/0.03)_{100}$ was monitored during the switching, see top left of Fig. 7.3. It can be inferred from Fig. 7.3 that the c(2×8) oxide signal vanished immediately (on the order of 20 s) when the O_2 flow was switched from f_{O2}=2 $\frac{\mathrm{ml}}{\mathrm{min}}$ to f_{O2}=1 $\frac{\mathrm{ml}}{\mathrm{min}}$ and thus to oxygen understoichiometry. This implies that - although the particles were under the previous conditions completely oxidized (see previous subsection) - the oxide structures could be completely lifted. The disappearance of the surface oxide signal came along with an instantaneous decrease in CO_2 production and the corresponding correlated increase in the CO signal.

The small CO_2 production rate at f_{O2}=1 $\frac{\mathrm{ml}}{\mathrm{min}}$ can likely be traced back to a Langmuir-Hinshelwood mechanism, as no oxide was monitored under these conditions. The reaction rate vanished at f_{O2}=0 $\frac{\mathrm{ml}}{\mathrm{min}}$ and reappeared to the same rate again when switching back to 1 $\frac{\mathrm{ml}}{\mathrm{min}}$ O_2 flow.

In the transition to the catalytic light-off, i.e. when increasing the O_2 flow from 1 to 2 $\frac{\mathrm{ml}}{\mathrm{min}}$, the c(2x8) structure signal was found to emerge again with some delay. It is noticeable that its intensity was strikingly lower compared to the previous condition at f_{O2}=3 $\frac{\mathrm{ml}}{\mathrm{min}}$. It regained this previous intensity level only after increasing the O_2 flow back to 3 $\frac{\mathrm{ml}}{\mathrm{min}}$. This finding suggests that the c(2x8) structure present at 2 $\frac{\mathrm{ml}}{\mathrm{min}}$ O_2 flow either consisted of a thinner surface oxide layer compared to the one present under oxygen overstoichiometry, or even of single surface oxide patches only. Fitting of the c(2×8) surface oxide peak width in Fig. 7.2 yielded an surface oxide in-plane domain size of about 80% of the (001)-type top particle facet size under stoichiometric conditions. The notion of surface oxide patches would also be in line with a recent experimental and theoretical approach that declared the border between O-Rh-O oxide islands and the metallic $Pt_{25}Rh_{75}$ surface to be ideal sites for hosting a large number of reactants and to lower the energy barrier for CO_2 production [85]. Such borders would, however, also be present if the whole area of the

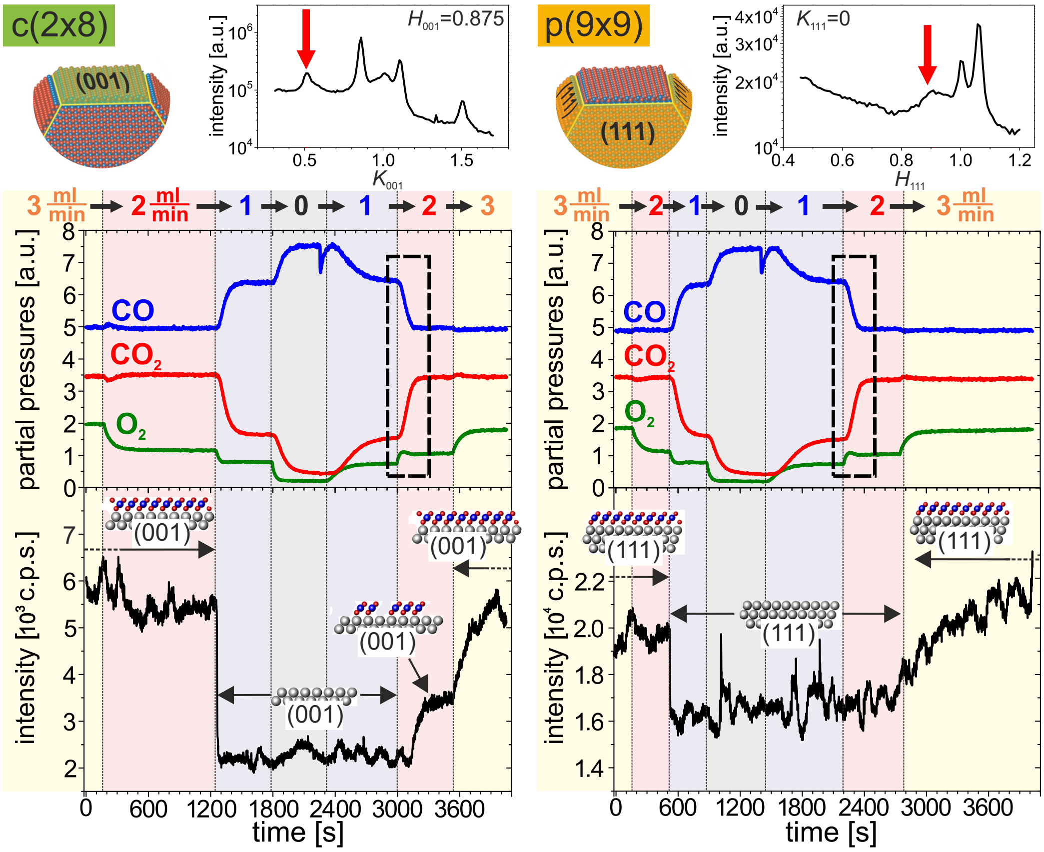

Figure 7.3: **Time-resolved in-situ gas switching while monitoring ultrathin surface oxides on particle facets:** mass spectrum and simultaneous timescans performed at positions of oxide structure signals (**left:** c(2x8); **right:** p(9x9), indicated by red arrows in the insets at the top) while switching the O_2 flow between 0 and 3 $\frac{\text{ml}}{\text{min}}$ at a constant CO flow of f_{CO}=4 $\frac{\text{ml}}{\text{min}}$. The dashed boxes indicate the timespan of the '*light-offs*', a more detailed view of which is shown in Fig. 7.4.

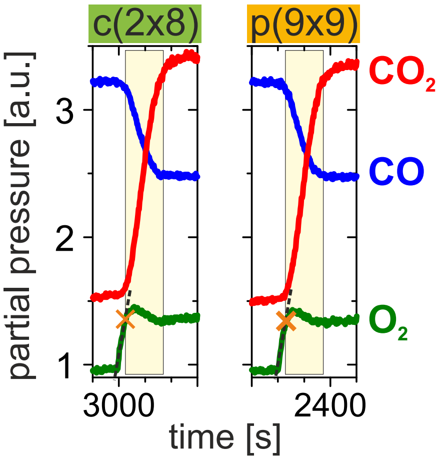

Figure 7.4: **'Light-off':** close-up on the dashed boxes in Fig. 7.3 showing the interplay between the partial pressures of CO, CO_2 and O_2 during '*light-off*'. The CO signal was divided by a factor of 2, the O_2-signal multiplied by a factor of 1.3 compared to the values in Fig. 7.3 to allow better comparison.

(001)-type facets was covered with a thin surface oxide layer, namely at the particle edges between the (001)- and the (111)-type facets, as the latter are clearly not oxidized under stoichiometric conditions.
The signal intensity increase in the transition to f_{O2}=3 $\frac{\text{ml}}{\text{min}}$ O_2 flow can also, at least partly, be traced back to the surface oxide growing into the RhO_2 bulk oxide phase as the latter gives rise to shoulders to the c(2×8) surface oxide signal peaks. These shoulders are indicated by grey arrows in Fig. 7.2. Since the emergence of the c(2×8) surface oxide signals (without peak shoulders) at f_{O2}=2 $\frac{\text{ml}}{\text{min}}$ clearly correlated with the highest CO_2 production rate and since under the presence of the bulk oxides (see next subsection) the CO_2 production decreased, the c(2×8) Rh surface oxide, or rather patches thereof along with clean metal surfaces, are likely to be the catalytically most active phases.
To track the p(9x9) Rh surface oxide on the (111)-type facets, the signal at $(1/0/0.03)_{111}$ was monitored during the in-situ gas switching, see top right of Fig. 7.3. From the time-resolved changes of the oxide signal it can be inferred that - although the p(9x9) Rh surface oxide appeared only at an oxygen flow of 3 $\frac{\text{ml}}{\text{min}}$ - also for this surface oxide an O_2 flow as low as 1 $\frac{\text{ml}}{\text{min}}$ was needed to reduce it. This hysteresis implies that, once the oxide has formed, it is nevertheless characterized by a certain stability that needs understoichiometry in O_2 flow in order to be removed again. When switching from 2 to 3 $\frac{\text{ml}}{\text{min}}$ O_2 flow the signal intensity reappeared, however, only very slowly (on the order of 10 minutes) compared to the c(2x8) Rh surface oxide signal.
The respective values of the partial gas pressures as measured with the RGA during the in-situ gas switching were found to be highly reproducible. This can also be deduced from Fig. 7.4 which shows a zoom into the dashed areas of Fig. 7.3 which correspond to the gas composition changes that were monitored in the transition from f_{O2}=2 $\frac{\text{ml}}{\text{min}}$ to f_{O2}=3 $\frac{\text{ml}}{\text{min}}$ (‘*light-off*’). It shows that the oxygen partial pressure first reaches a maximum value, then it decreases again and stabilizes at a constant level. It is interesting to note that the c(2x8) Rh surface oxide structure signal just starts to appear when the O_2 partial pressure has reached its maximum value, thereafter the oxide signal intensity keeps increasing as long as the O_2 partial pressure is decreasing. Both, the c(2x8) oxide signal intensity and O_2 partial pressure stabilize at the same time and stay constant thereafter. This implies that the difference between the maximum and the lower constant level of the O_2 partial pressure corresponds to a constant number of oxygen molecules needed to replenish the c(2x8) surface

oxide structure which is continuously consumed during the reaction. Note that the increase in c(2x8) structure signal comes along with an increase in CO_2 production and a decrease in CO signal, which both stabilize at the same time as the surface oxide signal and the O_2 partial pressure.

It is striking that the oxygen partial pressure changes monitored in the transition to high catalytic activity shown in Fig. 7.2 do not show such a characteristic oscillation. The main difference between the gas switching conditions shown in Fig 7.2 and Fig. 7.3 can be found in the total time of the switching cycles: it was by a factor of 10 slower for the data displayed in Fig 7.2, as can be inferred from the corresponding time axes. A tentative explanation could thus be that in the case of the measurement shown in Fig 7.2 oxygen molecules at 1 $\frac{\mathrm{ml}}{\mathrm{min}}$ O_2 flow had more time to accumulate on the particle surface and when the O_2 flow was switched to 2 $\frac{\mathrm{ml}}{\mathrm{min}}$ not much excess oxygen from the atmosphere was needed to form the c(2x8) Rh surface oxide. The same explanation may account for the absence of a pronounced CO_2 production decrease in the transition to 3 $\frac{\mathrm{ml}}{\mathrm{min}}$ O_2 flow in the fast gas switching cycles of Fig. 7.3: in contrast to the data of Fig. 7.2 there was not enough time to accumulate enough oxygen on the surface to immediately build up a bulk oxide poisoning the catalyst surface.

Bulk oxide formation

The radial scan in [111]-direction, whose position with respect the particle Bragg peaks in reciprocal space is shown in Fig. 7.5 b), is sensitive to signals from potential Rh bulk oxides [112]. It was thus repeatedly performed under the aforementioned sample conditions in the course of the in-situ CO oxidation experiment to keep track of potential Rh bulk oxide formation.

A selection of these scans is given in Fig. 7.5 a), along with the anticipated positions of Rh-bulk oxides indicated by vertical black lines. When, at a constant CO flow of 4 $\frac{\mathrm{ml}}{\mathrm{min}}$, the oxygen pressure was stepwise increased towards higher catalytic activity, it was repeatedly found that at an oxygen flow of 3 $\frac{\mathrm{ml}}{\mathrm{min}}$ first indications of additional signals occurred (orange line). After about 11 hours of keeping the same level of oxygen flow they grew into two pronounced peaks (yellow line) which indicate the clear presence of bulk oxides. Under 10 $\frac{\mathrm{ml}}{\mathrm{min}}$ of pure O_2 flow the peaks grew even more intense (purple line), implying that the oxides had become thicker under these conditions. In each case the

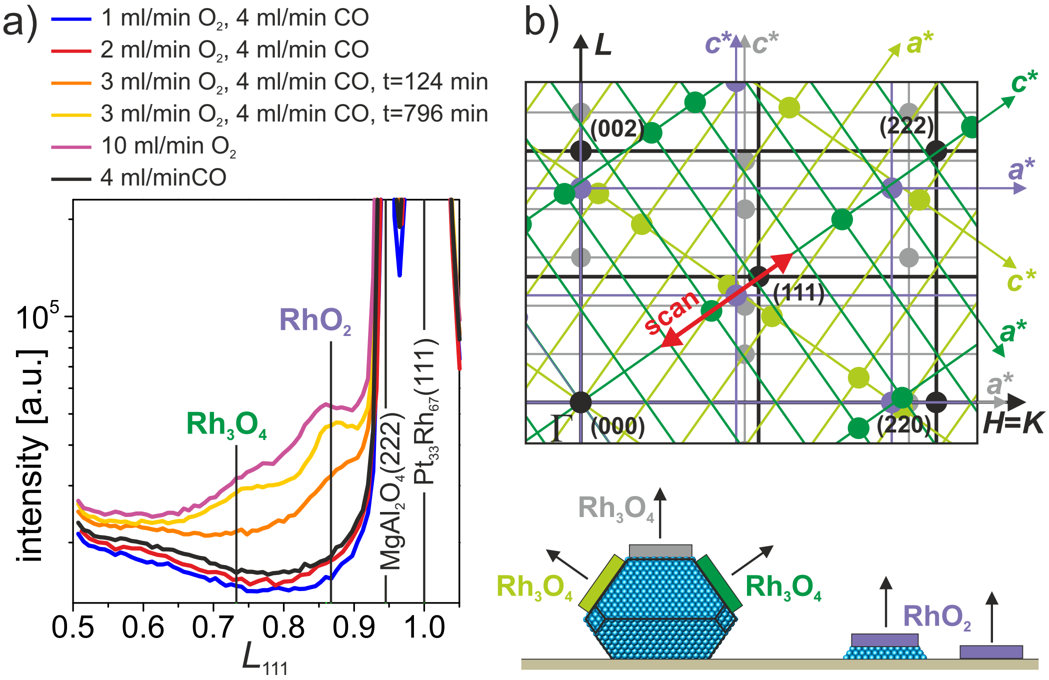

Figure 7.5: **Identification of bulk oxides: a):** reference scan for bulk oxides performed at 673 K under different stages of oxidation, Bragg peak positions of RhO$_2$ and of the spinel-like Rh$_3$O$_4$ are indicated; **b):** sketch of potential Rh bulk oxides growing on particle facets whose Bragg peak positions are indicated in the reciprocal space map at the figure top along with particle Bragg peak positions (black circles). The position of the reference scan shown in a) is represented by the red arrow. See section 7.1 for explanation of the coordinate systems.

peaks could be entirely removed again under 4 $\frac{\mathrm{ml}}{\mathrm{min}}$ pure CO flow (black line), which can be explained by the total lifting of the bulk oxides under reducing conditions.

Fig. 7.5 b) sketches the growth of different Rh bulk oxides on various particle facets, whose Bragg peak signals can explain the peaks found in the reference scans of Fig. 7.5 a). Their corresponding reciprocal lattices with respect to the scan and the particle Bragg peak positions in the (H=K, L)-plane are displayed at the top of 7.5 b), which sticks to the colour coding of the bottom part.

It reveals that the peak that occurs at approximately L_{111}=0.74 can be traced back to the formation of a distorted spinel-like Rh$_3$O$_4$ bulk oxide (a=b=6.16 Å, c=17.7 Å; α=β=90°, γ=120°) growing in a (001)-orientation on the particle (111)-type facets [112] (see also section 3.1.5). This oxide was recently identified for the first time in an in-situ oxidation study of MgAl$_2$O$_4$(001)-supported Rh-Pd nanoparticles [112], and was also concluded to appear on the particle

(100)-type facets.
The peak that is located at L_{111}=0.86 is compatible with a rutile RhO_2 structure (a=b=3.09 Å, c=4.49 Å; α=β=γ=90°) growing either on the (001)-type top facets of the nanoparticles or epitaxial to the substrate as the result of the complete oxidation of smaller particles. The latter scenario was proposed in the aforementioned study [112].

7.3 Activity-driven particle shape changes and sintering

The previous section dealt with the identification of the oxides that formed on the various particle facets under activity conditions. As was explained in subsection 3.2.2, oxides may trigger particle shape changes. The present section discusses the shape changes, triggered by the emergence of the c(2×8) and p(9×9) Rh surface oxides, which the particles underwent in the transition to high catalytic activity. Furthermore, the particle size and structure changes due to nanoparticle sintering will be addressed.

High resolution reciprocal space mapping under catalytic activity

Fig. 7.6 shows high resolution reciprocal space maps centered around the particle (111) peak that were measured during steady state conditions of CO oxidation at 3 $\frac{\mathrm{ml}}{\mathrm{min}}$ O_2 and 4 $\frac{\mathrm{ml}}{\mathrm{min}}$ CO flow at 673 K. As was shown in section 7.2 both, the c(2x8) Rh surface oxide on the (001)-top facets and the p(9x9) Rh surface oxide on the (111)-type facets, were present under these conditions.
Fig. 7.6 a) displays the (H+K=2, L)-map in out-of-plane direction which is sensitive to signals of particle facets whose surface normals lie in this plane. These include (111)-type facets, (001)-type top and (110)-type side facets whose surface normals are indicated by arrows surrounding the sketched nanoparticle on the left side of Fig. 7.6 a). The measured map reveals strong signals from (001)- and (111)-type facets, while any signals from higher indexed facets are absent. This implies that the particle shape was clearly dominated by (001)- and (111)-type facets and that the particles featured the well-defined shape of a truncated octahedron, even under high activity conditions for CO oxidation. The strong intensity of the (001)-type facet signal can not only be traced back to a large facet size but also to the presence of the c(2x8) Rh sur-

face oxide, whose surface rod signal coincides with the position of the particle (001)-rod (see Fig. 4.3 in subsection 4.1.1).

The (H=K, H+K=2, L=1)-in-plane map which is shown in Fig. 7.6 b) is in accordance with a truncated octahedral particle shape. The map is sensitive to signals from particle facets located along the particles' peripheries; the surface normals of some of them are indicated by the black arrows drawn around the particle sketch on the left side of Fig. 7.6 b). In the measured map subtle intensity protrusions along the [001]-direction at lower Q-values may indicate the presence of in-plane (100)-type facets. Their presence is highly likely since also the (100)-type *side* facets were found to be stabilized by the c(2x8) Rh surface oxide [4] (see also Fig. 7.11 and the corresponding discussion).

The elongation of the Bragg peak shape along the [H=K]-direction in the in-plane map of Fig. 7.6 b) hints at the presence of (110)-type side facets. Further signals of the (110)-type facets would be anticipated along the [H+K=2]-direction in the in-plane map of Fig. 7.6 b), and along the [H+K=2]-direction in the out-of-plane map of Fig. 7.6 a). These positions, however, coincide with the pronounced ring-shaped Bragg peak broadenings caused by the particles' mosaicity, which are in Fig. 7.6 a) and b) indicated by the dashed circle segments. In the out-of-plane map this smearing out of the Bragg peak intensity can be traced back to particles that are tilted with respect to the surface normal; in case of the in-plane map it is caused by particles tilted around the surface normal.

Apart from the features discussed so far, additional signals are present in the reciprocal space maps of Fig. 7.6, they will be explained in the following. The regions of increased intensity along the ring-like mosaicity broadening, which are labeled a and b, can be explained by (001)-oriented particles that are tilted by an angle of ≈35° around the substrate [110]-direction. Section 6.1 showed that the growth of such particles is promoted if the substrate pretreatment did not include repeated sputtering and annealing cycles, as was the case for this sample (see sample "spinel-1" in Table 6.1). The broad intensity lobes labeled c, d, e and f stem from internal twinning. The signal labeled g corresponds to a Bragg peak of the (110)-oriented particles, while the areas of increased intensity denoted h and i can be explained by diffuse scattering of the MgAl$_2$O$_4$(001)-substrate. The signals at the positions labeled j, k and l correspond to tails of Bragg peaks from (111)-oriented particles.

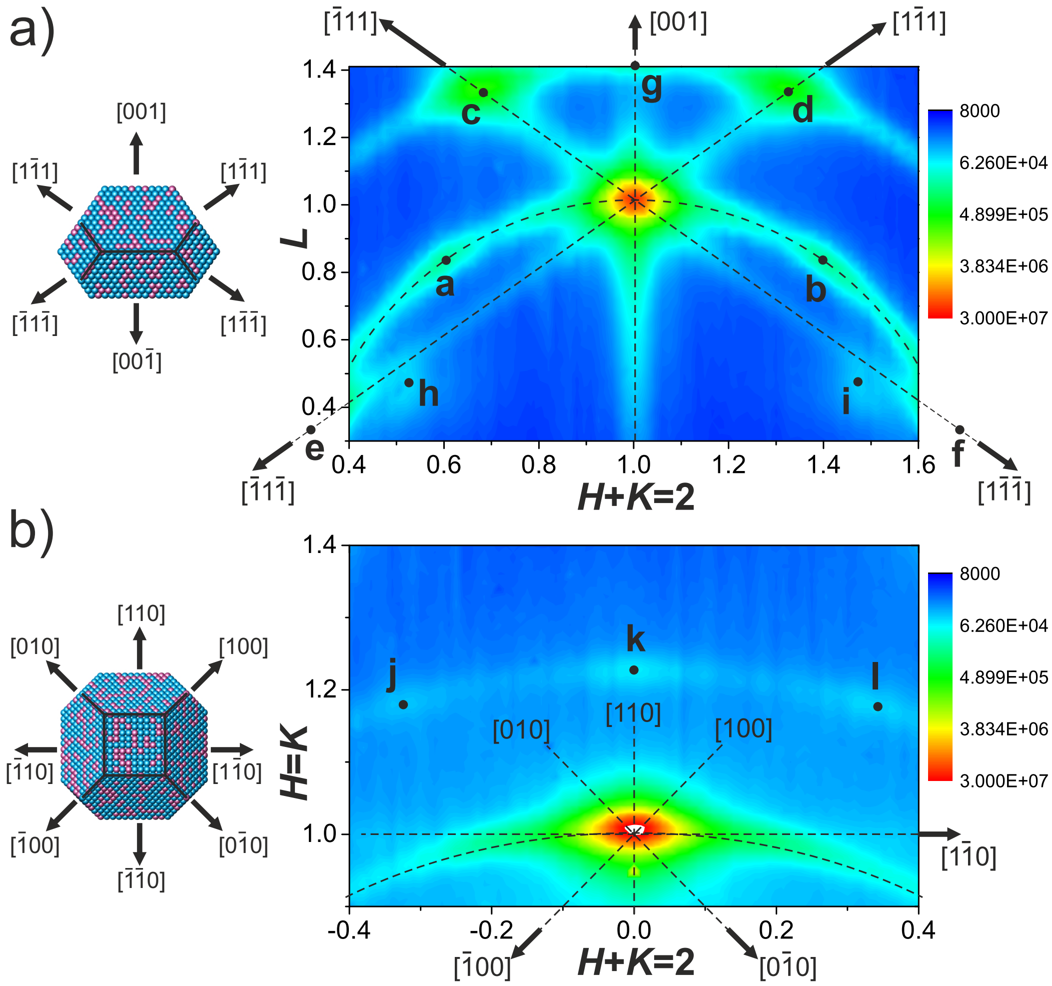

Figure 7.6: **High resolution reciprocal space maps measured under catalytic activity: a):** out-of-plane reciprocal space map in the (H+K=2, L)-plane; **b):** in-plane reciprocal space map in the (H=K, H+K=2, L=1)-plane. Both maps are centered around the particle (111) Bragg peak and were measured at activity conditions of 3 $\frac{\text{ml}}{\text{min}}$ O_2 and 4 $\frac{\text{ml}}{\text{min}}$ CO flow. See section 7.1 for explanation of the coordinate systems.

Qualitative particle shape changes

Section 7.2 showed that the c(2x8) and the p(9x9) Rh surface oxides, present on the particle facets under catalytic activity conditions (f_{O2}=3 $\frac{\mathrm{ml}}{\mathrm{min}}$, f_{CO}=4 $\frac{\mathrm{ml}}{\mathrm{min}}$), could be immediately lifted again when switching back to reducing conditions (f_{O2}=0 $\frac{\mathrm{ml}}{\mathrm{min}}$, f_{CO}=4 $\frac{\mathrm{ml}}{\mathrm{min}}$). Since the surface energies of the particle facets depend on the presence of adsorbed species, particle shape changes can be expected when switching between these different sample environments. By repeatedly mapping facet signals in reciprocal space under the different conditions, information on possible particle shape changes can be deduced [4].

Fig. 7.7 shows a sequence of high resolution reciprocal space maps measured in the (H+K=2, L)-plane under alternating conditions of UHV / reducing (f_{O2}=3 $\frac{\mathrm{ml}}{\mathrm{min}}$, f_{CO}=4 $\frac{\mathrm{ml}}{\mathrm{min}}$) and oxidizing atmospheres under catalytic activity (f_{O2}=3 $\frac{\mathrm{ml}}{\mathrm{min}}$, f_{CO}=4 $\frac{\mathrm{ml}}{\mathrm{min}}$). The right panel displays the corresponding difference maps which are sensitive to the changes in signal intensity. They were obtained from the measured maps of the left panel via $\frac{I_{n+1}-I_n}{I_n}$, where I_n represents the reciprocal space map measured under condition n. The maps were measured at selected points in time in the course of the experiment, the timeline of which including the various conditions can be deduced from Fig. 7.11.

The difference maps show that the intensity of the (001)-type top facets strongly increased in the transition to conditions of high catalytic activity. As mentioned above, this can be traced back to an enlargement of the (001)-type top facets and/or the appearance of the c(2x8) Rh surface oxide structure, which was shown to be present under these conditions.

The intensity changes along the (001)-rod were moreover found to be accompanied by subtle changes of the (111)-type facets' intensities, as can be inferred from the linescans performed at L=0.7 which are shown in Fig. 7.8. They reveal that an increase of the (001)-type facet intensity came along with a decrease in intensity of the (111)-type particle facet signals and vice versa when switching between reducing conditions and conditions of high catalytic activity. These data suggest that in the transition to high catalytic activity a restructuring of the $\mathrm{Pt}_{0.33}\mathrm{Rh}_{0.67}$ particles occurred which featured a simultaneous shrinking of the (111)-type facets and an enlargement of the (001)-type facets. The strong intensity increase of the (001)-type facet signal in the transition to catalytic activity cannot solely be ascribed to the formation of the c(2x8) surface oxide, since a shrinking of the (111)-type facets prerequisites an increase in the (001)-type facet size. This assumption is moreover underlined

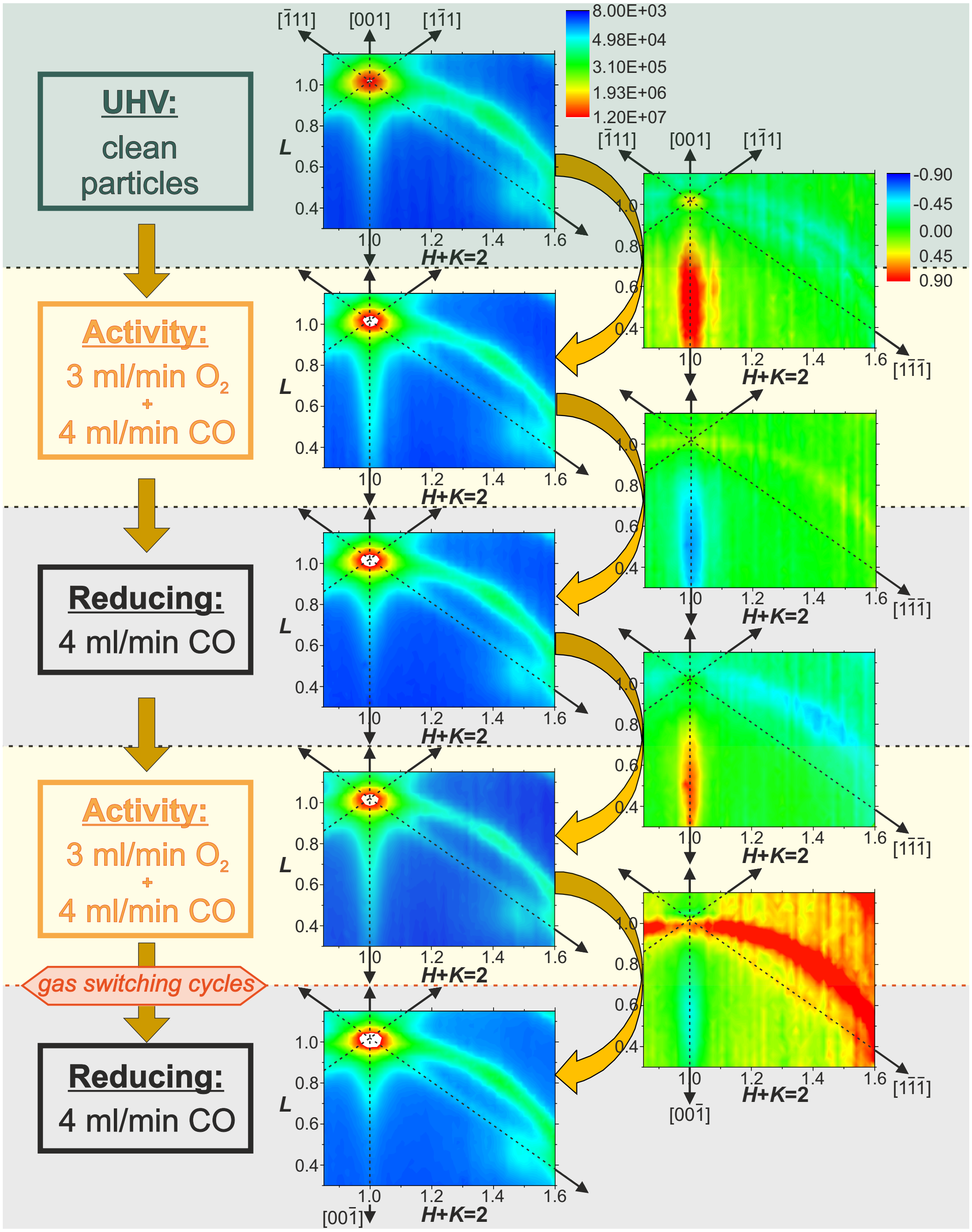

Figure 7.7: **Activity-induced particle shape changes: centre:** high resolution reciprocal space maps measured under alternately reducing conditions and conditions of high catalytic activity. The maps were measured (from top to bottom) under conditions A, C, D, E, and G (see Fig. 7.11 for timeline); **right:** difference maps obtained via $\frac{I_{n+1}-I_n}{I_n}$ from which signal changes can be deduced; the last difference map shows an increase in the ring-like signals from the mosaicity broadening: an increasing particle mosaicity can probably be traced back to the harsh conditions of repeated gas switching cycles between conditions E and G (see Fig. 7.11).

by the fact that no signals belonging to higher indexed facets, which could compensate for the decrease of the (111)-type facet size, were monitored. Thus, the particles retained their truncated octahedral shape.

After switching back to reducing conditions the intensities of the particle signals readopted their former values. These observations were repeatedly made during several cycles which suggests that the particles shape changes were reversible.

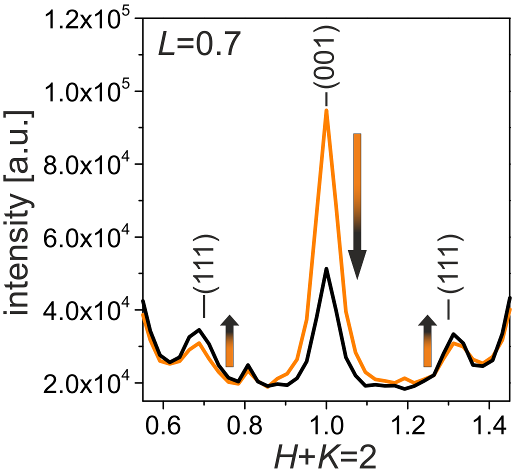

Figure 7.8: **Facet scans:** linescans which are sensitive to signals of the particle (001)- and (111)-type facets performed along the $[H{+}K{=}2]$-direction at $L{=}0.7$ under conditions of high catalytic activity (orange, $f_{\mathrm{O2}}{=}3\ \frac{\mathrm{ml}}{\mathrm{min}}$, $f_{\mathrm{CO}}{=}4\ \frac{\mathrm{ml}}{\mathrm{min}}$) and under reducing conditions (black, $f_{\mathrm{O2}}{=}0\ \frac{\mathrm{ml}}{\mathrm{min}}$, $f_{\mathrm{CO}}{=}4\ \frac{\mathrm{ml}}{\mathrm{min}}$).

Comparing the behaviour of the $\mathrm{Pt_{0.33}Rh_{0.67}}$ alloy particles just discussed to the ones of pure Rh and pure Pt particles during oxidation and reduction cycles [4, 152] leads to the conclusion that the alloy particles rather feature the characteristics of Rh than of Pt:

in the case of pure Rh particles, it was found that, in line with the above results, the size of the (001)-type facets increased at the expense of the (111)-type facets in the transition to oxidizing conditions, and no additional facets appeared. The shape changes were concluded to be driven by the same surface oxides as detected on the $\mathrm{Pt_{0.33}Rh_{0.67}}$ alloy particles and were found to be reversible upon CO exposure [4]. Contrary, in the case of pure Pt particles, the particle shape change in the transition to oxidizing conditions was not only featured by an increase of the (001)- and a decrease of the (111)-type facets, but also by the emergence of higher index facets. Moreover, the oxygen-induced Pt particle shape changes were found to be irreversible upon repeated CO exposures and strong annealing treatments [152].

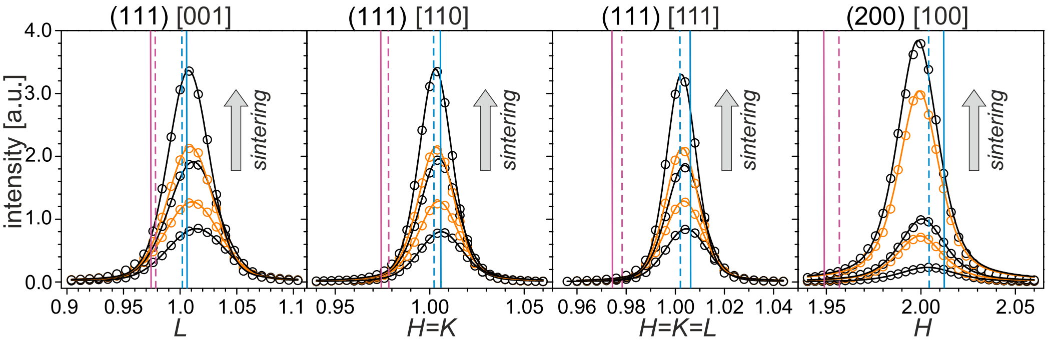

Figure 7.9: **High resolution Bragg peak scans:** they were performed through the particle (111) and (200) Bragg peaks along high symmetry directions which are denoted by square brackets; open circles represent experimental data, solid lines fit to the data using Pseudo-Voigt functions (black: f_{O2}=0 $\frac{\text{ml}}{\text{min}}$, f_{CO}=4 $\frac{\text{ml}}{\text{min}}$; orange: f_{O2}=3 $\frac{\text{ml}}{\text{min}}$, f_{CO}=4 $\frac{\text{ml}}{\text{min}}$; they correspond to conditions B, C, D, E, G in Fig. 7.11). The solid vertical lines indicate the calculated Bragg peak positions of bulk Pt (purple) and bulk Rh (blue) under consideration of the lattice parameter's thermal expansion. The dashed lines represent the respective peak positions assuming phase separation into $Pt_{0.87}Rh_{0.13}$ (purple) and $Pt_{0.12}Rh_{0.88}$ (blue).

Quantitative particle shape changes and sintering

The previous subsection discussed the *qualitative* particle shape changes that occurred in the transition to conditions of high catalytic activity. Here, the *quantitative* changes will be addressed. They were obtained from high resolution scans through the particle Bragg peaks performed along high symmetry directions as was discussed in subsection 4.2.2.

The experimental data of these scans and their Pseudo-Voigt fits are plotted in Fig. 7.9 for the alternating conditions of (1) no O_2 flow and f_{CO}=4 $\frac{\text{ml}}{\text{min}}$ (black) and (2) catalytic activity at f_{O2}=3 $\frac{\text{ml}}{\text{min}}$ and f_{CO}=4 $\frac{\text{ml}}{\text{min}}$ (orange).

For the quantitative analysis the FWHMs of the high symmetry scans shown in Fig. 7.9 were simulated as a function of the particle parameters N_P, N_E, N_T and N_B covering a large parameter space (N_P: 25-55, N_E: 0-28, N_T: 0-55, N_B: 0-55). The simulation took the particle size distribution into account, as it has an impact on the FWHMs of the particle Bragg peaks (see subsection 4.2.3). From SEM measurements performed after the CO oxidation the lateral size distribution was determined to comprise 76.81% (see Fig. 7.13 a) and inset thereof). In the simulation this size distribution was assumed to be valid along all probed high symmetry directions.

The simulated FWHMs were compared to the experimental ones employing $\chi^2=\sum\limits_i(\frac{FWHM(i)_{\text{cal}}}{FWHM(i)_{\text{exp}}}$ - $1)^2$, where i denote the probed high symmetry directions

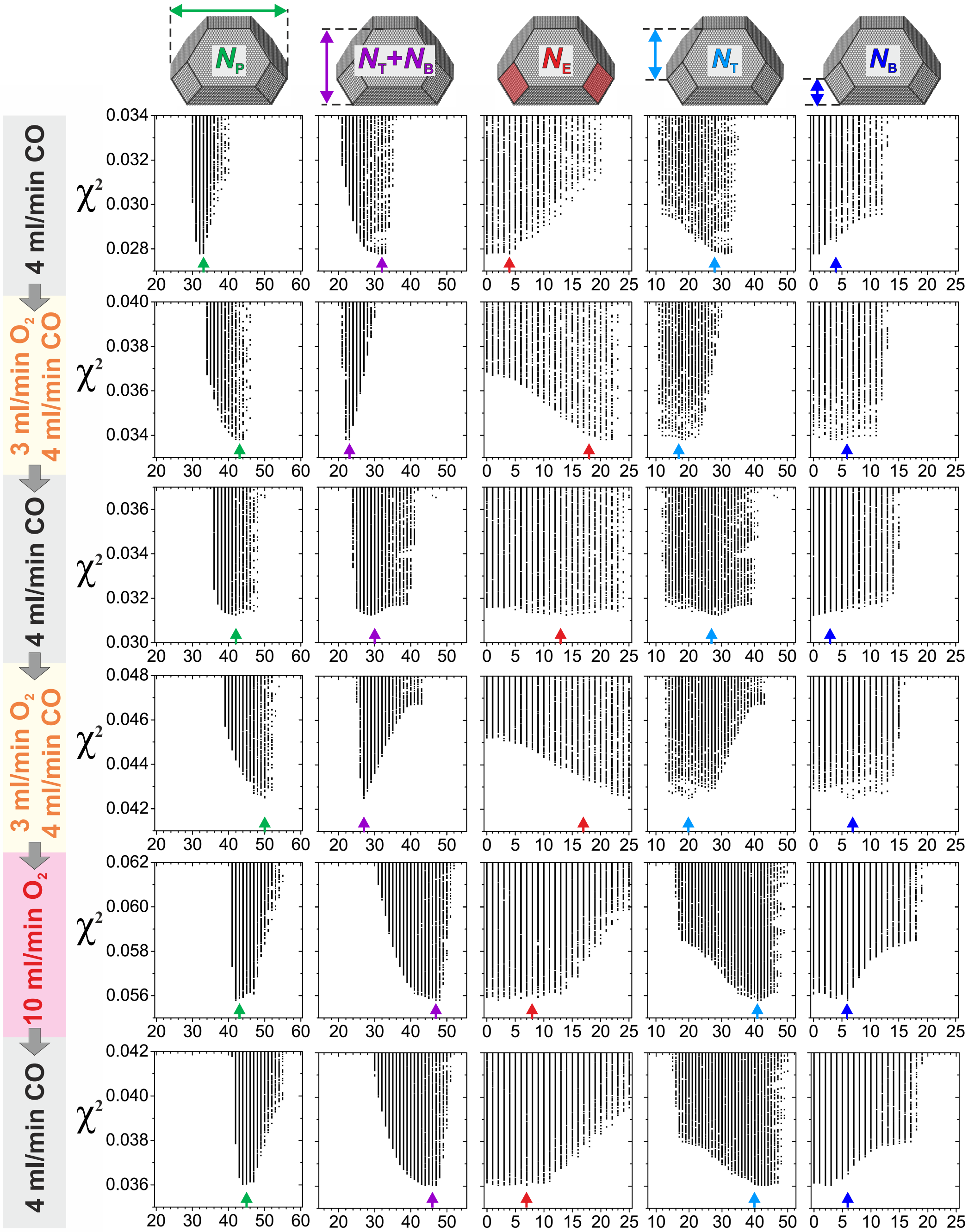

Figure 7.10: **Fit results of the high resolution Bragg peak scan analysis:** for the probed conditions B, C, D, E, F, G (from top to bottom, see Fig. 7.11 for timeline of the experiment) the figure of merit χ^2 is projected on the different particle parameters N_P, N_T+N_B, N_E, N_T and N_B. The coloured arrows represent the particle parameters that follow the general trends and that were used for the determination of the quantitative particle shapes shown at the bottom of Fig. 7.11.

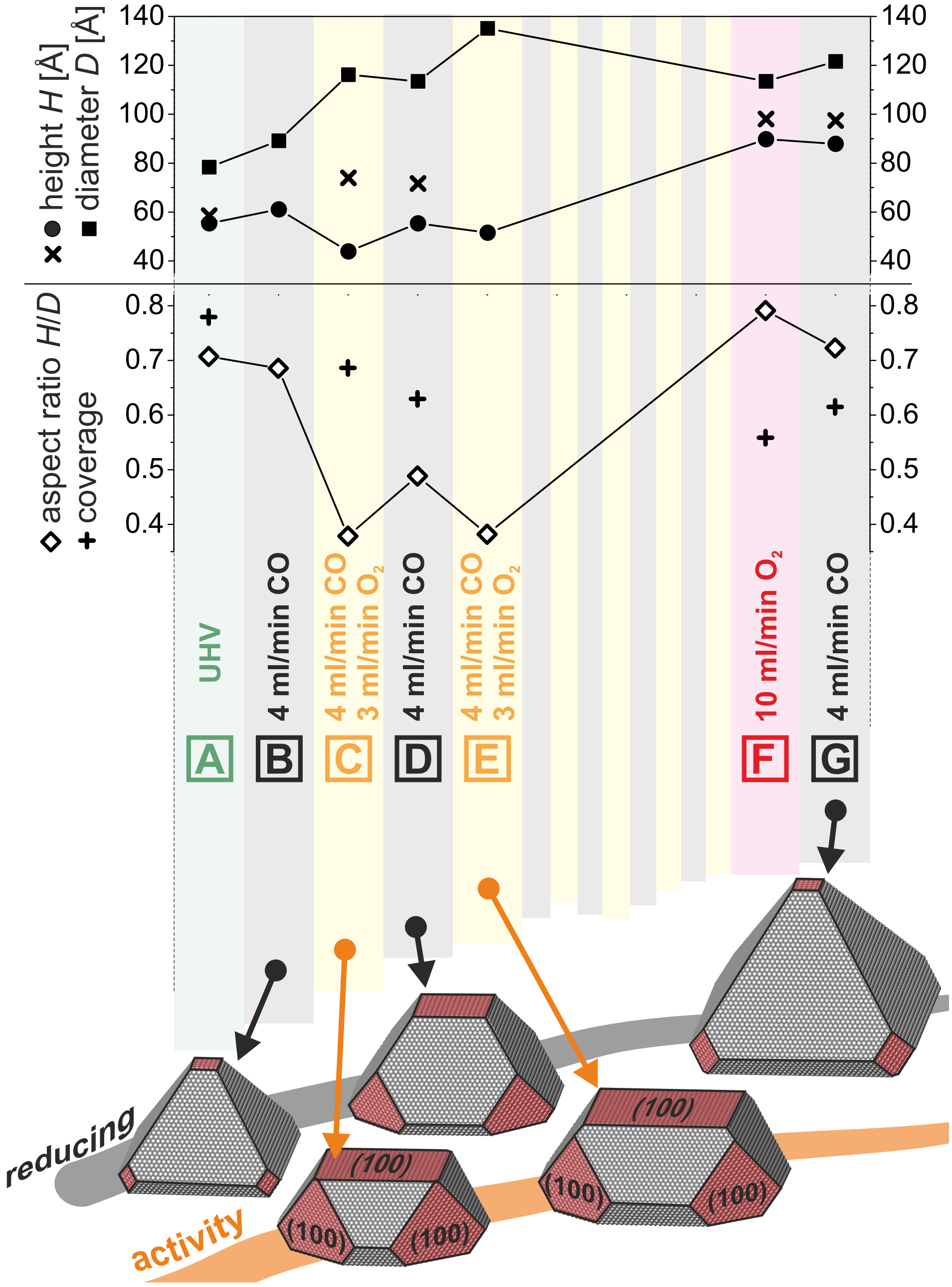

Figure 7.11: **Particle height, diameter and aspect ratio changes:** the filled circles, squares and the open diamonds represent the height, diameter and aspect ratios as obtained from the high resolution Bragg peak scan analysis under conditions A-G in the course of the experiment. The crosses were deduced from reflectivity measurements shown in Fig. 7.12 and correspond to the thus obtained particle heights and sample surface coverages. The bottom shows for some selected conditions the quantitative particle shapes as retrieved from the particle fit parameters indicated by arrows in Fig. 7.10.

of Fig. 7.9[1]. The obtained figures of merit χ^2, whose minima mark the best particle parameter match to the experimental data, are in Fig. 7.10 projected onto the different particle parameters as a function of sample condition. Fig. 7.11 summarizes the thus obtained particle heights, diameters and $\frac{H}{D}$ aspect ratios. Although distinct minima were not obtained for all parameters and/or conditions (especially parameter N_E), clear trends are observable which are indicated by the correspondingly coloured arrows in Fig. 7.10. The thus deduced quantitative particle shapes are plotted at the bottom of Fig. 7.11 for selected conditions, the trends will be discussed in the following.

For N_P and the sum N_T+N_B distinct minima in χ^2 are discernible for all sample conditions. It is striking that they shifted towards larger values of N_P and N_T+N_B in the course of the experiment, which implies that the $\mathrm{Pt}_{0.67}\mathrm{Rh}_{0.33}$ particles continuously sintered severely in both, height and diameter. Fig. 7.11 shows that their respective values increased from about 55 Å and 80 Å at the beginning, to 90 Å and 125 Å at the end of the experiment. The strong gradual sintering is also mirrored in the steady increase of the Bragg peak intensity from cycle to cycle, as is indicated by the grey arrows in Fig. 7.9 (note also the increasing peak intensities in the maps of Fig. 7.7).

The FWHM analysis moreover discloses that in the course of the cycles, characterized by reducing conditions and conditions of high catalytic activity, the height and diameter changed gradually but at the same time in an oscillatory manner, where the values for height and diameter showed an opposing trend: during high catalytic activity conditions the height was reduced and the diameter enlarged, which was both reversed again under reducing conditions (see Fig. 7.10 and 7.11). This trend is also mirrored in the particle aspect ratio $\frac{H}{D}$ included in Fig. 7.11, which reached minimal values under activity conditions, but fully recovered again under CO flow.

As it is only the metallic particle core that gives rise to the probed particle Bragg peak signals, the above observations can be explained in terms of the formation of bulk oxides on the nanoparticle (001)-top facets: a growing oxide removes metal atoms from their respective fcc sites and thus reduces the number of scattering layers along the monitored high symmetry direction, which would in this case mean along the [001]-direction, where the removal of one layer corresponds to a height decrease of about 2 Å. This assumption is in

---

[1] Parameter sets that describe unphysical particle shapes were not considered in the comparison. The parameters were ruled out if they fulfilled one or more of the following criteria: I.: N_T-N_B>0; II.: $\frac{N_\mathrm{P}}{2}$-N_E>0; III.: N_P-N_T>0; IV.: N_P-N_B>0.

line with the previously discussed finding that the (001)-type top facets of the $Pt_{0.67}Rh_{0.33}$ particles were found to be more prone to oxidation compared to the (111)-type facets. Furthermore, the shifting of the minimum χ^2 values towards smaller N_T parameters for conditions of high catalytic activity suggests a shrinking of the particle top part, while the parameter N_B and thus the particle bottom part remains rather stable, which is both in agreement with an oxide formation on the particle top (001)-facets.

Although no distinct minima were obtained for the particle parameter N_E, which is a measure for the size of the (100)-type side facets, some trends are clearly discernible. Fig. 7.10 discloses that under reducing conditions the best agreement between simulated and experimental data was obtained for very small N_E-values which indicates the presence of only tiny (100)-type side facets. Contrary, for conditions of high catalytic activity the χ^2-values suggest pronounced side facets. This is in line with the in-plane reciprocal space map shown in Fig. 7.6, which contained indications for (100)-type side facet signals during catalytic activity conditions. Since the (001)-top facets were found to be easily oxidized, this might also hold for the (100)-side facets, and they may undergo an oxygen-induced enlargement in the transition to high catalytic activity. A growth of the (100)-side facets under oxidizing environments and their decrease under reducing conditions was also monitored on pure Rh particles in the course of in-situ oxidation and reduction cycles [4].

In order to obtain complementary information on the particle height but also on the percentaged particle coverage on the substrate surface, **x-ray reflectivity measurements** were performed in the course of the experiment. Their sequence is depicted in Fig. 7.12 a) along with their fits and deduced electron density profiles, where in each case a two-layer box model was employed as underlying fit model. The obtained particle heights and percental coverages are in Fig. 7.11 represented by crosses. They reveal that the particle height increased in the course of the experiment at the expense of the percental coverage, which decreased from about 80% in the case of the as-prepared particles down to about 60% at the end of the experiment. Contrary to the Bragg peak scan results the heights obtained from the reflectivity measurements show a gradual increase and do not reflect an oscillatory behaviour, as x-ray reflectivity is not only sensitive to the crystalline fcc sites of the metal lattice but also to the oxidized parts of the particles. The general underestimation of the particle heights obtained from the x-ray reflectivity data can be traced back

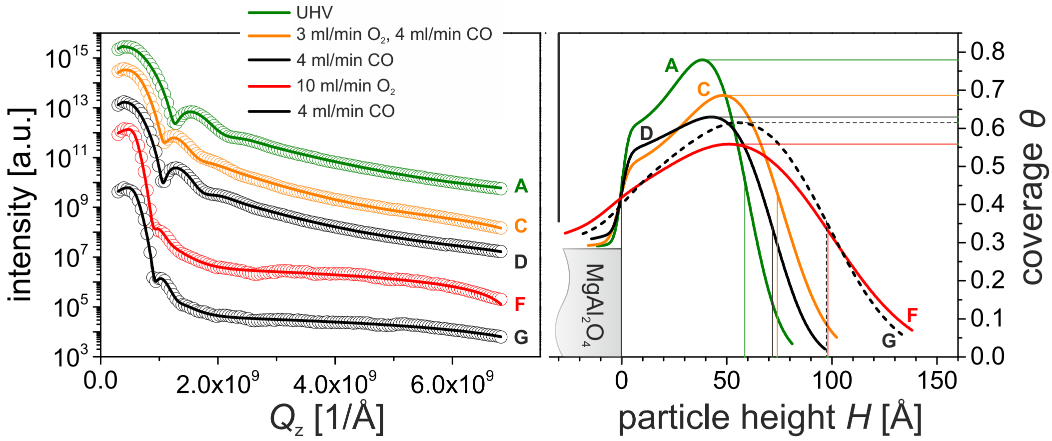

Figure 7.12: **Reflectivity measurement results: left:** reflectivity data (open circles) and fits (solid lines) for sample conditions A, C, D, F and G (see Fig. 7.11 for timeline of conditions), all fits were performed using a 2-layer box model; **right:** electron density profiles obtained from the fits that yield information on the particle height and percentaged coverage on the sample surface.

to the simple box model that are used in the fitting procedure [152].

The shapes of the reflectivity curves measured under the rather harsh conditions of 10 $\frac{\text{ml}}{\text{min}}$ pure O_2 flow after several cycles of switching between reducing and activity conditions, reveal a much stronger damping of the Kiessig oscillations compared to the curves measured during the first cycle. As can also be inferred from the respective electron density profiles the fit suggests for the strongly sintered particles an increased vertical size distribution, which also could not be recovered by the subsequent reducing conditions.

The **SEM and AFM data** of Fig. 7.13 a)-c) measured after the CO oxidation experiment confirmed the picture of greatly roughened particles that suffered from the harsh reaction conditions: the sintered particles reveal necked interconnections (Fig. 7.13 a)) or even mesh-like structures (Fig. 7.13 b)) which can only partially be explained by particle coalescence. These features stand in stark contrast to the particle morphology expected after deposition which is characterized by well-separated, individual particles as shown in Fig. 7.13 d), which displays SEM data measured on a comparable sample of as-prepared $MgAl_2O_4$(001)-supported $Pt_{0.67}Rh_{0.33}$ particles. This indicates that the mesh-like particle features can indeed be traced back to reaction-induced sintering and particle morphology changes and not to particle growth process during deposition.

The insets of Fig. 7.13 a) and d) yield the respective particle size distributions of the sintered and the as-prepared particles. They were obtained by assuming

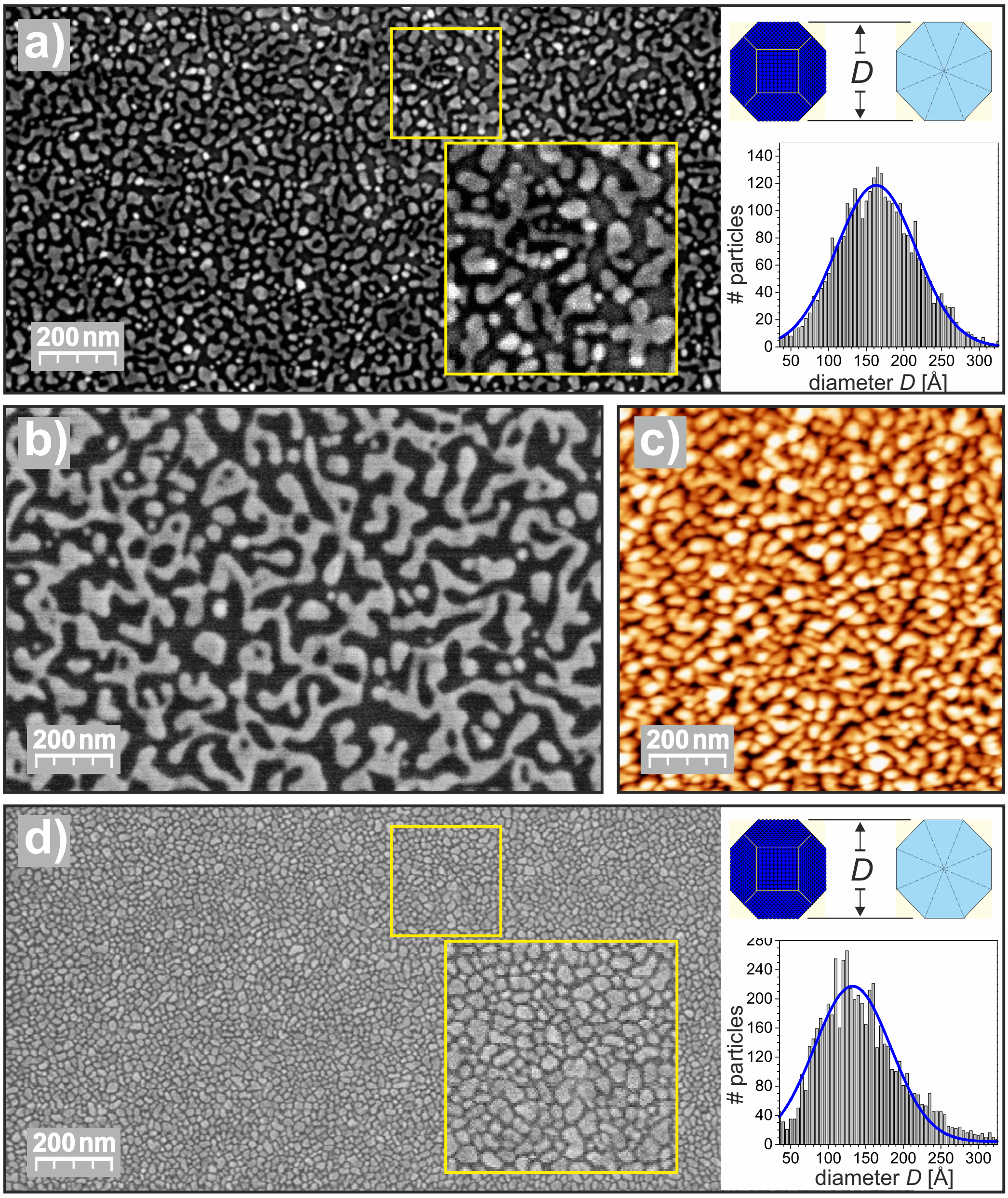

Figure 7.13: **Comparison of microscopy measurements performed after and before CO oxidation. a), b):** SEM images, and **c):** AFM image of the sintered $Pt_{0.33}Rh_{0.67}$ particles discussed in this chapter displaying structures of necked (a)) or even meshlike (b)) islands; **d):** SEM image of as-prepared $MgAl_2O_4(001)$-supported $Pt_{0.67}Rh_{0.33}$ particles of a comparable sample. The insets in **a)** and **d)** show the lateral particle size distribution based on assuming octagons as particle contours. The SEM images in a) and b) were performed by Carl Zeiss Microscopy, Oberkochen, the one in d) by the University of Jena. The AFM image in c) was measured by P. Müller.

octagons as underlying particle shapes, which correspond to the projection of truncated octahedrons. In the case of the sintered $Pt_{0.33}Rh_{0.67}$ particles the contours of obviously coalesced particles were for the analysis separated from each other by black lines. The Gaussian fit to their size distribution suggests an average diameter of 163 Å and a lateral size distribution of 76.81% (as mentioned earlier in this subsection), while the percentaged coverage was estimated to comprise 45%. These values are not too far off the x-ray data suggesting a diameter of about 130 Å and a percental coverage of approximately 60% after CO oxidation (see Fig. 7.11). Moreover, the SEM data are in line with the x-ray results' finding of a sinter-induced particle size increase at the expense of the percentaged particle coverage, since the SEM analysis of the as-prepared $Pt_{0.67}Rh_{0.33}$ particles of Fig. 7.13 d) reveal a slightly higher coverage of 50% along with a smaller lateral size of 132 Å. In general, such Pt-rich particles are characterized by a smaller height to diameter aspect ratio and thus larger values for the diameter compared to Rh-rich particles (see chapter 6). Thus, it is likely that the Rh-richer $Pt_{0.33}Rh_{0.67}$ particles of Fig. 7.13 a)-c) featured an even smaller lateral size prior to the CO oxidation experiment.

A **possible origin of the mesh-like structures** of the sintered particles depicted in Fig. 7.13 a)-c) can be found in the formation of wetting Rh oxides. In general it has been observed that metal oxides show a higher tendency to wet supports compared to their parent metals [199, 200, 201, 202]. Thus, the previously discussed Rh oxides that in the transition to high catalytic activity grow around the $Pt_{0.33}Rh_{0.67}$ particles may tend to further spread onto the $MgAl_2O_4(001)$ surface. This may even lead to the coalescence of adjacent particles resulting in the observed particle network.

A similar scenario was concluded for Pt-rich $Al_2O_3(0001)$-supported Pt-Rh alloy particles under annealing at 1073 K in an oxidative atmosphere, resulting in particle structures that highly resemble the ones displayed in Fig. 7.13 a)-c) [199], while the pure Pt and Rh particles were not affected and preserved their defined shapes.

The values of the **in- and out-of-plane particle lattice parameters** underpin the aforementioned Rh oxide wetting. They were deduced from the maxima of 3 different particle Bragg peaks that were scanned along various directions (see also Fig. 7.9). Fig. 7.14 depicts the $Pt_{0.33}Rh_{0.67}$ nanoparticle lattice parameters as a function of sample condition. The thermally expanded bulk lattice parameters of pure Pt and pure Rh would comprise 3.9371 Å and

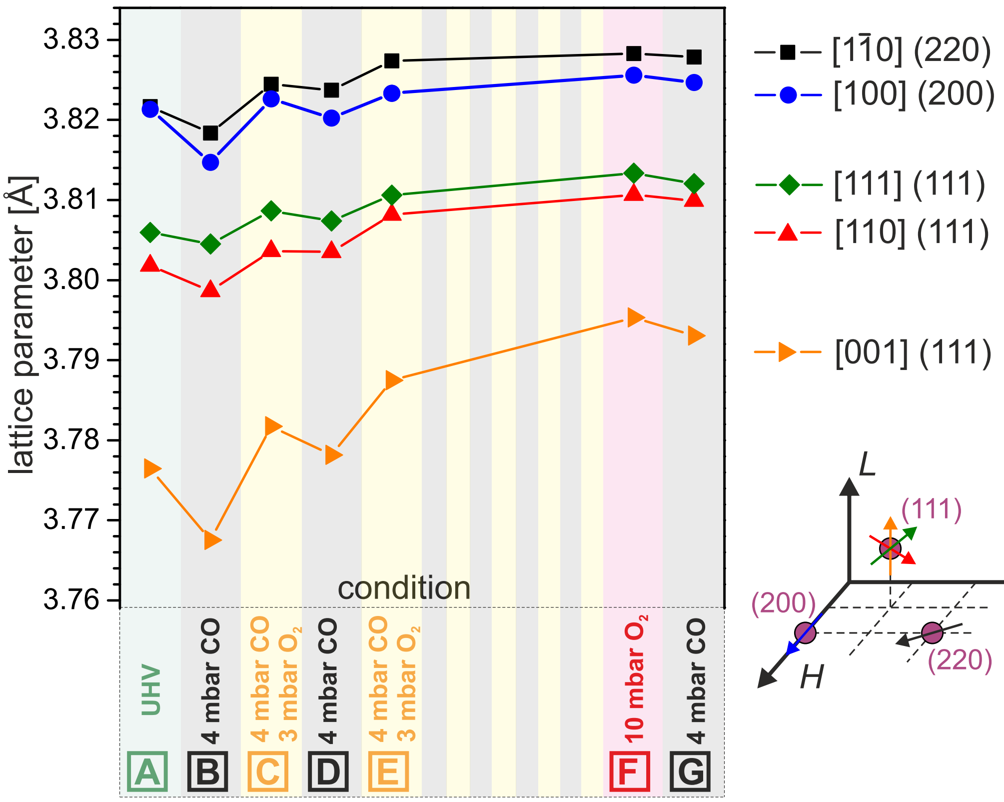

Figure 7.14: **Lattice parameter changes:** lattice parameters as a function of sample condition obtained from in- and out-of-plane particle Bragg peaks. They were deduced from Pseudo-Voigt fits to the Bragg peak scans along various directions, some of which are shown in Fig. 7.9. Their scan directions and the respective Bragg peaks are given in square and round brackets in the legend on the top right, the bottom right shows the scan directions and Bragg peak positions in reciprocal space.

3.8130 Å, respectively, at the measurement temperature of 673 K.

Throughout the experiment, the data from the out-of-plane peaks suggest smaller lattice parameters compared to the data from the in-plane peaks, which implies an in-plane expansion and out-of-plane compression of the particle lattice parameter based on the Poisson effect (see section 2.3.2). For all Bragg peaks and scan directions the deduced lattice parameter values increased steadily in the course of the CO oxidation experiment which suggests a continuous depletion of Rh from the particle core. It is striking that the data repeatedly reveal reduced lattice parameters under reducing conditions, especially pronounced in the case of the out-of-plane parameters, implying an enrichment of Rh inside the particle core. However, in the course of the experiment this Rh enrichment continuously subsides which indicates a Pt-richer core at the end of the experiment under reducing conditions compared to its beginning.

Despite the obvious Rh depletion from the particle core no Bragg peak splitting, indicating Pt-Rh phase separation, was discernible in the scans. Phase separation could, however, be anticipated as the Pt-Rh phase diagramme reveals a miscibility gap below 1033 K, which at 673 K would result in coexisting phases of $\mathrm{Pt}_{0.87}\mathrm{Rh}_{0.13}$ and $\mathrm{Pt}_{0.12}\mathrm{Rh}_{0.88}$ compositions. In Fig. 7.9 the calculated Bragg peak positions for pure Pt, pure Rh and for alloys of $\mathrm{Pt}_{0.87}\mathrm{Rh}_{0.13}$ and $\mathrm{Pt}_{0.12}\mathrm{Rh}_{0.88}$ according to Vegard's rule and corrected for thermal expansion are indicated by vertical lines. They reveal that phase separation can be ruled out.

The absence of any Bragg peak splitting moreover allows to exclude the bleeding out of the low melting point metal Pt from the Pt-Rh alloy nanoparticles as possible origin for the mesh-like particle structures of Fig. 7.13 a)-c). Such a scenario was recently concluded in the case of Pt-Rh alloy nanoparticles calcinated at 973 K, which resulted in large particles of pure Pt, while particles that maintained their original size were characterized by a higher Rh content [203]. Besides, the morphologies of these particles differed to a great extent from the ones shown in Fig. 7.13 a)-c).

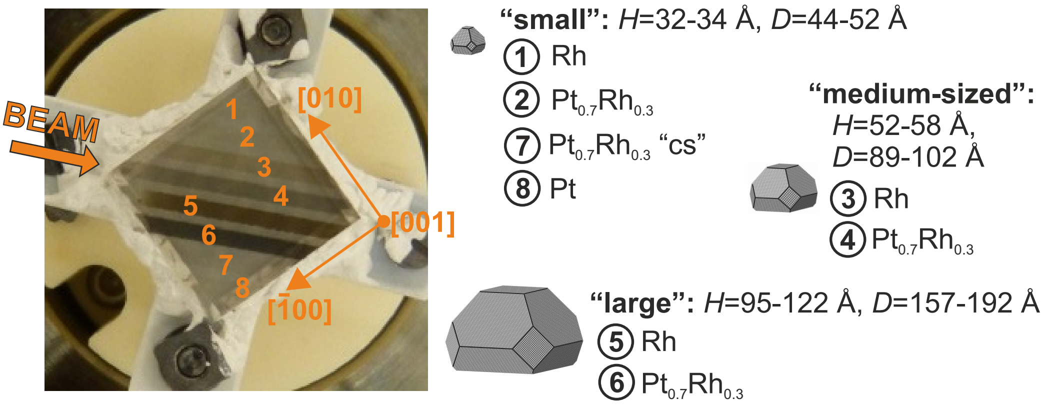

Figure 7.15: **Combinatorial sample "spinel-2":** it consists of $MgAl_2O_4$(001)-supported nanoparticles of varying compositions and size regimes, the particle stripes were grown along the [$\bar{1}$10]-direction of the substrate, see also Fig. 6.1 in section 6.1.

7.4 Size- and composition-dependent particle aspect ratio changes

The data discussed in the previous sections were obtained from nanoparticles that consisted of only one Pt-Rh composition (33%Pt, 67%Rh) and one initial particle size (H=60 Å, D=90 Å). Here, the results obtained for $MgAl_2O_4$(001)-supported particles of various sizes and Pt-Rh compositions exposed to similar reaction conditions (sample "spinel-2") will be addressed.

A systematic drawing of the sample is shown in Fig. 6.1, a photo is shown in Fig. 7.15: it contained pure Rh and $Pt_{0.7}Rh_{0.3}$ alloy particles of three different size regimes ("small": H=30-40 Å, D=40-60 Å; "medium-sized": H=50-65 Å, D=85-105 Å, "large": H=90-130 Å, D=155-210 Å) and in addition pure Pt and $Pt_{0.7}Rh_{0.3}$ "core-shell" particles of the "small" size regime (more information on the "core-shell" particles and the sample in general can be found in section 6.1).

The combinatorial sample was studied at beamline P07, Petra III, using an photon energy of 78 keV. As in the case of the sample previously discussed in this chapter (sample "spinel-1"), the total pressure inside the dome comprised 50 mbar and Ar (carrier gas), O_2 and diluted CO (10% CO in 90% Ar) were the gases used. The particle stripes were grown and probed with the x-ray beam along the [$\bar{1}$10]-direction of the $MgAl_2O_4$(001)-substrate (see left side of Fig. 7.15). This allowed for monitoring with a large 2D detector the respective (H=K, L)-planes of reciprocal space containing the particle (111)

Bragg peaks for each particle stripe and condition throughout the experiment. The corresponding peaks and their vicinities are shown in the top part of Fig. 7.16, the bottom part displays the partial gas pressures including the reaction product CO_2 as measured by the residual gas analyzer.

In the experiment the CO flow was set to 4 $\frac{\text{ml}}{\text{min}}$ while the oxygen flow was stepwise increased towards conditions of higher catalytic activity (see subsection 3.1.3). The sample was first probed at 653 K and later at 703 K, and hence close to the sample temperature of 673 K that was set during the study of the $Pt_{0.67}Rh_{0.33}$ particles (sample "spinel-1") discussed in section 7.2 and 7.3. The two studies differed in the set maximum partial oxygen flow which comprised 3 $\frac{\text{ml}}{\text{min}}$ in the $Pt_{0.33}Rh_{0.67}$ particles' study but only 2.5 $\frac{\text{ml}}{\text{min}}$ in the investigation of the combinatorial sample presented here.
The bottom of Fig. 7.16 reveals that at 1.9 $\frac{\text{ml}}{\text{min}}$ oxygen flow, and thus still at slightly understoichiometric conditions for oxygen, the characteristic features of the catalytic '*light-off*' were monitored in the mass spectrometer data: the oxygen partial pressure passed through a maximum, accompanied by a striking drop in CO signal as the latter was immediately being consumed in the reaction. At the same time a pronounced increase in the reaction product CO_2 was monitored.
When increasing the O_2 flow further to 2.5 $\frac{\text{ml}}{\text{min}}$ the rise of the CO_2 production and the decrease in CO partial pressure continued, resulting in a higher catalytic activity at 2.5 compared to 1.9 $\frac{\text{ml}}{\text{min}}$ O_2 flow. At 2.5 $\frac{\text{ml}}{\text{min}}$ O_2 flow no traces of bulk oxides signals were found for none of the particle sizes and/or compositions independent of the probed sample temperatures. Contrary, in the case of the $Pt_{0.33}Rh_{0.67}$ particles on sample "spinel-1", a transition from 2 to 3 $\frac{\text{ml}}{\text{min}}$ O_2 flow did not result in an increase but rather in a decrease in CO_2 production (see Fig. 7.2) and in the appearance of bulk oxide signals.
These observations suggest that an oxygen flow of 2.5 $\frac{\text{ml}}{\text{min}}$ is too low for bulk oxide formation, also at the slightly higher temperature of 703 K. Accordingly, it is likely that the high catalytic activity at 2.5 ml/min O_2 flow can indeed be traced back to thin surface oxides as catalytically active phase. Consequently, these findings fortify the assumption that the reduced CO_2 production at 3 $\frac{\text{ml}}{\text{min}}$ O_2 flow observed in the case of the $Pt_{0.33}Rh_{0.67}$ particles on sample "spinel-1" could be traced back to bulk oxide poisoning. The slightly higher temperature of 703 K did not lead to a pronounced increase of the CO_2 production compared to the production at 653 K, as can be deduced from the mass spec-

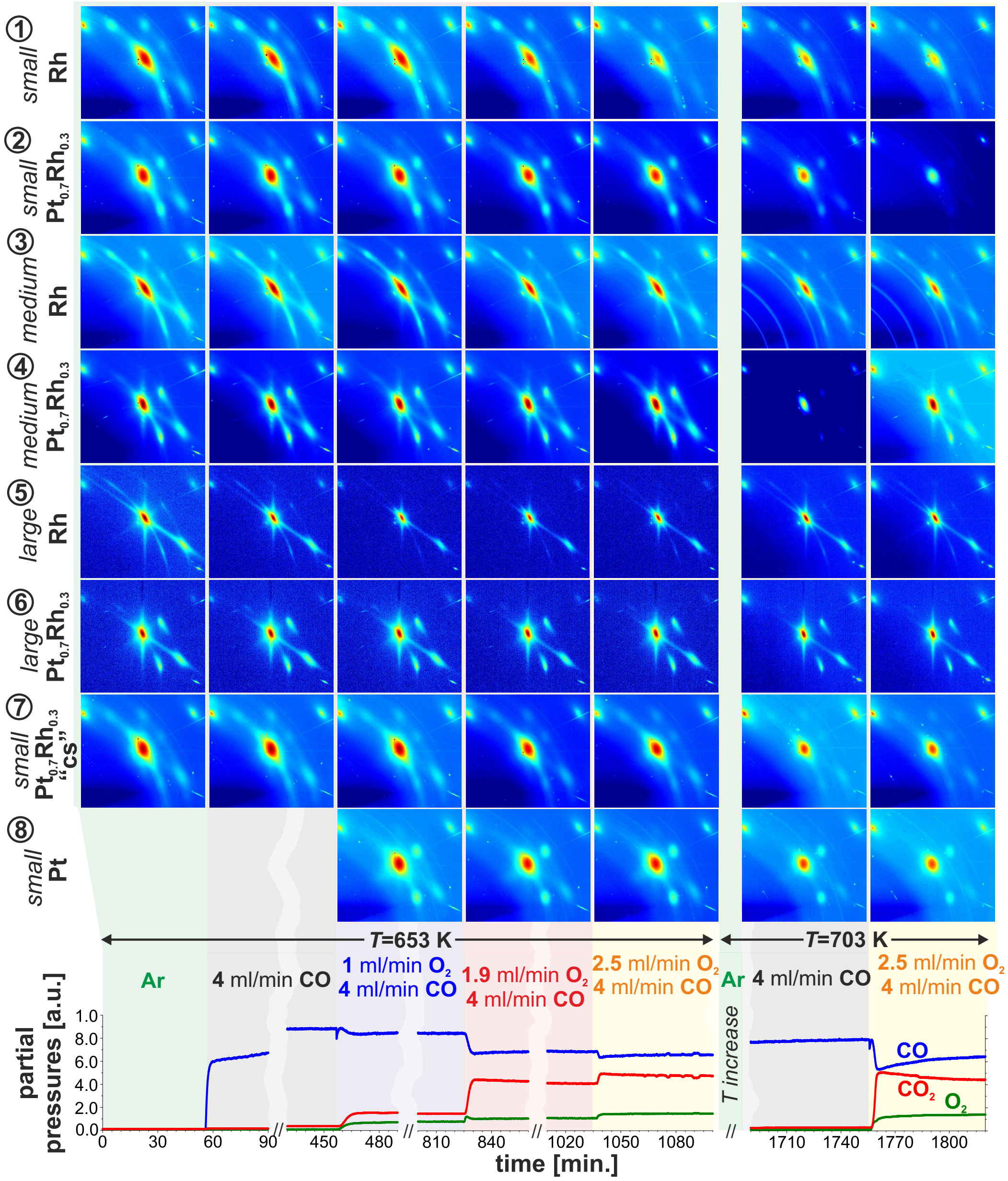

Figure 7.16: **In-situ monitoring of the particle (111) Bragg peak during CO oxidation on sample "alumina-2": top:** 2D maps centered around the particle (111) Bragg peaks measured for the various particle stripes and the different probed experimental conditions; **bottom:** extracts from the mass spectrometer data revealing the partial gas pressures of CO, O_2 and the reaction product CO_2 as a function of time, condition and temperature.

trometer data at the bottom of Fig. 7.16.

As the particle Bragg peak positions in Fig. 7.16 did only negligibly vary in the course of the CO oxidation experiment, it can be concluded that the respective lattice parameters remained relatively constant. Independent of particle size they were found to be in good agreement with the theoretical lattice parameters obtained for the respective Pt-Rh compositions at the probed temperatures, taking Vegard's rule and thermal expansion into account.

For the medium-sized and the large particles distinct (001)- and (111)-type facet signals could be observed. In the transition to conditions of high catalytic activity no additional facet signals emerged. This implies that the particles retained their octahedral shape even under reaction conditions, which is in line with the findings for the $Pt_{0.33}Rh_{0.67}$ particles of sample "spinel-1" discussed in sections 7.2 and 7.3.

Fig. 7.17 shows horizontal linescans extracted from the 2D maps of the large Rh and $Pt_{0.7}Rh_{0.3}$ particles (stripes 5 and 6, see Fig. 7.15) at 703 K under reducing conditions (black) and conditions of high catalytic activity (orange). They were extracted at L-values slightly below the particle (111) Bragg peak (Rh: L=0.897; $Pt_{0.7}Rh_{0.3}$: L=0.924) and were accordingly sensitive to potential particle facet signals. In the transition to catalytic activity an intensity increase of the (001)-type facet signal was found for both compositions, which implies on the one hand the formation of the catalytically active c(2x8) Rh surface oxide structure, on the other hand the enlargement of the respective (001)-facets, as was discussed earlier in section 7.2. Besides, the linescans in Fig. 7.17 measured on the pure Rh particles suggest that the intensity increase of the (001)-type facet signal came along with a decrease in the (111)-type facet signal intensity (at H=1.1). This implies that the Rh particles underwent shape changes characterized by a size increase of the (001)-type facets at the expense of the shrinking (111)-type facet size as found for the $Pt_{0.33}Rh_{0.67}$ particles on sample "spinel-1" (see section 7.3). However, the intensity change is only discernible for the facet rods at H=1.1, not at H=0.9. The enhanced intensity of the signal at H=1.1 can not only be traced back to the (111)-type facet signal, but also to the coinciding rod signal stemming from the crystal plane defined by the inverted stacking sequence caused by internal twinning (see Fig. 2.7 a) in chapter 2). Accordingly, to conclude a change in size of the particle (111)-type facets as cause for the intensity change is arguable.

To obtain information on the **aspect ratio changes** of the particles, linescans

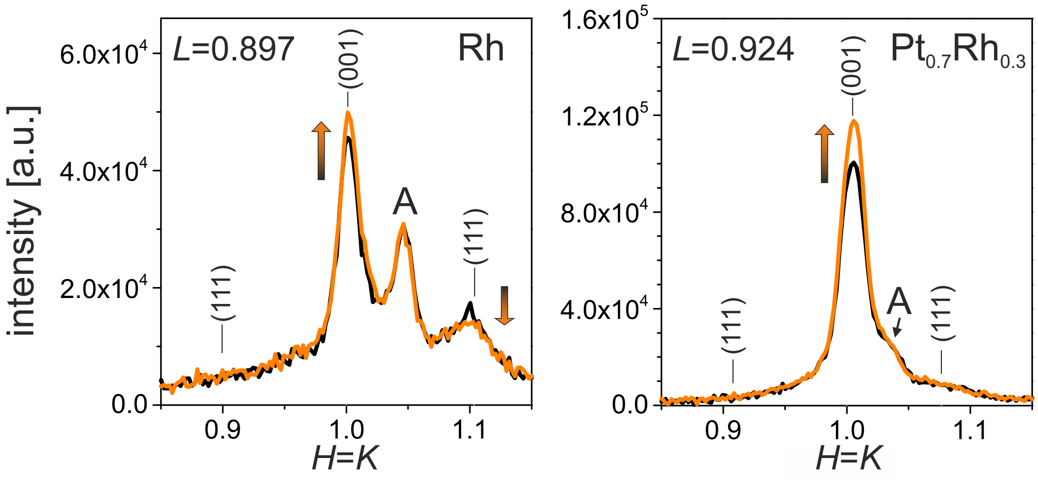

Figure 7.17: **Facet signal scans performed on the largest particles (stripes 5 and 6) on sample "spinel-2":** they were extracted from the 2D maps of Fig. 7.16 for pure Rh and $Pt_{0.7}Rh_{0.3}$ particles of largest size (stripe 5 and 6) under reducing conditions (black lines: 4 $\frac{\text{ml}}{\text{min}}$ CO) and conditions of high catalytic activity (orange lines: 2.5 $\frac{\text{ml}}{\text{min}}$ O_2 and 4 $\frac{\text{ml}}{\text{min}}$ CO) at T=703 K; peaks labeled A denote intensities from Debye-Scherrer rings caused by particle mosaicity.

running through the respective particle Bragg peaks in vertical and horizontal directions were extracted from the 2D maps and fitted with Pseudo Voigt functions. The thus obtained heights ($H=\frac{2\pi}{\Delta Q_{ver}}$), diameters ($D=\frac{2\pi}{\Delta Q_{hor}}$) and aspect ratios $\frac{H}{D}$ of the various particle size regimes are summarized in Fig. 7.18. The data reveal that the sintering behaviour of the nanoparticles is characterized by both, a composition- and a size-dependence, whose general trends will be discussed in the following.

In the transition to high catalytic activity the **small particles** show, independent of their composition, almost no change in diameter. Contrary, the particle heights increase, especially in the case of Pt-containing particles. In turn, their aspect ratios $\frac{H}{D}$ increase and reach at the end of the experiment values between 0.7 and 0.8, hence approaching the values of pure Rh. This implies that the pure Rh particles with their rather high $\frac{H}{D}$ values feature a more stable shape. The small $Pt_{0.7}Rh_{0.3}$ "core-shell" particles show exactly the same behaviour as the $Pt_{0.7}Rh_{0.3}$ alloy particles, and it is very likely that they were also in an alloyed state at the probed elevated temperatures.

The **medium-sized particles** proved to be surprisingly stable during reaction conditions for CO oxidation: neither the particle diameters nor the heights and in turn also not the aspect ratios varied remarkably for both compositions, Rh and Pt$_{0.7}$Rh$_{0.3}$. This stands in stark contrast to the strong sintering of the Pt$_{0.33}$Rh$_{0.67}$ particles of comparable size on sample “spinel-1” discussed earlier in sections 7.2 and 7.3. A tentative explanation can be found in the different substrate treatments prior to particle deposition: contrary to “spinel-1” the sample discussed here underwent a sufficient number of sputtering and annealing cycles to have nanometer-sized pits formed on the substrate surface with a coverage of 20-30% [48] (see subsection 2.4.2 and Fig. 2.12). As the particle diameters are of the same size as the pits, a majority of the particles may have grown inside the pits which might stabilize them and reduce sintering. A further reason for the absence of sintering can, however, also be found in the lower maximum oxygen gas flows employed in the reaction (here: 2.5 $\frac{\text{ml}}{\text{min}}$ vs. 3 $\frac{\text{ml}}{\text{min}}$ in the case of “spinel-1”). Moreover, the total duration of the experiment and thus the total exposure time to the different gas cycles was reduced in the present case (here: only about 30 h (2 reaction cycles) vs. 4 d (6 reaction cycles)). It is striking that under pure CO flow the particle heights and diameters increase tremendously while keeping their respective aspect ratios. This was also observed in the case of the small particles, although not as pronounced. As this was moreover monitored in the case of the Pt$_{0.33}$Rh$_{0.67}$ particles on sample “spinel-1” (see Fig. 7.11) and the α-Al$_2$O$_3$(0001)-supported Rh-rich alloy particles at comparable elevated temperatures of T=673 K (see Fig. 8.13 in subsection 8.1.5, Fig. C.3 in Appendix C), this seems to be a general behaviour. As discussed in section 7.3, it can be explained by the removal of oxide films and the resulting size increase of the pure metal core, where one metal layer corresponds to an increase of about 2 Å. As this height and diameter increase was found to also occur under reducing conditions preceded by pure Ar flow, it has to be assumed that the impurities inside the Ar gas (99.9990 Vol.-%) led to a partial oxidation of the particles.

In the case of the **large particles**, contrary to the cases of the small and medium-sized particles discussed above, not the real particle size was obtained from the FWHM-analysis of the particle Bragg peaks, but the heights and diameters of the crystalline *domain sizes* within the particles. This can be inferred from the discrepancies of the particle diameters obtained from the SEM images shown in Fig. 7.19 and the diameters deduced from the Bragg peak analysis, where the latter are about by a factor of 3 smaller compared to the diameters concluded from the SEM measurements.

For both compositions the SEM images feature an irregular shape of coalesced

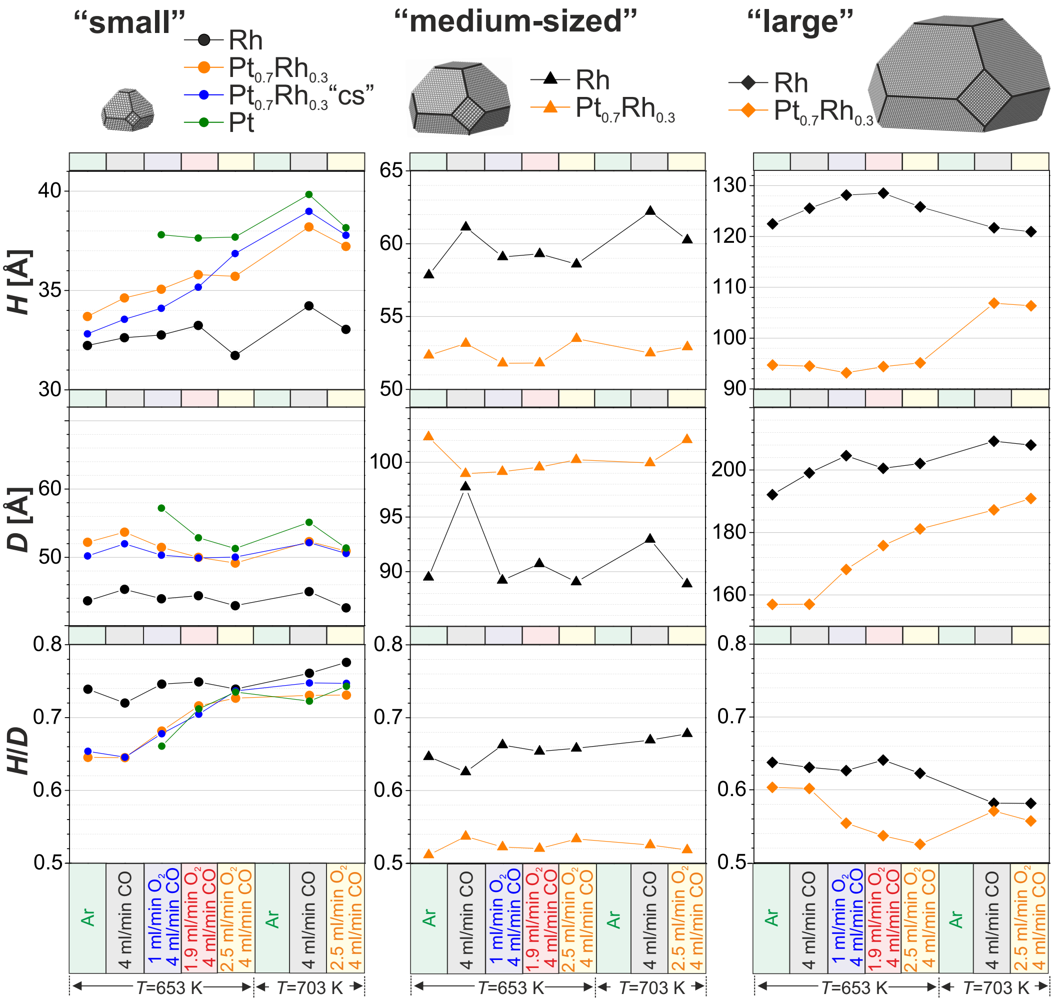

Figure 7.18: **Size- and composition-dependent aspect ratio changes of the particles on sample "spinel-2" during CO oxidation:** particle heights H, diameters D and aspect ratios $\frac{H}{D}$ in the course of the experiment as obtained for different particle size regimes and Pt-Rh compositions. The bottom shows the set sample conditions (gas flows and temperature). Note the different axis markings.

particles with domain boundaries. To which extent this coalescence occurred already during particle growth or during catalytic activity cannot be inferred from the x-ray data.

The Bragg peak scan analysis suggests for both compositions an increase in domain diameter as soon as CO oxidation set in. Contrary, the domain heights remained rather stable. It was only at the slightly elevated temperature of 703 K and only for the Pt-containing stripes that it increased. This resulted in a steady decrease of the respective aspect ratios in the transition to conditions of high catalytic activity.

Within an ensemble of coalesced particles such a diameter increase could be explained by the gradual grain growth due to the steady elimination of grain boundaries [204]. Such a constant, but slow, increase of the particle crystallite size was recently observed for aggregated gold nanoparticles combining x-ray diffraction and small angle x-ray scattering [204]: even long after (>5 h) the particles had aggregated, the grain growth continued during annealing at moderate temperatures (523-623 K) and was in addition accompanied by a decrease in twin fault density. A significant decrease in the signal from internal twinning was, however, not observed for any of the particle stripes of the sample discussed here.

A HREM study [205] disclosed that a steady increase in domain size diameter can also be explained by the coalescence of small particles with larger ones: the smaller particles align their planes with respect to the ones of the larger particles during approach, resulting in a larger coalesced crystallite [205].

A further explanation for the observed diameter increase can be found in Ostwald ripening, as it is characterized by an increase in the average diameter and as no small particles are present in the SEM images of Fig. 7.19 measured after CO oxidation.

The **general conclusions** that can be drawn from FWHM-analysis will be given in the following. For all size-regimes, the as-prepared Pt-containing particles are characterized by smaller aspect ratios, where in the case of both, pure Rh and Pt-Rh particles, the aspect ratio decreases with increasing particle size (see also chapter 6). The flat shapes of the Pt-rich particles correspond to the respective kinetic particle shapes, which the particles may overcome by sintering in height towards a more 3-dimensional shape (see also discussion in section 8.1.3). Accordingly, the CO oxidation induced size changes are more pronounced in the case of the Pt-containing particles; pure Rh particles are

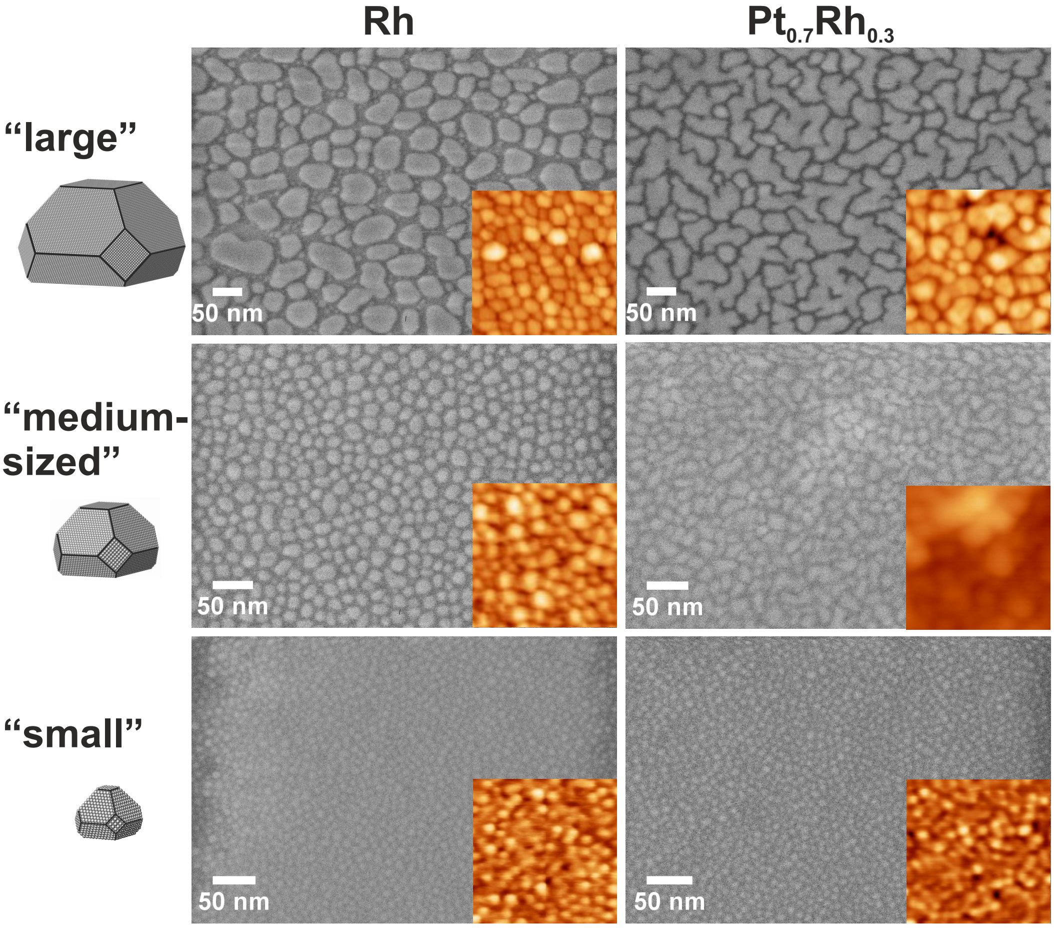

Figure 7.19: **SEM and AFM images measured after CO oxidation:** complementary microscopy images taken after the CO oxidation experiment on Rh and $Pt_{0.7}Rh_{0.3}$ particles of the three different particle size regimes. Greyscale images were obtained by SEM, the insets show the corresponding AFM measurements on the same length scale. Note that the scale bar size for the largest particles differs from the ones of the medium-sized and small particles. The SEM images were measured by the University of Jena.

found to be less prone to sintering. In the course of the experiment, the small Pt-containing particles adopt the $\frac{H}{D}$ values of the pure and stable Rh particles and hence their equilibrium shape. It is striking, that the "core-shell" particles show the same behaviour as the $Pt_{0.7}Rh_{0.3}$ alloy particles. Contrary to the small particles, the particles of medium-size are less prone to sintering, probably due to their stabilization by nm-sized pits in the substrate surface. These findings are in line with the results on the composition- and hence shape-dependent, particle sintering of α-Al_2O_3(0001)-supported alloy particles presented in chapter 8.

Fig. 7.19 summarizes **SEM and AFM measurement data** taken from the pure Rh and the $Pt_{0.7}Rh_{0.3}$ alloy particles of the three different size regimes after CO oxidation.

It is striking, that only the alloy particles feature worm-like particle morphologies which can also be explained by the wetting of the substrate by Rh oxides, as discussed earlier in section 7.3. They bear some similarity with the structures of the sintered $Pt_{0.33}Rh_{0.67}$ particles of sample "spinel-1" shown in Fig. 7.13 a)-c), although at an earlier stage with not yet fully developed interconnections. An explanation can be seen in the fact that the particles shown in Fig. 7.19 were only for a relatively short time exposed to CO oxidation conditions (here: 30 h vs. 4 d in the case of sample "spinel-1") and only to a lower maximum oxygen flow (here: 2.5 $\frac{\text{ml}}{\text{min}}$ O_2 vs. 3 $\frac{\text{ml}}{\text{min}}$ O_2 in the case of sample "spinel-1").

7.5 Summary and conclusion

The present chapter contains the results of structure-sensitive in-situ studies of $MgAl_2O_4$(001)-supported Pt-Rh alloy nanoparticles during catalytic CO oxidation. The first part (sections 7.2-7.3) presents the findings for $Pt_{0.33}Rh_{0.67}$ nanoparticles (sample "spinel-1") obtained by conventional surface x-ray diffraction (E=11.2 keV), the second part (section 7.4) the results as deduced from high energy reciprocal space mapping (E=78 keV) for a combinatorial sample containing pure Rh and $Pt_{0.7}Rh_{0.3}$ alloy particles of varying sizes (sample "spinel-2").

In the case of the $\mathbf{Pt_{0.33}Rh_{0.67}}$ alloy particles (sample "spinel-1"), time-resolved monitoring of transient oxide signals on (100)- and (111)-type facets while changing the p_{O2}/p_{CO} flow ratio allowed for deducing (1) which **oxide**

structures appear on which particle facets, (2) under which conditions they are stable, and (3) potential correlations between their appearance/dissolution and changes in the sample's catalytic activity, and thus the identification the catalytically most active phase.

When changing from reducing towards stoichiometric conditions for CO oxidation (f_{O2}=2 $\frac{\mathrm{ml}}{\mathrm{min}}$; f_{CO}=4 $\frac{\mathrm{ml}}{\mathrm{min}}$), the emergence of the c(2×8) Rh surface oxide on the (001)-type particle facets was concluded. Increasing the flow ratio further to f_{O2}=3 $\frac{\mathrm{ml}}{\mathrm{min}}$ and f_{CO}=4 $\frac{\mathrm{ml}}{\mathrm{min}}$ triggered in addition the appearance of the p(9×9) Rh surface oxide on the (111)-type particle facets. Under the same conditions but with time delay, the steady formation of the Rh bulk oxides $\mathrm{Rh_3O_4}$ and $\mathrm{RhO_2}$ on the (111)- and (001)-type facets, respectively, set in.

The mass spectrometry data suggest that a not fully closed layer of the c(2×8) Rh surface oxide is the **catalytically most active phase** since the catalytic *'light-off'* and the highest $\mathrm{CO_2}$ productivity clearly correlated with its presence under stoichiometric conditions. Contrary, the emergence of the p(9×9) structure did not increase the $\mathrm{CO_2}$ production further, probably since the mass transfer limited regime was already reached under stoichiometric conditions. The data suggest a slight but steady decline in catalytic activity correlating with a progressive buildup of bulk oxides.

Measurements of high resolution reciprocal space maps and linescans through particle Bragg peaks along high symmetry directions allowed for determining the **qualitative and quantitative particle shapes** under reducing conditions (f_{O2}=0 $\frac{\mathrm{ml}}{\mathrm{min}}$; f_{CO}=4 $\frac{\mathrm{ml}}{\mathrm{min}}$) and conditions of high catalytic activity (f_{O2}=3 $\frac{\mathrm{ml}}{\mathrm{min}}$; f_{CO}=4 $\frac{\mathrm{ml}}{\mathrm{min}}$). Independent of condition, the particles were made up of (001)- and (111)-type facets only, thus featuring exclusively truncated octahedral shapes. The oxygen-induced particle shape changes in the transition from reducing to conditions of high catalytic activity were characterized by an increase of the (001)-type top and side facets at the expense of the (111)-type facet size. This restructuring was characterized by a flattening of the particles with the height to diameter aspect ratio decreasing from 0.7 to 0.4. Upon switching back to reducing conditions all oxides could be reduced again and all shape changes were found to be reversible.

With shape change reversibility and the absence of any higher indexed facets under all tested conditions, the $\mathrm{Pt_{0.33}Rh_{0.67}}$ alloy particles show a behaviour more similar to pure Rh than to pure Pt particles. This is likely due to segregated Rh sitting at the particle surface under reaction conditions, forming the corresponding oxides and determining the particle shape characteristics.

On top of the aforementioned shape changes, the particles were concluded to undergo tremendous **sintering** in the course of repeated cycles of catalytic CO oxidation and reducing conditions. The size increase was found to be rather isotropic with the average height and diameter progressively increasing from 55 Å to 90 Å and from 80 Å to 125 Å, respectively, thus sustaining a particle aspect ratio of 0.7 under reducing conditions. The particle sintering was deduced to come along with a steady reduction of the particle coverage from ≈80% to ≈60% and a progressive smearing out of the electron density profile perpendicular to the substrate surface at the particle/substrate and the particle/gas interface, indicating a steady decline of a defined particle structure, especially after harsh conditions characterized by f_{O2}=10 $\frac{\mathrm{ml}}{\mathrm{min}}$ pure oxygen flow. This is in line with the increasing **depletion of Rh** from the Pt$_{0.33}$Rh$_{0.67}$ particles that was concluded from the progressive change in lattice parameter. Accordingly, microscopy measurements performed after the CO oxidation experiment revealed interconnected, mesh-like particle structures in accordance with depleted Rh oxides wetting the substrate surface.

To shed more light onto the particle size- and composition-dependent behaviour of MgAl$_2$O$_4$(001)-supported Pt-Rh alloy particles during CO oxidation, a **combinatorial sample** (sample "spinel-2"), containing mainly Rh and Pt$_{0.7}$Rh$_{0.3}$ particles of varying sizes, was studied under comparable conditions.

The reaction-induced particle sintering was concluded to show a size- and composition-dependence and was most pronounced for the small Pt-rich particles (H≈33 Å, D≈50 Å), while the small Rh particles (H≈32 Å, D≈44 Å) proofed to be completely sinter-resistant. With their kinetic particle shape being characterized by a smaller initial particle aspect ratio H/D≈0.65 compared to the one of the small pure Rh particles (H/D≈0.75) (see chapter 6), the Pt-rich particles sintered mainly in height while maintaining their diameter, resulting in more 3-dimensional equilibrium particle shapes with aspect ratios comparable to the ones of the stable Rh particles. Interestingly, particles on sample "spinel-2", which were in the same size regime as the strongly sintering Pt$_{0.33}$Rh$_{0.67}$ particles on sample "spinel-1", did not sinter at all. A reason can be seen in the differing substrate pretreatment with several sputtering and annealing cycles, resulting in stabilizing pits of a lateral size comparable to the one of the particles.

In accordance with the findings on the reaction-induced shape changes of the $Pt_{0.33}Rh_{0.67}$ particles on sample “spinel-1”, the facet signals contained in the high energy reciprocal space maps measured on sample “spinel-2” reveal in the transition from reducing to high catalytic activity an increase in the (001)-type facet signal intensity at the expense of the one from the (111)-type facets, indicating similar oxygen-induced shape changes.

Also on the combinatorial sample “spinel-2”, the alloy particles featured after the CO oxidation experiment worm-like structures, indicating a depletion of Rh from the alloy particles.

Chapter 8

Shape-Dependent Sintering of α-Al_2O_3(0001)-Supported and Pt-based Alloy Particles during CO Oxidation

Section 6.2 showed how the shape of α-Al_2O_3(0001)-supported and Pt-based alloy particles can be altered as a function of the alloy composition. In the investigations of the present chapter, these differing initial shapes served as starting point to systematically probe in-situ the composition- and hence shape-dependent particle sintering under various conditions of CO oxidation. The results will be presented for some selected samples ("alumina-1", "-2", "-3", and "-5", see Fig. 6.8 for overview of samples), where the ones of the Pt-Rh particles ("alumina-1", "-2", and "-3") will be discussed in section 8.1, the ones of the Pt-Pd particles ("alumina-5") in section 8.2.

Subsection 8.1.1 elucidates the experimental strategy that was employed to obtain all data presented in this chapter: the combination of combinatorial samples, grazing incidence high energy x-ray diffraction and in-situ mass spectrometry to allowed for monitoring in-situ the shape-dependent particle sintering under operational conditions.

The analysis of these data is subject matter of subsection 8.1.2: a new approach is described in detail on how to retrieve quantitative structural information on particle shapes during catalytic reactions by analyzing out-of-plane particle rods. Supporting explanations and descriptions can be found in Appendices A and B to this chapter.

The thus obtained results (8.1.1-8.1.2, 8.2.1, C.1) disclose that the determined sintering behaviour cannot be explained in terms of the classical mechanisms of Ostwald or Smoluchowski ripening, but have to be ascribed to a hitherto unknown mechanism, which we found to be highly shape-dependent (section 8.1.3): it is greatly suppressed for particles grown in their equilibrium shapes, whose adhesion energies on the α-Al$_2$O$_3$(0001)-support are calculated in 8.1.4. Further experimental affirmation of the sinter-resistance of equilibrium-shaped particles can be found in subsection 8.1.5 and Appendix C.2.

Based on the deduced particle lattice parameter changes and SEM images performed after the CO oxidation experiment, subsections 8.1.6 and 8.2.2 discuss the potential chemical restructuring and morphology changes that the particles underwent in the course of the experiment.

The chapter will close with a summary and conclusion part (section 8.3).

8.1 CO oxidation on Pt-Rh alloy particles

8.1.1 Operando monitoring of the composition- and shape-dependent particle sintering

All experimental results in this chapter were obtained by combining combinatorial samples, high energy grazing incidence x-ray diffraction and in-situ mass spectrometry. This subsection presents this common experimental approach and the thus obtained experimental results using the example of the Pt-Rh particles of sample **"alumina-1"**.

The **general experimental strategy** applied for all samples of chapter 8 is sketched in Fig. 8.1 for the example of sample "alumina-1". It shows the combinatorial sample mounted on the heating station inside the catalysis chamber's flow reactor. The composition of the introduced gases including the reaction products is monitored by the residual gas analyzer (RGA, see Fig. 8.1).

The high energy x-ray beam (here: E=78.7 keV) is collimated by a set of compound refractive lenses (CRLs) resulting in a beam size at the sample position of typically only a few micrometers in size (here: 8×25 μm). This highly focused x-ray beam facilitates the probing of one particle stripe at a time. By translating the sample perpendicular to the incident beam direction nanoparticles of different compositions and/or sizes can hence be studied subsequently under identical reaction conditions. In order to increase the signal to

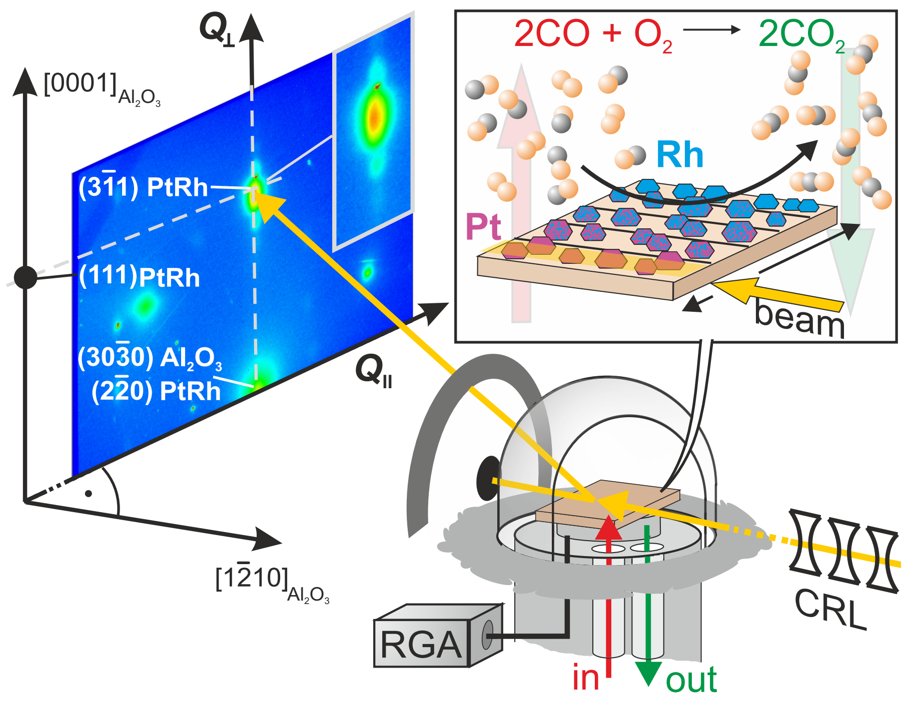

Figure 8.1: **Measurement principle:** the high energy x-ray beam is focused by compound refractive lenses (CRLs) on the sample surface containing particle stripes of various Pt-Rh compositions. The diffraction pattern is collected by a 2D detector while the heated sample is exposed to a computer-controlled gas flow mixture. The composition of the gas phase is controlled by leaking into a residual gas analyzer (RGA). The diffraction pattern was measured on the as-prepared pure Pt particles, its inset shows a close-up on the particle $(3\bar{1}1)$ Bragg peak.

noise ratio, the incident angle α_{in} of the high energy x-ray beam is set close to the substrate critical angle (here: α_{in}=0.0333°; α_{Al2O3}=0.0294°). This shallow angle results in a beam footprint of 13.8 mm which covers the whole length of the particle stripes (sample dimensions: 10 mm×10 mm×1 mm).

Fig. 8.1 a) displays the thus obtained 2D reciprocal space map in the substrate $(10\bar{1}0, L)$-plane measured on the as-prepared Pt particles of "alumina-1"[1].

---

[1] To probe a certain reciprocal space plane including the particle peak of interest, in the present case the substrate $(10\bar{1}0, L)$-plane containing the particle $(3\bar{1}1)$ reflection, the particle stripes have to be grown along the direction perpendicular to that plane, i.e. here along the substrate $[1\bar{2}10]$-direction (see Fig. 8.1). To fulfill the diffraction condition, the sample is aligned such that the particle stripes are tilted with respect the incident beam direction by the in-plane Bragg angle θ_{B} of the corresponding in-plane Bragg peak (here: the particle $(2\bar{2}0)$ reflection, see Fig. 8.1). The $\boldsymbol{Q}$-vector then probes the direction perpendicular to the particle stripes, which is in this case the requested substrate $[10\bar{1}0]$-direction (see Fig. 8.1). Due to the use of high x-ray energies, the Bragg angles θ_{B} for Pt, Pd and Rh are on the order of only 3.3°. Thus, despite the stripes' rotation by θ_{B} with respect to the incident beam direction, the whole length of the beam still covers the probed particle stripe, whose width is on the order of 0.8 mm (tan(3.3°)×10 mm=0.59 mm<0.8 mm).

The inset shows a close up on the particle $(3\bar{1}1)$ peak with its distinct Laue oscillations. While the L spacing of their minima is inversely proportional to the particle height, the oscillations' characteristic damping contains immediate information on the particle structure, as will be shown later in this chapter. Thus, monitoring the partial gas pressures inside the reactor along with the respective Bragg peaks of the various particle stripes allows a direct correlation between changes in particle structure and the sample's catalytic activity.

The following will discuss the thus obtained data and deduced **results for sample "alumina-1"**. The focus will lie on the five stripes containing particles of varying Pt-Rh composition (Pt, $Pt_{0.85}Rh_{0.15}$, $Pt_{0.7}Rh_{0.3}$, $Pt_{0.5}Rh_{0.5}$, Rh) for which the same amount of material was deposited. The results of the pure Rh particles of differing size (Rh, Rh "L" and Rh "S") are summarized in Appendix C.2.

The clean, as-prepared particles were first probed under a reducing atmosphere (condition A: no O_2, CO flow $f_{\text{CO}}= 2\ \frac{\text{ml}}{\text{min}}$, T=550 K). For all subsequent settings (conditions B→F) the CO flow was kept constant at $f_{\text{CO}}=10\ \frac{\text{ml}}{\text{min}}$, while the O_2 flow was in steps increased up to $f_{\text{O2}}=7\ \frac{\text{ml}}{\text{min}}$, thus to conditions characterized by an overstoichiometry in oxygen with a O_2:CO ratio of 0.7:1 (condition B: $f_{\text{O2}}=2\ \frac{\text{ml}}{\text{min}}$, $f_{\text{CO}}=10\ \frac{\text{ml}}{\text{min}}$; C: $f_{\text{O2}}=4\ \frac{\text{ml}}{\text{min}}$, $f_{\text{CO}}=10\ \frac{\text{ml}}{\text{min}}$; D: $f_{\text{O2}}=5\ \frac{\text{ml}}{\text{min}}$, $f_{\text{CO}}=10\ \frac{\text{ml}}{\text{min}}$; F: $f_{\text{O2}}=7\ \frac{\text{ml}}{\text{min}}$, $f_{\text{CO}}=10\ \frac{\text{ml}}{\text{min}}$). Only between conditions E and F the sample was exposed to two cycles of gas switching between CO oxidation ($f_{\text{O2}}=5\ \frac{\text{ml}}{\text{min}}$, $f_{\text{CO}}=10\ \frac{\text{ml}}{\text{min}}$) and reducing conditions (no O_2, $f_{\text{CO}}=2\ \frac{\text{ml}}{\text{min}}$). Throughout the experiment Ar was used as carrier gas adding up to a constant total flow of $f_{\text{Ar}}=100\ \frac{\text{ml}}{\text{min}}$ while keeping a total pressure of p_{tot}=200 mbar in the reactor. The sample temperature was held constant at 550 K.

Fig. 8.2 b) shows the RGA signals of CO, O_2 and the reaction product CO_2 as a function of the aforementioned conditions. They are proportional to the respective effective partial pressures inside the reactor. When switching to higher oxygen partial flows the CO_2-signal increased accordingly, indicating a rise in CO_2 production. It was accompanied by a steady decrease in CO-signal, pointing towards the consumption of CO in the catalytic reaction.

Under the probed sample conditions, characterized by a rather low sample temperature of 550 K and a CO flow of $f_{\text{CO}}=10\ \frac{\text{ml}}{\text{min}}$ (corresponding to a partial pressure of 20 mbar inside the reactor), the reaction can be expected to occur via a Langmuir-Hinshelwood mechanism since the Pt-Rh surfaces are at least partially covered by CO [62, 72]. Low index Pt, Rh as well as Pt-Rh

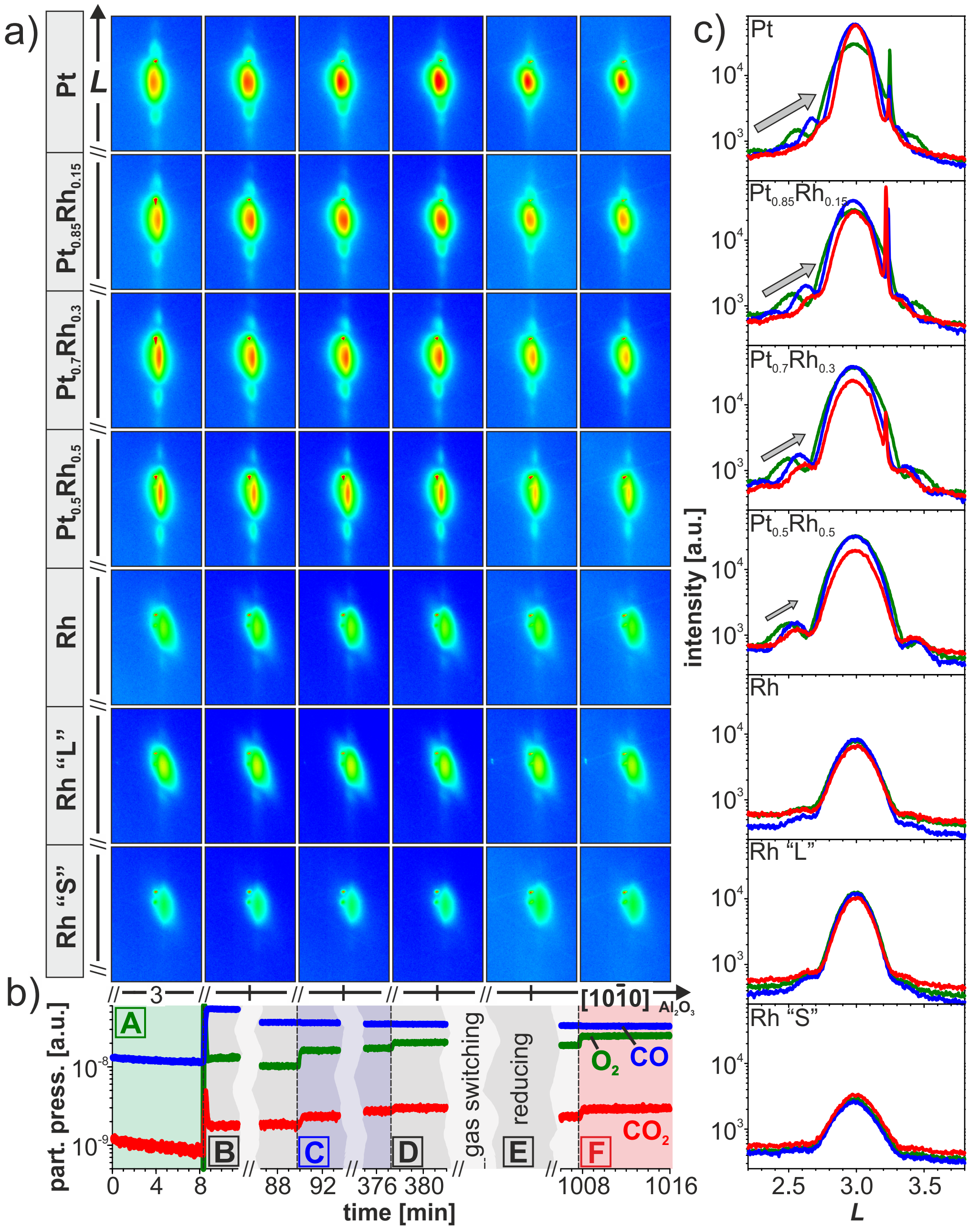

Figure 8.2: **In-situ monitoring of the shape-dependent particle sintering during CO oxidation on sample "alumina-1": a):** particle $(3\bar{1}1)$ Bragg peak maps (exposure time: 50 s) collected for the different Pt-Rh compositions at 550 K and p_{tot}=200 mbar when successively changing towards conditions of higher catalytic activity (A→F). Set partial flows: **A**: no O_2, $f_{\mathrm{CO}}=2\ \frac{\mathrm{ml}}{\mathrm{min}}$; **B**: $f_{\mathrm{O2}}=2\ \frac{\mathrm{ml}}{\mathrm{min}}$, $f_{\mathrm{CO}}=10\ \frac{\mathrm{ml}}{\mathrm{min}}$; **C**: $f_{\mathrm{O2}}=4\ \frac{\mathrm{ml}}{\mathrm{min}}$, $f_{\mathrm{CO}}=10\ \frac{\mathrm{ml}}{\mathrm{min}}$; **D**: $f_{\mathrm{O2}}=5\ \frac{\mathrm{ml}}{\mathrm{min}}$, $f_{\mathrm{CO}}=10\ \frac{\mathrm{ml}}{\mathrm{min}}$; **F**: $f_{\mathrm{O2}}=7\ \frac{\mathrm{ml}}{\mathrm{min}}$, $f_{\mathrm{CO}}=10\ \frac{\mathrm{ml}}{\mathrm{min}}$. Between D and F: two cycles of gas switching between $f_{\mathrm{O2}}=5\ \frac{\mathrm{ml}}{\mathrm{min}}$, $f_{\mathrm{CO}}=10\ \frac{\mathrm{ml}}{\mathrm{min}}$ and no O_2, $f_{\mathrm{CO}}=2\ \frac{\mathrm{ml}}{\mathrm{min}}$ (condition **E**); **b):** measured partial pressures of CO, O_2 and CO_2 as a function of the different conditions (A-F) and of time; **c):** linescans along *L*-direction through the respective peak maxima extracted from the 2D maps for selected sample conditions (A, C and F).

alloy surfaces and nanoparticles were reported to be catalytically active for CO oxidation at 550 K [62, 72]. Hence, the set conditions correspond to regime i) described in subsection 3.1.3.

Fig. 8.2 a) shows close-ups on the respective Bragg peaks of the different Pt-Rh compositions (vertical panels) measured under the probed conditions (A-F; horizontal panels) of the CO oxidation experiment. The deduced initial particle shapes under reducing conditions (condition A, first vertical panel) are thoroughly discussed in section 6.2. As was shown therein, the fit results of the respective Bragg peak FWHMs and the x-ray reflectivity measurements agree on an initial particle height of 21±3 Å for all five stripes, which is also mirrored in the equal periodicity of the Laue oscillations in the 2D maps of condition A. By combining results from rocking scans and AFM measurements, the particle diameter was found to scale with increasing Pt composition, varying from 54 Å for pure Rh to 125 Å for pure Pt (see Appendices A.2 and A.3). An increase in Pt content thus changes the shape from rather compact (pure Rh) to more disk-like particle shapes (high Pt content). For all stripes the initial relative particle coverage was determined to comprise 50%-60% (see results of the x-ray reflectivity measurements in Fig. 8.3).

Two key observations can be deduced from the 2D maps of Fig. 8.2 a) that occurred in the transition to higher CO$_2$ production:

first, for the Pt-rich particles, there is a progressive shift of the Laue oscillation maxima towards the Bragg peak positions. These oscillation shifts are also discernible in the linescans of Fig. 8.2 c), where they are indicated by arrows. The linescans were extracted from the 2D maps along L-direction through the respective particle Bragg peaks. They indicate that the heights of these particles significantly increased when CO oxidation set in and kept progressively increasing while reaching conditions of even higher catalytic activity.

Second, the shift of the fringes is progressively suppressed for particles with increasing Rh content, as can again be deduced from both, the 2D maps in Fig. 8.2 a) and the linescans in Fig. 8.2 c). This implies, that the vertical sintering was strongly reduced for Rh-rich particles and thus for particles with a non-disk-like but more compact three-dimensional shape.

The particle heights, obtained from the FWHMs of the Bragg peak fits to the linescans, confirm and quantify the aforementioned qualitative observations (see Fig. 8.5 b)): while in the case of the pure Pt particles the height almost doubled from 24 Å to 42 Å, the height increase was already strongly reduced

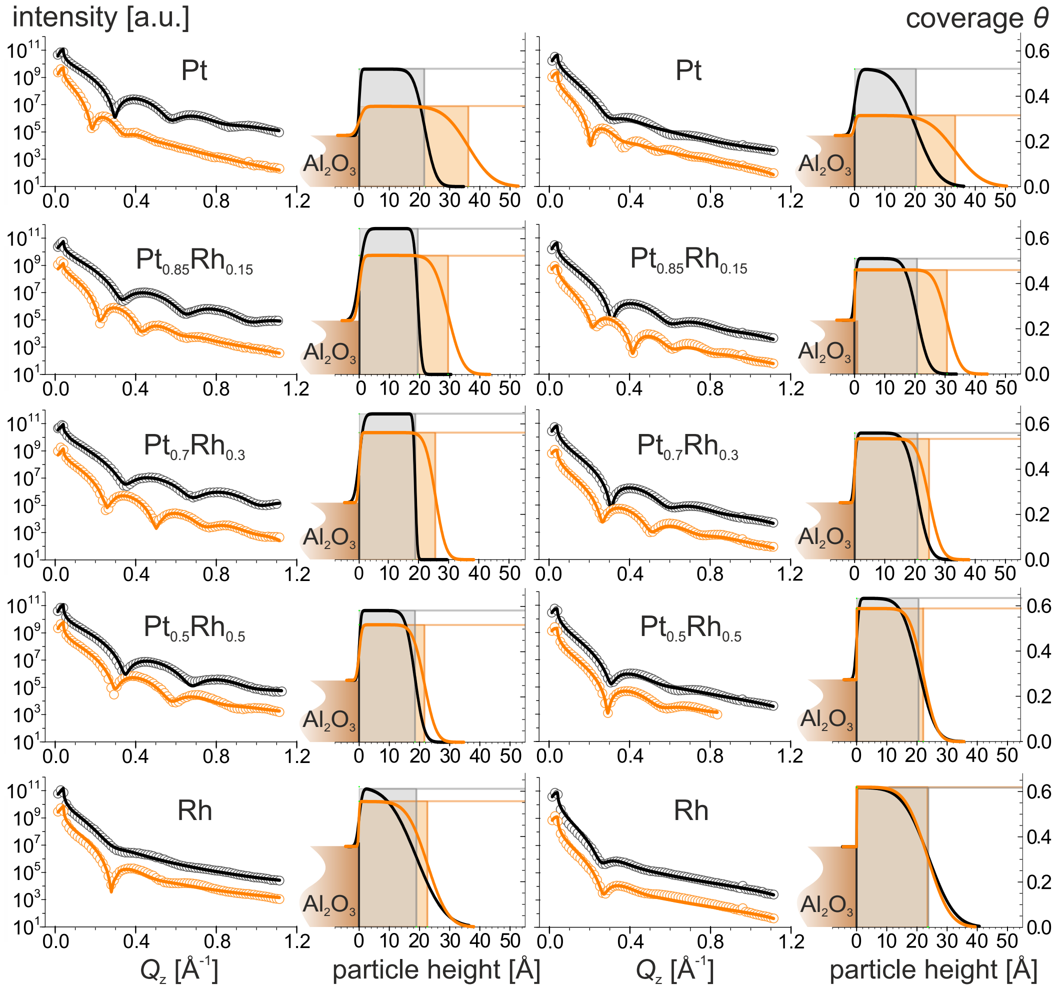

Figure 8.3: **Juxtaposition of the composition-dependent x-ray reflectivity results for the comparable samples "alumina-1" and "-2": left:** sample "alumina-1"; **right:** sample "alumina-2". Circles: measured data, solid lines: fit to the data; black: before, orange: during CO oxidation ("alumina-1": condition F: $f_{\mathrm{O2}}=7\ \frac{\mathrm{ml}}{\mathrm{min}}$, $f_{\mathrm{CO}}=10\ \frac{\mathrm{ml}}{\mathrm{min}}$; "alumina-2": condition d: $f_{\mathrm{O2}}=8\ \frac{\mathrm{ml}}{\mathrm{min}}$, $f_{\mathrm{CO}}=10\ \frac{\mathrm{ml}}{\mathrm{min}}$). To the right of the corresponding reflectivity curves: electron density profiles obtained from the fits, which yield the particle heights H and the fractions θ of the surface covered by nanoparticles.

for the $Pt_{0.85}Rh_{0.15}$ particles (changing from 23 Å to 31 Å), whereas the height of the pure Rh particles stayed nearly constant (26 Å compared to the initial height 24 Å). Also for the pure Rh particles of the other sizes (Rh "L" and Rh "S", see Appendix C.2) the height was preserved. This composition-dependent vertical sintering of Pt-Rh particles during CO oxidation was reproduced in the study of the comparable sample "alumina-2", which probed the particle $(11\bar{1})$ Bragg peaks in the substrate $(1\bar{2}10, L)$-plane (see Appendix C.1).

For both samples ("alumina-1" and "-2") these height changes were also supported by the x-ray reflectivity fit results shown in Fig. 8.3: their qualitative inspection reveals that the decrease in distance between the particle height-dependent interference fringes is much more pronounced in the case of pure Pt and Pt-rich particles, as compared to the pure Rh particles. For sample "alumina-1" the fits reveal that the average height of the pure Pt particles increased from 22 Å to 36 Å, whereas, in accordance with the Bragg peak fit results, the height increase was found to be less pronounced for the $Pt_{0.85}Rh_{0.15}$ particles (from 19 Å to 29 Å) and even more suppressed for particles with higher Rh content ($Pt_{0.7}Rh_{0.3}$: from 18 Å to 26 Å, $Pt_{0.5}Rh_{0.5}$: from 18 Å to 22 Å, pure Rh: from 19 Å to 23 Å). The fit results of sample "alumina-2" yielded comparable results (see right side in Fig. 8.3).

The particle heights obtained from the reflectivity data are in general smaller than the ones deduced from the Bragg peak fits in Fig. 8.2 c) and Fig. C.2 c). This is due to the fact that the simple box model used for fitting the reflectivity data introduces a systematic error on the particle height since it does not take into account the details of the particle shape [152].

It is striking that the height increase was found to be proportional to the reduction of the particle surface coverage, as can be deduced from the shaded boxes in the electron density profiles obtained from the fit results (see Fig. 8.3), thus keeping the integral of the electron density profiles approximately constant. The reduction in coverage was accordingly most pronounced for the pure Pt particles for which it decreased from 52% to 35%. The reflectivity results thus strongly suggest a huge mass transport to have taken place on the sample surface during the activity-induced restructuring of the Pt-rich nanoparticles. In addition, they prove the conservation of catalyst material, represented by the areas of the shaded boxes, which remained constant within error bars for all Pt-Rh compositions.

Despite this tremendous material transport during catalytic reaction, the sam-

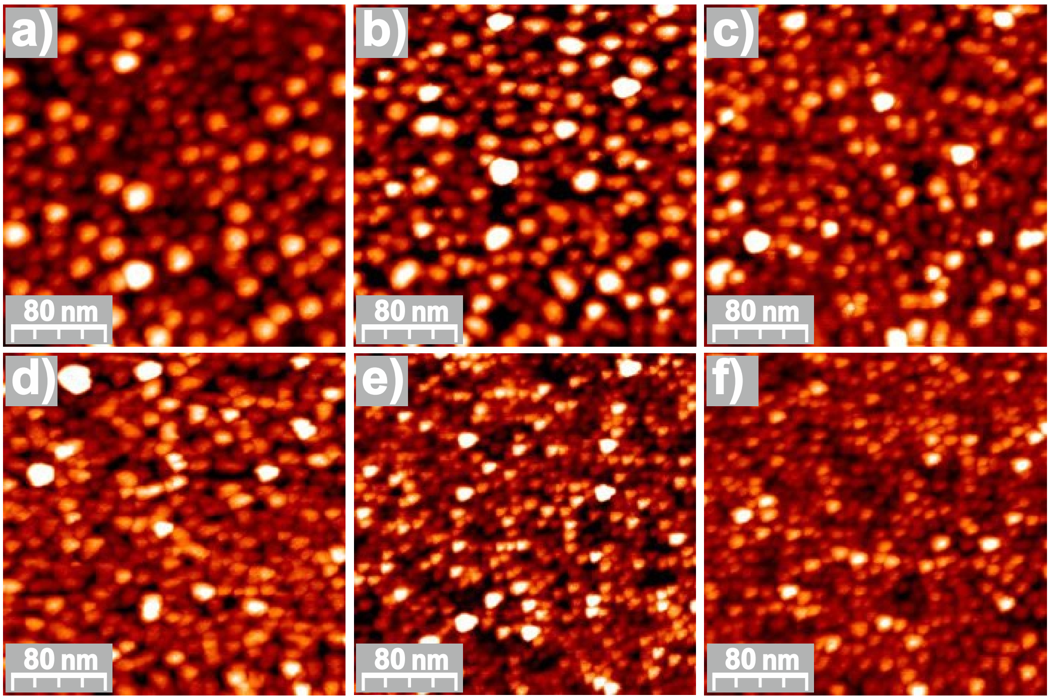

Figure 8.4: **AFM images performed after the CO oxidation experiment on sample “alumina-1”:** the measurements were performed in air on **a):** Pt, **b):** $Pt_{0.85}Rh_{0.15}$, **c):** $Pt_{0.7}Rh_{0.3}$, **d):** $Pt_{0.5}Rh_{0.5}$, and **e):** Rh particles of the same initial height; **f):** Rh particles of slightly higher initial height (Rh “L”). The measurements were performed by Omicron Nanotechnology GmbH, Taunusstein, Germany.

ple still featured separated and well-defined nanoparticles for all Pt-Rh compositions. This was inferred from the AFM measurements that were performed after the CO oxidation experiment on sample “alumina-1”, they are shown in Fig. 8.4. This finding was moreover supported by the preservation of the particle Bragg peak patterns and the absence of Debye-Scherrer powder diffraction rings, which suggest the conservation of the epitaxial arrangement of the particles, even under high catalytic activity (e.g. condition F). The AFM images mirror in addition the aforementioned composition-dependent particle shapes ranging from disk-like Pt-rich particles characterized by a large diameter, up to compact Rh-rich particles.

8.1.2 Quantitative size and shape changes determined from the particle rod analysis

The previous subsection discussed the *general characteristics* of the composition- and thus shape-dependent particle sintering of Pt-Rh particles during CO oxidation reactions. This subsection deals with the detailed *quantitative* analysis of this composition-dependent particle shape restructuring and yields insights into the underlying *driving forces*.

First, the **quantitative size changes** of the particles on sample "alumina-1" will be discussed. They are summarized in Fig. 8.5 for the different Pt-Rh compositions as a function of the different probed sample conditions (A-F).

Fig. 8.5 b) displays the particle heights as obtained from the FWHMs of the respective particle Bragg peak fits mentioned earlier. They reveal the composition-dependent particle height increase discussed in the previous subsection. The data reveal in addition that the two cycles of gas switching - i.e. the cycling between reducing conditions (condition D) and conditions of catalytic activity (condition E) - had the largest impact on the pure Pt particles, while the Rh-containing particles preserved their heights.

Against the background of the drastic height increase found in the case of the Pt-rich particles, it was very surprising that the diameters for all Pt-Rh compositions were found to stay constant within error bars throughout the experiment. Their average values, as obtained from rocking scan measurements, are shown in Fig. 8.5 a), represented by black open symbols. These data were confirmed by the diameters deduced from the AFM images performed after the CO oxidation experiment, represented by red symbols in Fig. 8.5 a). More information on the particle diameter determination from rocking scans and from the AFM data can be found in Appendices A.2 and A.3, respectively.

These results allowed for plotting the average particle aspect ratios $\frac{H}{D}$ for the different Pt-Rh compositions as a function of the reaction condition, their values are displayed in Fig. 8.5 c). Due to the preservation of the particle diameter independent of the Pt-Rh composition and the strong height increase of the Pt-rich particles in the course of the experiment, the increase of the $\frac{H}{D}$-values during CO oxidation scaled in turn with the Pt-content of the particles. The aspect ratios of the Pt-containing particles thus progressively approached the values of the pure Rh particles, which stayed constant at a larger value of $\frac{H}{D}\approx 0.47$ throughout the experiment. These findings suggest a greater stability for particle shapes that are characterized by a higher height-to-diameter aspect ratio $\frac{H}{D}$.

In order to obtain a deeper insight into the particle **structure and shape changes** the corresponding particle out-of-plane rods (shown in Fig. 8.2 c)) were analyzed, where different **particle shape models** were used to simulate

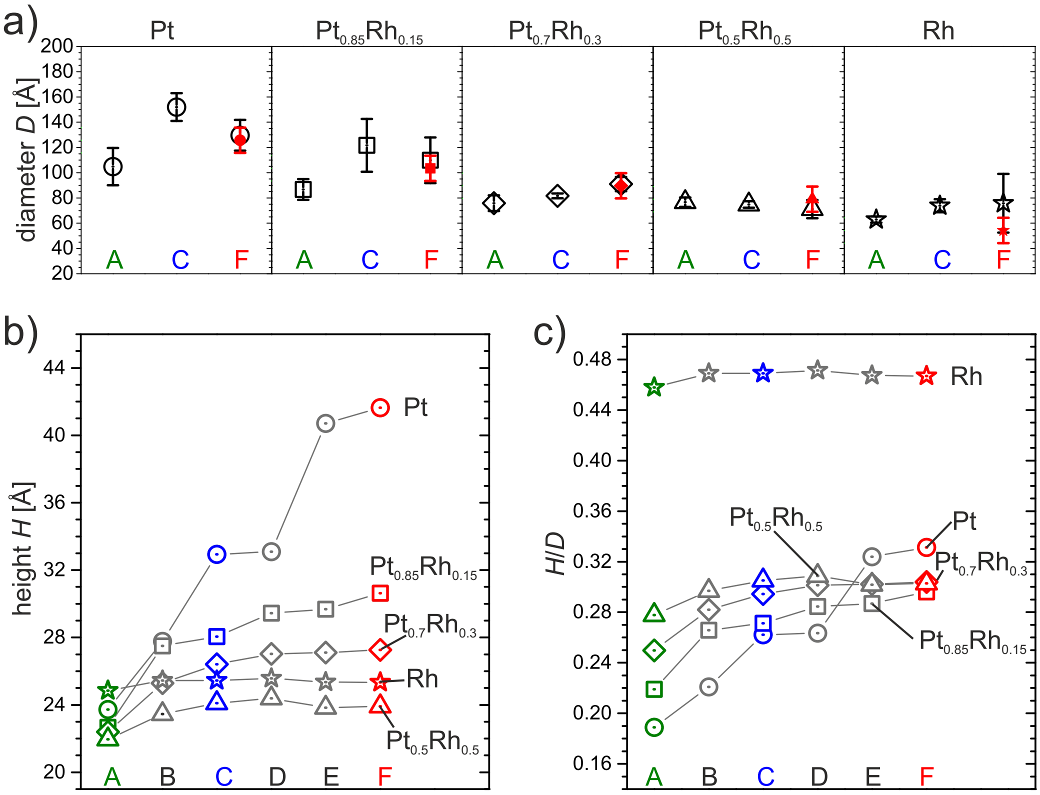

Figure 8.5: **Particle diameters, heights and aspect ratios of the different Pt-Rh compositions on sample "alumina-1":** the sample temperature, the total reactor pressure and the total gas flow were held constant at T=550 K, p_{tot}=200 mbar and $f_{\text{tot}}=100\ \frac{\text{ml}}{\text{min}}$, respectively. Set gas flows: condition **A**: no O_2, $f_{\text{CO}}=2\ \frac{\text{ml}}{\text{min}}$; **B**: $f_{\text{O2}}=2\ \frac{\text{ml}}{\text{min}}$, $f_{\text{CO}}=10\ \frac{\text{ml}}{\text{min}}$; **C**: $f_{\text{O2}}=4\ \frac{\text{ml}}{\text{min}}$, $f_{\text{CO}}=10\ \frac{\text{ml}}{\text{min}}$; **D**: $f_{\text{O2}}=5\frac{\text{ml}}{\text{min}}$, $f_{\text{CO}}=10\ \frac{\text{ml}}{\text{min}}$; **E**: no O_2, $f_{\text{CO}}=2\ \frac{\text{ml}}{\text{min}}$; **F**: $f_{\text{O2}}=7\ \frac{\text{ml}}{\text{min}}$, $f_{\text{CO}}=10\ \frac{\text{ml}}{\text{min}}$; between D and E: two cycles of gas switching between $f_{\text{O2}}=5\ \frac{\text{ml}}{\text{min}}$, $f_{\text{CO}}=10\ \frac{\text{ml}}{\text{min}}$ and no O_2, $f_{\text{CO}}=2\ \frac{\text{ml}}{\text{min}}$; **a):** particle diameters; black open symbols: values obtained from the rocking scan analysis (see Appendix A.2) for conditions A, C and F; red symbols: values from AFM measurements (see Appendix A.3); **b):** particle heights obtained from particle Bragg peak fits; **c):** particle height-to-diameter aspect ratios $\frac{H}{D}$ as obtained from the particle heights in b) and the diameters from the AFM analysis in a).

and fit the characteristic Laue oscillations. Prior to the fitting, the particle rods were intensity-corrected for the background in the 2D maps, for the stationary sample and detector and for the Lorentz-factor (see Appendix B.1).

As was discussed in subsection 2.3.1, the general shape of a (111)-oriented particle consists mainly of (111)-type top and bottom facets as well as (111)- and (100)-type side facets. Accordingly, higher indexed facets will be neglected in the following. For free, unsupported particles the equilibrium shape can be generated via the Wulff construction and depends only on the ratio $g=\frac{\gamma_{100}}{\gamma_{111}}$ of the (100)- and (111)-type particle facets' surface energies γ (Gibbs free energy per surface unit) [24]. For supported particles, as studied in the present case, the equilibrium shape is fully described by the surface energy ratio $g=\frac{\gamma_{100}}{\gamma_{111}}$, the particle height H and the diameter D. The extent of truncation and thus the particle height are determined by the interfacial energy according to the Wulff-Kashiew theorem [208].

For each Pt-Rh composition and each of the conditions A, C and F, ten different **particle shape models** were probed. All of them adhered to the respective particle diameters D deduced from the AFM measurements (see Fig. 8.5 a)). Moreover, in each case the particle height H was chosen such that the finite height Laue oscillations were best reproduced. The thus obtained heights agree with the values deduced from the Bragg peak FWHMs shown in Fig. 8.5 b). Thus, the shapes put to the test comprised eight truncated (111)-oriented particle models based on the Wulff construction, which displayed a gradient in the facet surface energy ratio $g=\frac{\gamma_{100}}{\gamma_{111}}$, ranging from g=0.9 to $g=\sqrt{3}$=1.73.[2] In addition, a truncated sphere and a simple layer model were tested. The top parts of Fig. 8.7 and Fig. 8.8 present these different model shapes for the case of the $Pt_{0.7}Rh_{0.3}$ particles under condition A.

The particle rods were fitted using the programme package ROD [173]. It is a programme used to simulate and fit the intensity modulation along crystal truncation rods, where a structure model is refined in the course of the fitting procedure. Among others, possible fitting parameters include the relaxation of the atomic layers in vertical direction (displacement parameters) and the percentaged occupancy of a certain layer (occupancy parameters).

The aforementioned nanoparticle model shapes put to the test could be described by a certain number of atoms per layer and thus by an atomic density profile in vertical direction. Hence, the particle shape in the structure model was accounted for by adjusting the occupancy parameters for each atomic layer accordingly.

In order to illustrate the **fitting procedure and the parameters** varied therein, Fig. 8.6 shows as an example the fit performed for the underlying model shape of $Pt_{0.7}Rh_{0.3}$ particles under condition A. Having the particle

---

[2] Under vacuum conditions, the ratio g varies from 1.05 for Pt to 1.16 for Rh [25, 151]. In the case of CO and CO/O$_2$ mixtures, no systematic investigation of the surface energy of Pt, Rh as well as Pt-Rh alloy surfaces as a function of coverage and chemical potentials is reported, which would allow a direct prediction of the particle shape using the Wulff construction.

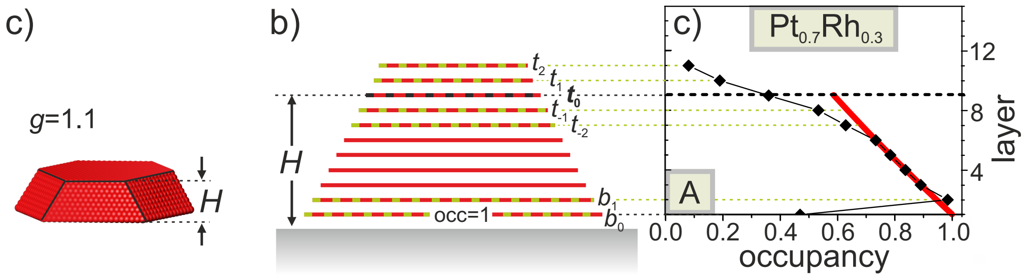

Figure 8.6: **Particle models and fit parameters: a)**: shape of the $Pt_{0.7}Rh_{0.3}$ particles under condition A with height H=18 Å, diameter D=90 Å, and particle facet surface energy ratio $g=\frac{\gamma_{001}}{\gamma_{111}}=1.1$; **b)**: sketch of the corresponding structure model that clarifies the different fit parameters. The total number of layers is determined by the particle height H, as obtained from the finite thickness oscillations around the particle Bragg peak, where up to two additional layers (t_1, t_2) were added to compensate for the vertical particle size distribution. During the fitting procedure the occupancy values of layers t_2, t_1, t_0, t_{-1}, t_{-2}, b_1, and b_0 were allowed to vary as well as the displacement parameters of up to three topmost layers and up to two layers at the interface; **c)**: occupancy values according to the underlying particle shape model displayed in a) (red line) and fitted occupancy values (black diamonds). The text occ=1 in panel b) indicates that in this example the theoretical occupancy value of the lowest layer of the unfitted model, b_0, corresponds to 100 %; the unfitted occupancy values of the other layers are normalized to this nominal occupancy and represent the ideal case depicted in a).

height determined to comprise H=18 Å, the particle was concluded to consist of nine atomic layers. Fig. 8.6 a) shows the particle model for the surface energy ratio of g=1.1 (H=18 Å, D=90 Å). Fig. 8.6 b) displays the corresponding layer model that illustrates the fit parameters. The ninth and thus the topmost layer (occupancy value t_0) is indicated by black dashes. Each layer has an occupancy value according to the atomic density determined by the particle shape. Fig. 8.6 c) shows these occupancy values (solid red line) according to the model shape of Fig. 8.6 a).

In order to compensate for the particle height distribution up to two layers were added to the layer model. During the fitting procedure the occupancy values of these two layers (t_1, t_2), the ones of layers t_{-1}, t_{-2}, t_0 and of the two layers at the interface (b_0, b_1) were allowed to vary. If the fit suggested unphysical values, the number of parameters was reduced accordingly (e.g. only one layer was added on top and only the occupancy values t_1, t_0, t_{-1}, b_0 and b_1 were used as fit parameters, or even no layer was added on top and only the occupancy values t_0, b_0 and b_1 were used as fit parameters). The values of the occupancy parameters were considered as physical as long as with increasing

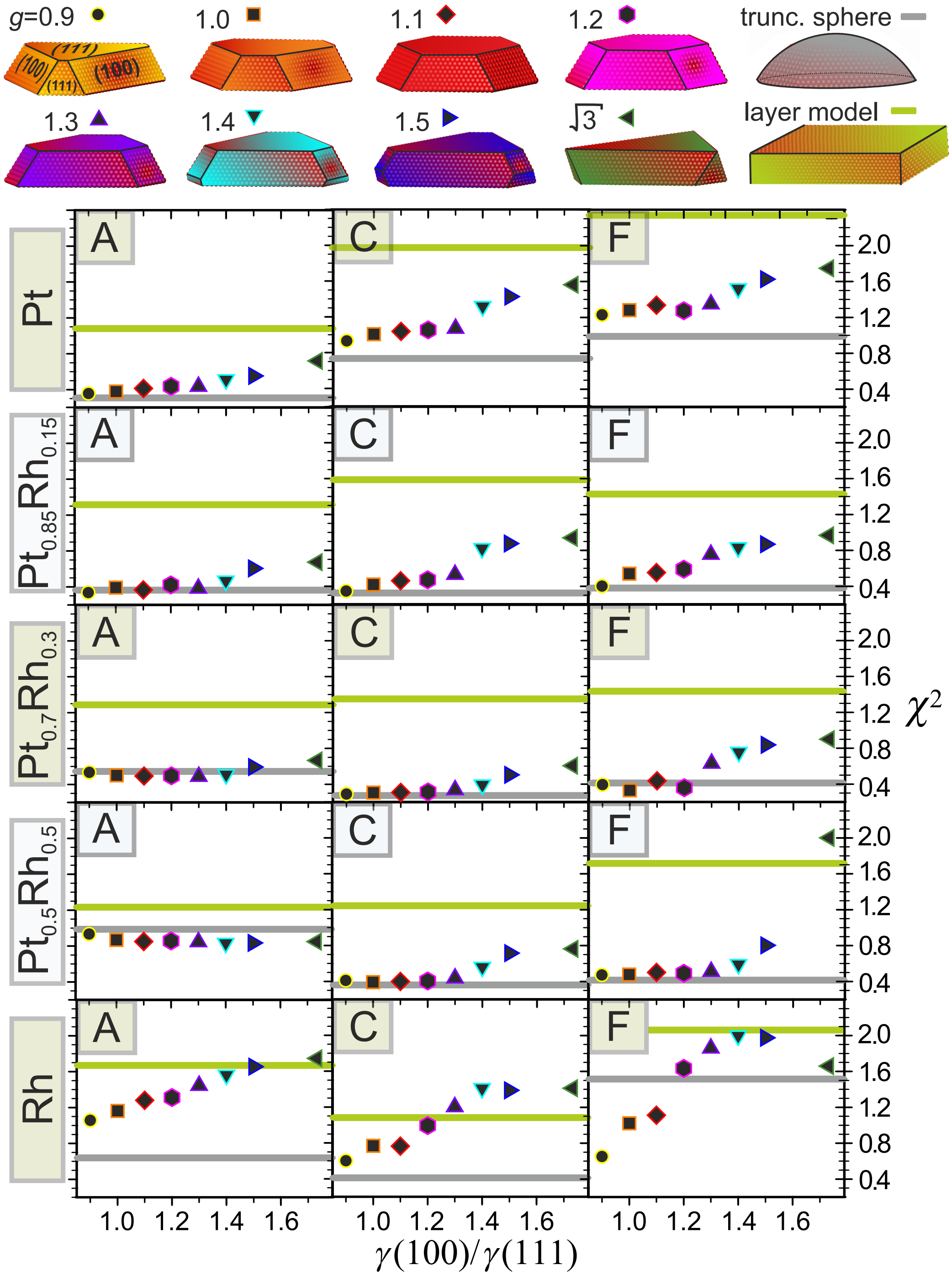

Figure 8.7: **Goodness of fit for different model shapes:** comparison of figures of merit χ^2 obtained from fitting the particle rods using different underlying model shapes with varying particle facet surface energy ratios $g=\frac{\gamma_{(100)}}{\gamma_{(111)}}$ of the Wulff shape (represented by differently shaped symbols, see top of figure for colour coding). Horizontal grey and light-green lines represent figures of merit obtained for the model shapes of a truncated sphere and a closed layer, respectively. The data are shown for the different Pt-Rh compositions and conditions A, C and F. Top part: underlying model shapes for the case of the $Pt_{0.7}Rh_{0.3}$ particles under condition A.

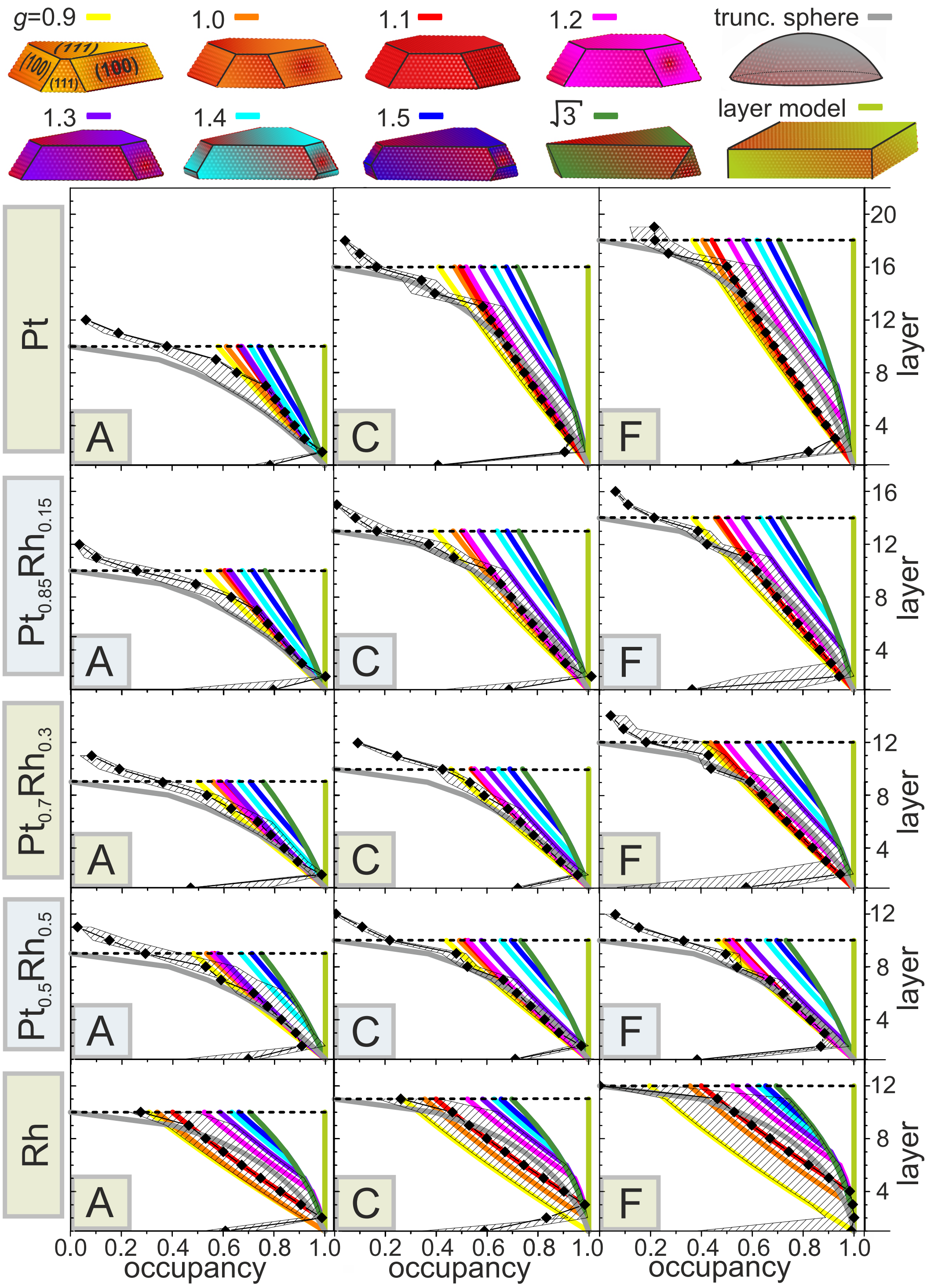

Figure 8.8: **Comparison of occupancy values:** comparison of fitted (black diamonds, based on the particle shape model with g=1.1) and theoretical (solid lines) occupancy values of other underlying model shapes (see top of figure for colour coding). Black-dashed area: parameter space of fit results obtained from the five best fits of all tested g-values and of the truncated sphere model. Horizontal black dashed line: particle heights deduced from the x-ray data, the fitted occupancy values mirror the smearing out of electron density in vertical direction. Top part: model shapes for the case of the $Pt_{0.7}Rh_{0.3}$ particles under condition A.

distance of the atomic layers to the particle bulk the corresponding occupancy values decreased (i.e. $t_{-2} \geq t_{-1} \geq t_0 \geq t_1 \geq t_2$ and $b_1 \geq b_0$).

In the following the thus obtained **fit results** will be discussed and the comparison of the underlying model shapes will be elucidated.

Fig. 8.7 yields an overview of the figures of merit χ^2 obtained for the different models for all Pt-Rh compositions and the sample conditions A, C and F.[3] As a general trend for all conditions and compositions good fit results were obtained for (111)-oriented particle shapes with ratios of $g=\frac{\gamma_{100}}{\gamma_{111}}$ ranging between 0.9 and 1.3. The model particle shapes shown at the top of Fig. 8.7 and Fig. 8.8 reveal that these g-values are compatible with particles possessing distinct (100)-type facets. Particles with highly diminished (100)-type facets ($g>1.3$) like prism-shaped particles are unlikely to occur. Also the simple layer model could be ruled out. This is in agreement with DFT-calculations that suggest for all conditions particle shapes with a g-value ranging between 0.9 and 1.3 [25]. The data suggest that for conditions of increased catalytic activity (especially condition F) this trend towards smaller g-values and thus larger (100)-type facets was even more pronounced. A tentative explanation could be that in the case of an increasing catalytic activity, and thus under higher oxygen partial pressures, surface oxides tend to form on the particle facets. Surface oxide formation is energetically favourable on the more open (100)-type facets [151], which in turn become stabilized by the adsorbed oxygen and, as a consequence, grow.

In addition to the particle shape models characterized by small g-values, the truncated sphere model was also found to yield low figures of merit. In Fig. 8.8 the parameter space of the fitted occupancy values of the five best fits of all tested g-values and of the truncated sphere model are represented by dashed areas. They superimpose the original occupancy values of the initial particle shape models represented by the respectively coloured solid lines. It is striking that the dashed areas, i.e. the parameter space of best fits, are very narrow in the vicinity of the topmost layer (horizontal black dashed line), although the occupancy values of these layers were allowed to vary in the fit (see Fig. 8.6 b)). This implies that the same fit results were obtained for the various probed starting models.

---

[3] The number of used fit parameters for a certain condition and Pt-Rh composition was the same for all tested models in order to ensure a comparability, but could vary from one condition or particle stripe to the next. In each case it was chosen such that none of the fits ran into unphysical values.

The black diamonds in Fig. 8.8 represent the occupancy values of a more refined fitting using g=1.1, which represent the general trends as they are in all cases close to the centres of the dashed areas. Their values obtained for the topmost particle layers are in line with the smearing out of the electron density profiles deduced from the fit of the reflectivity measurements (see Fig. 8.3). It can be explained by a moderate particle height distribution and/or the presence of higher indexed facets, which were not taken into account in the underlying particle model and which would be in accordance with a rounder shape [208]. According to the fits, the occupancy parameters of the interface layer range for nearly all compositions and conditions between 0.4 and 0.7. This points to misfit induced defects at the interface to the substrate (e.g. strain effects, steps or edges, see subsection 2.3.2), which locally disturb the lattice. These interfacial occupancy values were found to decrease after the reaction-promoted sintering, pointing to a growing number of interfacial defects such as misfit dislocations, which is in line with previous findings [27].
The results of the fitted displacement parameters when using g=1.1 are summarized in Table B.1 in Appendix B.2. In the case of the sintering Pt-rich particles the first and second metal layer distance at the interface showed a tendency to increase in the transition to conditions of catalytic activity, likely because of a reduced interaction with the α-$Al_2O_3(0001)$ substrate.

In Fig. 8.9 a)-e) the corresponding fits for g=1.1 (solid lines) to the intensity-corrected data of the particle rods (open symbols) are shown for all Pt-Rh compositions and conditions A, C and F. The fits reproduce nicely the overall shape, the damping character and the periodicity of the finite height oscillations.
The accordingly deduced 3D models for particles with g=1.1 are depicted in Fig. 8.9 f)-g) before and after sintering, yielding an overview of the probed shape-dependent coarsening and summarizing the results discussed so far. They illustrate that the restructuring is characterized by a strong particle height increase which scales with the Pt content of the particles, while the diameters are maintained throughout, independent of the Pt-Rh composition. The growth in height occurs at the expense of the particle surface coverage, which in turn becomes strongly reduced in the case of Pt-rich particles. Hence, a tremendous mass transfer occurs on the sample surface during reaction conditions in which the total amount of catalyst material is preserved and which can only be explained by coexisting *inter*- as well as *intra*-particle mass trans-

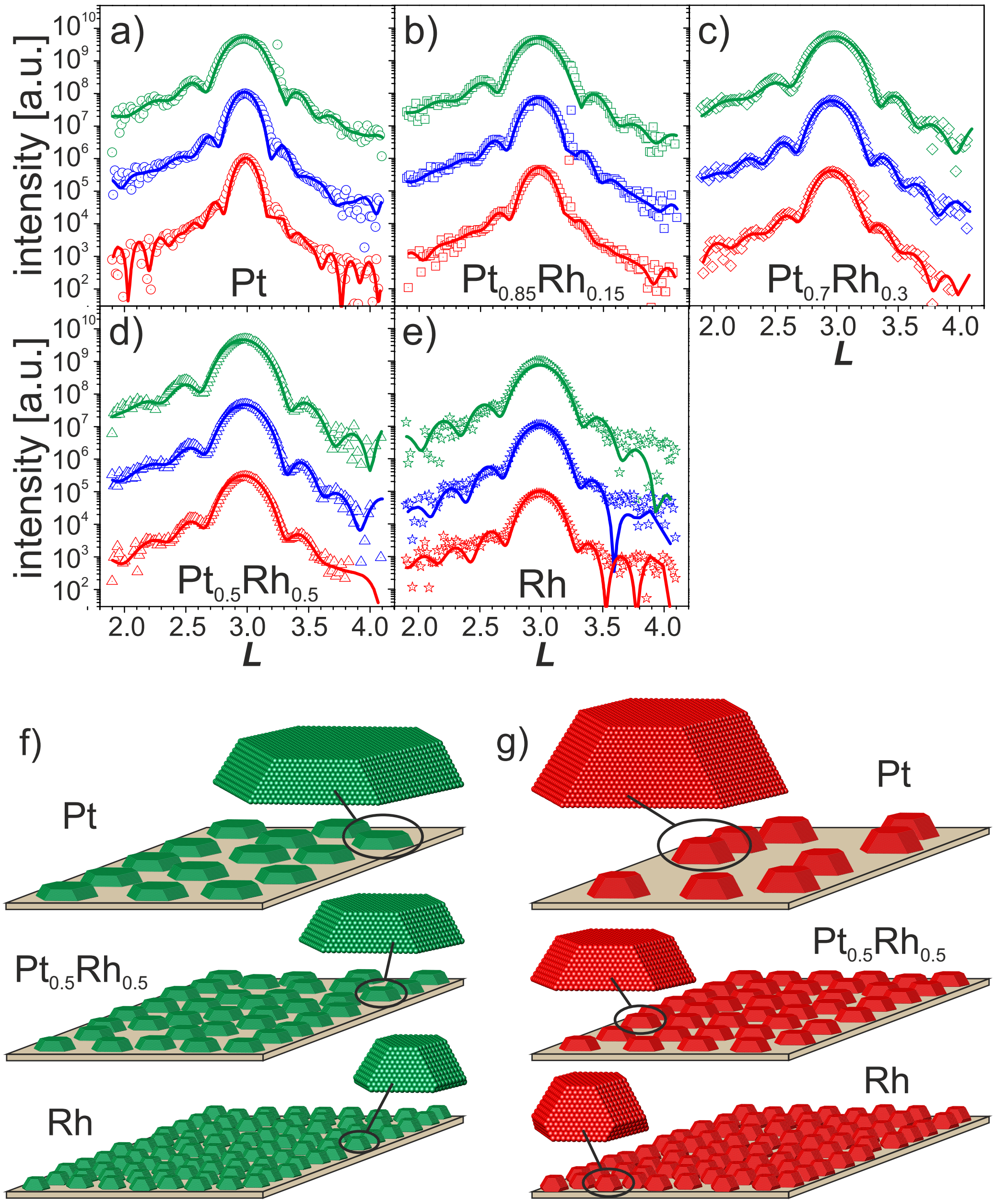

Figure 8.9: **Sintering-induced shape changes of the particles on sample "alumina-1":** linescans along L-direction (open symbols: intensity-corrected data; solid lines: fit using an underlying model particle shape with $g=\frac{\gamma_{001}}{\gamma_{111}}$) through the respective particle $(3\bar{1}1)$ Bragg peaks extracted from the 2D maps of Fig. 8.2: **a):** Pt, **b):** $Pt_{0.85}Rh_{0.15}$, **c):** $Pt_{0.7}Rh_{0.3}$, **d):** $Pt_{0.5}Rh_{0.5}$, and **e):** Rh for conditions A (green), C (blue), and F (red). Average particle shapes and sample morphology **f):** before and **g):** after sintering as deduced from the Bragg peak and reflectivity fits using g=1.1.

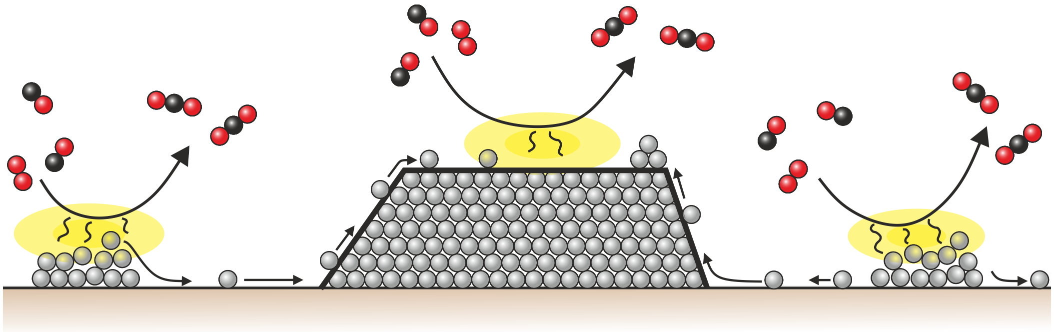

Figure 8.10: **Proposed sinter mechanism:** smaller particles become destabilized by the heat of reaction; as a consequence a mass flux towards larger and more stable particles occurs, which results in their restructuring characterized by an increase in aspect ratio.

ports. Rh-rich particles, which featured already after growth a compact shape, are found to resist sintering under identical conditions and maintain an advantageous higher dispersion.

8.1.3 Proposed sinter mechanism and driving force

As will be discussed in the following, the reasons for the sintering of the Pt-rich particles can be found in their initial flat particle shapes and in their large lateral size distribution.

The results of the previous subsections revealed that the pure Rh and Rh-rich particles did not undergo any considerable size or shape changes under reaction conditions. This implies that the shape they adopted already during particle growth, characterized by a high height to diameter aspect ratio, was close to the respective stable equilibrium shape.

Contrary, the as-prepared disk-like Pt particles were found to be highly unstable: they underwent a tremendous restructuring, characterized by a height increase at the expense of the surface coverage, while the particle diameter stayed constant. Hence, they adopted compact shape comparable to the one of the Rh particles, which proved to be also very stable (see subsection 8.1.5). Moreover, AFM measurements revealed that especially Pt-rich particles disclose a large lateral size distribution (see Fig. A.6) and hence feature the presence of smaller particles, which are, below a certain critical size, unstable in the Ostwald ripening process (see section 3.3).

Accordingly, a realistic scenario for the underlying sinter mechanism is as follows: during the CO oxidation reaction smaller particles, present in the case of Pt-rich samples, become destabilized by the heat of reaction, the energy of which amounts for Pt to 3 eV per produced CO_2 molecule [206]. As a consequence, a mass flux towards the larger and more stable particles occurs (see Fig. 8.10). Contrary to classical Ostwald ripening (see section 3.3), the larger particles do not show an increase in diameter. Instead they grow only vertically in a Volmer-Weber-like fashion to adopt a more compact shape. The observed phenomenon for the Pt-rich particles can thus be viewed as a CO oxidation promoted non-classical Ostwald-ripening process, in which the particles overcome their low height-to-diameter aspect ratio shapes in which they are kinetically trapped after growth, to adopt a shape closer to the one of thermodynamic equilibrium. This strife towards equilibrium-shaped particles can be viewed as underlying driving force of this novel sinter mechanism.

8.1.4 Adhesion energy determination

Based on the assumption that the particles have adopted their equilibrium shapes after the CO oxidation induced sintering discussed in subsections 8.1.1-8.1.3, the adhesion energies E_{adh} were determined for the different Pt-Rh compositions from the respective extent of truncation for the particle shapes shown in Fig. 8.9 g) and using reference values for (111)- and (100)-type particle facet surface energies [25, 207], see also Table 2.1.

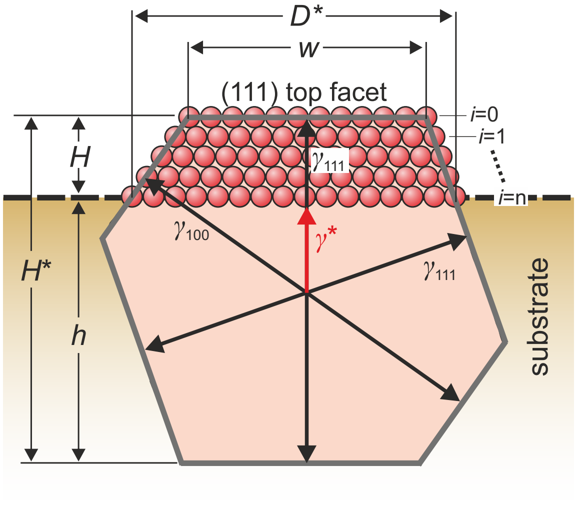

Figure 8.11: **Wulff-construction of a strongly truncated particle:** side view of a supported, strongly truncated (111)-oriented particle consisting of (111)- and (100)-type facets drawn according to the Wulff construction. H denotes the particle height, γ_{100} and γ_{111} the facet surface energies and γ^* the effective surface energy $\gamma^*=\gamma_{\mathrm{interface}}-\gamma_{\mathrm{substrate}}$ [207].

Fig. 8.11 shows the side view of a strongly truncated particle, similar to the ones of Fig. 8.9 g). The cross section of the untruncated particle corresponds to the Wulff construction of a free particle [24]. Since the height H of the truncated particle is less than half the height of the unsupported particle, the effective surface energy γ^* can be written as $\gamma^*=\gamma_{\text{interface}}$ - $\gamma_{\text{substrate}}$ [207, 208]. Knowing the particle height H, the length w of the top facets, the surface energy ratio $g=\frac{\gamma_{100}}{\gamma_{111}}$ and the surface energy of the (111)-type facets, the effective surface energy can be expressed as [207]:

$$\gamma^* = \gamma_{111} \cdot (\sqrt{\frac{3}{2}} \cdot \frac{H}{w} \cdot g - 1), \tag{8.1}$$

from which in turn the adhesion energy E_{adh} can be determined:

$$E_{\text{adh}} = \gamma_{111} - \gamma^*. \tag{8.2}$$

Only in the case of the pure Rh particles equations 8.1 and 8.2 were not used since the height of their truncated particles was deduced to be higher than half of the height of the unsupported particles. Instead, the Wulff-Kaishew theorem (see subsection 2.3.1)

$$E_{\text{adh}} = \gamma_{111} \cdot \frac{2h}{H+h} \tag{8.3}$$

was employed, where h corresponds to the height of the “buried” part of the particle, as can be deduced from Fig. 8.11.

The thus obtained adhesion energy values E_{adh} for the equilibrium-shaped particles with a surface energy ratio of $g=\frac{\gamma_{100}}{\gamma_{111}}=1.1$ are summarized in bold in Table 8.1. The results for the values of $g=0.9$ and $g=1.3$ - for which similar fit results to the particle crystal truncation rod data were obtained, see section 8.1.2 - are included and can be considered as the maximum and minimum values of the respective error bars (systematic error bar ± 0.2 $\frac{\text{J}}{\text{m}^2}$).

A composition-dependent trend is discernible, which is characterized by an increase in E_{adh} with increasing Rh content to a maximum of 2.57 $\frac{\text{J}}{\text{m}^2}$, followed by a decrease down to 1.89 $\frac{\text{J}}{\text{m}^2}$ for pure Rh. This trend reflects the competing influence of the increasing chemical interaction from Pt to Rh for stoichiometric α-Al_2O_3(0001) surfaces [32], and the variation in misfit to the α-Al_2O_3(0001) substrate. As was shown in Table 2.2 in subsection 2.4.1, a perfect match to the substrate is expected for a composition of $Pt_{0.7}Rh_{0.3}$. Due to an increasing misfit towards the Rh-rich side the adhesion energy is expected to decrease [27, 209]. Since at the same time the chemical interaction is increasing, the

composition	$\boldsymbol{H}$ [Å]	γ_{111} $[\frac{eV}{Å^2}]$	$\boldsymbol{g}=\frac{\gamma_{100}}{\gamma_{111}}$	$\boldsymbol{w}$ [Å], $\boldsymbol{h}$ [Å]	$\boldsymbol{E}_{\textbf{adh}}$ $[\frac{\mathrm{J}}{\mathrm{m}^2}]$
Pt	38.61	0.093	0.9	w=84.31	2.23
			1.1	w=77.08	**1.98**
			1.3	w=81.90	1.86
Pt$_{0.85}$Rh$_{0.15}$	29.39	0.09765	0.9	w=69.53	2.40
			1.1	w=64.73	**2.17**
			1.3	w=69.53	2.07
Pt$_{0.7}$Rh$_{0.3}$	24.75	0.1023	0.9	w=59.65	2.53
			1.1	w=52.50	**2.24**
			1.3	w=59.65	2.20
Pt$_{0.5}$Rh$_{0.5}$	20.12	0.1085	0.9	w=59.27	2.83
			1.1	w=52.16	**2.57**
			1.3	w=54.53	2.46
Rh	24.20	0.124	0.9	h=24.20	1.99
			1.1	h=22.00	**1.89**
			1.3	h=24.20	1.99

Table 8.1: **Adhesion energies:** determined for the particles of Fig. 8.9 g) after sintering (condition F) using equations 8.1 and 8.2 (Pt-containing particles) or using equation 8.3 (pure Rh particles). The values for the surface energies γ_{111} of the pure Pt and Rh particles were taken from [25], see also Table 2.1; the surface energies $\gamma_{Pt_xRh_{1-x}}$ of the alloy particles Pt$_x$Rh$_{1-x}$ were calculated by making use of the equation $\gamma_{Pt_xRh_{1-x}}$ = x·$\gamma_{111,\mathrm{Pt}}$ + (1-x)·$\gamma_{111,\mathrm{Rh}}$, see discussion in subsection 2.3.1.

maximum of the adhesion energy shifts to a higher Rh composition, found here for the Pt$_{0.5}$Rh$_{0.5}$ particles.

The obtained values are comparable to literature values for Pd nanoparticles on ultrathin Al$_2$O$_3$ surfaces [207].

8.1.5 Testing the particle stability under operational conditions at elevated temperatures

The previous subsections on the Pt-Rh particles of sample **“alumina-1”** showed how the activity-induced sintering resulted in equilibrium-shaped particles, whose adhesion energies to the α-Al$_2$O$_3$(0001) substrate were discussed in subsection 8.1.4. The experiments discussed in the following probed the sta-

bility of these sintered particles on “alumina-1” by exposing them to harsh reaction conditions at elevated temperatures (T=670K) and repeated gas switching cycles.
As in the in-situ CO oxidation study at 550 K discussed in sections 8.1.1 and 8.1.2, the total pressure and total gas flow were kept constant at p_{tot}=200 mbar and $f_{\mathrm{tot}}=100\ \frac{\mathrm{ml}}{\mathrm{min}}$, respectively. The measurements were performed at the elevated temperature of 670 K and accordingly CO poisoning of the catalyst surfaces could be excluded (see subsection 3.1.3).

The various probed gas settings comprised at first conditions for CO oxidation (A*→D*) in which the oxygen flow was stepwise increased up to overstoichiometry in oxygen with a O_2/CO ratio of 1:1 (conditions: A*: no O_2, $f_{\mathrm{CO}}=2\ \frac{\mathrm{ml}}{\mathrm{min}}$; B*: $f_{\mathrm{O2}}=2\ \frac{\mathrm{ml}}{\mathrm{min}}$, $f_{\mathrm{CO}}=10\ \frac{\mathrm{ml}}{\mathrm{min}}$; C*: $f_{\mathrm{O2}}=4\ \frac{\mathrm{ml}}{\mathrm{min}}$, $f_{\mathrm{CO}}=10\ \frac{\mathrm{ml}}{\mathrm{min}}$; D*: $f_{\mathrm{O2}}=10\ \frac{\mathrm{ml}}{\mathrm{min}}$, $f_{\mathrm{CO}}=10\ \frac{\mathrm{ml}}{\mathrm{min}}$). Subsequently, the sample was exposed to three cycles of gas switching between pure oxygen flow (E*: $f_{\mathrm{O2}}=25\ \frac{\mathrm{ml}}{\mathrm{min}}$, no CO) and reducing conditions (F*: no O_2, $f_{\mathrm{CO}}=10\ \frac{\mathrm{ml}}{\mathrm{min}}$), where in each case Ar was added as carrier gas.
Fig. 8.12 b) depicts the mass spectrometer data as a function of condition and time. In line with the experiment performed at the lower temperature of T=550 K, the CO_2 production increases as a function of the O_2 flow, indicating a stepwise increase in catalytic activity. Direct comparison with the CO_2 production rate at 550 K (see Fig. 8.2 b)) reveals a higher catalytic activity in the present case, as can be expected at elevated temperatures (see subsection 3.1.3).
The 2D reciprocal space maps, measured under each probed condition on the various particles stripes, are centered around the respective particle $(3\bar{1}1)$ Bragg peaks and are summarized in Fig. 8.12 a). The linescans extracted for some selected conditions (A*, D*, E*, and F*) through the peaks along L-direction are shown in Fig. 8.12 c).

In order to quantify potential particle height changes, the linescans of Fig. 8.12 c) were fitted with Pseudo-Voigt functions, the obtained heights are depicted in Fig. 8.13 b). In cases where the detector image was oversaturated (pure Pt particles: conditions A*-E*; $Pt_{0.85}Rh_{0.15}$: condition E*), the height was estimated from the distance of the Laue oscillation minima.
The obtained values reveal that for all Pt-Rh compositions no considerable particle height increase occurred during CO oxidation at 670 K (conditions A*→D*). This confirms that the Pt-rich particles really adopted a stable

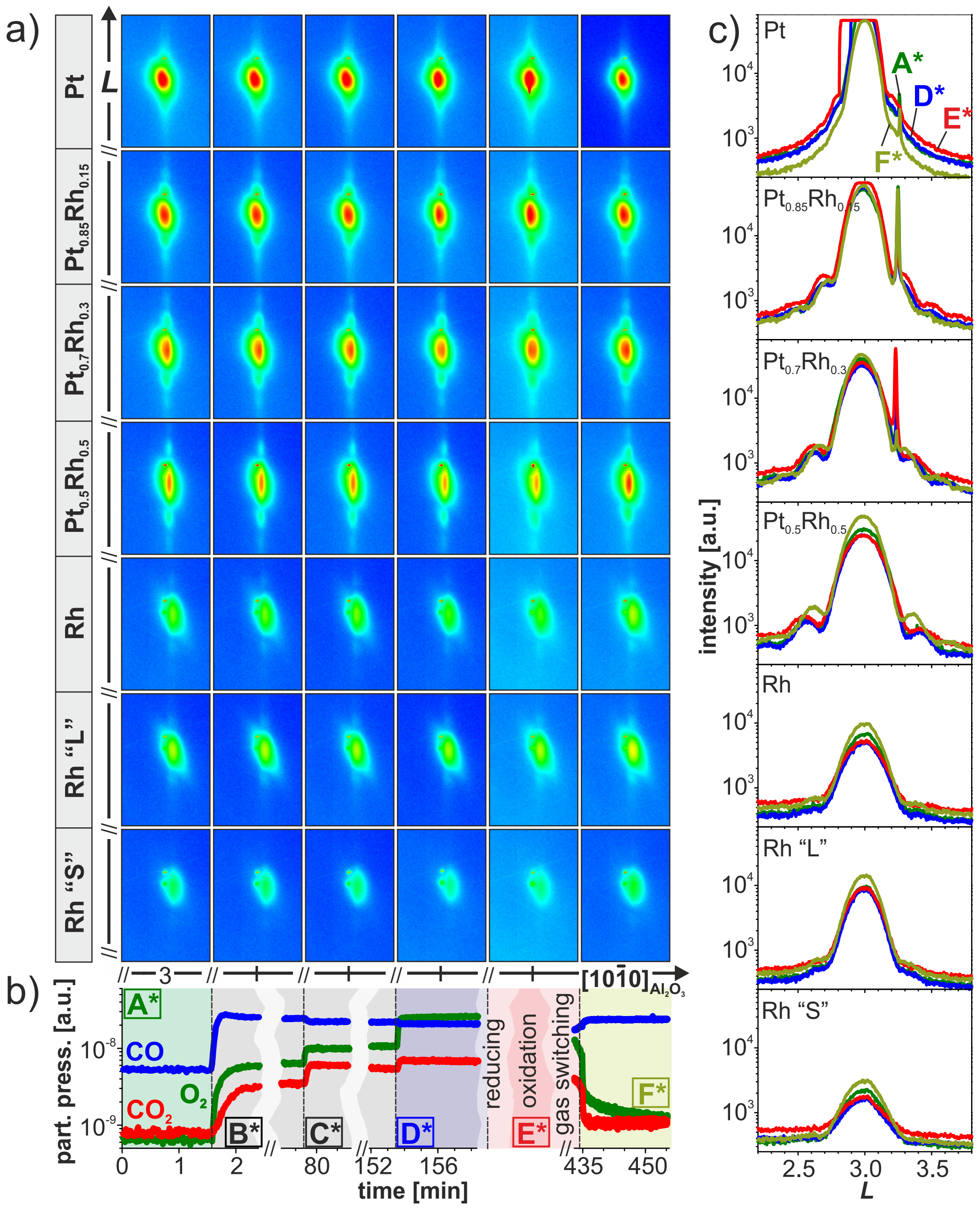

Figure 8.12: **In-situ monitoring of the Pt-Rh (3$\bar{1}$1) Bragg peaks of sample "alumina-1" during CO oxidation at elevated temperatures: a):** 2D maps collected at 670 K and p_{tot}=200 mbar (exposure time: 50 s). Set partial flows: **A***: no O$_2$, $f_{\mathrm{CO}}=2\ \frac{\mathrm{ml}}{\mathrm{min}}$; **B***: $f_{\mathrm{O2}}=2\ \frac{\mathrm{ml}}{\mathrm{min}}$, $f_{\mathrm{CO}}=10\ \frac{\mathrm{ml}}{\mathrm{min}}$; **C***: $f_{\mathrm{O2}}=4\ \frac{\mathrm{ml}}{\mathrm{min}}$, $f_{\mathrm{CO}}=10\ \frac{\mathrm{ml}}{\mathrm{min}}$; **D***: $f_{\mathrm{O2}}=10\ \frac{\mathrm{ml}}{\mathrm{min}}$, $f_{\mathrm{CO}}=10\ \frac{\mathrm{ml}}{\mathrm{min}}$; **E***: $f_{\mathrm{O2}}=25\ \frac{\mathrm{ml}}{\mathrm{min}}$, no CO; **F***: no O$_2$, $f_{\mathrm{CO}}=10\ \frac{\mathrm{ml}}{\mathrm{min}}$. Between condition D* and E*: no O$_2$, $f_{\mathrm{CO}}=10\ \frac{\mathrm{ml}}{\mathrm{min}}$. Between E* and F*: two cycles of gas switching between $f_{\mathrm{O2}}=25\ \frac{\mathrm{ml}}{\mathrm{min}}$, no CO, and no O$_2$, $f_{\mathrm{CO}}=10\ \frac{\mathrm{ml}}{\mathrm{min}}$. **b):** Partial pressures measured as a function of condition (A*-F*) and time; **c):** linescans along L-direction through the respective peak maxima extracted from the 2D maps for selected sample conditions (A*, D*, E* and F*).

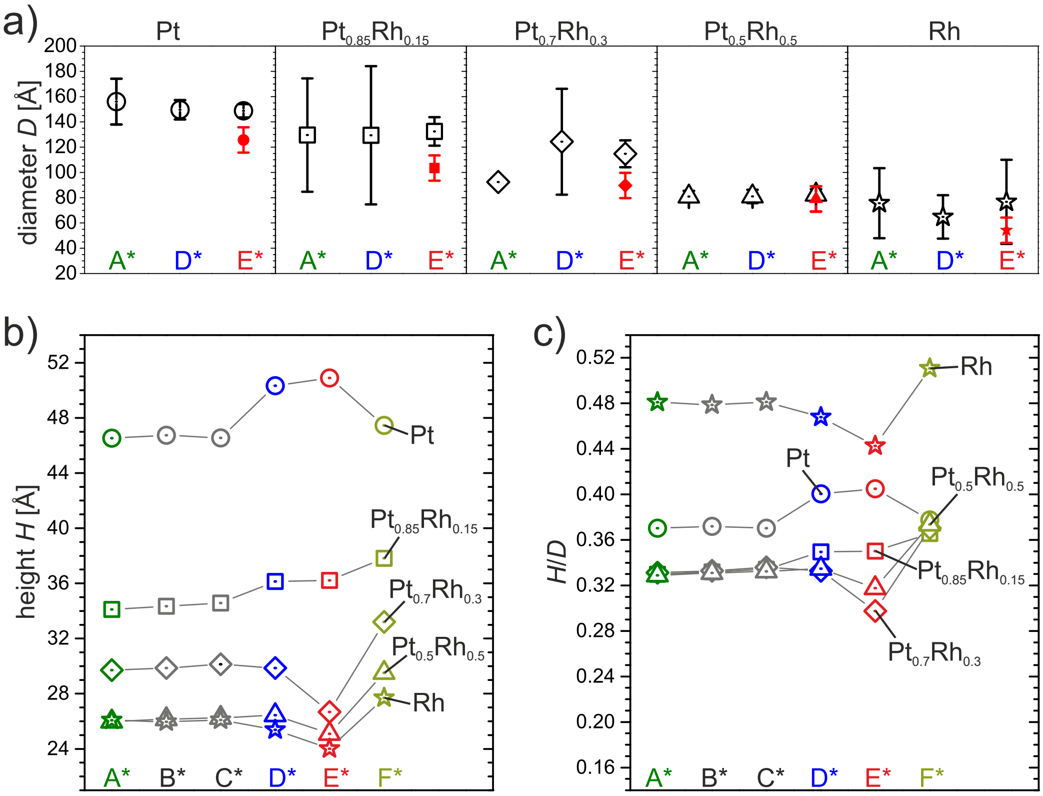

Figure 8.13: **Particle diameters, heights and aspect ratios of the different Pt-Rh compositions on sample "alumina-1" under various conditions at 673 K:** condition **A***: no O_2, $f_{\mathrm{CO}}=2\ \frac{\mathrm{ml}}{\mathrm{min}}$; **B***: $f_{\mathrm{O2}}=2\ \frac{\mathrm{ml}}{\mathrm{min}}$, $f_{\mathrm{CO}}=10\ \frac{\mathrm{ml}}{\mathrm{min}}$; **C***: $f_{\mathrm{O2}}=4\ \frac{\mathrm{ml}}{\mathrm{min}}$, $f_{\mathrm{CO}}=10\ \frac{\mathrm{ml}}{\mathrm{min}}$; **D***: $f_{\mathrm{O2}}=10\ \frac{\mathrm{ml}}{\mathrm{min}}$, $f_{\mathrm{CO}}=10\ \frac{\mathrm{ml}}{\mathrm{min}}$; **E***: $f_{\mathrm{O2}}=25\ \frac{\mathrm{ml}}{\mathrm{min}}$, no CO; **F***: no O_2, $f_{\mathrm{CO}}=10\ \frac{\mathrm{ml}}{\mathrm{min}}$; **a):** particle diameters; black open symbols represent the diameters of conditions A*, C* and F* as obtained from the θ-scan analysis (see Appendix A.2), red symbols denote the diameters deduced from AFM measurements performed after the CO oxidation experiment (see appendix A.3); **b):** particle heights deduced from the particle Bragg peak analysis; **c):** particle aspect ratios $\frac{H}{D}$ retrieved from the particle heights in b) and the diameters obtained from AFM measurements shown in a).

equilibrium shape during their sintering at 550 K (sections 8.1.1, 8.1.2). It was only at the very end of the CO oxidation experiment at 670 K, after the gas switching cycles between oxidizing and reducing conditions (E*→F*), that the particles underwent a slight height increase ΔH resulting in heights differing from the ones deduced for condition A*. Since ΔH did not exceed 3-4 Å, this vertical sintering is negligible compared to the drastic particle restructuring that the Pt-rich particles underwent at 550 K. Moreover, since it occurred for all compositions, this type of sintering might not be related to a missing equilibrium particle shape but to a general coarsening due to aging.

The most drastic change, a *decrease* in height, occurred under oxidizing atmospheres (condition E*) and was found to be more pronounced for the Rh-rich particles. This observation can be explained by a partial oxidation of the particles (oxide shell), leaving a smaller remaining metallic core that gives rise to the probed Bragg peak signal. Since Rh is more easily oxidized than Pt (see section 3.1.5), the resulting particle height decrease in Fig. 8.13 b) scales with the Rh content of the particles.

Fig. 8.13 a) discloses the particle diameters for some selected conditions (A*, E* and F*) as obtained from the rocking scan analysis along with their systematic error bars (see Appendix A.2). It also contains the diameters as deduced from the AFM measurements performed after the CO oxidation experiment (see Appendix A.3), which were already included in Fig. 8.5 a). These data moreover confirm the preservation of the particle diameter throughout the experiment, also at elevated temperatures of 670 K.

Fig. 8.13 c) shows the particle height-to-diameter aspect ratios $\frac{H}{D}$ as obtained from the particle heights in b) and the diameter values determined from the AFM data. Their consistency reflects the absence of further activity-induced particle sintering and affirm the stability of the particles once they have adopted their equilibrium shape, characterized by a higher aspect ratio.

In the following the CO oxidation induced particle size changes on sample **"alumina-3"** will be discussed. As was shown in section 6.2, the sample contained Rh and Pt$_{0.7}$Rh$_{0.3}$ particles of three different size regimes (I: H=25-35 Å, D=50-60 Å; II: H=35-50 Å, D=100-160 Å; and III: H=50-65 Å, D=160-270 Å). The particle size of regime I is comparable to the one of the previously discussed sample "alumina-1". Based on the aforementioned explanations, sintering could be expected to be greatly reduced for these particles since they,

already after growth, featured an even higher aspect ratio ($\frac{H}{D}$ between 0.5 and 0.6, see Fig. 8.14) than the sintered particles on sample "alumina-1".
The probed sample conditions comprised three cycles (i-iii) of switching from reducing conditions (no O_2, f_{CO}=4 $\frac{\mathrm{ml}}{\mathrm{min}}$) to conditions of CO oxidation (up to a O_2/CO ratio of 0.625/1 with f_{O2}=2.5 $\frac{\mathrm{ml}}{\mathrm{min}}$ and f_{CO}=4 $\frac{\mathrm{ml}}{\mathrm{min}}$), where in each case Ar was added as carrier gas to keep up a constant total reactor flow of f_{tot}=50 $\frac{\mathrm{ml}}{\mathrm{min}}$. The cycles differed in the total reactor pressure p_{tot} and/or in the sample temperature T (cycle i: p_{tot}=50 mbar, T= 650 K; ii: p_{tot}=200 mbar, T= 650 K; iii: p_{tot}=200 mbar, T= 770 K; see also bottom of Fig. 8.14). All probed temperatures were thus comparable or higher than the ones used in the CO oxidation experiments of sample "alumina-1". The total pressure was at first lower (p_{tot}=50 mbar) but towards the end equal (p_{tot}=200 mbar) to the total pressure used in the experiment of sample "alumina-1". In order to avoid uncontrolled conditions, the changes in temperature and pressure were performed under pure Ar flow. Contrary to sample "alumina-1" the sample was never exposed to pure oxygen flow.
Information on the particle heights and diameters was obtained from the FWHMs of the respective particle Bragg peaks in vertical and horizontal direction. This approach is feasible since on this sample the particle $(11\bar{1})$ Bragg peaks were probed, which makes strain broadening effects negligible (see Appendix A.1). Fig. 8.14 summarizes the thus obtained values for the respective particle heights H, diameters D, and aspect ratios $\frac{H}{D}$ for the different probed compositions and sizes.
First, the results for the **particles of size I** will be discussed. The data in Fig. 8.14 show that, indeed, no size changes occurred for the $\mathrm{Pt}_{0.7}\mathrm{Rh}_{0.3}$ particles, neither in height nor diameter. This holds for both, the particles that were already grown as alloy particles (orange symbols) and the "core-shell" particles (blue symbols), that were grown by the sequential deposition of Rh and Pt (see chapter 6 for more information), indicating that they feature a similar behaviour during catalytic activity. For the Pt-rich particles on samples "alumina-1" and "-2" the most pronounced sintering occurred for gas settings in the range from reducing conditions up to an O_2:CO ratio of 0.5 (see subsections 8.1.1, 8.1.2 and Appendix C.1). This range was clearly covered in the present study which probed the particles under a O_2:CO ratio of up to 0.625. Hence, despite the lack of harsh cycling conditions or the flow of pure oxygen, the experiment of sample "alumina-3" proved the stability of $\mathrm{Pt}_{0.7}\mathrm{Rh}_{0.3}$ parti-

cles that featured high initial aspect ratios, even under the set elevated sample temperatures.

Contrary, the pure Rh particles of size I sintered in height, while their diameter stayed constant, which led to an increase in aspect ratio from 0.59 to 0.8. Based on the results discussed so far in this chapter, this finding is unexpected. A tentative explanation can be found in the assumption that the absolute value of the stable aspect ratio for a certain particle composition scales with the individual substrate characteristics, which are determined by the density of defect sites or potential adsorbates. Thus, it is striking that the Pt$_{0.7}$Rh$_{0.3}$ particles on sample "alumina-1" and "-2" became stabilized at $\frac{H}{D}$-values close to 0.37 (see Fig. 8.13 c) and Fig. C.2 d)), the particles of the same composition on the present sample at $\frac{H}{D}$=0.54, which is by a factor $\frac{0.54}{0.37}$=1.46 higher. Applying this factor to the $\frac{H}{D}$-value of 0.52 of the stable Rh particles on sample "alumina-1" (see Fig. 8.13 c)), the expected aspect ratio for stable particles on the present sample would become $1.46 \cdot 0.52 = 0.76$, which is close to the experimentally found one presented in Fig. 8.14.

The data obtained for the Pt$_{0.7}$Rh$_{0.3}$ and Rh **particles of sizes II and III** demonstrate the limits of the applied particle size analysis based on particle Bragg peak FWHMs: a comparison of the particle sizes presented in Fig. 8.14 with the particle diameters of the SEM images shown in Fig. 8.17 reveals that the sizes deduced from the FWHM analysis are too small. This deviation is already visible for the particles of size II but becomes dramatic for size III. This indicates that not the real particle diameters, but the coherently scattering intra-particle domain sizes give rise to the respective Bragg peak widths. Thus, the data presented in Fig. 8.14 represent only to some extent the real particle sizes. This is not the case for the smaller particles of size I, for which the coherently scattering areas correspond to the real particle sizes, as the comparison with the SEM images in Fig. 8.17 shows.

It is striking that also for sizes II and III the domain diameter values did not change for any of the compositions in the course of the whole experiment. As was discussed in section 6.2, the initial $\frac{H}{D}$-value scales inversely with the particle size and is thus lowest for the particles of size regime III. According to the previous discussions these should be most prone to sintering. Indeed, the data reveal that the heights of the domain sizes increased strongest for the lowest initial $\frac{H}{D}$-values, which also led to a steady increase of the aspect ratio towards the respective values of stability.

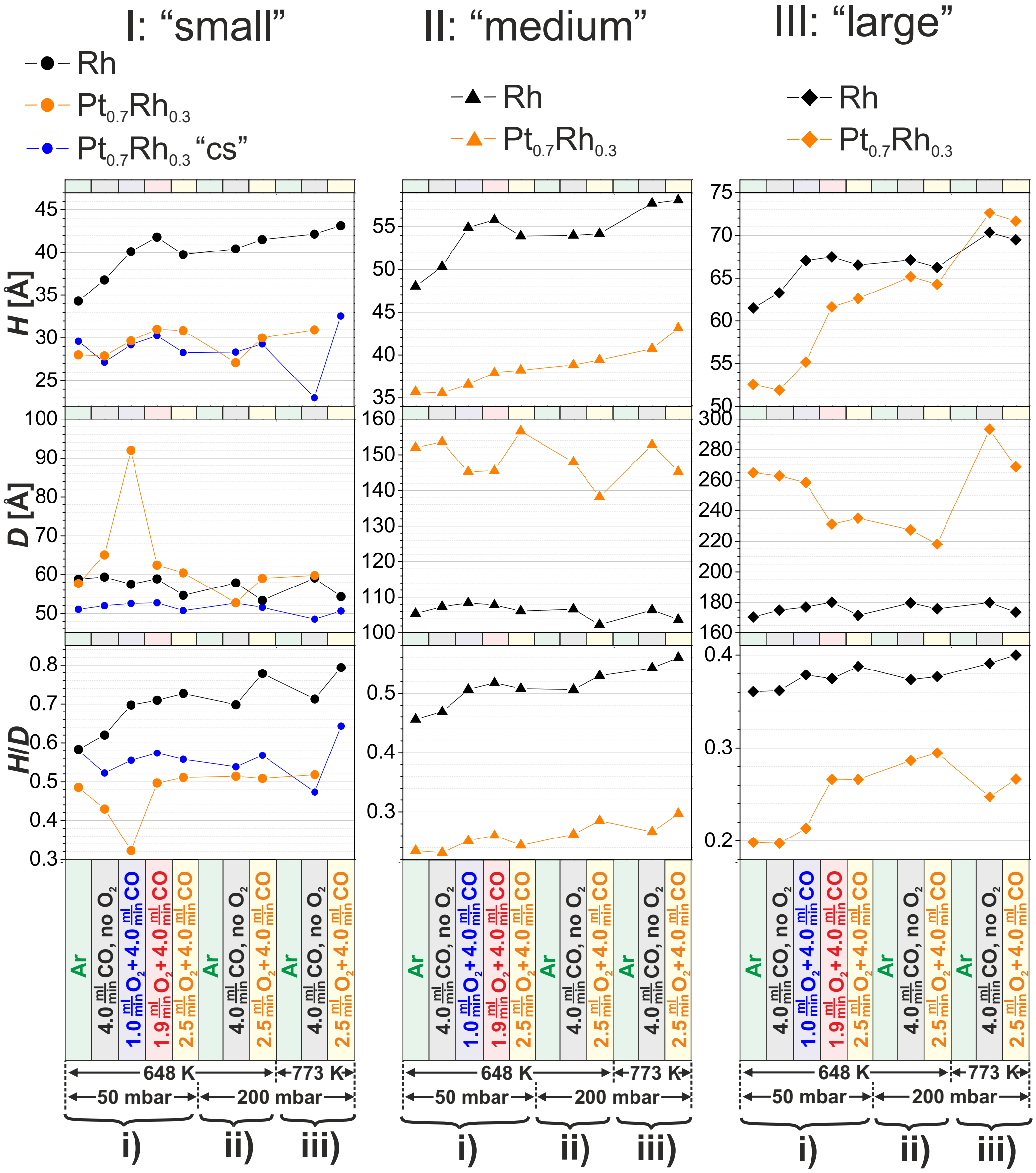

Figure 8.14: **Development of particle diameters, heights and aspect ratios of pure Rh and $Pt_{0.7}Rh_{0.3}$ particles of various sizes during CO oxidation on sample "alumina-3":** the heights H, diameters D and aspect ratios $\frac{H}{D}$ (horizontal panels) are given for the three different size regimes I, II and III (vertical panels) for Rh (black), $Pt_{0.7}Rh_{0.3}$ alloy (orange) and $Pt_{0.7}Rh_{0.3}$ "core-shell" (blue) particles; they were probed during three cycles of switching from reducing conditions to conditions of catalytic CO oxidation (cycle i: $p_{\text{tot},1}$=50 mbar, T_1=650 K; cycle ii: $p_{\text{tot},2}$=200 mbar, T_1=650 K; cycle iii: $p_{\text{tot},2}$=200 mbar, T_2=770 K; see also legend at the figure bottom); throughout the experiment the total gas flow was held constant at f_{tot}=50 $\frac{\text{ml}}{\text{min}}$.

8.1.6 Gas-induced particle lattice parameter changes

The previous subsections 8.1.1-8.1.5 presented the *size and shape changes* that the particles underwent as a function of the different gas settings. As was discussed in subsection 3.2.2, the particles' exposure to varying oxidizing and reducing atmospheres may in addition trigger a *chemical restructuring* [111, 112], which will be subject matter of this subsection.

Fig. 8.15 shows the development of the in- and out-of-plane lattice parameters of the particles of varying Pt-Rh composition on sample **"alumina-1"**. The values were obtained from the respective positions of the particle Bragg peak main maxima in the 2D maps of Fig. 8.2 and Fig. 8.12. They are plotted as a function of the various conditions probed at 550 K (conditions A→F, see caption of Fig. 8.2) and 670 K (conditions A*→F*, see caption of Fig. 8.12). Taking Vegard's law and thermal lattice expansion into account, the lattice parameter values amount at 550 K (670 K) to 3.9330 Å (3.9371 Å) for pure Pt, to 3.9145 Å (3.9186 Å) for $Pt_{0.85}Rh_{0.15}$, to 3.8958 Å (3.8999 Å) for $Pt_{0.7}Rh_{0.3}$, to 3.8712 Å (3.8751 Å) for $Pt_{0.5}Rh_{0.5}$ and to 3.8092 Å (3.8130 Å) for pure Rh. They are comparable to the experimental values shown in Fig. 8.15. The discrepancy between the in- and out-of-plane parameters is probably due to intra-particle strain effects based on the Poisson effect. The strain is caused as the particles try to adapt their in-plane lattice parameters at the interface to the one of the substrate. As is shown in Table 2.2, the mismatch is largest in the case of Rh. As a consequence, the strain and hence the discrepancy between in- and out-of-plane lattice parameters in Fig. 8.15 scales with Rh content. The in-plane lattice parameter of the substrate at the two probed temperatures is in Fig. 8.15 indicated by red lines.

The lattice parameters of the alloy particles (especially of $Pt_{0.85}Rh_{0.15}$ and $Pt_{0.7}Rh_{0.3}$) dramatically increased in the course of the CO oxidation experiment. This finding can be explained by the progressive segregation of Rh to the particle surface under increasingly oxidizing conditions, as it is more easily oxidized compared to Pt. This results in a Pt-richer core with correspondingly expanded lattice parameters. Accordingly, under pure oxygen flow (condition E*: $f_{O2}=25\ \frac{\mathrm{ml}}{\mathrm{min}}$, no CO) the lattice parameter reached a maximum value as the Rh segregation was probably strongest.

The lattice parameter expansions were found to be much more pronounced in horizontal than in vertical direction. Their development can also be deduced from the shifts of the particle Bragg peak main maxima found in the

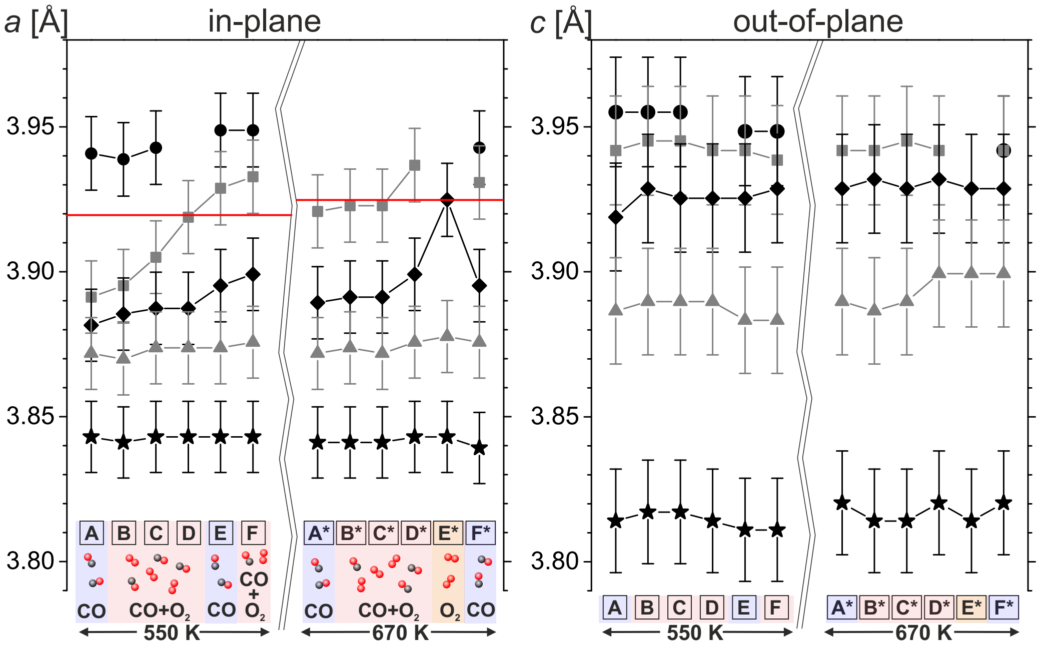

Figure 8.15: **Overview of the Pt-Rh particle lattice parameters of sample "alumina-1" in the course of the CO oxidation experiment: left:** in-plane parameter a, **right:** out-of-plane parameter c (Pt: circles; $Pt_{0.85}Rh_{0.15}$: squares; $Pt_{0.7}Rh_{0.3}$: diamonds; $Pt_{0.5}Rh_{0.5}$: triangles; Rh: stars). All lattice parameters are given as fcc bulk values. They were obtained from the positions of the respective particle $(3\bar{1}1)$ Bragg peak main maxima. Red horizontal lines on the left side: in-plane lattice parameter of the α-$Al_2O_3(0001)$ substrate at the probed temperatures. Missing data points are due to oversaturation of the detector under certain conditions.

horizontal Bragg peak scans (see scans in Fig. A.2 measured at 550 K and in Fig. A.3 measured at 670 K). A tentative explanation can be found in the vertical particle growth during sintering characterized by a piling up of atoms. The resulting weight of the growing number of additional layers may act as a counterforce to the lattice parameter expansion in out-of-plane direction. Accordingly, the expansion of the out-of-plane lattice parameters of the pure and strongly sintering Pt particles was progressively suppressed in the course of the experiment.

The lattice parameter changes of the alloy particles were concluded to be composition-dependent since they were the smaller the higher the Rh content was inside the particles. Since Pt-rich particles sinter more strongly, they feature an increased atom mobility which may also have eased the chemical restructuring. Furthermore, the Rh-rich particles feature a larger reservoir of Rh atoms to "feed on". Hence, segregation of Rh to the particle surface may

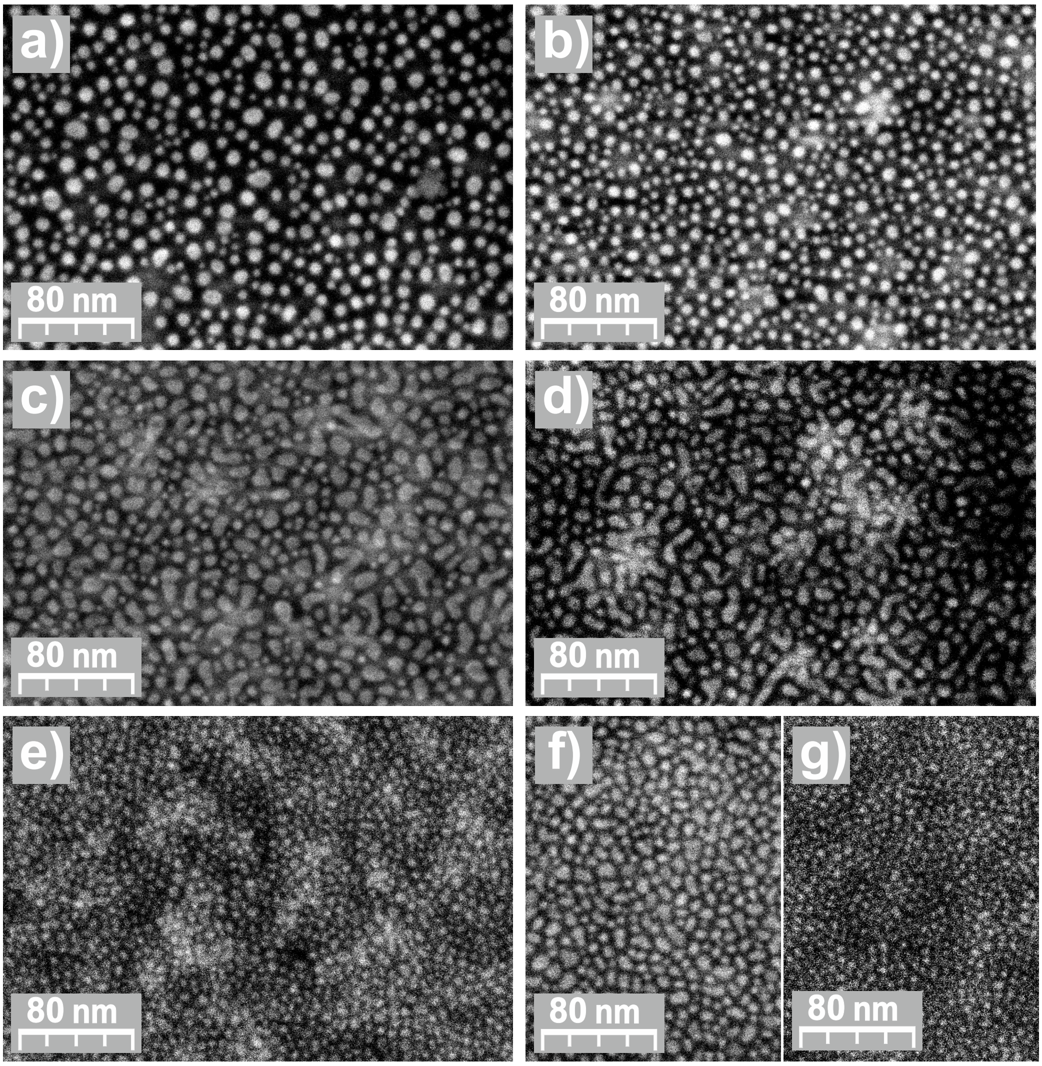

Figure 8.16: **SEM measurements performed after CO oxidation on sample "alumina-1":** they show particles of **a):** pure Pt, **b):** Pt$_{0.85}$Rh$_{0.15}$, **c):** Pt$_{0.7}$Rh$_{0.3}$, **d):** Pt$_{0.5}$Rh$_{0.5}$, **e)-g):** pure Rh. While the particles shown in **a)-e)** had the same initial particle height prior to sintering (nominal layer thickness "NLT"=10 Å), the Rh particles shown in **f):** "Rh L" ("NLT"=14 Å), and **g):** "Rh S" ("NLT"=7.5 Å) were slightly larger and smaller, respectively. The measurements were performed by Carl Zeiss Microscopy, Oberkochen, Germany.

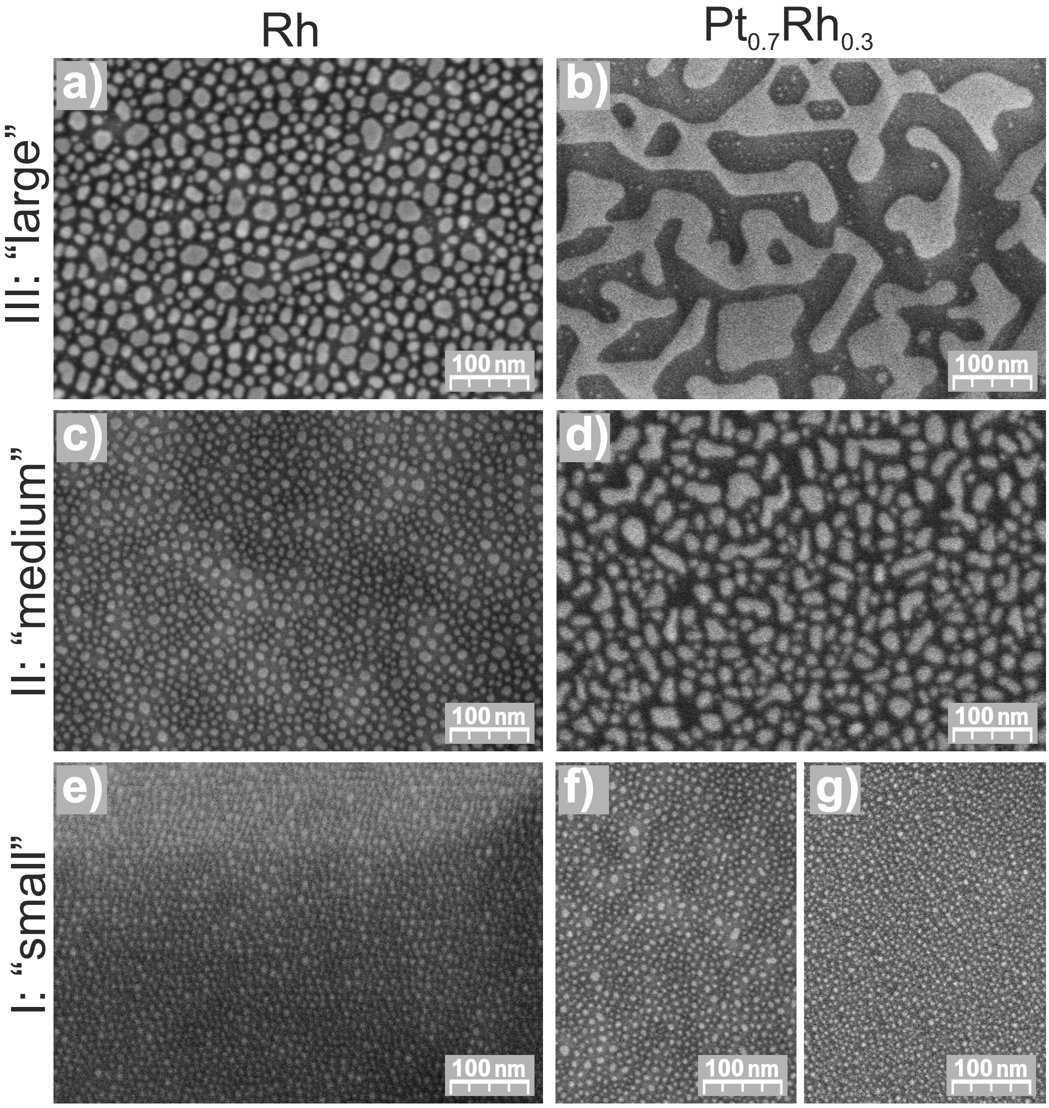

Figure 8.17: **SEM measurements performed after CO oxidation on sample "alumina-3":** they show particles of **a), c), e):** pure Rh, and of **b), d), f), g):** $Pt_{0.7}Rh_{0.3}$ composition for the three different size regimes I-III. While the $Pt_{0.7}Rh_{0.3}$ particles in **b), d)** and **f)** were grown as alloy particles by the simultaneous deposition of Pt and Rh, the particles displayed in **g)** were grown as "core-shell" particles (sequential deposition of Rh and Pt, see section 6.1). The measurements were performed by Hitachi High-Technologies Europe, Krefeld, Germany.

have left enough Rh atoms in the core to make the lattice parameter changes less pronounced.

The main trend of the ongoing lattice parameter increase was found to be superimposed by rather subtle decreases triggered off by switching back to reducing conditions (see conditions E, A* and F*): upon CO exposure the Rh-oxide can be expected to be lifted and Pt be assumed to segregate to the particle surfaces instead. As a consequence, the particle core becomes enriched in Rh which results in a reduction of the particle lattice parameter. However, even under reducing conditions, the lattice parameters of the sintered alloy particles did not readopt their original values. This offset implies a gradual depletion of Rh from the particles in the course of the experiment. Note, even after sintering, the alloy particles' lattice parameters scaled with the original Pt content of the particles, indicating that Vegard's law was maintained and complete phase separation can be excluded.

Also the SEM images shown in Fig. 8.16, which were performed after CO oxidation, are in line with the notion of Rh depletion: while the pure Pt and Rh particles feature well-defined roundish shapes, the alloy particles are characterized by frayed out and worm-like structures. As was discussed for the $MgAl_2O_4$(001)-supported $Pt_{0.33}Rh_{0.67}$ particles in section 7.3, this can be explained by Rh oxides that formed from the segregated Rh: these oxides have the tendency to wet oxide substrate surfaces and to create mesh-like structures as the ones shown in Fig. 8.16. A reason for the absence of these features in the case of the $Pt_{0.85}Rh_{0.15}$ particles may be the particles' low Rh content, which may not have sufficed for their formation. Their particle morphology does not feature large particles along with small, dispersed particles. Accordingly, another scenario proposed in literature which would result in the aforementioned particle morphology and which suggests a bleeding out of the lower melting point metal Rh and leaving large Pt and highly dispersed Rh-rich particles behind [199], can be excluded in the present case, probably also because the probed sample temperatures were too low.

It is striking that the $Pt_{0.7}Rh_{0.3}$ particles (both alloy and "core-shell") of comparable size on sample "alumina-3" did not show these features (see SEM images for size I in Fig. 8.17, note the different scale bar dimensions compared to Fig. 8.16). This may be due to the fact that the reaction was performed only at moderate oxygen flows (highest O_2/CO ratio: 0.625) and that, contrary to "alumina-1", the sample was never exposed to pure oxygen.

The worm-like structures found for the $Pt_{0.7}Rh_{0.3}$ particles of size regimes II and III differ in morphology from the ones in Fig. 8.16 and are likely to be traced back to coalescence during growth. Evidence for particle coalescence is also distinguishable for the large pure Rh particles of size III (Fig. 8.17). In these cases, the high amount of deposited material exceeded the one that enables controlled growth of well-dispersed particles, but rather switched over to layer growth. The absence of any mentionable lattice parameter changes for all particle stripes on sample “alumina-3” in the course of the experiment is in agreement with the notion that no Rh segregation occurred on this sample. A comparable onset towards layer growth can also be deduced for the pure Rh particles of larger size (“Rh L”) on sample ”alumina-1” (see Fig. 8.16 f)): also in this case traces of coalescence are visible, in contrast to the smaller Rh particles in Fig. 8.16 e) and g), indicating that the formation of worm-like structures scales with the amount of deposited material.

8.2 CO oxidation on Pt-Pd alloy particles

One of the major results of section 8.1 is that the extent of the activity-induced coarsening can be ascribed to the initial shape of the Pt-Rh particles. Besides, the growth studies in section 6.2 revealed that for Pt-based particles not only the addition of Rh, but also of Pd, leads to a rounder initial particle shape. Hence, a composition- and thus shape-dependent sintering behaviour as encountered for the Pt-Rh particles could also be anticipated for Pt-Pd particles. The results of the in-situ CO oxidation experiment probing this assumption are subject matter of this section.

8.2.1 Activity-induced particle size changes

The experiment was performed on sample **“alumina-5”** which contained particle stripes of Pt, $Pt_{0.7}Pd_{0.3}$, $Pt_{0.5}Pd_{0.5}$ and $Pt_{0.3}Pd_{0.7}$ composition (see Fig. 6.8). As was discussed in section 6.2, the as-prepared particles featured a diameter that scaled with the Pt content, ranging from rather compact Pd-rich particles to flat and disk-like Pt particles (see Fig. 6.19 d)).

During the experiment, the sample heating was held constant at the elevated temperature of 650 K, a value comparable to the temperatures used in the experiments on the Pt-Rh particles discussed in subsection 8.1.5. Hence, also in this experiment, CO poisoning of the particles could be excluded. Contrary, the total pressure inside the reactor was kept constant at a lower value of p_{tot}=50 mbar.

The sample was probed under pure Ar flow (condition A), reducing conditions (B: no O$_2$, $f_{\mathrm{CO}}=4\ \frac{\mathrm{ml}}{\mathrm{min}}$) and finally under two different conditions of catalytic activity for CO oxidation (C: $f_{\mathrm{O2}}=1\ \frac{\mathrm{ml}}{\mathrm{min}}$, $f_{\mathrm{CO}}=4\ \frac{\mathrm{ml}}{\mathrm{min}}$, i.e. understoichiometric in oxygen; D: $f_{\mathrm{O2}}=2.5\ \frac{\mathrm{ml}}{\mathrm{min}}$, $f_{\mathrm{CO}}=4\ \frac{\mathrm{ml}}{\mathrm{min}}$, i.e. with a small excess in oxygen). In each step Ar was used as carrier gas to add up to the constant total gas flow of $f_{\mathrm{tot}}=50\ \frac{\mathrm{ml}}{\mathrm{min}}$.

The mass spectrometer data of Fig. 8.18 b) reveals a stepwise increasing CO$_2$ as response to the stepwise increase in the set oxygen flow. Comparison with the mass spectrometry data in Fig. 8.12 b) obtained from the Pt-Rh alloy particles at similar elevated temperatures reveals that the CO$_2$ production rates were comparable. Fig. 8.18 a) depicts close-ups on the respective particle $(3\bar{1}1)$ Bragg peaks as measured on the various Pt-Pd compositions as a function of the probed conditions. Fig. 8.18 c) shows the corresponding linescans extracted along L-direction though the particle Bragg peak maxima. Due to the more three-dimensional shape and the higher vertical size distribution of the Pd-rich particles, pronounced Laue oscillations are only present in the case of the Pt-rich particles (pure Pt, Pt$_{0.7}$Pd$_{0.3}$), as can be deduced from both, the 2D maps and the linescans. Their position with respect to the Bragg peak main maxima as a function of sample condition reveals that the Pt-rich particles, especially pure Pt, underwent the most pronounced height increase in the transition from reducing to activity conditions (B→C).

These observations were quantified by fitting the Bragg peak scans of Fig. 8.18 c) with Pseudo-Voigt functions, the results of which are summarized in Fig. 8.19 b). They confirm the drastic height increase of the Pt particles (from 39 Å to 56 Å), which was found to be already greatly reduced in the case of the Pt$_{0.7}$Pd$_{0.3}$ particles (from 44 Å to 48 Å) and in principle not noticeable for the Pd-richer particles (height increase smaller than 2 Å).

In line with the results obtained on the Pt-Rh particles, the particle diameter was concluded to remain constant throughout the experiment, independent of the respective Pt-Pd composition. Its preservation was independently deduced from the rocking scan analysis (see Appendix A.2) and from the fitting of horizontal linescans through the particle Bragg peaks with either a single or a double peak function (see Appendix A.1, Fig. A.1). The results are shown in Fig. 8.19 a) and reveal the diameter values obtained from the various analyses, which in each case were found to stay relatively constant without variation in any systematic way.

As can be expected, the values deduced from the Bragg peak fits using a one peak function make up a lower limit for the diameters, the values obtained from the rocking scan analysis an upper limit (see Appendix A.2). Apart from the case of the pure Pt particles, these rocking scan values deviate strongly from the ones derived from the other analysis techniques. This can be explained by the respective particle size distributions, which are very small for the Pd-containing particle compositions, hence increasing the error of the rocking scan results. The diameter values obtained from Bragg peak fits using a double peak function (see Appendix A.1, Fig. A.1) agree best with the values deduced from the SEM measurements performed after the CO oxidation experiment (see Appendix A.3, Fig. A.6 b)). Their weighted average D_{av} was concluded to best describe the real particle diameters and was used to calculate the particle aspect ratios presented in Fig. 8.19 c).

The particle aspect ratio values shown as a function of sample condition summarize the composition-dependent particle sintering scenario. It is characterized by Pt-rich particles growing vertically via the non-classical Ostwald ripening process discussed in subsection 8.1.3, while keeping the diameter approximately constant, thus adopting a more three-dimensional and thermodynamically more stable shape. Contrary, comparable to the Rh-containing particles, the Pd-rich particles did not undergo any appreciable size changes, indicating that they assumed a stable shape already during particle growth. These results suggest that Pd in Pt-Pd particles resumes the role of Rh in Pt-Rh particles: its addition to Pt promotes the growth of equilibrium-shaped particles which are more resistant against sintering.

Hence, one of the key results of the present sintering study on Pt-Pd particles is the fortification that the degree of sintering depends on the initial particle shape. Pd and Rh appear to be interchangeable when it comes to improving the stability of Pt-based particles during CO oxidation, since both metals promote the growth of equilibrium-shaped particles.

In this context it is worth mentioning that there is experimental evidence to be found in literature about the reduction of activity-induced particle sintering by the addition of Pd to Pt, however, with any explanation lacking so far [117]. It is striking that the absolute particle height-to-diameter aspect ratio values before and after sintering in Fig. 8.19 c) differ from the ones obtained for

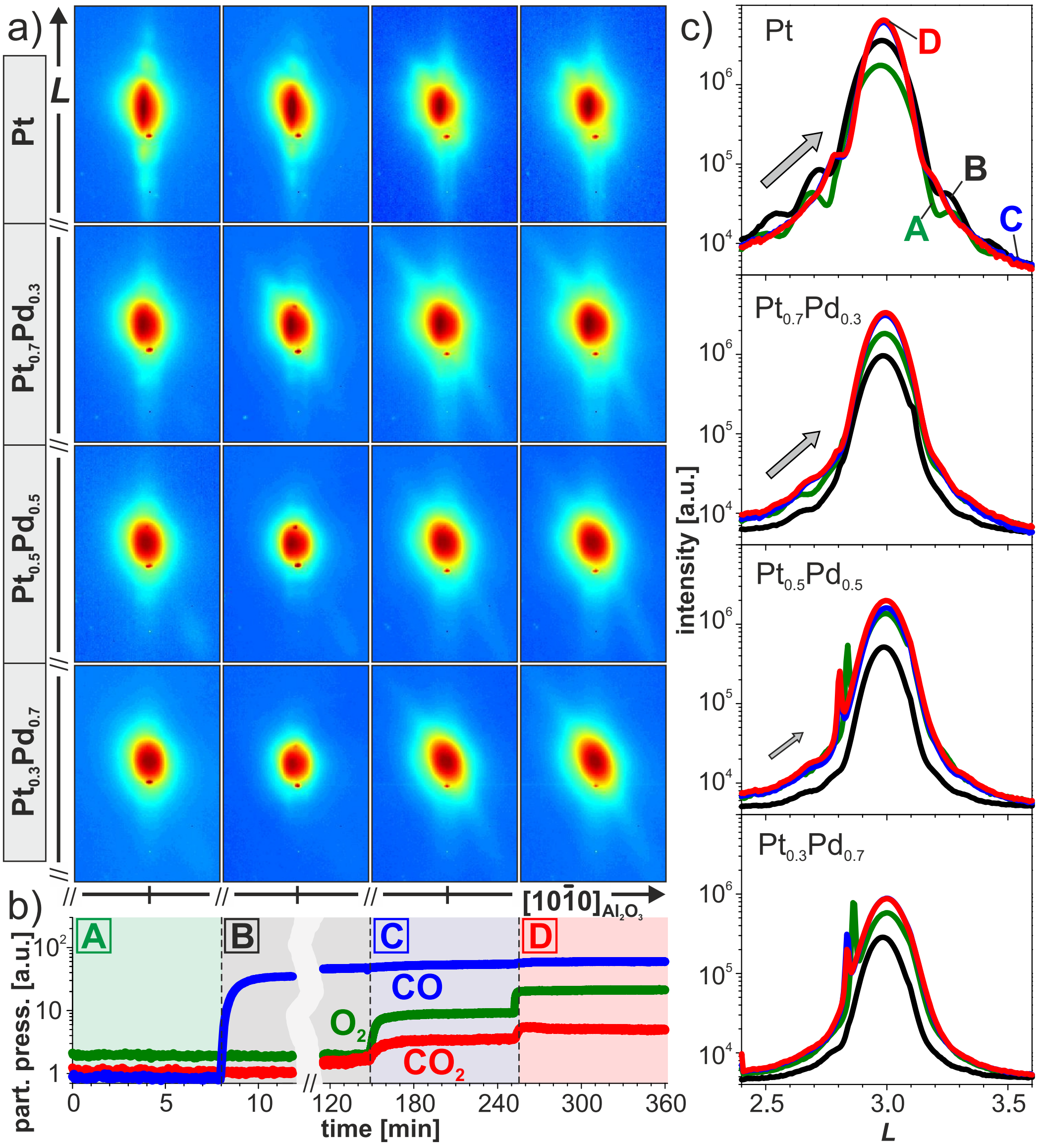

Figure 8.18: **In-situ monitoring of the Pt-Pd (3$\bar{1}$1) particle Bragg peaks in transition to catalytic activity for CO oxidation on sample "alumina-5": a):** 2D maps (exposure time: 100 s) measured on the different Pt-Pd compositions under the probed conditions (a-d) at 650 K, p_{tot}=50 mbar and a total flow f_{tot}=50 $\frac{\mathrm{ml}}{\mathrm{min}}$; **b):** partial pressures as measured under the probed conditions and as a function of time; sample conditions: **A**: only Ar (f_{Ar}=50 $\frac{\mathrm{ml}}{\mathrm{min}}$), no O$_2$, no CO; **B**: no O$_2$, f$_{\mathrm{CO}}$=4 $\frac{\mathrm{ml}}{\mathrm{min}}$; **C**: f$_{\mathrm{O2}}$=1 $\frac{\mathrm{ml}}{\mathrm{min}}$, f$_{\mathrm{CO}}$=4 $\frac{\mathrm{ml}}{\mathrm{min}}$; **D**: f$_{\mathrm{O2}}$=2.5 $\frac{\mathrm{ml}}{\mathrm{min}}$, f$_{\mathrm{CO}}$=4 $\frac{\mathrm{ml}}{\mathrm{min}}$; **c):** linescans along L-direction through the respective peak maxima extracted from the 2D maps of conditions a-d.

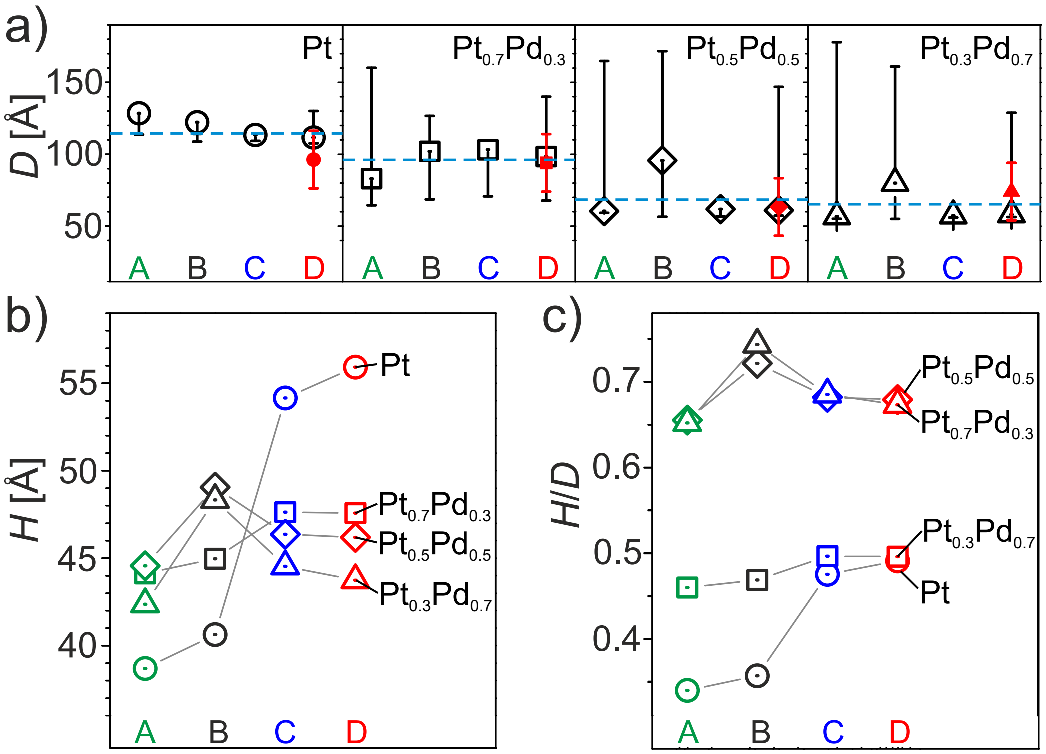

Figure 8.19: **Overview of the composition-dependent Pt-Pd particle size changes on sample "alumina-5" for sample conditions A-D: a):** particle diameters; black opened symbols: values obtained from fitting the horizontal linescans with two peaks; the error bar values represent the diameters obtained from the θ-scan analysis (upper limit) and from the Bragg peak fitting using only one peak function (lower limit); red closed symbols: diameter values obtained from the SEM image analysis; the respective weighted diameter average D_{av} is represented by blue dashed lines and comprises: 114 Å (Pt), 96 Å ($\text{Pt}_{0.7}\text{Pd}_{0.3}$), 68 Å ($\text{Pt}_{0.5}\text{Pd}_{0.5}$), 65 Å ($\text{Pt}_{0.3}\text{Pd}_{0.7}$); **b):** particle heights deduced from fitting the linescans through the respective particle Bragg peaks along L-direction (see Fig. 8.18 c)), their respective error (not shown here) was estimated to be on the order of ±5 %; **c):** particle aspect ratios $\frac{H}{D_{\text{av}}}$.

the Pt-Rh alloy particles (sample “alumina-1”) discussed in subsections 8.1.1 and 8.1.2: while on sample “alumina-1” the as-prepared Pt particles featured a $\frac{H}{D}$-ratio of 0.19, the sintered ones adopted a stable equilibrium shape with an aspect ratio of 0.35. Contrary, the Pt-particles on this sample (“alumina-5”) already featured initial values of $\frac{H}{D}$=0.34 and resumed a stable shape at $\frac{H}{D}$=0.49, which are values comparable to the results found for the Pt particles on sample “alumina-2” ($\frac{H}{D}$ changed from 0.28 to 0.44). These findings underline that not only the initial particle shape, but also the final equilibrium shape is greatly dependent on the substrate surface character, which may be strongly altered by the defect density, the hydroxylation state or the presence of any other adsorbates.

8.2.2 Particle shape changes and chemical restructuring

From the 2D maps of Fig. 8.18 a) it can be inferred that the particle peaks and thus the particles themselves undergo shape changes when switching between different sample conditions. These **peak shape changes** are for all Pt-Pd compositions most pronounced in the transition from reducing conditions (B) to conditions of mild catalytic activity (C), i.e. when oxygen adsorption can be expected to set in. Fig. 8.20 a) and b) show close-ups on the Bragg peaks of the pure Pt and Pt$_{0.3}$Pd$_{0.7}$ particles, respectively, measured under high catalytic activity (condition D) .

It is striking that the shape changes of the Bragg peak signals measured on the Pt-rich particles (pure Pt, Pt$_{0.7}$Pd$_{0.3}$) differ from the ones measured on the particles with higher Pd content (Pt$_{0.5}$Pd$_{0.5}$, Pt$_{0.3}$Pd$_{0.7}$), see Fig. 8.18 a).

The peak patterns of the as-prepared Pt-rich particles are dominated by the strong signal from the (111)-type particle facets. Under activity conditions, the Bragg peaks feature in addition protrusions along certain directions, indicating the emergence of higher indexed facets which may become stabilized upon oxygen adsorption [25]. Especially on alloy particles such higher indexed facets are promising to increase the catalytic activity via synergy effects with the electronic structures [210, 211]. The observed peak protrusions cannot be ascribed to any specific particle facets, but the ($3\bar{1}\bar{1}$)-, the (513)- and the (312)-type facets appear to be likely candidates. In addition, the particle Bragg peaks become smeared out along the respective Debye Scherrer ring directions (indicated by black arrows in Fig. 8.20). This implies that some of the particles become less well ordered and tilt themselves around the in-plane

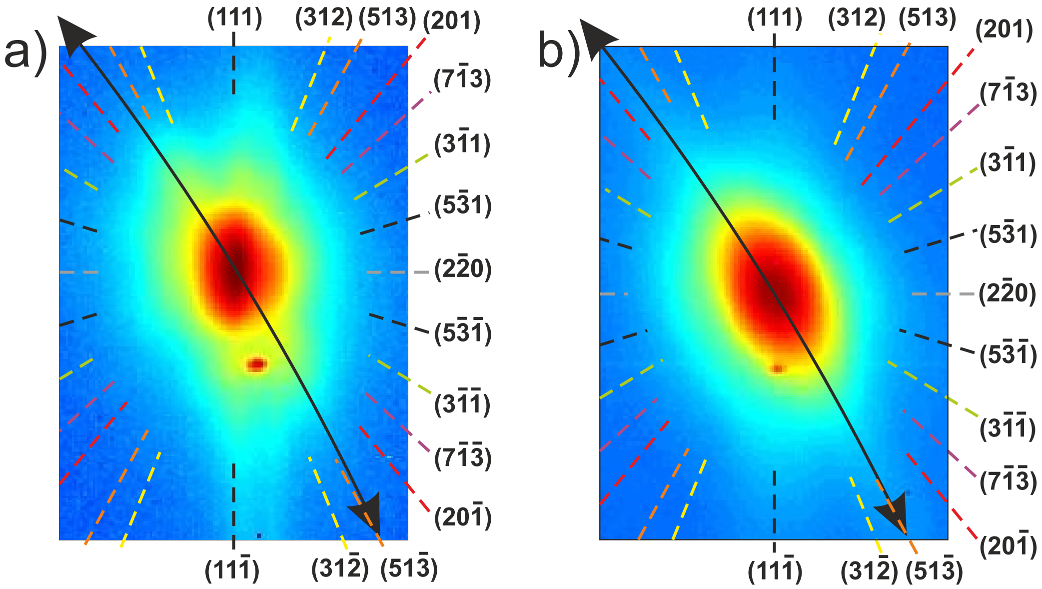

Figure 8.20: **Potential particle facet signals:** the 2D maps were measured under conditions of high catalytic activity (condition D: f_{O2}=2.5 $\frac{\text{ml}}{\text{min}}$, f_{CO}=4 $\frac{\text{ml}}{\text{min}}$) on the **a):** Pt, and **b):** Pt$_{0.3}$Pd$_{0.7}$ particles. Dashed lines: guide to the eye for potential facet signal directions; black arrows: guide to the eye for signals from particles tilted around the substrate [1$\bar{2}$10]-direction, which can be anticipated in the probed reciprocal space plane.

substrate [1$\bar{2}$10]-direction during catalytic activity.

Contrary, in the case of the Bragg peaks of the Pd-rich particles (Pt$_{0.5}$Pd$_{0.5}$, Pt$_{0.3}$Pd$_{0.3}$) no additional facet signals appear. Note, however, that the Pd-rich particles are much smaller and rounder compared to the Pt-richer ones, which results in smaller and less well established facets. Also here, an intensity increase along the respective Debye Scherrer ring is observed indicating a tilt around the in-plane normal for some of the particles. Interestingly, the sharp peaks belonging to particles that are tilted by 35° (see section 6.2) dissolve into the mosaicity broadening around the particle (3$\bar{1}$1) Bragg peak when catalytic activity conditions set in, suggesting their destabilization and potential restructuring into particles of the main epitaxy.

It is worth mentioning that comparable composition-dependent Bragg peak features are also present in the 2D maps of the Pt-Rh particles, especially at elevated temperatures (see Fig. 8.12). The peak shapes of the Pt-rich Pt-Rh particles are similar to the ones of the Pt-rich Pt-Pd particles, as are the peak shapes of the Rh-rich particles to the ones of the Pd-rich particles, which is in line with their respective comparable particle shapes.

To obtain information on the **alloying state** of the Pt-Pd particles and on possible **segregation profiles**, the lattice parameters were deduced from the position of the respective particle Bragg peak main maxima. They are depicted in Fig. 8.21 for the in- (a)) and out-of-plane (b)) direction as a function of sample condition.

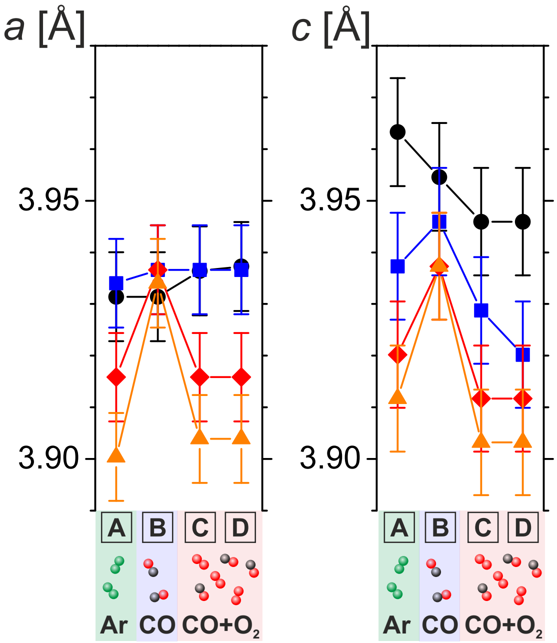

Figure 8.21: **Pt-Pd lattice parameters as a function of the sample condition: left:** in-plane, and **right:** out-of-plane lattice constants given as fcc bulk values as obtained from the particle $(3\bar{1}1)$ Bragg peak positions in the respective 2D reciprocal space maps (Pt: black circles; $Pt_{0.7}Pd_{0.3}$: blue squares; $Pt_{0.5}Pd_{0.5}$: red diamonds; $Pt_{0.3}Pd_{0.7}$: orange triangles). The corresponding conditions (A-D) are indicated at the figure bottom.

Taking Vegard's law and thermal lattice expansions (T=650 K) into account, the fcc bulk values of the respective lattice parameters comprise 3.9365 Å (Pt), 3.9276 Å ($Pt_{0.7}Pd_{0.3}$), 3.9217 Å ($Pt_{0.5}Pd_{0.5}$) and 3.9158 Å ($Pt_{0.3}Pd_{0.7}$). The obtained lattice parameters of the as-prepared particles (condition A) reflect these values within error bars, when taking intra-particle strain according to the Poission effect into account. This implies that the particles are initially in their alloyed state. As was discussed in subsection 8.1.6, also here, the strain may be caused by the misfit of the in-plane particle lattice parameter to the one of the substrate. As can be deduced from Table 2.2, the mismatch is largest for the pure Pt particles and is negligible for pure Pd. Accordingly, the discrepancy between the in- and out-of-plane lattice parameter in Fig. 8.21 is largest for the pure Pt particles, as the particles try to adapt to the smaller substrate in-plane lattice parameter of the substrate.

Under a reducing CO atmosphere (condition B), the lattice parameters of the alloy particles approach the values of the pure Pt particles, suggesting a Pt-rich particle core due to Pd segregation to the particle surfaces. Upon activity conditions for CO oxidation (CO+O_2, conditions C and D), the lattice parameters readopt values which indicate Pt-Pd alloying. The out-of-plane lattice parameters of the most strongly sintering particles (Pt, $Pt_{0.7}Pd_{0.3}$) are greatly decreased under activity conditions, which is in line with the results found for the Pt-Rh particles. Also here, it may also be traced back to the increasing weight from the growing number of additional atomic layers (see discussion in subsection 8.1.6).

These findings are partially in line with High Pressure XPS results obtained on $Pt_{0.5}Pd_{0.5}$ particles [111], which conclude a Pt core and a Pd shell under reducing conditions based on the fact that CO is found to bind more strongly to Pd than to Pt [212, 213, 214, 215] and since Pd has the lower surface energy compared to Pt [130, 160, 216] (see also Table 2.1 in subsection 2.3.1).

Contrary to our results, these High Pressure XPS studies further suggest the preservation of the Pd-shell also under activity (NO+CO) and oxidizing (NO) conditions since Pt is less readily oxidized [217]. However, there is also experimental and theoretical evidence in literature that Pt-Pd particles feature an alloy under oxidizing atmospheres, rendering the state of the particles under such conditions a contentious issue: hence, a combined HRTEM, XRD and XAS study on the aging of Pt-Pd catalysts under oxidizing conditions at 1020 K in air revealed the preservation of the alloyed state of the particles [118]. Moreover, XRD measurements showed that initially separated alumina-supported Pt and Pd particles even alloyed during catalytic activity for NO oxidation [117]. Furthermore, calculations imply that oxygen binds more strongly to Pt(111) than to Pd(111) [114, 115] while at the same time the energy gain may not suffice for Pt to fully overcome the segregation energy of Pd [116], which makes alloying of the two metals feasible.

It is striking that the SEM images performed after the CO oxidation experiment, which are shown in Fig. 8.22, reveal for all Pt-Pd compositions a **post-sinter particle morphology** that is characterized by separated, well-defined roundish particles. This stands in stark contrast to the wormy features found in the Pt-Rh case (see Fig. 7.13, Fig. 7.19, Fig. 8.16, and Fig. 8.17) which were traced back to the substrate wetting of the Rh oxides. Such wetting tendencies are not reported for neither Pt- nor Pd-oxides, which might explain the absence of these mesh-like features. In this context it is worth mentioning that the addition of Pt to Pd in particles was found to suppress the presence of any oxide formation on the resulting alloy particles while aging in air [118],

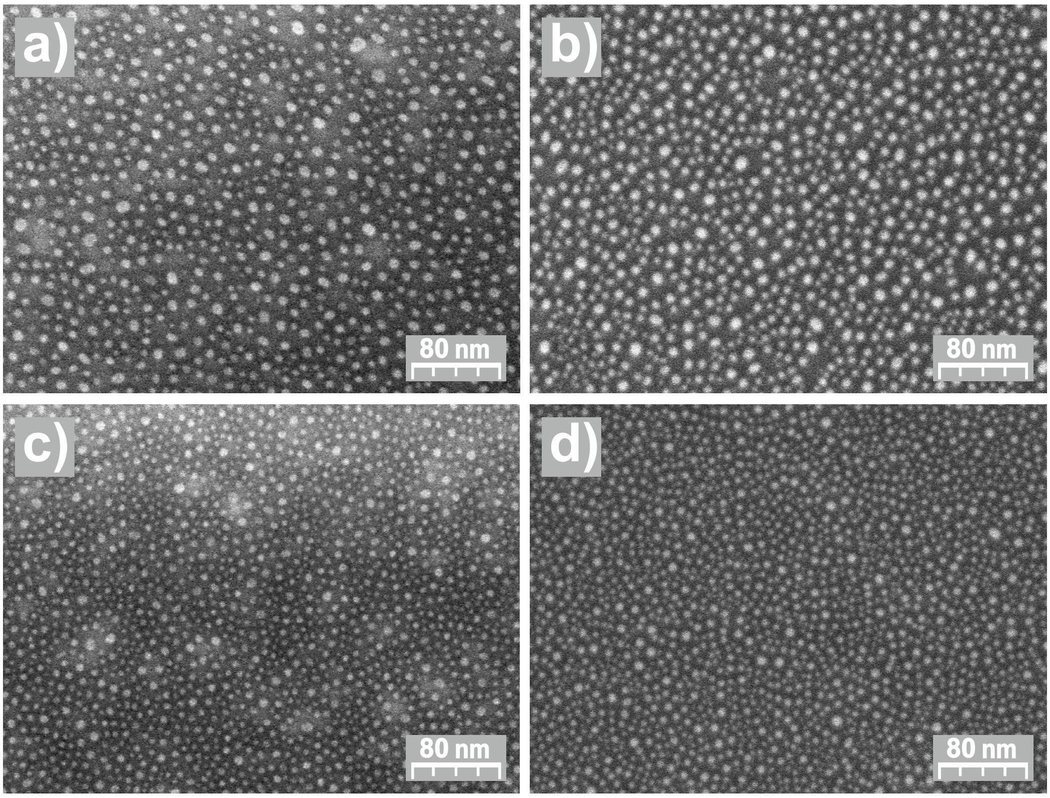

Figure 8.22: **SEM images measured after CO oxidation on the Pt-Pd particles of sample "alumina-5": a):** pure Pt; **b):** $Pt_{0.7}Pd_{0.3}$; **c):** $Pt_{0.5}Pd_{0.5}$; **d):** $Pt_{0.3}Pd_{0.7}$. The measurements were performed by JEOL GmbH, Eching, Germany.

and that pure Pt species were even found to be trapped by PdO, resulting in alloy Pd-Pt particles [218]. These findings are in line with the bulk phase diagramme of Pt-Pd, which - in contrast to bulk Pt-Rh - does not feature any miscibility gap. Hence, the tendency to form a Pt-Pd alloy may suppress the formation of any oxide, especially since the kinetic barriers for PdO formation were found to be particularly high in the case of nanoparticles [112], see also subsections 3.1.5 and 3.2.2.

8.3 Summary and conclusion

This chapter contains the results of the alloy- and hence shape-dependent sintering behaviour of α-Al_2O_3(0001)-supported Pt-Rh and Pt-Pd nanoparticles during catalytic CO oxidation at near-ambient pressures studied by means of high energy surface x-ray diffraction ($E \approx 78$ keV) using combinatorial samples ("alumina-1", "-2", "-3", and "-5", see Fig. 6.8). It explains how high energy surface x-ray diffraction was established as a routine tool for the operando investigation of particle model catalyst systems under realistic reaction conditions.

The data presented in this chapter demonstrate that probing the finite height **Laue oscillations** by using a 2D detector while changing gas composition allows for the **in-situ tracking** of the vertical particle **sintering** during catalytic CO oxidation. Furthermore it was shown that **fitting the particle rods**, extracted along L-direction from the 2D reciprocal space maps, allows for deducing the **quantitative particle shape**. As example the data obtained on sample "alumina-1" was used to show that the extracted linescans could be fitted using the programme package ROD, where a layer model with different layer occupancies was used to mimic various underlying particle model shapes. An important key result is that as-prepared particles, which are after deposition often trapped in a flat **kinetic particle shape**, may use the energy released in the catalytic CO oxidation reaction to restructure into a shape more similar to the respective thermodynamic **equilibrium shape**, characterized by a higher height-to-diameter aspect ratio. As was discussed in chapter 6, especially Pt and Pt-rich particles are often characterized by very flat, disk-like kinetic shapes after growth: the initial particle shapes on samples "alumina-1" and "-2" featured, independent of the Pt-Rh composition, the same heights of ≈20 Å, but differed in diameter with values ranging on "alumina-1" from 125 Å (85 Å on "alumina-2") for pure Pt down to 50 Å (50 Å) for pure Rh, resulting in aspect ratios of 0.19 (0.28) for pure Pt and of 0.34 (0.47) for pure Rh particles.

During CO oxidation, the pure Pt particles sintered tremendously with the particle height on sample "alumina-1" almost doubling from 24 Å to 42 Å (sample "alumina-2": from 25 Å to 37 Å). The reaction-induced height increase was found to be progressively reduced as a function of Rh content inside the alloy particles. Since the particle diameter was maintained for particles of all Pt-Rh compositions, the sintering resulted in an increase in aspect ratio, again most pronounced for the pure Pt and Pt-rich particles (Pt particles on "alumina-1": $\frac{H}{D}$ changed from 0.19 to 0.34; on "alumina-2": from 0.28 to 0.45), towards their values of stable equilibrium-shaped particles. The $\frac{H}{D}$-values of the Rh particles remained relatively stable at 0.47 on both samples.

The sintering was found to be accompanied by a reduction of the particle coverage on the sample surface that scaled with the extent of sintering. It was accordingly most pronounced for the pure Pt particles, for which the coverage on sample “alumina-1” decreased from 50% to 35% (sample “alumina-2”: from 52% to 32%). This finding is in line with the notion that the sintering particles incorporate atoms from surrounding, probably smaller and less stable particles, which as a consequence shrink or dissolve in an Ostwald-ripening manner. However, as the particles were found to sinter in height only, we ascribed the scenario to a “non-classical” Ostwald-ripening mechanism not reported in literature so far. Surprisingly, even under harsh reaction conditions, the x-ray data did not reveal any powder signals, instead, the diffraction patterns of the sintered particles still displayed distinct Laue oscillations. Thus, it is likely that the growing particles are indeed anchored to the substrate and are supplied with atoms from surrounding particles.

Once having adopted their equilibrium shape, the particles were found to be resistant against further sintering, even under harsh reaction conditions at elevated temperatures or conditions including pure oxygen flow. Particles of various Pt-Rh alloy compositions already grown with shapes close to equilibrium and characterized by a high height-to-diameter aspect ratio (sample “alumina-3”) were found to not sinter strongly, hence supporting the notion of the particles’ strife towards their equilibrium shape as underlying driving force for the vertical sintering as encountered for samples “alumina-1” and “-2”.

The quantitative particle shape analysis based on the extracted particle rods concluded (111)-oriented particles consisting of (111)- and (100)-type facets determined by rather small facet surface energy ratios $g=\frac{\gamma_{(001)}}{\gamma_{(111)}}$ between 0.9 and 1.3, where the tendency towards smaller values and hence larger (100)-type facets was found to increase in the course of the particle sintering. This is in line with the findings for the MgAl$_2$O$_4$(001)-supported Pt$_{0.33}$Rh$_{0.67}$ particles, in the case of which an oxygen-induced increase of the (100)-type facets was concluded in the transition to high catalytic activity conditions (see chapter 7). In line with the x-ray reflectivity results the data moreover suggest an increased smearing-out of the electron density along out-of-plane direction for the sintered particles, which implies an increased vertical particle size distribution.

In line with the findings for the Pt-Rh particles supported on MgAl$_2$O$_4$(001) (see chapter 7), a progressive **depletion of Rh** from the Pt-Rh alloy particles supported on α-Al$_2$O$_3$(0001) was concluded to occur in the course of, and especially during harsh conditions of, catalytic CO oxidation. Also in their case, electron microscopy images performed after the CO oxidation experiment revealed worm-like particle structures for the Pt-Rh alloy particles, indicating the formation of Rh oxides from depleted Rh, wetting the sample surface. Further experimental evidence on the shape-dependent particle sintering was obtained from another sample system: in the case of the α-Al_2O_3(0001)-supported Pt-Pd alloy particles (sample “alumina-5”), the aspect ratio of the as-prepared particles was also smallest for the pure Pt particles. Accordingly, in line with the aforementioned explanations, the reaction-induced vertical particle sintering was found to be strongest for the pure Pt particles, thereby adopting a shape close to the equilibrium shape. In contrast to the Pt-Rh particles, no depletion of any metal was concluded for the Pt-Pd system, which might be due to complete miscibility of the two elements.

Chapter 9

Summary and Outlook

Summary

In the framework of this thesis surface x-ray diffraction was used to systematically investigate (1) the growth of Pt-Rh, Pt-Pd and Pd-Rh alloy nanoparticles on $MgAl_2O_4(001)$ and on α-$Al_2O_3(0001)$ substrates, as well as (2) these particles' behaviour under catalytic CO oxidation at near atmospheric pressures. The approach of combining surface sensitive x-ray diffraction with a dedicated in-situ catalysis chamber allowed for obtaining unprecedented atomic scale information on nanoparticle-based model catalyst systems at work. Hence, the use of conventional photon energies (E=11.2 keV) allowed for correlating the formation of ultrathin surface oxides on the nanoparticle facets to the sample's catalytic activity and enabled a quantitative analysis of the particle shape changes under reaction conditions. Furthermore, high energy x-ray diffraction (E=78-85 keV) was established as a routine tool for the quantitative operando investigation of nanoparticle-based model catalyst systems, including their sintering behaviour, under realistic reaction conditions. Thanks to the combination of high energy reciprocal space mapping and combinatorial samples, the investigation could be performed on a high number (46!) of different sample systems, allowing to obtain statistically relevant information on the key questions presented in the introduction (chapter 1).

i Tailoring of monometallic and alloy catalyst particles
The results obtained on particle growth show indeed, that tailoring of the nanoparticles and hence of catalyst characteristics is possible to some extent. Choosing either $MgAl_2O_4(001)$ or α-$Al_2O_3(0001)$ as substrate allows for grow-

ing the particles predominantly in a (001)- or a (111)-type epitaxy. Furthermore, independent of the substrate used, the particle height-to-diameter aspect ratio $\frac{H}{D}$ can be tailored by means of the particle alloy composition and was found to scale according to Pt<Pd<Rh. The aspect ratio was also found to feature a particle size dependence, where the $\frac{H}{D}$-values progressively decrease with increasing particle size. The data of this thesis suggest moreover that the aspect ratio of α-$Al_2O_3(0001)$-supported Pt-rich particles are reduced even more in case the substrate surface is covered by hydroxyls. For both substrates, the sequential deposition of Rh and Pt ("core-shell" particles) was found to result in Pt-Rh alloy particles which, however, feature the characteristics of pure Rh particles, both with respect to the morphology of the main epitaxy as well as to the presence or absence of minor epitaxies. In the case of $MgAl_2O_4(001)$, the percentage of particle defects (internal twinning), tilted particles and minor epitaxies could greatly be reduced by performing at least five sputtering and annealing cycles prior to particle deposition. A novel growth mechanism was concluded in which particles are stabilized by tilting themselves such that the projection of their atomic row distances matches the atomic row distances of the substrate. Their percentage on the sample surface was concluded to be dependent on the particles' alloy composition and size.

ii Reaction-induced shape changes of alloy particles at near ambient pressures

Under catalytic CO oxidation conditions of catalytic activity, $MgAl_2O_4(001)$-supported $Pt_{0.33}Rh_{0.67}$ particles were concluded to undergo reversible oxygen-induced shape changes characterized by an increase in the (001)-type particle facets at the expense of the size of the (111)-type facets. They are similar to the changes found for supported Rh particles under sequential oxidation and reduction cycles, but differ greatly from the behaviour of pure Pt particles. A further source for particle shape changes can be seen in the sintering of the particles. In the case of the α-$Al_2O_3(0001)$-supported particles, this type of shape change was characterized by an increase of the particle aspect ratio. The sintering of the $MgAl_2O_4(001)$-supported $Pt_{0.33}Rh_{0.67}$ particles was concluded to be characterized by a steady increase in both, diameter and height, hence maintaining the aspect ratio.

iii Segregation effects under reaction conditions

The data of this thesis suggest for Pt-Rh particles a segregation of Rh to the particle surface under conditions of catalytic activity characterized by overstoichiometry in oxygen. In general, it was concluded that switching back to reducing conditions results in Rh returning back to the particle core, but in the course of the CO oxidation experiments a steady, unwanted depletion of Rh from the particle core occurred. For the Pt-Pd system, Pd was concluded to segregate to the particle surface under reducing conditions, but no evidence of phase separation was found.

iv Oxide formation on alloy nanoparticles

On the $MgAl_2O_4(001)$-supported $Pt_{0.33}Rh_{0.67}$ alloy particles Rh oxides were found that had before been evidenced on pure Rh particles (the c(2×8) Rh surface oxide on the particle (100)-type facets, the p(9×9) Rh surface oxide on the particle (111)-type facets, the RhO_2 bulk oxide) as well as on Pd-Rh alloy particles (bulk oxides RhO_2 and Rh_3O_4). At 673 K and p_{tot}=50 mbar a not fully closed layer of the c(2×8) Rh surface oxide was stable under gas flow conditions characterized by $f_{\mathrm{O2}}=2\ \frac{\mathrm{ml}}{\mathrm{min}}$ and $f_{\mathrm{CO}}=4\ \frac{\mathrm{ml}}{\mathrm{min}}$. Formation of the p(9×9) Rh surface oxide and the RhO_2 and Rh_3O_4 bulk oxides (with some time delay) was only observed at oxygen overstoichiometry ($f_{\mathrm{O2}}=3\ \frac{\mathrm{ml}}{\mathrm{min}}$, $f_{\mathrm{CO}}=4\ \frac{\mathrm{ml}}{\mathrm{min}}$).

v Catalytically active phases

For the $MgAl_2O_4(001)$-supported $Pt_{0.33}Rh_{0.67}$ particles the catalytic light off was found to correlate with the presence of not fully closed layers of the c(2×8) Rh surface oxide on the (001)-type particle facets, while there is experimental evidence that the RhO_2 and Rh_3O_4 bulk oxides tend to poison the reaction.

vi Catalyst deactivation

On the basis of this thesis' data, a non-classical Ostwald ripening mechanism was suggested for the sintering behaviour of α-$Al_2O_3(0001)$-supported Pt-rich alloy particles, which feature a flat, disk-like kinetic shape after growth. During the sintering process, the energy released in the catalytic CO oxidation reaction leads to the destabilization of, probably smaller, particles. In turn, they dissolve and their atoms are being incorporated into the larger and more stable particles, which thereby increase their height resulting in more compact particle shapes with higher aspect ratios and closer to the equilibrium shape.

Particle sintering on α-Al_2O_3(0001) was found to be greatly suppressed for particles that featured their equilibrium shape already after growth which could be achieved by alloying the Pt-based particles with Rh or Pd. In addition, the data of this thesis suggest that the initial flat particle shapes could be avoided by reducing hydroxylation of the α-Al_2O_3(0001) substrate surface. On $MgAl_2O_4$(001), sintering is likely to be reduced by nm-sized pits which are created at the substrate surface after several (at least five) sputtering and annealing cycles prior to particle deposition.

The results listed above were obtained from the model catalysts studied in this thesis, but are also of fundamental importance for real catalyst systems. Hence, the finding that a major cause for particle sintering is that the as-prepared particles are trapped in their kinetic shape may alter the catalyst production towards the preparation of catalyst particles in their equilibrium shapes. According to the results of this thesis, this may easily be achieved for Pt particles by the addition of Pd or Rh. Moreover, since industrial catalysts are produced from wet impregnation procedures resulting in an undefined degree of support hydroxylation, the finding that the extent of hydroxylation might greatly alter the particle shape, is of great importance. To ensure that affected particles still adopt their equilibrium shapes, extended calcination could be performed after impregnation.
Furthermore, the finding that unclosed layers of the c(2×8) Rh surface oxide on the particle (001)-type facets correlate with the sample's highest catalytic activity is also of great general importance. Hence, finding ways to increase and stabilize the size of the (001)-type facets in real catalyst systems (e.g. via support configuration or additives) may result in an enhancement of catalyst performance.

Outlook

By today, one hundred and eighty years after the discovery of catalysis, extensive investigations have provided insights into its principles, but many aspects still need to be unraveled. Accordingly, the results of this thesis shed light onto particle growth and on the atomic-scale processes during catalytic reactions, but stimulate at the same time questions to be addressed in further investigations.

The growth studies of this thesis revealed the whole complexity of the studied sample systems, characterized by a coexistence of different particle epitaxies and defects. The investigation of samples with varying amounts of deposited material only yielded limited insight into their development as a function of deposited material. Hence, future *in-situ* growth studies, realized by mounting an evaporator on top of the chamber and using high energy reciprocal space mapping, would allow for obtaining a deeper understanding of the developments on the sample surface during growth. A detailed knowledge of the growth behaviour would provide the possibility to stabilize certain sample characteristics of interest, e.g. a smaller particle size distribution, and would in turn facilitate investigations of specific sample characteristics during catalytic reactions. Since this thesis revealed that the particle growth characteristics are very sensitive to the substrate preparation, the substrate treatment prior to particle deposition should become an important growth parameter to be studied systematically.

This thesis' use of combinatorial samples allowed for obtaining information on the particle restructuring of various sample systems under identical catalytic reaction conditions, while simultaneous in-situ mass spectrometry monitored the *sum* of the catalytic activities over all particle stripes. On the basis of the gained insight into the structural changes that occur during reaction, future investigations should focus on the *individual catalytic activities* of selected sample systems (e.g. of the strong sintering of α-$Al_2O_3(0001)$-supported Pt-rich particles vs. stable Rh-rich particles) that were so far only studied in the combinatorial approach. They would deepen the insight into the correlation between particle structures and catalytic activity. The studies of catalytic activity could also be extended to new sample systems with tailored characteristics of interest, such as certain particle sizes with narrow size distributions, or particle shapes not studied so far. To tailor these characteristics, substrate templates (defined particle size and *inter* particle distance) could be used along with other particle preparation methods such as micelle-based (defined particle size and inter particle distance) or wet-chemical (defined particle shape) approaches.

This thesis focused on the study of *nanoparticle* structures during reaction conditions, however, the measured data on the $MgAl_2O_4(001)$ sample system hold evidence that also the structure of the *substrate surface* changed in the transition to reaction conditions. Crystal truncation rod measurements performed on the oxide substrates during different sample conditions including catalytic CO oxidation would allow a detailed understanding of the substrate surface and the particle/substrate interface structure and its potential role in chemical reactions.

Furthermore, the data of this thesis suggest segregation of one element to the alloy particle surface under harsh catalytic CO oxidation conditions, and, in the case of the Pt-Rh system, even phase separation to occur. Detailed segregation profiles could in the future be obtained by means of anomalous x-ray diffraction: using variable x-ray energies below and above the absorption edge of one of the elements inside the alloy particles would allow to highlight the respective components of interest.

In addition, the experimental approaches employed in this thesis can in the future also be expanded to both, further sample systems and further catalytic reactions to be investigated. Reactions that are important for car catalytic converters and for which the catalysts employed contain the same materials as studied in this thesis include the reduction of nitride oxides ($\mathrm{NO_x}$) or the oxidation of unburnt hydrocarbons ($\mathrm{H_mC_n}$). Examples of reactions that use other catalyst materials and which are of utmost importance for the reduction of carbon monoxide in the feed gas of fuel cells include (1) the water-gas shift reaction, i.e. the reaction of carbon monoxide and water vapour to carbon dioxide and hydrogen, which is usually catalyzed by catalysts containing CuO, ZnO, $\mathrm{Fe_2O_3}$ or $\mathrm{Cr_2O_3}$, or (2) the PReferential oxidation of CO (PROX) from a gas mixture of carbon monoxide and hydrogen, usually catalyzed by Pt, Pt-Fe, Pt-Ru or Au nanoparticles on ceramic supports. Besides, also the reverse water gas shift reaction, i.e. the reaction of carbon dioxide and hydrogen to hydrocarbons, is of great general interest. Another important reaction includes the Fischer Tropsch process, in which hydrocarbons are produced from hydrogen and carbon monoxide over catalysts such as Co, Fe, Ni or Ru.

Appendix A

Complementary Approaches for Particle Diameter Determination

Appendix A summarizes and elucidates the different methods that were used in this thesis to determine particle diameters from grazing incidence high energy x-ray diffraction data. For particle Bragg peaks with small Q-values (e.g. the particle $(11\bar{1})$ peaks probed on samples "alumina-2", "-3", and "-4", "spinel-2", and "-3") the diameters were directly derived from simple Bragg peak fits (see Appendix A.1). For particle Bragg peaks with higher Q-values (e.g. the particle $(3\bar{1}1)$ peaks probed on samples "alumina-1", and "-5") the diameters were deduced from sample rocking scans (if the particle size distribution was high enough, see Appendix A.2), from complementary microscopy techniques (AFM and SEM, see Appendix A.3), by fitting the particle Bragg peaks with double peak functions (see Appendix A.1), and/or by combining several of these approaches.

A.1 Fitting horizontal linescans

The broadening of a particle Bragg peak can not only be traced back to the finite particle size D, but also to strain effects. While size broadening is independent of the scattering vector magnitude Q, broadening due to strain scales with increasing Q-values [219]. Accordingly, for the low Q-value particle $(11\bar{1})$-type Bragg peaks studied in this thesis, a particle diameter determination via $D=\frac{2\pi}{Q}$ could be used, since strain effects could be neglected (used e.g. in the case of sample alumina-2" in Fig. C.2). Contrary, the $(3\bar{1}1)$-type Bragg peaks probed in the case of samples "alumina-1" and "-3" display in horizontal direction asymmetric shapes, which can be fitted by double peak functions keeping the peak maximum of one function fixed at the in-plane $Q_{\|}$-value corresponding to the substrate in-plane lattice parameter (vertical red lines in Fig. A.1, Fig. A.2 and Fig. A.3). This implies that some particles grow with their own in-plane lattice parameter d_0, while others adopt the one of the substrate, resulting after Bragg's law $\lambda = 2(d_0 \pm \Delta d)\ \sin(\theta_{\mathrm{B}} \mp \Delta\theta)$ in diffraction signals not only at the Bragg angle θ_{B}, but also at $\theta_{\mathrm{B}} \mp \Delta\theta$, which impedes the determination of the particle diameter from the peak FWHM.

In Fig. A.1, Fig. A.2 and Fig. A.3, the data (circles) were fitted with two Pseudo-Voigt functions, where the peak maximum of the red curve was kept fixed at the $Q_{\|}$-value corresponding to the in-plane lattice parameter of the substrate. The position of the green function was determined by the main maxima of the horizontal linescan, which was found to change as a function of the particle composition and the probed sample condition. In general, the main maxima of the particle Bragg peaks in Fig. A.1, Fig. A.2 and Fig. A.3 mirror the gas-atmosphere-induced lattice parameter changes discussed in subsections 8.1.6 and 8.2.2.

In some cases, especially if the particle in-plane lattice parameter differs greatly from the one of the substrate, e.g. for the pure Rh particles of sample "alumina-1" (see Fig. A.2 and A.3), it was still possible to deduce the particle diameter from the horizontal linescans. Therefore, the peaks were fitted with double functions and the FWHM of the fitted incommensurate particle peak (green lines) was used to calculate the particle diameter. In other cases, i.e. especially for particle in-plane lattice parameters close to the one of the substrate, the particle diameters were obtained from the rocking scan analysis (see Appendix A.2) and/or from complementary microscopy data (see Appendix A.3).

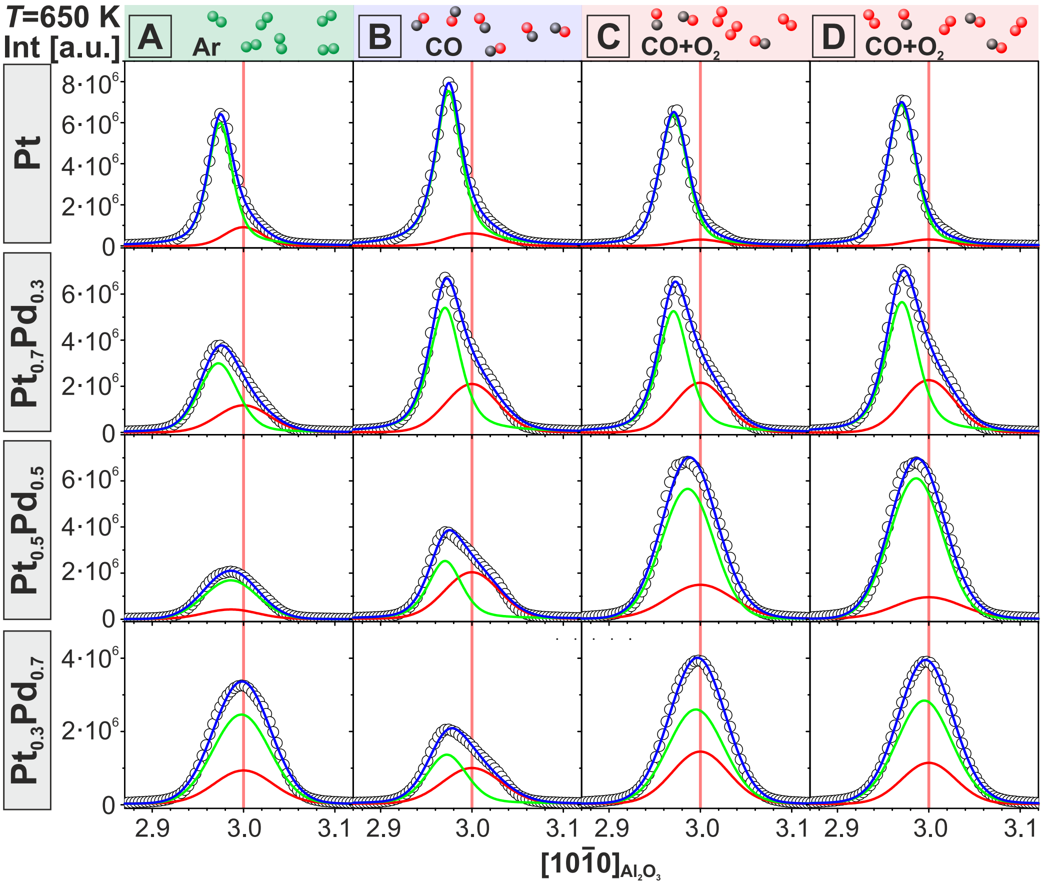

Figure A.1: **Horizontal linescans through the Pt-Pd particle (3$\bar{1}$1) Bragg peaks of sample "alumina-5" at 650 K:** linescans were extracted from the 2D maps of Fig 8.18 a) along the substrate $[10\bar{1}0]_{Al2O3}$-direction. The data (circles) were fitted with double peak functions (solid lines; red: peak maximum fixed at $H_{Al2O3}=3$; green: peak maximum fixed at the maximum values of the experimental data; blue: sum of both), where in each case Pseudo-Voigt functions were used.

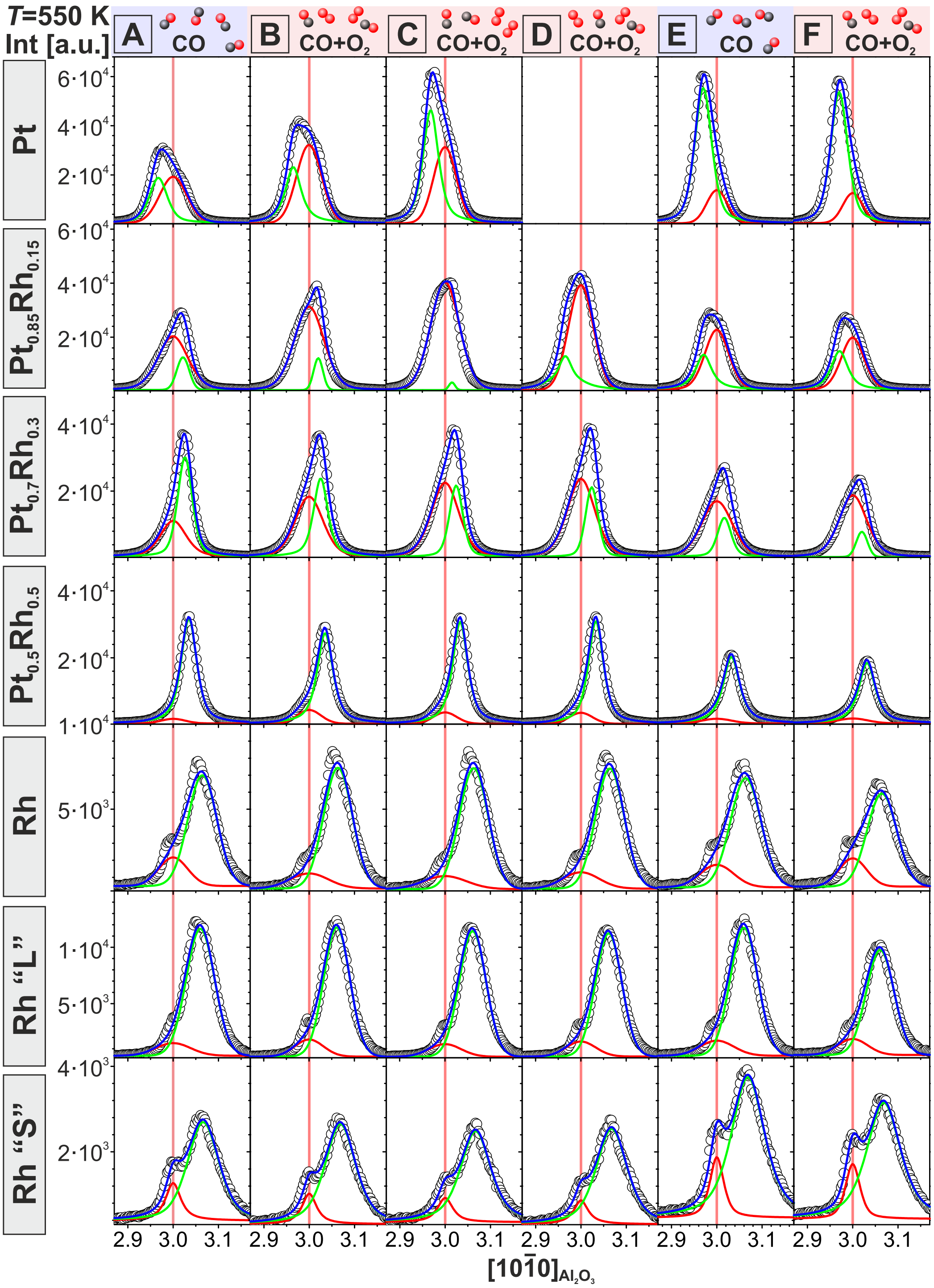

Figure A.2: **Horizontal linescans through the particle (3$\bar{1}$1) Bragg peaks of sample "alumina-1" at 550 K:** linescans were extracted from the 2D maps for the various Pt-Rh compositions and sample conditions of the CO oxidation experiment along the substrate [10$\bar{1}$0]$_{\mathrm{Al2O3}}$-direction. The data (circles) were fitted with double peak functions (solid lines; red: peak maximum fixed at H_{Al2O3}=3; green: variable peak maximum; blue: sum of both), where in each case Pseudo-Voigt functions were used.

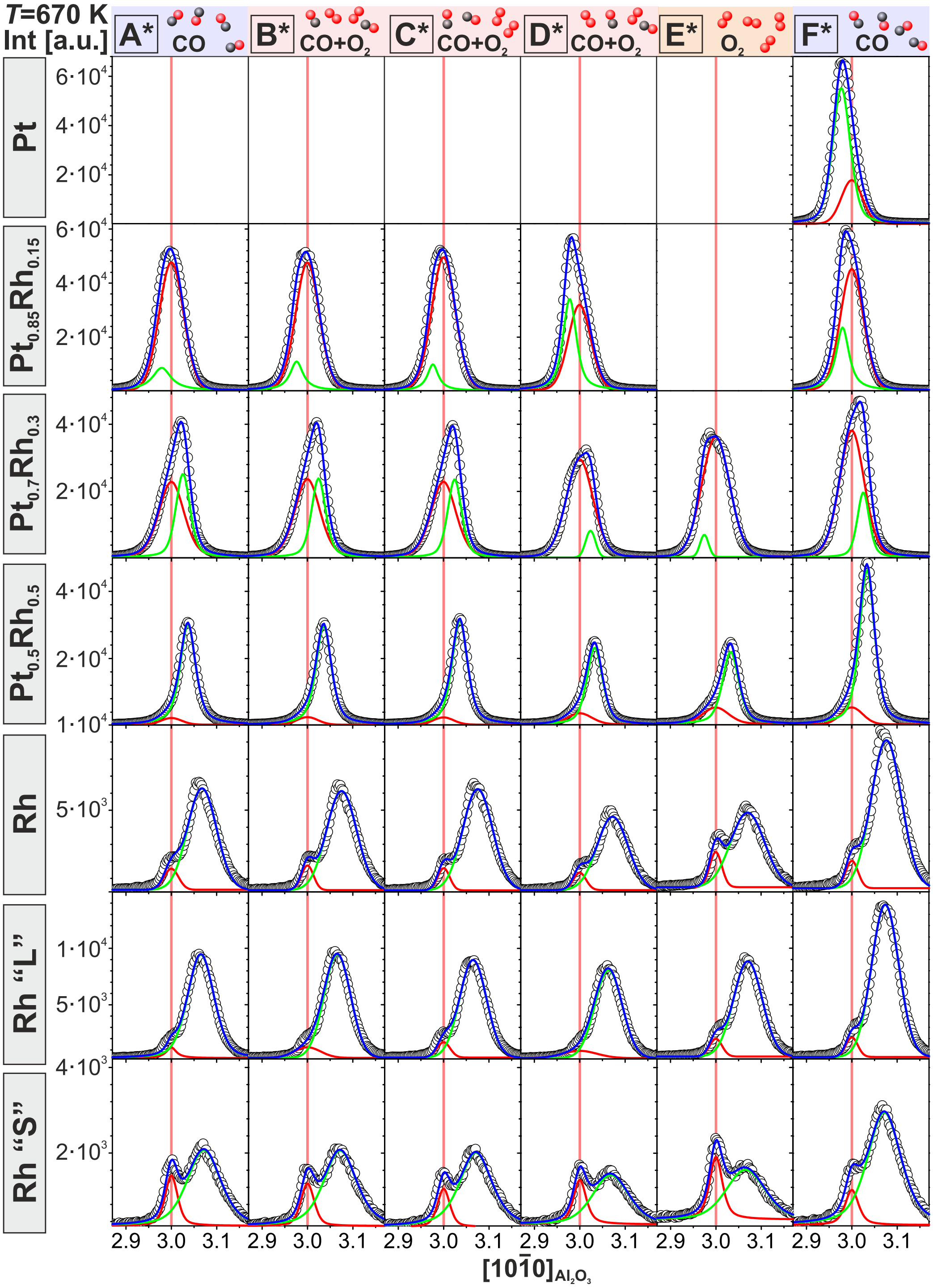

Figure A.3: **Horizontal linescans through the particle $(3\bar{1}1)$ Bragg peaks of sample "alumina-1" at 670 K:** linescans were extracted from the 2D maps for the various Pt-Rh compositions and sample conditions of the CO oxidation experiment along the substrate $[10\bar{1}0]_{Al2O3}$-direction. The data (circles) were fitted with double peak functions (solid lines; red: peak maximum fixed at $H_{Al2O3}=3$; green: variable peak maximum; blue: sum of both), where in each case Pseudo-Voigt functions were used.

A.2 Rocking scans

$\boldsymbol{dr}$ Section A.1 discussed that the particle diameter determination based on the Bragg peak analysis may fail for peaks at higher Q-values (e.g. the particle $(3\bar{1}1)$-peaks) due to lattice parameter distributions in the nanoparticle ensemble, especially in case some particles exhibit an in-plane lattice parameter comparable to the one of the substrate. The present section will address how, independent of such lattice parameter strain effects, an upper limit of the particle diameter can be deduced from sample rocking scans (here: θ-scans). In Fig. A.4 a) the high energy x-ray diffraction geometry is plotted for the in-plane component of the $(3\bar{1}1)$ reflection (which is the $(2\bar{2}0)$ reflection) in the (H,K)-plane parallel to the sample surface. $\boldsymbol{k}_0$ and $\boldsymbol{k'}$ denote the incident and the scattered wave vectors, where $\boldsymbol{k}_0=\boldsymbol{k'}=\frac{2\pi}{\lambda}$. For Pt, Rh and Pd particles and a typical wavelength of λ=0.1575 Å (as used in the high energy experiment of section 8.1), the in-plane Bragg angle θ_B is on the order of 3.3°. It is related via $\boldsymbol{Q}=\frac{4\pi}{\lambda}\sin\theta_\mathrm{B}$ to the magnitude of the scattering vector $\boldsymbol{Q}=\boldsymbol{k'}\text{-}\boldsymbol{k}_0$. The reciprocal lattice vector $\boldsymbol{G}$ points from the origin of reciprocal space Γ to the reciprocal lattice point $(3\bar{1}1)$. Due to the (average) finite diameter $\overline{D}$ of the nanoparticles, the Bragg reflection (circle in Fig. A.4) is broadened in the H and K direction by $\Delta H = \Delta K = \frac{2\pi}{\overline{D}}$ (thereby assuming a round particle shape and for the moment negligible inhomogeneous strain broadening of the Bragg reflections).

Diffraction occurs, if the reciprocal lattice is intersecting the Ewald sphere, and the intersection point defines the direction of the diffracted wave vector $\boldsymbol{k'}$. This situation is illustrated in Fig. A.4 b), representing a close-up of the Bragg peak region: due to the high energies and the correspondingly small Bragg angles, in a rocking (θ) scan with rotation axis perpendicular to the (H,K)-plane, the width of the Bragg peak is probed along H and the corresponding peak width is given by $\Delta\theta_{\overline{D}} = \frac{d_{2\bar{2}0}}{\overline{D}}$, where $d_{2\bar{2}0}$ denotes the lattice spacing of the $(2\bar{2}0)$ planes. For a real nanoparticle system, a certain angular distribution of the particles (mosaicity) with in-plane mosaic spread $\Delta\theta_M$ will be present, which is superimposed to $\Delta\theta_{\overline{D}}$. In a rocking scan with open detector slits (i.e. integration of the Bragg peak over K on the 2D detector), the peak width $\Delta\theta_{M,\overline{D}}$ is thus the convolution of mosaicity and particle broadening effect and reads: $\Delta\theta_{M,\overline{D}}=\sqrt{(\Delta\theta_M)^2 + (\Delta\theta_{\overline{D}})^2}$.

The K-direction of Fig. A.4 corresponds to the in-plane direction probed by the 2D detector (e.g. the substrate $[10\bar{1}0]$-direction containing the particle

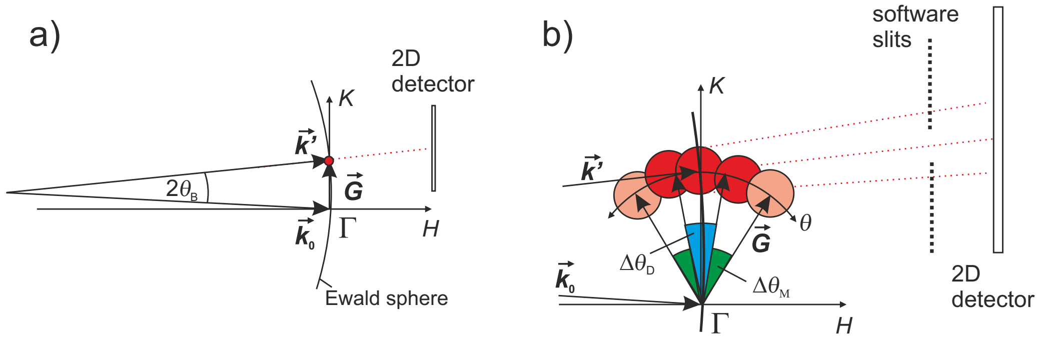

Figure A.4: **High energy x-ray diffraction geometry a)**: Scattering geometry in the (H,K) surface plane **b)**: zoom of the region close to the Bragg reflection, see text for more information.

($3\bar{1}1$)-Bragg peak). As was discussed in section A.1 it is prone to Bragg peak broadening due to possible lattice parameter distributions in the nanoparticle ensemble. Thus, $\overline{D}$ cannot be directly obtained from ΔK. Contrary, the broadening along H (for K=0), which is probed in the rocking scans, is insensitive to such inhomogeneous strain effects and allows the particle diameter determination for particle ensembles with lattice parameter distributions.

To obtain the pure mosaicity contribution ($\Delta\theta_M$), successive θ-scans were performed with differently set regions of interest ("ROIs", software slits in Fig. A.4 b)), which were centered around the Bragg peak maximum and over which the intensity was integrated during the scans. This is illustrated in Fig. A.5 a) in which the sizes of the different ROIs are indicated by arrows. They are drawn with respect to the Bragg peak maximum indicated by the white cross. The numbers correspond to ROI width in pixels, where all ROIs share the same vertical height of 4 pixels.

Fig. A.5 b) shows for the case of the as-prepared $\mathrm{Pt}_{0.7}\mathrm{Rh}_{0.3}$ particles on sample "alumina-1" the FWHMs of the performed θ-scans as a function of the horizontal ROI sizes. The FWHMs were obtained by fitting the respective θ-scans with Pseudo-Voigt functions. An example is shown in the inset of Fig. A.5 b) which represents the fitted θ-scan obtained for the largest horizontal ROI size of ROI=2·240 pixels.

When the ROI size along K is decreased, the contribution of smaller particles within the size distribution to the Bragg peak signal is decreased accordingly (because smaller particles give rise to wider Bragg reflections), and in the θ scan an effectively larger average particle size $\overline{D}$ is probed. In the limit of zero ROI width, an upper limit for θ_M can thus be determined (and a lower limit

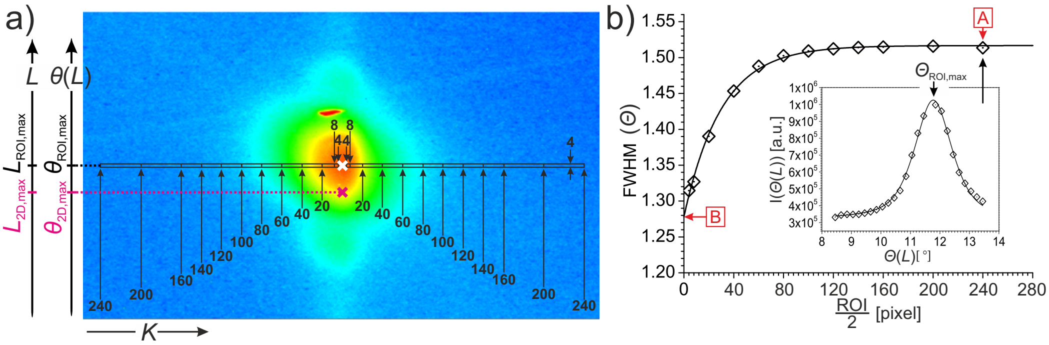

Figure A.5: **Particle diameter determination from θ-scans: a)**: 2D image of the Bragg peak of the as-prepared $Pt_{0.7}Rh_{0.3}$ particles on sample “alumina-1”, the white cross denotes the peak maximum. Black rectangles of varying horizontal size indicate regions of interest (“ROIs”) set during different θ-scans. The pairs of identical numbers, located symmetrically to the Bragg peak position, represent their respective horizontal borders. These numbers are proportional to the distance from the peak maximum position. The magenta cross corresponds to the position of the θ-value $\theta_{\mathrm{2D,max}}$ at which the 2D image was taken; **b)**: FWHMs obtained from θ-scans with different horizontal ROI sizes for the case shown in a). The inset displays the θ-scan performed with $\frac{\mathrm{ROI}}{2}$=240 pixels (here: 1 pixel=52.58×52.58 μm^2).

for $\Delta\theta_{\overline{D}}$). An upper limit for the average particle diameters $\overline{D}$ was finally obtained via $\overline{D} = \frac{d_{(2\bar{2}0)}}{\Delta\theta_{\overline{D}}}$, where $\Delta\theta_{\overline{D}}=\sqrt{(\Delta\theta_{M,\overline{D}})^2 - (\Delta\theta_M)^2}$. As this approach makes use of particle size dependent contributions to the Bragg peak widths, it is best applicable for samples featuring large particle size distributions as are present on sample “alumina-1” (see Fig. A.6 a)).

For the example of the $Pt_{0.7}Rh_{0.3}$ particles shown in Fig. A.5, a diameter of 97 Å is thus obtained, which in good agreement with the AFM value of 90 Å (see Fig. 8.5 a), Fig. 8.13 a) and Fig. A.6 a)).

For all particle stripes on sample “alumina-1” the results for the upper limits of the average diameters $\overline{D}$ are summarized in Fig. 8.5 a) and Fig. 8.13 a) for various Pt-Rh compositions and conditions, where systematic error bars obtained from the fits are included. They show that the particle diameters neither vary to a great extent nor in any systematic way under the different conditions of catalytic activity. This finding is in line with the results gained for the second comparable sample “alumina-2” for which the particle diameters obtained from the Bragg peak analysis were also found to stay rather constant independent of the sample condition (see Appendix C.1). The results for the upper limits of the average particle diameters of sample “alumina-5” are shown in Fig. 8.19 a). Their deviation from the values obtained by other methods (Bragg peak analysis, SEM) can be explained by the small lateral size distribution of the Pd-containing particles (see Appendix A.3).

A.3 AFM and SEM measurements

In order to verify the particle diameters obtained from the x-ray data, complementary microscopy techniques (AFM and SEM) were performed on the various particle stripes. All microscopy data were measured in air and after the CO oxidation experiments. For α-Al_2O_3(0001)-supported particles the thus obtained values also describe the diameters of the as-prepared particles (see section 6.2), since all x-ray data concordantly indicate the preservation of the particles' lateral size throughout the CO oxidation experiment.

Fig. A.6 a) shows the AFM images measured on the Pt-Rh particles of sample "alumina-1" (results on sintering behaviour: section 8.1), Fig. A.6 b) the SEM images of the Pt-Pd particles of sample "alumina-5" (results on sintering behaviour: section 8.2). The respective bottom panels display the particle diameter distributions that were obtained assuming circularly shaped particles. The diameter distributions are fitted with Gaussian functions and the values of the respective diameters are represented by the obtained peak maxima. In the case of the AFM data, the thus deduced value D^*_{AFM} was corrected for the cantilever tip convolution to obtain the real diameter D_{AFM} using $D_{\mathrm{AFM}}=D^*_{\mathrm{AFM}}$-20 Å.

Both, the Pt-Rh and Pt-Pd particles, show composition-dependent trends which are more pronounced in the Pt-Rh case and well-supported by various x-ray results. First, the particle diameter is found to scale with the Pt-content, where the absolute diameter values obtained from the complementary x-ray techniques are in good agreement with the microscopy results (see Fig. 8.5, Fig. 8.13 and Fig. 8.19). Second, the particle density is composition-dependent: while there are only few pure Pt particles, the particle number and surface coverage rises with increasing Rh and Pd composition. This tendency is also mirrored in the electron density profiles obtained from the respective x-ray reflectivity data measured on the sintered particles (see Fig. 8.3 for Pt-Rh particles of samples "alumina-1" and "-2").

All particles on sample "alumina-1" (Fig A.6 a)) display higher particle size distributions than the ones on "alumina-5" (Fig. A.6 b)). Accordingly, the diameter values determined from the rocking scan analysis may deviate from the values obtained by other methods (see Appendix A.2 for explanation).

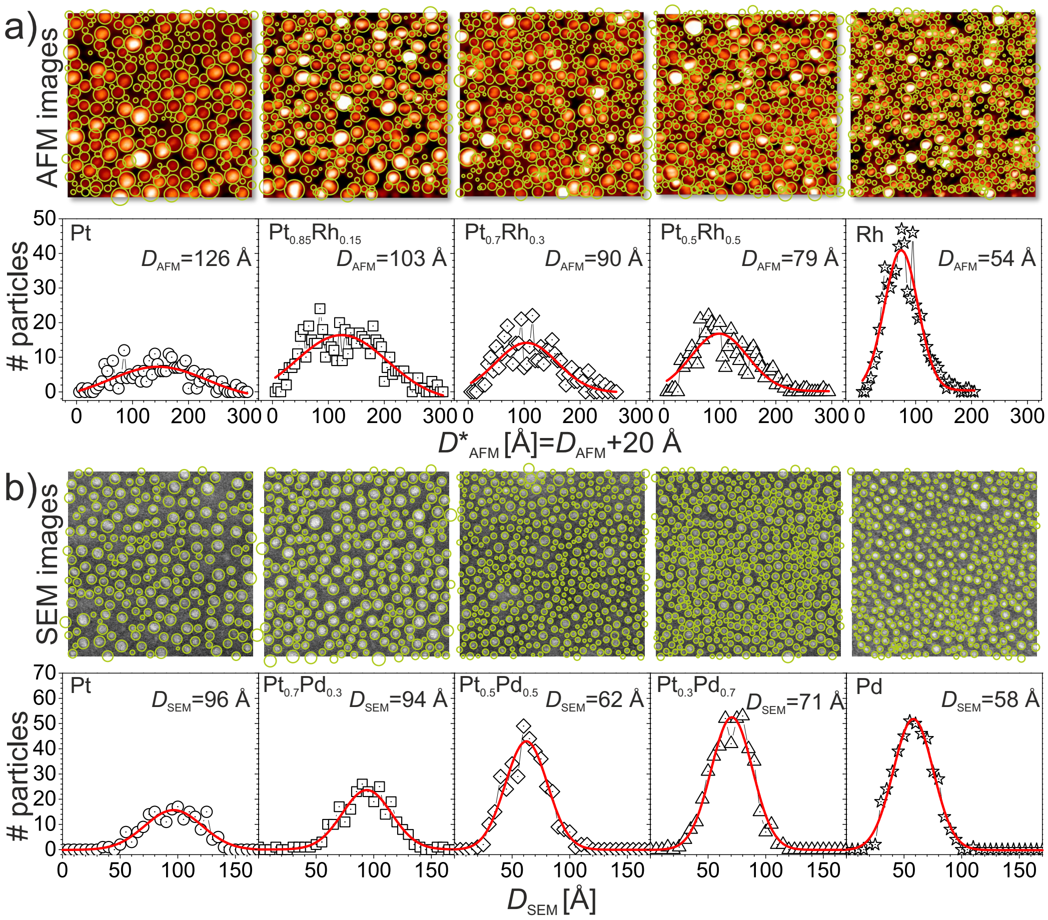

Figure A.6: **Complementary microscopy measurements performed on the Pt-Rh and Pt-Pd particles of samples "alumina-1" and "alumina-5": a): AFM:** images measured after CO oxidation on the Pt-Rh particles of sample "alumina-1" (section 8.1; frame size: 290 nm); **b): SEM:**: images measured after CO oxidation on the Pt-Pd particles of sample "alumina-5" (section 8.2; frame size: 200 nm). Green circles indicate the particle peripheries that were used to determine the lateral particle size distributions displayed in the respective bottom panels; red lines: Gaussian fits to the data. Peak maxima represent the average particle diameters $D*_{\mathrm{AFM}}$ and D_{SEM}, where $D*_{\mathrm{AFM}}$ was corrected for the tip convolution to obtain the real average diameter D_{AFM}=$D*_{\mathrm{AFM}}$-20 Å.

Appendix B

Details on the Particle Rod Analysis

Subsection 8.1.2 describes in detail how the L-scans running through the Bragg peaks of the Pt-Rh particles (particle rods) were fitted using different underlying models in order to obtain information on the particle structure. In the following it will be described how these L-scans were intensity corrected prior to the fitting procedure (section B.1), and which fit results were obtained for the displacement parameters of the various particle model layers (section B.2).

B.1 Particle rod intensity correction

The particle rods were obtained from the 2D maps by extracting scans in L-direction through the corresponding main maximum of the particle Bragg peak. The scans were intensity-corrected for the background, the stationary sample and detector geometry, and the Lorentz factor [220].

For **background correction** the positions above and below the Bragg peaks at which the particle signal subsides were determined. They served as intersection points for the linear background, which was subtracted from the extracted raw data.

In order to correct for the **stationary sample and detector**, we had to compensate for the intensity modulation along the particle rod based on the angular distribution of the particles. Therefore θ-scans (rocking scans) were performed with a broad region of interest ("ROI", here: $\frac{\mathrm{ROI}}{2}$=240 pixels, see Fig. A.5), i.e. detector area, that was extended in horizontal direction. This ensured that the influence of the particle diameter D was fully included in the intensity distribution of the scan (see Appendix A.2). Such a θ-scan is shown in the inset of Fig. A.5 b), yielding the intensity distribution $I(\theta(L))$. The position of its maximum $\theta_{\mathrm{ROI,max}}$ corresponds to the position on the particle rod given by the ROI position represented by the black box shown in Fig. A.5 a). Its centre coincides with the Bragg peak maximum indicated by the white cross.

Since the experimental 2D images, from which the L-scans were extracted, were taken at a slightly different θ-value, which we call $\theta_{\mathrm{2D,max}}$ in the following, we had to compensate for this offset by expressing $\theta(L)$ as $\theta^{*}(L)=\theta(L)-\Delta\theta$, where $\Delta\theta=\theta_{\mathrm{2D,max}}-\theta_{\mathrm{ROI,max}}$ (see Fig. A.5 a)). Thus, the correction factor F_θ for the angular distribution of the particles reads:

$$F_\theta = \frac{I(\theta_{\mathrm{2D,max}})}{I(\theta^{*}(L))}, \tag{B.1}$$

where $F_\theta=1$ if $\theta^{*}(L)=\theta_{\mathrm{2D,max}}$, otherwise $F_\theta<1$.

Taking moreover the **Lorentz factor** $F_L=\frac{1}{\sin(\gamma)}$, which corrects for the stationary geometry of sample and detector [220], into account, the total correction factor F amounts to:

$$F = F_\theta \cdot F_L = \frac{I(\theta_{\mathrm{2D,max}})}{I(\theta^{*}(L)) \cdot \sin(\gamma)}. \tag{B.2}$$

This expression was multiplied by the background-subtracted L-scans in order to obtain the intensity-corrected scans that were used for the structure analysis of the nanoparticles.

B.2 Fit results of the displacement parameters

stripe	**cond.**	b_0	b_1	t_{-2}	t_{-1}	t_0	t_1	t_2
Pt	**A**	-0.1076	-0.0240	-	-	-	-	-0.0644
	C	-0.2488	-	-	-	-	-0.0116	-0.0583
	F	-0.0971	-	▨	-	-	0.0315	▨
Pt$_{0.85}$Rh$_{0.15}$	**A**	-0.1163	-	-	-	-	-	-0.0096
	C	-0.1402	-0.0260	-	-	-	-	-0.1839
	F	-0.1174	-0.0416	-	-	-	-	-0.0314
Pt$_{0.7}$Rh$_{0.3}$	**A**	-0.2074	-	-	-	-	-	-0.2568
	C	-0.1375	-0.0061	-	-	0.0211	0.0374	0.1824
	F	-0.1262	-	-	-	-	-	0.0000
Pt$_{0.5}$Rh$_{0.5}$	**A**	-0.1354	-	-	-	-	0.1184	0.1442
	C	-0.1500	-0.0081	-	-	-	-	-0.0188
	F	-0.1849	-	-	-	-	0.0055	0.0614
Rh	**A**	-0.1285	-	▨	▨	0.0870	▨	▨
	C	-0.1647	-	▨	▨	0.0889	▨	▨
	F	-0.1218	-	▨	▨	0.1540	▨	▨

Table B.1: **Fitted parameters:** the table contains results that were obtained based on particle model shapes with $g=\frac{\gamma_{(100)}}{\gamma_{(111)}}=1.1$. The colours of the table elements hold information whether for a certain Pt-Rh composition and condition (A, C, F) the respective occupancy of atomic layers b_0, b_1, t_{-2}, t_{-1}, t_0, t_1 and t_2 was allowed to vary in the fit (white elements), or whether it was kept fixed to its theoretical model value in order to maintain the physical constraints of the layer sequence (grey elements). The fitted occupancy values are displayed as black diamonds in Fig. 8.8. The numbers of the table elements constitute the fitted displacement parameters of the corresponding layers, which represent the deviation (in Å) from the respective theoretical layer positions of the underlying model shape. A dash indicates that the displacement parameter was kept fixed during the fitting in order to fulfill physical constraints.

Appendix C

Data Reproducibility

C.1 Results of the Pt-Rh particles on sample "alumina-2"

The reproducibility of the shape-dependent sintering of Pt-Rh particles discussed for sample "alumina-1" in section 8.1 was confirmed by the study of a second comparable sample, "alumina-2" (see Fig. 6.8), its results will be presented here. The data moreover affirm the composition-independent preservation of the particle diameter throughout the CO oxidation experiment.

As is illustrated in section 6.2, the initial particle shapes of the various Pt-Rh compositions on samples "alumina-1" and "-2" are comparable. Apart from the shared alloy compositions (Pt, $Pt_{0.85}Rh_{0.15}$, $Pt_{0.7}Rh_{0.3}$, $Pt_{0.5}Rh_{0.5}$, Rh), sample "alumina-2" includes in addition two alloy particle stripes with higher Rh content ($Pt_{0.3}Rh_{0.7}$, $Pt_{0.15}Rh_{0.85}$). Contrary to sample "alumina-1", the particle stripes were grown along the $[10\bar{1}0]$-direction of the substrate, which allowed for monitoring reciprocal space maps including the particle $(11\bar{1})$ Bragg peak. As the value of its in-plane scattering vector $\boldsymbol{Q}_{\|}$ is reduced by a factor of $\sqrt{3}$ compared to the one of the particle $(3\bar{1}1)$ Bragg peak probed in case of "alumina-1", the FWHM-analysis for particle diameter determination is feasible[1], since strain broadening effects due to particles growing commensurately on the alumina substrate become negligible (see Appendix A.1). This can also be inferred from the symmetric shape of the horizontal linescans

---

[1] The diameter thus was determined via $D = \frac{a^*}{\Delta Q_{\|}}$, where $a^* = \frac{2\pi \cdot 2\sqrt{2}}{\sqrt{3} \cdot a_{fcc}}$ and $\Delta Q_{\|}$ corresponds to the FWHM of the in-plane scan through the particle Bragg peak. It yields the domain size along the probed direction and thus the lower limit for the corresponding particle size which is here close to the correct value for the average particle diameter.

through the respective particle Bragg peaks depicted in Fig. C.2 a), which do not indicate any superposition of two peaks.

The sample was studied under equal sample conditions (T=550 K; p_{tot}=200 mbar; total flow f_{tot}=100 $\frac{\mathrm{ml}}{\mathrm{min}}$; Ar used as carrier gas) and the same experimental settings and equipment (photon energy E=78.7 keV; incident angle α_{i}=0.0333°; FReLoN 2D camera) as in the experiment described in section 8.1. Fig. C.1 a) yields an overview of the close-ups on the Pt-Rh $(11\bar{1})$ Bragg peaks probed for various gas flow settings (condition a: no O_2, f_{CO}=2 $\frac{\mathrm{ml}}{\mathrm{min}}$; b: f_{O2}=2 $\frac{\mathrm{ml}}{\mathrm{min}}$, f_{CO}=10 $\frac{\mathrm{ml}}{\mathrm{min}}$; c: f_{O2}=5 $\frac{\mathrm{ml}}{\mathrm{min}}$, f_{CO}=10 $\frac{\mathrm{ml}}{\mathrm{min}}$; d: f_{O2}=8 $\frac{\mathrm{ml}}{\mathrm{min}}$, f_{CO}=10 $\frac{\mathrm{ml}}{\mathrm{min}}$). Also in this case the stepwise increase of the oxygen flow (condition a→d) resulted in an increase in CO_2 production, as can be inferred from the mass spectrometer data shown in Fig. C.1 b). The partial gas pressures were on a comparable level as found for “alumina-1” (see Fig. 8.2 b)).
Also in the case of this sample distinct Laue oscillations were present for Pt-rich particles, as can be inferred from the 2D maps of Fig. C.1 a) and the linescans extracted in L-direction through the respective particle Bragg peaks as shown in Fig. C.1 c). In line with “alumina-1”, the distances between their positions and the corresponding Bragg peak main maxima were progressively reduced in the transition to higher catalytic activity, implying a gradual particle height increase. Also here, the movement of the Laue oscillation signals was progressively extenuated as a function of the particles' Rh content.
Hence, it can be concluded that also on this sample the activity-induced vertical particle sintering was most pronounced for the Pt-rich particles, while its suppression scaled with the Rh content inside the particles. Also the gradual Bragg peak intensity increase in the transition to higher catalytic activity, which was found to be the less pronounced the higher the Rh content, is in agreement with this conclusion. It is moreover striking that both, the largest shift of the oscillations' position and the most pronounced peak intensity increase, occur in the transition from condition a to b, i.e. when changing from reducing to moderate conditions of CO oxidation. This was also found for sample “alumina-1” (see Fig. 8.2) and indicates that the onset of the activity-induced particle restructuring occurs faster and costs less energy than at a later stage, at which the restructuring speed slows down as the particle reach their respective equilibrium shape, despite involving even higher CO_2 production rates and thus more potential excess energy from the reaction.

To quantify the shape-dependent particle sintering, the linescans through the

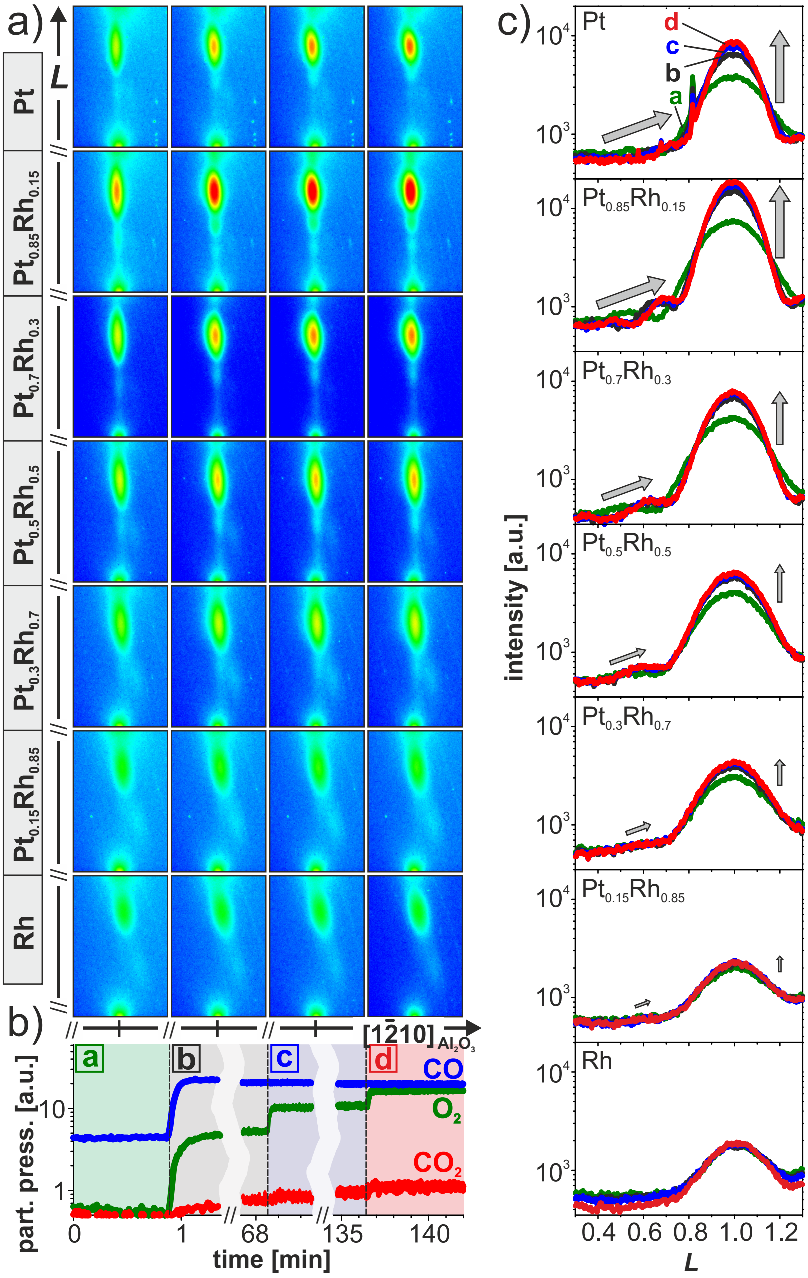

Figure C.1: **In-situ monitoring of particle Pt-Rh (11$\bar{1}$) Bragg peaks during CO oxidation on sample "alumina-2": a):** 2D maps collected at 550 K and p_{tot}=200 mbar (exposure time: 50 s). Set partial flows: **a**: no O$_2$, f_{CO}=2 $\frac{\mathrm{ml}}{\mathrm{min}}$; **b**: f_{O2}=2 $\frac{\mathrm{ml}}{\mathrm{min}}$, f_{CO}=10 $\frac{\mathrm{ml}}{\mathrm{min}}$; **c**: f_{O2}=5 $\frac{\mathrm{ml}}{\mathrm{min}}$, f_{CO}=10 $\frac{\mathrm{ml}}{\mathrm{min}}$; **d**: f_{O2}=8 $\frac{\mathrm{ml}}{\mathrm{min}}$, f_{CO}=10 $\frac{\mathrm{ml}}{\mathrm{min}}$; **b):** partial pressures as measured under the different conditions (a-d) and as a function of time; **c):** linescans along L-direction through the respective peak maxima extracted from the 2D maps.

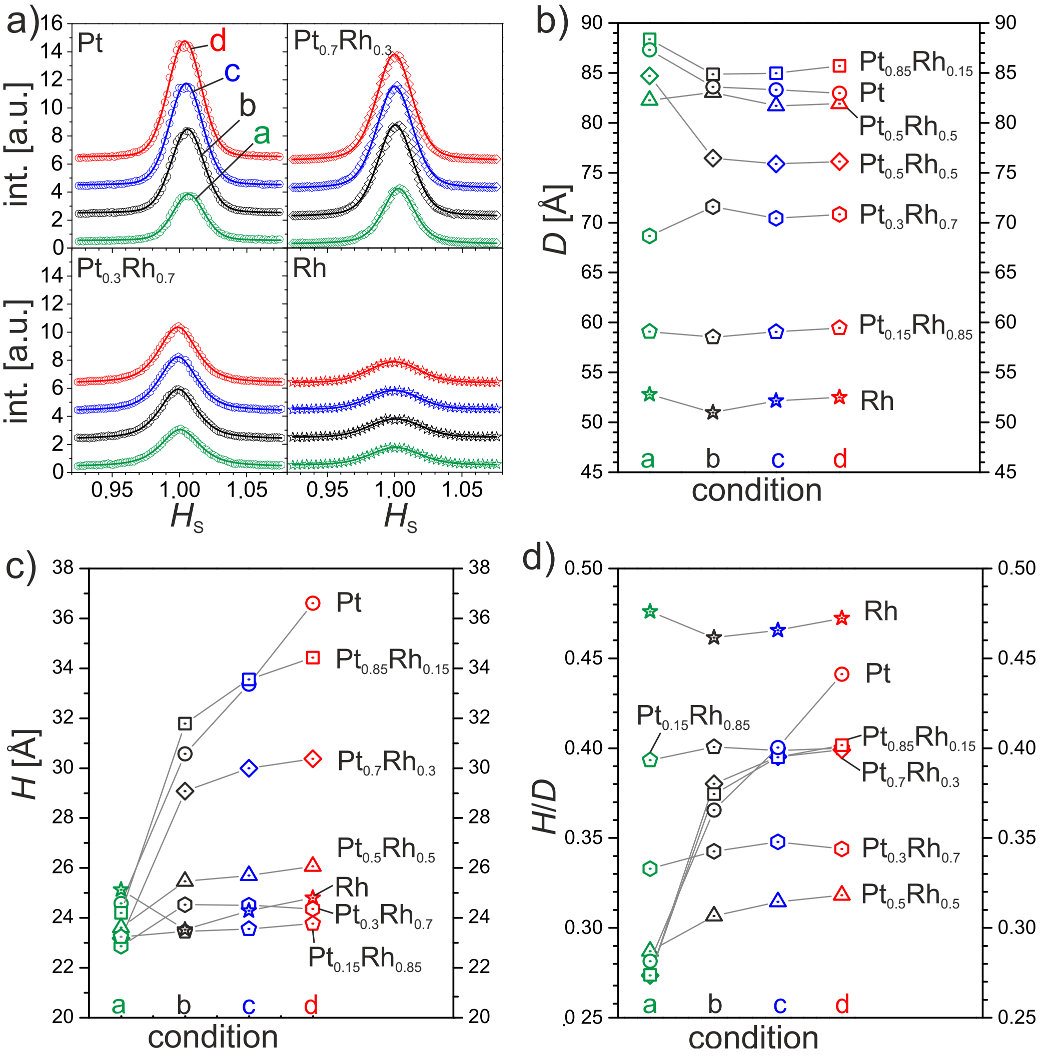

Figure C.2: **Heights, diameters and aspect ratios of the Pt-Rh particles of “alumina-2” in the course of CO oxidation: a)**: linescans through the particle $(11\bar{1})$ Bragg peak extracted from the reciprocal space maps in horizontal direction for various Pt-Rh compositions and conditions (a-d, see caption of Fig. C.1) drawn with an offset for clarity (open circles: data; solid lines: Pseudo-Voigt fits). The coordinate system of the particle surface unit cell (S) is used, where the probed direction H_S=$[100]_S$ corresponds to the $[11\bar{2}]$-direction of the bulk fcc coordinate system used otherwise; **b)**: particle diameters obtained from the FWHMs of the peak fits in a); **c)**: particle heights determined from the L-scans in Fig. C.1 by fitting the Bragg peaks with Pseudo-Voigt functions and considering the FWHMs; **d)**: aspect height-to-diameter ratios $\frac{H}{D}$ as deduced from the data displayed in b) and c).

respective particle Bragg peaks along horizontal (Fig. C.2 a)) and vertical (Fig. C.1 c)) direction were fitted with Pseudo-Voigt functions. The particle diameters, heights and aspect ratios $\frac{H}{D}$ obtained from the corresponding FWHMs are depicted in Fig. C.2 b), c) and d), respectively, as a function of sample condition.

The data reveal that, for all Pt-Rh compositions, the diameters remained relatively constant, despite the tremendous height increase of the Pt-rich particles. This finding, based on the FWHM analysis of the particle Bragg peaks, is essential, as it is in line with the outcome of the unconventional rocking scan analysis performed for sample "alumina-1" derived in Appendix A.2.

The quantitative results obtained for the particle heights, shown in Fig. C.2 c), are also in accordance: the particles of the various Pt-Rh compositions had the same initial height of about 24 Å and followed the aforementioned composition- and thus shape-dependent sintering behaviour that scales with Pt content. The particle height increases of the various compositions are comparable to the ones found for sample "alumina-1" (see Fig. 8.5 b)). The slightly smaller final heights found for the sintered particles of "alumina-2" can be ascribed to the fact that no gas cycles were performed and that the total time of the CO oxidation experiment was shorter (1 vs. 3 days).

Also on this sample, the aspect ratios of the Pt-rich particles increase towards the higher values of their thermodynamic equilibrium particle shapes. Thanks to the presence of additional Pt-Rh compositions on "alumina-2", the composition-dependent particle shape change tendencies could be extended by the results of the $Pt_{0.3}Rh_{0.7}$ and $Pt_{0.15}Rh_{0.85}$ particles, which totally match the expected overall trends.

For both samples "alumina-1" and "alumina-2", the results obtained from the x-ray reflectivity measurements, performed before and during CO oxidation, are in agreement as well. This can be inferred from Fig. 8.3 which yields an overview of the fitted reflectivity curves along with the obtained electron density profiles for some selected Pt-Rh compositions on both samples. As was discussed in section 8.1, the activity-induced particle height increase comes along with a decrease in the percental particle coverage, which both scale with the Pt content of the particles. This indicates a huge mass transport on the sample surface for Pt-rich particles during CO oxidation. Accordingly, also the results obtained from sample "alumina-2" indicate a non-classical Ostwald ripening mechanism as described in section 8.1.

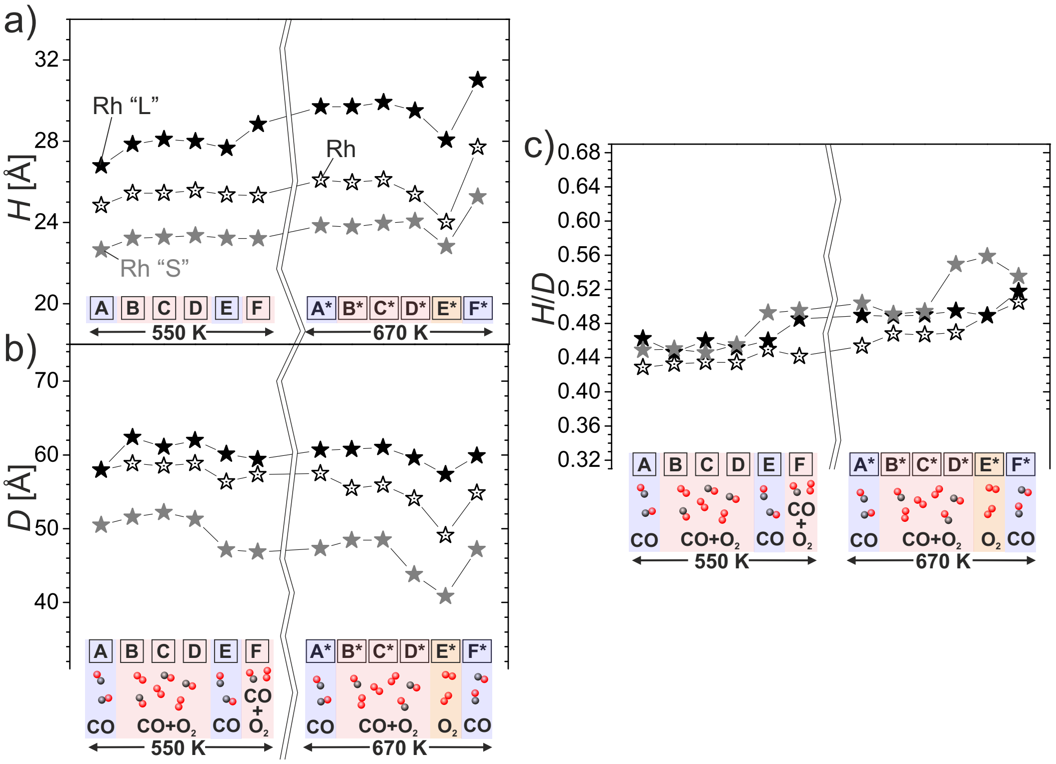

Figure C.3: **Heights, diameters and aspect ratios of the pure Rh particles on sample "alumina-1": a)**: heights as obtained from Pseudo-Voigt fits to the particle Bragg peaks; **b)**: diameters obtained from the horizontal linescan fits in Fig. A.2 and Fig. A.3; **c)**: aspect ratios $\frac{H}{D}$ as deduced from the data in a) and b).

C.2 Rh particles of varying sizes on sample "alumina-1" under different sample conditions

Section 8.1 showed that the sizes and shapes of the pure Rh particles on sample "alumina-1" did not change noticeably during CO oxidation. In addition to the Rh particles discussed therein, sample "alumina-1" contained two more test stripes of pure Rh particles of slightly larger (Rh "L") and smaller (Rh "S") particle size. The particle heights, diameters and aspect ratios of these three Rh stripes are summarized in Fig. C.3 a), b), and c), respectively, as a function of sample condition. The respective particle $(3\bar{1}1)$ Bragg peaks of the two additional test stripes at 550 K and 670 K are included in Fig. 8.2 a) and

8.12 a), respectively.

As key result one can conclude, that the Rh particles of all probed sizes showed the same stability and sinter-resistance. The most noticeable size change occurred under pure oxygen flow (condition E*: $f_{O2}=25\ \frac{\mathrm{ml}}{\mathrm{min}}$) which was characterized by a decrease in the heights and diameters, probably due to oxidation of the particle shells. The particles readopted their former height and diameter values under reducing atmospheres (condition F*), since it is likely that CO reduced the formed oxide shells. A similar behaviour was also concluded for other Rh-containing particles (see Fig. 7.11, Fig. 7.18 and Fig. 8.13). The particles' stability is also mirrored in their height-to-diameter aspect ratio values, which increased only very slightly in the course of the whole experiment.

Appendix D

Acronyms

AES : Auger Electron Spectroscopy
AFM: Atomic Force Microscopy
(AP-) XPS: (Ambient Pressure) X-ray Photoelectron Spectroscopy
DFT: Density Functional Theory
EXAFS: Extended X-ray Absorption Fine Structure
fcc: face centered cubic
FWHM: Full Width at Half Maximum
GIXRD: Grazing Incidence X-Ray Diffraction
HESXRD: High Energy X-Ray Diffraction
(HP-) AFM: (High Pressure) Atomic Force Microscopy
(HP-) STM: (High Pressure) Scanning Tunneling Microscopy
(HP-) TEM: (High Pressure) Transmission Electron Microscopy
HREM: High Resolution Electron Microscopy
IR: Infrared
LEED: Low Energy Electron Diffraction
PM-IRAS: Polarization-Modulation Infrared Reflection Absorption Spectroscopy
SFG: Sum Frequency Generation Spectroscopy
SXRD: Surface X-Ray Diffraction
SEM: Scanning Electron Microscopy
TPD: Temperature-Programmed Desorption
TPR: Temperature-Programmed Reduction
UHV: Ultra-High Vacuum
XAS: X-ray Absorption Spectroscopy
XPS: X-ray Photoelectron Spectroscopy
XRD: X-Ray Diffraction

Bibliography

[1] J. J. Berzelius, Considerations respecting a new power which acts in the formation of organic bodies, *Edinburgh New Philosophical Journal* **21**, 223 (1836), with some substitution of modern wording.

[2] A. J. B. Robertson, The early history of catalysis, *Platinum Metals Rev.* **19**, 64-69 (1975).

[3] Acmite Market Intelligence, *Market Report: Global Catalyst Market* (2015).

[4] P. Nolte, A. Stierle, N. Y. Jin-Phillipp, N. Kasper, T. U. Schulli and H. Dosch, Shape changes of supported Rh nanoparticles during oxidation and reduction cycles, *Science* **321**, 1654-1658 (2008).

[5] T. W. Hansen, P. L. Hansen, S. Dahl and C. J. H. Jacobsen, Support effect and active sites on promoted ruthenium catalysts for ammonia synthesis, *Catal. Lett.* **84**, 7-12 (2002).

[6] C. R. Henry, Morphology of supported nanoparticles, *Prog. Surf. Sci.* **80**, 92-116 (2005).

[7] C. R. Henry, Surface studies of supported model catalysts, *Surf. Sci. Rep.* **31**, 231-325 (1998).

[8] M. Bäumer and H.-J. Freund, Metal deposits on well-ordered oxide films, *Prog. Surf. Sci.* **61**, 127-198 (1999).

[9] Q. Fu and T. Wagner, Interaction of nanostructured metal overlayers with oxide surfaces, *Surf. Sci. Rep.* **62**, 431-498 (2007).

[10] H. Lüth, *Solid surfaces, interfaces and thin films*, Springer-Verlag, Berlin Heidelberg (2015).

[11] A. Zangwill, *Physics at surfaces*, Cambridge University Press, Cambridge New York Melbourne (1996).

[12] I. V. Markov, *Crystal growth for beginners*, World Scientific Publishing Co. Pte. Ltd., Singapore Hackensack London (2003).

[13] A. Pimpinelli and J. Villain, *Physics of crystal growth*, Cambridge University Press, New York (1998).

[14] R. D. Moorhead and H. Poppa, In situ oxygen conditioning of (001) MgO thin-film substrates for film growth-studies by electron-microscopy, *Thin Solid Films* **58**, 169-173 (1979).

[15] O. Benamara, E. Snoeck, M. Respaud and T. Blon, Growth of platinum ultrathin films on Al_2O_3(0001), *Surf. Sci.* **605**, 1906-1912 (2011).

[16] A. Schmidt, V. Schünemann and R. Anton, Monte Carlo simulation of the nucleation and growth of binary-alloy particles of Au, Ag, and Pd on NaCl(100) substrates, *Phys. Rev. B* **41**, 11875-11880 (1990).

[17] L. Vegard, Die Konstitution der Mischkristalle und die Raumfüllung der Atome, *Z. Phys.*, **5**, 17-26 (1921).

[18] W. G. Moffatt, *The handbook of binary phase diagrams*, Schenectady, N. Y.: General Electric Comp. (1980).

[19] S. N. Tripathi and S. R. Bharadwaj, The Pd-Rh (Palladium-Rhodium) system, *J. Phase Equilib.* **15**, 208-212 (1994).

[20] H. Okamoto, Pd-Pt (Palladium-Platinum), *J. Phase Equilib.* **12**, 617-618 (1991).

[21] B. R. Cuenya and F. Behafarid, Nanocatalysis: size- and shape-dependent chemisorption and catalytic reactivity, *Surf. Sci. Rep.* **70**, 135-187 (2015).

[22] M. Sankar, N. Dimitratos, P. J. Miedziak, P. P. Wells, C. J. Kiely and G. J. Hutchings, Designing bimetallic catalysts for a green and sustainable future, *Chem. Soc. Rev.* **41**, 8099-8139 (2012).

[23] R. Ferrando, J. Jellinek and R. L. Johnston, Nanoalloys: from theory to applications of alloy clusters and nanoparticles, *Chem. Rev.* **108**, 845-910 (2008).

[24] G. Wulff, On the question of speed of growth and dissolution of crystal surfaces, *Z. Kristallogr. Miner.* **34**, 449-530 (1901).

[25] N. Seriani and F. Mittendorfer, Platinum-group and noble metals under oxidizing conditions, *J. Phys.: Condens. Matter* **20**, 184023-1 - 184023-11 (2008).

[26] E. Ringe, R. P. van Duyne and L. D. Marks, Wulff construction for alloy nanoparticles, *Nano Lett.* **11**, 3399-3403 (2011).

[27] H. Graoui, S. Giorgio and C. R. Henry, Effect of the interface structure on the high-temperature morphology of supported metal clusters, *Philos. Mag. B* **81**, 1649-1658 (2001).

[28] W. K. Burton, N. Cabrera and F. C. Frank, The growth of crystals and the equilibrium structure of their surfaces, *Philos. Trans. R. Soc. London A* **243**, 299-358 (1951).

[29] H. Brune and K. Kern, Heteroepitaxial metal growth: the effects of strain, in *The chemical physics of solid surfaces and heterogeneous catalysis* vol. 8, Elsevier, 149-206 (1997).

[30] P. Müller and R. Kern, Equilibrium nano-shape changes induced by epitaxial stress (generalised Wulff-Kaishew theorem), *Surf. Sci.* **457**, 229-253 (2000).

[31] J. Olander, R. Lazzari, J. Jupille, B. Mangili, J. Goniakowski and G. Renaud, Size- and temperature-dependent epitaxy for a strong film-substrate mismatch: the case of Pt/MgO(001), *Phys. Rev. B* **76**, 075409-1 - 075409-16 (2007).

[32] H.-T. Li, L.-F. Chen, X. Yuan, W.-Q. Zhang, J. R. Smith and A. G. Evans, Interfacial stoichiometry and adhesion at metal/α-Al_2O_3 interfaces, *J. Am. Ceram. Soc.* **94**, S154-S159 (2011).

[33] R. Lazzari and J. Jupille, Wetting and interfacial chemistry of metallic films on the hydroxylated α-Al_2O_3(0001) surface, *Phys. Rev. B* **71**, 045409-1 - 045409-13 (2005).

[34] Q. Fu, T. Wagner and M. Rühle, Hydroxylated α-Al_2O_3(0001) surfaces and metal/α-Al_2O_3(0001) interfaces, *Surf. Sci.* **600**, 4870-4877 (2006).

[35] S. A. Chambers, T. Droubay, D. R. Jennison and T. R. Mattsson, Laminar growth of ultrathin metal films on metal oxides: Co on hydroxylated α-Al_2O_3(0001), *Science* **297**, 827-831 (2002).

[36] M. Sterrer and H.-J. Freund, Towards realistic surface science models of heterogeneous catalysts: influence of support hydroxylation and catalyst preparation method, *Catal Lett.* **143**, 375-385 (2013).

[37] D. R. Jennison and T. R. Mattsson, Atomic understanding of strong nanometer-thin metal/alumina interfaces, *Surf. Sci.* **544**, L689-L696 (2003).

[38] M. C. R. Jensen, K. Venkataramani, S. Helveg, B. S. Clausen, M. Reichling, F. Besenbacher and J. V. Lauritsen, Morphology, dispersion, and stability of Cu nanoclusters on clean and hydroxylated α-Al_2O_3(0001) substrates, *J. Phys. Chem. C* **112**, 16953-16960 (2008).

[39] J. F. Sanz and N. C. Hernández, Mechanism of Cu deposition on the α-Al_2O_3 (0001) surface, *Phys. Rev. Lett.* **94**, 016104-1 - 016104-4 (2005).

[40] D. Mei, V.-A. Glezakou, V. Lebarbier, L. Kovarik, H. Wan, K. O. Albrecht, M. Gerber, R. Rousseau and R. A. Dagle, Highly active and stable $MgAl_2O_4$-supported Rh and Ir catalysts for methane steam reforming: a combined experimental and theoretical study, *J. Catal.* **316**, 11-23 (2014).

[41] G. Gusmano, G. Montesperelli and E. Traversa, Microstructure and electrical properties of $MgAl_2O_4$ thin films for humidity sensing, *J. Am. Ceram. Soc.* **76**, 743-750 (1993).

[42] A. B. Larbot, G. Philip, M. Persin and L. Cot, $MgAl_2O_4$ spinel as material for ultrafiltration membranes, *Key Eng. Mat.* **132-136**, 1719-1722 (1997).

[43] J. Guo, H. Lou, H. Zhao, D. Chai and X. Zheng, Dry reforming of methane over nickel catalysts supported on magnesium aluminate spinels, *Appl. Catal. A: Gen.* **273**, 75-82 (2004).

[44] J. Sehested, A. Carlsson, T. V. W. Janssens, P. L. Hansen and A. K. Datye, Sintering of nickel steam-reforming catalysts on $MgAl_2O_4$ spinel supports, *J. Catal.* **197**, 200-209 (2001).

[45] W.-Z. Li, L. Kovarik, D. Mei, J. Liu, Y. Wang and C. H. F. Peden, Stable platinum nanoparticles on specific $MgAl_2O_4$ spinel facets at high temperatures in oxidizing atmospheres, *Nat. Commun.* **4**, 2481-1 -2481-8 (2013).

[46] G. B. Andreozzi, F. Princivalle, H. Skogby and A. della Giusta, Cation ordering and structural variations with temperature in $MgAl_2O_4$ spinel: an x-ray single-crystal study, *Am. Mineral.* **85**, 1164-1171 (2000).

[47] K. E. Sickafus, J. M. Wills and N. W. Grimes, Structure of spinel, *J. Am. Ceram. Soc.* **82**, 3279-3292 (1999).

[48] M. K. Rasmussen, A. S. Foster, B. Hinnemann, F. F. Canova, S. Helveg, K. Meinander, N. M. Martin, J. Knudsen, A. Vlad, E. Lundgren, A. Stierle, F. Besenbacher and J. V. Lauritsen, Stable cation inversion at the $MgAl_2O_4(100)$ surface, *Phys. Rev. Lett.* **107**, 036102-1 - 036102-4 (2011).

[49] J. Goniakowski, F. Finocchi and C. Noguera, Polarity of oxide surfaces and nanostructures *Rep. Prog. Phys.* **71** 016501-1 - 016501-55 (2008).

[50] C. H. Bartholomew, Mechanisms of catalyst deactivation, *Appl. Catal. A: Gen.* **212**, 17-60 (2001).

[51] V. P. Zhdanov and B. Kasemo, Steady-state kinetics of CO oxidation on Pt: extrapolation from 10^{-10} to 1 bar, *Appl. Surf. Sci.* **74**, 147-164 (1994).

[52] S. M. McClure and D. W. Goodman, New insights into catalytic CO oxidation on Pt-group metals at elevated pressures, *Chem. Phys. Lett.* **469**, 1-13 (2009).

[53] H. S. Gandhi, G. W. Graham and R. W. McCabe, Automotive exhaust catalysis, *J. Catal.* **216**, 433-442 (2003).

[54] I. Chorkendorff and J. W. Niemantsverdriet, *Concepts of modern catalysis and kinetics*, Wiley, Weinheim (2003).

[55] K. Christmann, *Introduction to surface physical chemistry*, Springer, Darmstadt (1991).

[56] D. D. Eley and E. K. Rideal, Parahydrogen conversion on tungsten, *Nature* **146**, 401-402 (1940).

[57] P. Mars and D. W. van Krevelen, Oxidations carried out by means of vanadium oxide catalysts, *Chem. Eng. Sci.* **3**, 41-59 (1954).

[58] T. Engel and G. Ertl, Elementary steps in the catalytic oxidation of carbon monoxide on platinum metals, *Adv. Catal.* **28**, 1-78 (1979).

[59] M. Chen, Y. Zheng and H. Wan, Kinetics and active surfaces for CO oxidation on Pt-group metals under oxygen rich conditions, *Top. Catal.* **56**, 1299-1313 (2013).

[60] F. Gao, Y. Wang, Y. Cai and D. W. Goodman, CO oxidation on Pt-group metals from ultrahigh vacuum to near atmospheric pressures. 2. Palladium and platinum, *J. Phys. Chem. C* **113**, 174-181 (2009).

[61] F. Gao, Y. Cai, K. K. Gath, Y. Wang, M. S. Chen, Q. L. Guo and D. W. Goodman, CO oxidation on Pt-group metals from ultrahigh vacuum to near atmospheric pressures. 1. Rhodium, *J. Phys. Chem. C* **113**, 182-192 (2009).

[62] X. Su, P. S. Cremer, Y. R. Shen and G. A. Somorjai, High-pressure CO oxidation on Pt(111) monitored with infrared-visible sum frequency generation (SFG), *J. Am. Chem. Soc.* **119**, 3994-4000 (1997).

[63] R. L. Palmer and J. N. Smith Jr., Molecular-beam study of CO oxidation on a (111) platinum surface, *J. Chem. Phys.* **60**, 1453-1463 (1974).

[64] T. Matsushima, Kinetic studies on the CO oxidation over platinum by means of carbon 13 tracer, *Surf. Sci.* **79**, 63-75 (1979).

[65] T. Engel, A molecular-beam investigation of He, CO, and O_2 scattering from Pd(111), *J. Chem. Phys.* **69**, 373-385 (1978).

[66] H. Over, Y. D. Kim, A. P. Seitsonen, S. Wendt, E. Lundgren, M. Schmid, P. Varga, A. Morgante and G. Ertl, Atomic-scale structure and catalytic reactivity of the RhO_2(110) surface, *Science* **287**, 1474-1476 (2000).

[67] R. van Rijn, O. Balmes, R. Felici, J. Gustafson, D. Wermeille, R. Westerström, E. Lundgren and J. W. M. Frenken, Comment on “CO oxidation

on Pt-group metals from ultrahigh vacuum to near atmospheric pressures. 2. Palladium and platinum", *J. Phys. Chem. C* **114**, 6875-6876 (2010).

[68] F. Gao, S. McClure, M. Chen and D. W. Goodman, Comment on "Catalytic activity of the Rh surface oxide: CO oxidation over Rh(111) under realistic conditions", *J. Phys. Chem. C* **114**, 22369-22371 (2010).

[69] J. Gustafson, R. Westerström, O. Balmes, A. Resta, R. van Rijn, X. Torrelles, C. T. Herbschleb, J. W. M. Frenken and E. Lundgren, Reply to "Comment on 'Catalytic activity of the Rh surface oxide: CO oxidation over Rh(111) under realistic conditions' ", *J. Phys. Chem. C* **114**, 22372-22373 (2010).

[70] B. L. M. Hendriksen, S. C. Bobaru and J. W. M. Frenken, Oscillatory CO oxidation on Pd(100) studied with in situ scanning tunneling microscopy, *Surf. Sci.* **552**, 229-242 (2004).

[71] R. van Rijn, O. Balmes, A. Resta, D. Wermeille, R. Westerström, J. Gustafson, R. Felici, E. Lundgren and J. W. M. Frenken, Surface structure and reactivity of Pd(100) during CO oxidation near ambient pressures, *Phys. Chem. Chem. Phys.* **13**, 13167-13171 (2011).

[72] C. H. F. Peden, D. W. Goodman, D. S. Blair, P. J. Berlowitz, G. B. Fisher and S. H. Oh, Kinetics of CO oxidation by O_2 or NO on Rh(111) and Rh(100) single crystals, *J. Phys. Chem.* **92**, 1563-1567 (1988).

[73] S. H. Oh, G. B. Fisher, J. E. Carpenter and D. W. Goodman, Comparative kinetic studies of CO-O_2 and CO-NO reactions over single crystal and supported Rhodium catalysts, *J. Catal.* **100**, 360-376 (1986).

[74] J. Gustafson, M. Shipilin, C. Zhang, A. Stierle, U. Hejral, U. Rütt, O. Gutowski, P.-A. Carlsson, M. Skoglundh and E. Lundgren, High-energy surface x-ray diffraction for fast surface structure determination, *Science* **343**, 758-761 (2014).

[75] M. Shipilin, U. Hejral, E. Lundgren, L. R. Merte, C. Zhang, A. Stierle, U. Rütt, O. Gutowski, M. Skoglundh, P.-A. Carlsson and J. Gustafson, Quantitative surface structure determination using in situ high-energy SXRD: surface oxide formation on Pd(100) during catalytic CO oxidation, *Surf. Sci.* **630**, 229-235 (2014).

[76] M. Shipilin, J. Gustafson, C. Zhang, L. R. Merte, A. Stierle, U. Hejral, U. Rütt, O. Gutowski, M. Skoglundh, P.-A. Carlsson and E. Lundgren, Transient structures of PdO during CO oxidation over Pd(100), *J. Phys. Chem. C* **119**, 15469-15476 (2015).

[77] P. J. Berlowitz, C. H. F. Peden and D. W. Goodman, Kinetics of CO oxidation on single-crystal Pd, Pt, and Ir, *J. Phys. Chem.* **92**, 5213-5221 (1988).

[78] R. Toyoshima, M. Yoshida, Y. Monya, Y. Kousa, K. Suzuki, H. Abe, B. S. Mun, K. Mase, K. Amemiya and H. Kondoh, In situ ambient pressure XPS study of CO oxidation reaction on Pd(111) surfaces, *J. Phys. Chem. C* **116**, 18691-18697 (2012).

[79] Z. Duan and G. Henkelman, CO oxidation on the Pd(111) surface, *ACS Catal.* **4**, 3435-3443 (2014).

[80] J. T. Hirvi, T.-J. J. Kinnunen, M. Suvanto, T. A. Pakkanen and J. K. Nørskov, CO oxidation on PdO surfaces, *J. Chem. Phys.* **133**, 084704-1 - 084704-6 (2010).

[81] J. Gustafson, R. Westerström, A. Resta, A. Mikkelsen, J. N. Andersen, O. Balmes, X. Torrelles, M. Schmid, P. Varga, B. Hammer, G. Kresse, C. J. Baddeley and E. Lundgren, Structure and catalytic reactivity of Rh oxides, *Catal. Today* **145**, 227-235 (2009).

[82] J. Gustafson, R. Westerström, O. Balmes, A. Resta, R. van Rijn, X. Torrelles, C. T. Herbschleb, J. W. M. Frenken and E. Lundgren, Catalytic activity of the Rh surface oxide: CO oxidation over Rh(111) under realistic conditions, *J. Phys. Chem. C* **114**, 4580-4583 (2010).

[83] J. Gustafson, R. Westerström, A. Mikkelsen, X. Torrelles, O. Balmes, N. Bovet, J. N. Andersen, C. J. Baddeley and E. Lundgren, Sensitivity of catalysis to surface structure: the example of CO oxidation on Rh under realistic conditions, *Phys. Rev. B* **78**, 045423-1 - 045423-6 (2008).

[84] J. I. Flege and P. Sutter, In situ structural imaging of CO oxidation catalysis on oxidized Rh(111), *Phys. Rev. B* **78**, 153402-1 - 153402-3 (2008).

[85] R. Westerström, J. G. Wang, M. D. Ackermann, J. Gustafson, A. Resta, A. Mikkelsen, J. N. Andersen, E. Lundgren, O. Balmes, X. Torrelles, J. W. M. Frenken and B. Hammer, Structure and reactivity of a model catalyst alloy under realistic conditions, *J. Phys.: Condens. Matter* **20**, 184018-1 - 184018-6 (2008).

[86] M. Ackermann, Operando SXRD: A new view on catalysis, PhD Thesis, Leiden University (2007).

[87] A. Farkas, K. Zalewska-Wierzbicka, C. Bachmann, J. Goritzka, D. Langsdorf, O. Balmes, J. Janek and H. Over, High pressure carbon monoxide oxidation over platinum (111), *J. Phys. Chem. C* **117**, 9932-9942 (2013).

[88] D. Miller, H. S. Casalongue, H. Bluhm, H. Ogasawara, A. Nilsson and S. Kaya, Different reactivity of the various platinum oxides and chemisorbed oxygen in CO oxidation on Pt(111), *J. Am. Chem. Soc.* **136**, 6340-6347 (2014).

[89] B. L. M. Hendriksen and J. W. M. Frenken, CO oxidation on Pt(110): scanning tunneling microscopy inside a high-pressure flow reactor, *Phys. Rev. Lett.* **89**, 046101-1 - 046101-4 (2002).

[90] M. A. van Spronsen, G. J. C. van Baarle, C. T. Herbschleb, J. W. M. Frenken and I. M. N. Groot, High-pressure operando STM studies giving insight in CO oxidation and NO reduction over Pt(110), *Catal. Today* **244**, 85-95 (2015).

[91] M. D. Ackermann, T. M. Pedersen, B. L. M. Hendriksen, O. Robach, S. C. Bobaru, I. Popa, C. Quiros, H. Kim, B. Hammer, S. Ferrer and J. W. M. Frenken, Structure and reactivity of surface oxides on Pt(110) during catalytic CO oxidation, *Phys. Rev. Lett.* **95**, 255505-1 - 255505-4 (2005).

[92] D. R. Butcher, M. E. Grass, Z. Zeng, F. Aksoy, H. Bluhm, W.-X. Li, B. S. Mun, G. A. Somorjai and Z. Liu, In situ oxidation study of Pt(110) and its interaction with CO, *J. Am. Chem. Soc.* **133**, 20319-20325 (2011).

[93] M. S. Chen, Y. Cai, Z. Yan, K. K. Gath, S. Axnanda and D. W. Goodman, Highly active surfaces for CO oxidation on Rh, Pd, and Pt, *Surf. Sci.* **601**, 5326-5331 (2007).

[94] G. Zheng and E. I. Altman, The reactivity of surface oxygen phases on Pd(100) toward reduction by CO, *J. Phys. Chem. B* **106**, 1048-1057 (2002).

[95] J. F. Weaver, J.-J. Chen and A. L. Gerrard, Oxidation of Pt(111) by gas-phase oxygen atoms, *Surf. Sci.* **592**, 83-103 (2005).

[96] H. Gabasch, A. Knop-Gericke, R. Schlögl, M. Borasio, C. Weilach, G. Rupprechter, S. Penner, B. Jenewein, K. Hayek and B. Klötzer, Comparison of the reactivity of different Pd-O species in CO oxidation, *Phys. Chem. Chem. Phys.* **9**, 533-540 (2007).

[97] W. X. Li and B. Hammer, Reactivity of a gas/metal/metal-oxide three-phase boundary: CO oxidation at the Pt(111)-c(4×2)-2CO/α-PtO_2 phase boundary, *Chem. Phys. Lett.* **409**, 1-7 (2005).

[98] E. M. C. Alayon, J. Singh, M. Nachtegaal, M. Harfouche and J. A. van Bokhoven, On highly active partially oxidized platinum in carbon monoxide oxidation over supported platinum catalysts, *J. Catal.* **263**, 228-238 (2009).

[99] T. Bligaard, J. K. Nørskov, S. Dahl, J. Matthiesen, C. H. Christensen and J. Sehested, The Brønsted-Evans-Polanyi relation and the volcano curve in heterogeneous catalysis, *J. Catal.* **224**, 206-217 (2004).

[100] H. Falsig, B. Hvolbæk, I. S. Kristensen, T. Jiang, T. Bligaard, C. H. Christensen and J. K. Nørskov, Trends in the catalytic CO oxidation activity of nanoparticles, *Angew. Chem. Int. Ed.* **47**, 4835-4839 (2008).

[101] M. M. Jaksic, Volcano plots along the periodic table, their causes and consequences on electrocatalysis for hydrogen electrode reactions, *J. New Mat. Elect. Syst.* **3**, 153-168 (2000).

[102] J. K. Nørskov, T. Bligaard, B. Hvolbæk, F. Abild-Pedersen, I. Chorkendorff and C. H. Christensen, The nature of the active site in heterogeneous metal catalysis, *Chem. Soc. Rev.* **37**, 2163-2171 (2008).

[103] B. Hammer, Y. Morikawa and J. K. Nørskov, CO chemisorption at metal surfaces and overlayers, *Phys. Rev. Lett.* **76**, 2141-2144 (1996).

[104] A. T. Fromhold Jr. and E. L. Cook, Kinetics of oxide film growth on metal crystals: thermal electron emission and ionic diffusion *Phys. Rev.* **163**, 650-664 (1967).

[105] A. T. Fromhold Jr. and E. L. Cook, Schottky emission as a rate-limiting factor in thermal oxidation of metals *Phys. Rev. Lett.* **17**, 1212-1216 (1966).

[106] A. T. Fromhold Jr. and E. L. Cook, Kinetics of oxide film growth on metal crystals: electron tunneling and ionic diffusion *Phys. Rev.* **158**, 600-612 (1967).

[107] N. Cabrera and N. F. Mott, Theory of the oxidation of metals, *Rep. Prog. Phys.* **12**, 163-184 (1948).

[108] J. Rogal, K. Reuter and M. Scheffler, CO oxidation on Pd(100) at technologically relevant pressure conditions: first-principles kinetic Monte Carlo study, *Phys. Rev. B* **77**, 155410-1 - 155410-12 (2008).

[109] J. Rogal, K. Reuter and M. Scheffler, First-principles statistical mechanics study of the stability of a subnanometer thin surface oxide in reactive environments: CO oxidation at Pd(100), *Phys. Rev. Lett.* **98**, 046101-1 - 046101-4 (2007).

[110] G. R. Wallwork, The oxidation of alloys, *Rep. Prog. Phys.* **39**, 401-485 (1976).

[111] F. Tao, M. E. Grass, Y. Zhang, D. R. Butcher, J. R. Renzas, Z. Liu, J. Y. Chung, B. S. Mun, M. Salmeron and G. A. Somorjai, Reaction-driven restructuring of Rh-Pd and Pt-Pd core-shell nanoparticles, *Science* **322**, 932-934 (2008).

[112] P. Müller, U. Hejral, U. Rütt and A. Stierle, In situ oxidation study of Pd-Rh nanoparticles on $MgAl_2O_4(001)$, *Phys. Chem. Chem. Phys.* **16**, 13866-13874 (2014).

[113] M. Dalmiglio, M. Amati, L. Gregoratti, T. O. Mentes, M. A. Nino, L. Felisari and M. Kiskinova, Oxidation of supported PtRh particles: size and morphology effects, *J. Phys. Chem. C* **114**, 16885-16891 (2010).

[114] D. C. Ford, Y. Xu and M. Mavrikakis, Atomic and molecular adsorption on Pt(111), *Surf. Sci.* **587**, 159-174 (2005).

[115] J. A. Herron, S. Tonelli and M. Mavrikakis, Atomic and molecular adsorption on Pd(111), *Surf. Sci.* **606**, 1670-1679 (2012).

[116] J. A. Herron and M. Mavrikakis, On the composition of bimetallic near-surface alloys in the presence of oxygen and carbon monoxide, *Catal. Commun.* **52**, 65-71 (2014).

[117] G. W. Graham, H.-W. Jen, O. Ezekoye, R. J. Kudla, W. Chun, X. Q. Pan and R. W. McCabe, Effect of alloy composition on dispersion stability and catalytic activity for NO oxidation over alumina-supported Pt-Pd catalysts, *Catal. Lett.* **116**, 1-8 (2007).

[118] T. R. Johns, J. R. Gaudet, E. J. Peterson, J. T. Miller, E. A. Stach, C. H. Kim, M. P. Balogh and A. K. Datye, Microstructure of bimetallic Pt-Pd catalysts under oxidizing conditions, *ChemCatChem* **5**, 2636-2645 (2013).

[119] A. Baraldi, Structure and chemical reactivity of transition metal surfaces as probed by synchrotron radiation core level photoelectron spectroscopy, *J. Phys.: Condens. Matter* **20**, 093001-1 - 093001-19 (2008).

[120] M. V. Ganduglia-Pirovano, M. Scheffler, A. Baraldi, S. Lizzit, G. Comelli, G. Paolucci and R. Rosei, Oxygen-induced Rh $3d_{5/2}$ surface core-level shifts on Rh(111), *Phys. Rev. B* **63**, 205415-1 - 205415-11 (2001).

[121] L. H. Dubois, Vibrational spectra of atomic adsorbates: carbon, oxygen, and sulfur on Rh(100), *J. Chem. Phys.* **77**, 5228-5233 (1982).

[122] J. Gustafson, A. Mikkelsen, M. Borg, E. Lundgren, L. Köhler, G. Kresse, M. Schmid, P. Varga, J. Yuhara, X. Torrelles, C. Quirós and J. N. Andersen, Self-limited growth of a thin oxide layer on Rh(111), *Phys. Rev. Lett.* **92**, 126102-1 - 126102-4 (2004).

[123] J. Gustafson, A. Mikkelsen, M. Borg, J. N. Andersen, E. Lundgren, C. Klein, W. Hofer, M. Schmid, P. Varga, L. Köhler, G. Kresse, N. Kasper, A. Stierle and H. Dosch, Structure of a thin oxide film on Rh(100), *Phys. Rev. B* **71**, 115442-1 - 115442-9 (2005).

[124] C. Dri, C. Africh, F. Esch, G. Comelli, O. Dubay, L. Köhler, F. Mittendorfer, G. Kresse, P. Dudin and M. Kiskinova, Initial oxidation of the Rh(110) surface: ordered adsorption and surface oxide structures, *J. Chem. Phys.* **125**, 094701-1 - 094701-9 (2006).

[125] J. M. D. Coey, The crystal structure of Rh_2O_3, *Acta Crystallogr. B* **26**, 1876-1877 (1970).

[126] O. Muller and R. Roy, Formation and stability of the platinum and rhodium oxides at high oxygen pressures and the structures of Pt_3O_4, β-PtO_2 and RhO_2, *J. Less-Common Met.* **16**, 129-146 (1968).

[127] W. Yu, M. D. Porosoff and J. G. Chen, Review of Pt-based bimetallic catalysis: from model surfaces to supported catalysts, *Chem. Rev.* **112**, 5780-5817 (2012).

[128] J. H. Sinfelt, Catalysis by alloys and bimetallic clusters, *Accounts Chem. Res.* **10**, 15-20 (1977).

[129] A. K. Singh and Q. Xu, Synergistic catalysis over bimetallic alloy nanoparticles, *ChemCatChem* **5**, 652-676 (2013).

[130] S. Duan and R. Wang, Bimetallic nanostructures with magnetic and noble metals and their physicochemical applications, *Progr. Nat. Sci.: Mater. Int.* **23**, 113-126 (2013).

[131] X. Liu, D. Wang and Y. Li, Synthesis and catalytic properties of bimetallic nanomaterials with various architectures, *Nano Today* **7**, 448-466 (2012).

[132] F. F. Tao, S. Zhang, L. Nguyen and X. Zhang, Action of bimetallic nanocatalysts under reaction conditions and during catalysis: evolution of chemistry from high vacuum conditions to reaction conditions, *Chem. Soc. Rev.* **41**, 7980-7993 (2012).

[133] D. Uzio and G. Berhault, Factors governing the catalytic reactivity of metallic nanoparticles, *Catal. Rev.* **52**, 106-131 (2010).

[134] V. Ponec, Alloy catalysts: the concepts, *Appl. Catal. A: Gen.* **222**, 31-45 (2001).

[135] B. Lim, M. Jiang, P. H. C. Camargo, E. C. Cho, J. Tao, X. Lu, Y. Zhu and Y. Xia, Pd-Pt bimetallic nanodendrites with high activity for oxygen reduction, *Science* **324**, 1302-1305 (2009).

[136] V. R. Stamenkovic, B. Fowler, B. S. Mun, G. Wang, P. N. Ross, C. A. Lucas and N. M. Markovic, Improved oxygen reduction activity on $Pt_3Ni(111)$ via increased surface site availability, *Science* **315**, 493-497 (2007).

[137] J. Y. Park, Y. Zhang, M. Grass, T. Zhang and G. A. Somorjai, Tuning of catalytic CO oxidation by changing composition of Rh-Pt bimetallic nanoparticles, *Nano Lett.* **8**, 673-677 (2008).

[138] J. R. Renzas, W. Huang, Y. Zhang, M. E. Grass, D. T. Hoang, S. Alayoglu, D. R. Butcher, F. F. Tao, Z. Liu and G. A. Somorjai, $Rh_{1\text{-}x}Pd_x$ nanoparticle composition dependence in CO oxidation by oxygen: catalytic activity enhancement in bimetallic systems, *Phys. Chem. Chem. Phys.* **13**, 2556-2562 (2011).

[139] S. Alayoglu and B. Eichhorn, Rh-Pt bimetallic catalysts: synthesis, characterization, and catalysis of core-shell, alloy, and monometallic nanoparticles, *J. Am. Chem. Soc.* **130**, 17479-17486 (2008).

[140] Z. Paál, N. Győrffy, A. Wootsch, L. Tóth, I. Bakos, S. Szabó, U. Wild and R. Schlögl, Preparation, physical characterization and catalytic properties of unsupported Pt-Rh catalyst, *J. Catal.* **250**, 254-263 (2007).

[141] G. W. Graham, H.-W. Jen, O. Ezekoye, R. J. Kudla, W. Chun, X. Q. Pan and R. W. McCabe, Effect of alloy composition on dispersion stability and catalytic activity for NO oxidation over alumina-supported Pt-Pd catalysts, *Catal. Lett.* **116**, 1-8 (2007).

[142] G. R. Rao, Chemistry of bimetallic surfaces, *Curr. Sci.* **75**, 901-910 (1998).

[143] M. Mavrikakis, B. Hammer and J. K. Nørskov, Effect of strain on the reactivity of metal surfaces, *Phys. Rev. Lett.* **81**, 2819-2822 (1998).

[144] J. R. Kitchin, J. K. Nørskov, M. A. Barteau and J. G. Chen, Modification of the surface electronic and chemical properties of Pt(111) by subsurface *3d* transition metals, *J. Chem. Phys.* **120**, 10240-10246 (2004).

[145] J. R. Kitchin, J. K. Nørskov, M. A. Barteau and J. G. Chen, Role of strain and ligand effects in the modification of the electronic and chemical properties of bimetallic surfaces, *Phys. Rev. Lett.* **93**, 156801-1 - 156801-4 (2004).

[146] Catalysis by design, *Nat. nanotechnol.* **3**, 575-575 (2008).

[147] J. Greeley and M. Mavrikakis, Alloy catalysts designed from first principles, *Nat. Mater.* **3**, 810-815 (2004).

[148] F. Besenbacher, I. Chorkendorff, B. S. Clausen, B. Hammer, A. M. Molenbroek, J. K. Nørskov and I. Stensgaard, Design of a surface alloy catalyst for steam reforming, *Science* **279**, 1913-1915 (1998).

[149] F. F. Tao and M. Salmeron, In situ studies of chemistry and structure of materials in reactive environments, *Science* **331**, 171-174 (2011).

[150] F. Tao, M. E. Grass, Y. Zhang, D. R. Butcher, F. Aksoy, S. Aloni, V. Altoe, S. Alayoglu, J. R. Renzas, C.-K. Tsung, Z. Zhu, Z. Liu, M. Salmeron and G. A. Somorjai, Evolution of structure and chemistry of bimetallic nanoparticle catalysts under reaction conditions, *J. Am. Chem. Soc.* **132**, 8697-8703 (2010).

[151] F. Mittendorfer, N. Seriani, O. Dubay and G. Kresse, Morphology of mesoscopic Rh and Pd nanoparticles under oxidizing conditions, *Phys. Rev. B* **76**, 233413-1 - 233413-4 (2007).

[152] U. Hejral, A. Vlad, P. Nolte and A. Stierle, In situ oxidation study of Pt nanoparticles on MgO(001), *J. Phys. Chem C* **117**, 19955-19966 (2013).

[153] P. Nolte, A. Stierle, N. Kasper, N. Y. Jin-Phillipp, N. Jeutter and H. Dosch, Reversible shape changes of Pd nanoparticles on MgO(100), *Nano Lett.* **11**, 4697-4700 (2011).

[154] P. L. Hansen, J. B. Wagner, S. Helveg, J. R. Rostrup-Nielsen, B. S. Clausen and H. Topsøe, Atom-resolved imaging of dynamic shape changes in supported copper nanocrystals, *Science* **295** 2053-2055 (2002).

[155] K. Reuter and M. Scheffler, Oxide formation at the surface of late *4d* transition metals: insights from first-principles atomistic thermodynamics, *Appl. Phys. A* **78**, 793-798 (2004).

[156] K. T. Jacob and D. Prusty, Thermodynamic properties of RhO_2, *J. Alloys Compd.* **507**, L17-L20 (2010).

[157] J. Rogal, K. Reuter and M. Scheffler, CO oxidation at Pd(100): a first-principles constrained thermodynamics study, *Phys. Rev. B* **75**, 205433-1 - 205433-11 (2007).

[158] N. Kasper, P. Nolte and A. Stierle, Stability of surface and bulk oxides on Pd(111) revisited by in situ x-ray diffraction, *J. Phys. Chem. C* **116**, 21459-21464 (2012).

[159] N. Seriani, W. Pompe and L. C. Ciacchi, Catalytic oxidation activity of Pt_3O_4 surfaces and thin films, *J. Phys. Chem. B* **110**, 14860-14869 (2006).

[160] H. L. Skriver and N. M. Rosengaard, Surface energy and work function of elemental metals, *Phys. Rev. B* **46**, 7157-7168 (1992).

[161] M. Sporn, E. Platzgummer, E. L. D. Gruber, M. Schmid, W. Hofer and P. Varga, A quantitative LEED analysis of the oxygen-induced p(3×1) reconstruction of $Pt_{25}Rh_{75}$(100), *Surf. Sci.* **416**, 384-395 (1998).

[162] P. J. F. Harris, Growth and structure of supported metal catalyst particles, *Int. Mater. Rev.* **40**, 97-115 (1995).

[163] M. J. J. Jak, C. Konstapel, A. van Kreuningen, J. Verhoeven and J. W. M. Frenken, Scanning tunneling microscopy study of the growth of small palladium particles on TiO_2(110), *Surf. Sci.* **457**, 295-310 (2000).

[164] K. Morgenstern, G. Rosenfeld and G. Comsa, Local correlation during Ostwald ripening of two-dimensional islands on Ag(111), *Surf. Sci.* **441**, 289-300 (1999).

[165] P. A. Thiel, M. Shen, D.-J. Liu and J. W. Evans, Coarsening of two-dimensional nanoclusters on metal surfaces, *J. Phys. Chem. C* **113**, 5047-5067 (2009).

[166] H. Birgersson, L. Eriksson, M. Boutonnet and S. G. Järås, Thermal gas treatment to regenerate spent automotive three-way exhaust gas catalysts (TWC), *Appl. Catal. B: Environ.* **54**, 193-200 (2004).

[167] A. Cao, R. Lu and G. Veser, Stabilizing metal nanoparticles for heterogeneous catalysis, *Phys. Chem. Chem. Phys.* **12**, 13499-13510 (2010).

[168] J. Als-Nielsen: *Elements of modern x-ray physics*, John Wiley and Sons, Ltd (2001).

[169] B. E. Warren, *X-ray diffraction*, Dover Publications, Inc, New York (1990).

[170] I. K. Robinson and D. J. Tweet, Surface x-ray diffraction, *Rep. Prog. Phys.* **55** 599-651 (1992).

[171] R. Feidenhans'l, Surface structure determination by x-ray diffraction, *Surf. Sci. Rep.* **10**, 105-188 (1989).

[172] G. Renaud, Oxide surfaces and metal/oxide interfaces studied by grazing incidence x-ray scattering, *Surf. Sci. Rep.* **32** 5-90 (1998).

[173] E. Vlieg, ROD: a program for surface x-ray crystallography. *J. Appl. Crystallogr.* **33**, 401-405 (2000).

[174] H. Dosch, Evanescent absorption in kinematic surface Bragg diffraction, *Phys. Rev. B* **35**, 2137-2143 (1987).

[175] G. H. Vineyard, Grazing-incidence diffraction and the distorted-wave approximation for the study of surfaces, *Phys. Rev. B* **26**, 4146-4159 (1982).

[176] N. Kasper, A. Stierle, P. Nolte, Y. Jin-Phillipp, T. Wagner, D. G. de Oteyza and H. Dosch, In situ oxidation study of MgO(100) supported Pd nanoparticles, *Surf. Sci.* **600**, 2860-2867 (2006).

[177] P. Nolte, A. Stierle, N. Kasper, N. Y. Jin-Phillipp, H. Reichert, A. Rühm, J. Okasinski, H. Dosch and S. Schöder, Combinatorial high-energy x-ray microbeam study of the size-dependent oxidation of Pd nanoparticles on MgO(100), *Phys. Rev. B* **77**, 115444-1 - 115444-7 (2008).

[178] L. G. Parratt, Surface studies of solids by total reflection of x-rays, *Phys. Rev.* **95**, 359-369 (1954).

[179] S. K. Sinha, E. B. Sirota and S. Garoff, X-ray and neutron scattering from rough surfaces, *Phys. Rev. B* **38**, 2297-2311 (1988).

[180] D. K. G. de Boer, Influence of the roughness profile on the specular reflectivity of x-rays and neutrons, *Phys. Rev. B* **49**, 5817-5820 (1994).

[181] D. K. G. de Boer, X-ray reflection and transmission by rough surfaces, *Phys. Rev. B* **51**, 5297-5305 (1995).

[182] D. K. G. de Boer and A. J. G. Leenaers, Probing interface roughness by x-ray scattering, *Physica B* **221**, 18-26 (1996).

[183] L. Névot and P. Croce, Characterization of surfaces by grazing x-ray reflection - application to the study of polishing of some silicate-glasses, *Rev. Phys. Appl.* **15**, 761-779 (1980).

[184] FEWLAY: programme for the fitting of reflectivity curves by A. Stierle (andreas.stierle@desy.de)

[185] H. Butt, K. Graf and M. Kappl, *Physics and chemistry of interfaces*, Wiley-VHC, Weinheim (2006).

[186] M. Hosokawa, K. Nogi, M. Naito and T. Yokoyama, *Nanoparticle technology handbook*, Elsevier, Amsterdam (2012).

[187] O. Balmes, R. van Rijn, D. Wermeille, A. Resta, L. Petit, H. Isern, T. Dufrane and R. Felici, The ID03 surface diffraction beamline for in-situ and real-time x-ray investigations of catalytic reactions at surfaces, *Catal. Today* **145**, 220-226 (2009).

[188] R. van Rijn, M. D. Ackermann, O. Balmes, T. Dufrane, A. Geluk, H. Gonzalez, H. Isern, E. de Kuyper, L. Petit, V. A. Sole, D. Wermeille, R. Felici and J. W. M. Frenken, Ultrahigh vacuum/high-pressure flow reactor for surface x-ray diffraction and grazing incidence small angle x-ray scattering studies close to conditions for industrial catalysis, *Rev. Sci. Instr.* **81**, 014101-1 - 014101-8 (2010).

[189] Leiden Probe Microscopy: www.leidenprobemicroscopy.com

[190] J. Strempfer, S. Francoual, D. Reuther, D. K. Shukla, A. Skaugen, H. Schulte-Schrepping, T. Kracht and H. Franz, Resonant scattering and diffraction beamline P09 at Petra III, *J. Synchrotron Rad.* **20**, 541-549 (2013).

[191] H. Reichert, V. Honkimäki, A. Snigirev, S. Engemann and H. Dosch, A new x-ray transmission-reflection scheme for the study of deeply buried interfaces using high-energy microbeams, *Physica B* **336**, 46-55 (2003).

[192] P. Nolte, In situ oxidation study of supported Rh and Pd nanoparticles, PhD Thesis, University of Stuttgart (2009).

[193] P. Müller, Oxidation von Legierungsnanopartikeln untersucht mit in situ Röntgenbeugung, Diploma Thesis, University of Siegen (2012).

[194] Homepage of beamline P07, Petra III:

http://photon-science.desy.de/facilities/petra_iii/beamlines/p07_high_energy_materials_science/index_eng.html.

[195] A. V. Kalinkin, A. V. Pashis and V. I. Bukhtiyarov, CO oxidation over the Pt-Rh system. 3. Reaction on a heterophase surface, *React. Kinet. Catal. Lett.* **78**, 121-127 (2003).

[196] F. Esch, S. Günther, E. Schütz, A. Schaak, I. G. Kevrekidis, M. Marsi, M. Kiskinova and R. Imbihl, Chemical waves and adsorbate-induced segregation on a Pt(100) surface microstructured with a thin Rh/Pt film, *Surf. Sci.* **443**, 245-252 (1999).

[197] M. Behrens, F. Studt, I. Kasatkin, S. Kühl, M. Hävecker, F. Abild-Pedersen, S. Zander, F. Girgsdies, P. Kurr, B.-L. Kniep, M. Tovar, R. W. Fischer, J. K. Nørskov and R. Schlögl, The active site of methanol synthesis over Cu/ZnO/Al_2O_3 industrial catalysts, *Science* **336**, 893-897 (2012).

[198] E. Lundgren, J. Gustafson, A. Resta, J. Weissenrieder, A. Mikkelsen, J. N. Andersen, L. Köhler, G. Kresse, J. Klikovits, A. Biederman, M. Schmid and P. Varga, The surface oxide as a source of oxygen on Rh(111), *J. Electron Spectrosc. Relat. Phenom.* **144**, 367-372 (2005).

[199] K. Okumura, S. Hyodo, S. Noda and Y. Maruyama, Growth of Pt-Rh alloy crystallites on α-Al_2O_3 studied by atomic force microscopy and Rutherford backscattering spectroscopy, *J. Phys. Chem. B* **102**, 2350-2355 (1998).

[200] L. D. Schmidt and T. Wang, Morphology and surface composition of alloy particles in reactive atmospheres, *J. Vac. Sci. Technol.* **18**, 520-528 (1981).

[201] M. Chen, T. Wang and L. D. Schmidt, Morphology of Pt-Rh alloy crystallites on amorphous SiO_2, *J. Catal.* **60**, 356-368 (1979).

[202] E. Ruckenstein and Y. F. Chu, Redispersion of platinum crystallites supported on alumina - role of wetting, *J. Catal.* **59**, 109-122 (1979).

[203] A. Cao and G. Veser, Exceptional high-temperature stability through distillation-like self-stabilization in bimetallic nanoparticles, *Nat. Mater.* **9**, 75-81 (2010).

[204] B. Ingham, T. H. Lim, C. J. Dotzler, A. Henning, M. F. Toney and R. D. Tilley, How nanoparticles coalesce: an in situ study of Au nanoparticle aggregation and grain growth, *Chem. Mater.* **23**, 3312-3317 (2011).

[205] M. José-Yacamán, C. Gutierrez-Wing, M. Miki, D.-Q. Yang, K. N. Piyakis and E. Sacher, Surface diffusion and coalescence of mobile metal nanoparticles, *J. Phys. Chem. B* **109**, 9703-9711 (2005).

[206] G. Ertl in *Catalysis: Science and Technology* (J. R. Anderson and M. Boudart Eds., vol. 4, Springer-Verlag, Berlin, 245, 1983).

[207] K. H. Hansen, T. Worren, S. Stempel, E. Lægsgaard, M. Bäumer, H.-J. Freund, F. Besenbacher and I. Stensgaard, Palladium nanocrystals on Al_2O_3: structure and adhesion energy, *Phys. Rev. Lett.* **83**, 4120-4123 (1999).

[208] W. L. Winterbottom, Equilibrium shape of a small particle in contact with a foreign substrate, *Acta Met.* **15**, 303-310 (1967).

[209] W. Vervisch, C. Mottet and J. Goniakowski, Effect of epitaxial strain on the atomic structure of Pd clusters on MgO(100) substrate - a numerical simulation study, *Eur. Phys. J. D* **24**, 311-314 (2003).

[210] Y.-H. Wen, R. Huang, X.-M. Zeng, G. F. Shao and S.-G. Sun, Tetrahexahedral Pt-Pd alloy nanocatalysts with high-index facets: an atomistic perspective on thermodynamic and shape stabilities, *J. Mater. Chem. A* **2**, 1375-1382 (2014).

[211] Y.-J. Deng, N. Tian, Z.-Y. Zhou, R. Huang, Z.-L. Liu, J. Xiao and S.-G. Sun, Alloy tetrahexahedral Pd-Pt catalysts: enhancing significantly the catalytic activity by synergy effect of high-index facets and electronic structure, *Chem. Sci.* **3**, 1157-1161 (2012).

[212] J. Park, A. Oh, H. Baik, Y. S. Choi, S. J. Kwon and K. Lee, One pot synthesis of nanoscale phase-segregated PdPt nanoarchitectures *via* unusual Pt-doping induced structural reorganization of a Pd nanosheet into a PdPt nanotent, *Nanoscale* **6**, 10551-10555 (2014).

[213] W. Andreoni and C. M. Varma, Binding and dissociation of CO on transition-metal surfaces, *Phys. Rev. B* **23**, 437-444 (1981).

[214] A. B. Anderson and M. K. Awad, Factors determining CO adsorption sites on Pd and Pt (100) and (111) surfaces: theoretical study, *J. Am. Chem. Soc.* **107**, 7854-7857 (1985).

[215] F. Abild-Pedersen and M. P. Andersson, CO adsorption energies on metals with correction for high coordination adsorption sites - a density functional study, *Surf. Sci.* **601**, 1747-1753 (2007).

[216] K. Yun, Y.-H. Cho, P.-R. Cha, J. Lee, H.-S. Nam, J. S. Oh, J.-H. Choi and S.-C. Lee, Monte Carlo simulations of the structure of Pt-based bimetallic nanoparticles, *Acta Mater.* **60**, 4908-4916 (2012).

[217] M. Salmeron, L. Brewer and G. A. Somorjai, The structure and stability of surface platinum oxide and of oxides of other noble metals, *Surf. Sci.* **112**, 207-228 (1981).

[218] C. Carrillo, T. R. Johns, H. Xiong, A. DeLaRiva, S. R. Challa, R. S. Goeke, K. Artyushkova, W. Li, C. H. Kim and A. K. Datye, Trapping of mobile Pt species by PdO nanoparticles under oxidizing conditions, *J. Phys. Chem. Lett.* **5**, 2089-2093, (2014).

[219] G. K. Williamson and W. H. Hall, X-ray line broadening from filed aluminum and wolfram, *Acta Met.* **1**, 22-31 (1953).

[220] E. Vlieg, Integrated intensities using a six-circle surface x-ray diffractometer, *J. Appl. Crystallogr.* **30**, 532-543 (1997).

List of Publications

7.) **U. Hejral**, P. Müller, O. Balmes, D. Pontoni and A. Stierle, Tracking the shape-dependent sintering of platinum-rhodium model catalysts under operando conditions, *Nature Comm.* **7**, 10964-1 - 10964-8 (2016).

6.) D. Franz, N. Blanc, J. Coraux, G. Renaud, S. Runte, T. Gerber, C. Busse, T. Michely, P. Feibelman, **U. Hejral** and A. Stierle, Atomic structure of Pt nanoclusters supported by grapheme/Ir(111) and reversible transformation under CO exposure, *Phys. Rev. B.* **93**, 045426-1 - 045426-8 (2016).

5.) M. Shipilin, J. Gustafson, C. Zhang, L. R. Merte, A. Stierle, **U. Hejral**, U. Rütt, O. Gutowski, M. Skoglundh, P.-A. Carlsson and E. Lundgren, Transient structures of PdO during CO oxidation over Pd(100), *J. Phys. Chem. C* **119**, 15469-15476 (2015).

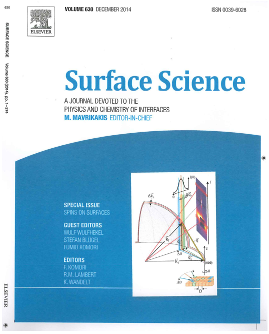

630

SURFACE SCIENCE Volume 630 (2014), pp. 1–374

ELSEVIER

VOLUME 630 DECEMBER 2014

ISSN 0039-6028

Surface Science

A JOURNAL DEVOTED TO THE
PHYSICS AND CHEMISTRY OF INTERFACES
M. MAVRIKAKIS EDITOR-IN-CHIEF

SPECIAL ISSUE
SPINS ON SURFACES

GUEST EDITORS
WULF WULFHEKEL
STEFAN BLÜGEL
FUMIO KOMORI

EDITORS
F. KOMORI
R.M. LAMBERT
K. WANDELT

ELSEVIER

4.) M. Shipilin, **U. Hejral**, E. Lundgren, L. R. Merte, C. Zhang, A. Stierle, U. Rütt, O. Gutowski, M. Skoglundh, P.-A. Carlsson and J. Gustafson, Quantitative surface structure determination using in situ high-energy SXRD: Surface oxide formation on Pd(100) during catalytic CO oxidation, *Surf. Sci.* **630**, 229-235 (2014).

3.) J. Gustafson, M. Shipilin, C. Zhang, A. Stierle, **U. Hejral**, U. Rütt, O. Gutowski, P.-A. Carlsson, M. Skoglundh and E. Lundgren, High-energy surface x-ray diffraction for fast structure determination, *Science* **343**, 758-761 (2014).

2.) P. Müller, **U. Hejral**, U. Rütt and A. Stierle, In situ oxidation study of Pd-Rh nanoparticles on $MgAl_2O_4(001)$, *Phys. Chem. Chem. Phys.* **16**, 13866-13874 (2013).

1.) U. Hejral, A. Vlad, P. Nolte and A. Stierle, In situ oxidation study of Pt nanoparticles on MgO(001), *J. Phys. Chem. C* **117**, 19955-19966 (2013).

Submitted manuscripts

M. Shipilin, L. R. Merte, J. Gustafson, A. Stierle, **U. Hejral**, N. M. Martin, C. Zhang, D. Franz, V. Kilic and E. Lundgren, The influence of incommensurability on the long range periodicity of the Pd(100)-$(\sqrt{5}\times\sqrt{5})R27°$-PdO(101), *submitted to Surface Science.*

Highlighted results

Tracking live how catalysts deteriorate, *ESRF News*, (2016).
http://www.esrf.eu/home/news/general/content-news/general/catalyst_deterioration.html

Katalysator-Verschleiß live im Blick, *DESY News*, (2016),
http://www.desy.de/aktuelles/news_suche/index_ger.html?openDirectAnchor=948

High-energy SXRD for fast surface structure determination, *Photon Science 2014, Highlights and Annual Report*, (2014).

Acknowledgements

The work on the exciting topic of nanoparticle catalysis and the use of synchrotron radiation facilities has allowed me to visit many places and to encounter many people, without whom the results of this thesis could not have been obtained.

First of all, I am greatly indebted to my supervisor **Prof. Dr. A. Stierle**, who offered me this interesting research topic. He always took his time for helpful discussions and greatly supported me in all respects. He decisively supported the progress on the data analysis and provided me with many useful advices concerning the writing of this thesis.

I am very thankful to **Prof. Dr. W. Wurth** for being the second advisor of this thesis, **Prof. Dr. D. Pfannkuche** for the chairmanship of the oral examination, as well as **Prof. Dr. E. Lundgren** and **Prof. Dr. P. Gaal** for being examiners therein.

I am very grateful to my colleagues **Dirk Franz** and **Patrick Müller**, who always supported me when working in the lab as well as during numerous exhausting nightshift beamtimes. We will never forget the tilted UFO ;-).

My special thanks go to all my other (also former) room mates in the NanoLab PhD office: **Björn Arndt**, **Konstantin Krausert**, **Emanuele Minutella** and **Dr. Sergey Volkov**, who created an incredible nice and enjoyable working atmosphere day by day and who supported and helped me in all possible respects.

This also holds for all other members of the **DESY NanoLab** group: **Marcus Creutzburg**, **Dr. Arti Dangwal Pandey**, **Simon Geile**, **Dr. Elin Grånäs**, **Satishkumar Kulkarni**, **Dr. Roman Shayduk** and **Susanne Weigert**. I would especially like to thank **Dr. Heshmat Noei** and **Dr. Vedran Vonk** for their support during the Easter P07 beamtime, as well as **PD Dr.-Ing. Thomas Keller** for organizing the SEM measurements with companies and other research groups.

I am very grateful to the **ID03 staff** at the ESRF: **Dr. Olivier Balmes**, **Dr. Roberto Felici**, **Dr. Helena Isern** and **Thomas Dufrane**, who welcomed me in their team very warmly during my three month's stay at the ESRF at the very beginning of my PhD, and who gave me the possibility to do my first measurements with the ID03 in-situ catalysis chamber. In this context, I also want to thank **Dr. Gertjan van Baarle** from Leiden Probe Microscopy, who always helped immediately in case there were any problems with the NanoLab UFO.

Moreover, I would like to thank the **P09 staff** at Petra III, and hence **Dr. Jörg Strempfer**, **Dr. Sonia Francoual**, **David Reuther** as well as **Dr. Arvid Skaugen**, who welcomed me in their group at DESY before the NanoLab started to exist. In addition, I am very grateful for their help and support during beamtimes at beamline P09. I also would like to thank **Dr. Jozef Bednarcik** and **Jana Michalikova** with whom I shared an office for quite some time at the beginning of my stay at DESY.

During beamtimes at the high energy beamlines P07, Petra III, and ID15A, ESRF, I could always count on the help and the assistance of the respective beamline staff. Hence, I would like to thank **Dr. Uta Rütt** and **Olof Gutowksi** at beamline P07 as well as **Dr. Diego Pontoni** and **Dr. Veijo Honkimäki** at beamline ID15A for their great support.

Apart from the people mentioned above, I was often helped by external group members during my measurements, was granted measurement time and could in addition be part of very interesting and fruitful collaborations. In this respect I am very grateful to **Mikhail Shipilin**, **Dr. Johan Gustafson**, **Dr. Willem Onderwaater**, **Dr. Richard van Rijn**, **Dr. Sander Robool**, **Dr. Per-Anders Carlsson**, **Prof. Dr. Magnus Skoglundh** as well as **Chu Zhang**: I always enjoyed and appreciated very much working with you.

Last but not least, my special thanks go to my family and friends, especially to **my parents**, to **Helge**, **Stephi** and **Merle** :-) as well as to **Georg**. I am very grateful for and appreciate very much your support in all respects. I am thankful for your understanding and patience, especially during the writing period of the thesis.